A CFD ANALYSIS ON THE FLUID-STRUCTURE INTERACTION OF OFFSHORE WAVE AND WIND ENERGY DEVICES

Xiang Li

A thesis submitted in fulfilment of the requirements for the degree of

Doctor of Philosophy

Department of Naval Architecture Ocean and Marine Engineering

University of Strathclyde

Supervised by: Professor Qing Xiao, Professor Atilla Incecik

Declaration

This thesis is the result of the author's original research. It has been composed by the author and has not been previously submitted for examination which has led to the award of a degree.

Xiang Li

Signature: Xiang Li Date: 1/6/2024

Acknowledgement

I wish to express my deepest gratitude to my primary supervisor, Professor Qing Xiao, for her steadfast support, patience, and expertise in CFD throughout my PhD journey. Her considerable dedication of time and effort in guiding my research is profoundly appreciated.

I am also profoundly thankful to my secondary supervisor, Professor Atilla Incecik, for his invaluable advice and assistance. His passion for life and work has been a constant source of inspiration.

I extend my thanks to the entire staff of the NAOME department for their kind assistance with administrative matters.

My sincere appreciation goes to my colleagues in the NAOME department for their help with my research and to all my friends in Glasgow for making my life more enjoyable.

I gratefully acknowledge the scholarship from the University of Strathclyde and the China Scholarship Council (CSC) through the University Research Studentship.

Finally, I am deeply indebted to my family for their boundless love and encouragement. I also wish to thank my beloved girlfriend, Miss Peng Su, for her understanding and support, which continually encourages me to delve deeper into the sea of research.

Abstract

The 21st century is recognised as the era of the ocean, where the global agreement on achieving net-zero emissions, together with the energy crisis caused by geopolitical factors, has led to substantial growth in the development of Offshore Renewable Energy (ORE). In this rapidly expanding field, this thesis specifically concentrates on offshore wave and wind energy. A high-fidelity numerical tool with Computational Fluid Dynamics (CFD) method is further developed based on the open-source CFD toolbox OpenFOAM. With high numerical accuracy, it enables the simulation of fluid-structure interaction (FSI) problems associated with wave energy converter (WEC) and floating offshore wind turbine (FOWT) in the time domain, offering a cost-effective alternative to physical testing in wave tanks or basins.

The aim of this study is to broaden the applicability of the present tool for the FSI analysis of WEC and FOWT. The main challenge in the present FSI study is the requirement for supplementary solvers for multiphysics simulations. Different structural solvers and aerodynamic models are needed for various scenarios. Therefore, an integrated multiphysics simulation framework is further developed by integrating an aerodynamic model for wind turbine analysis, different structural models for flexible and multi-body structures analysis, and mooring system models. This framework accounts for the complexities of various environmental conditions and operational contexts. With this tool, various scenarios of WECs and FOWTs are studied.

The thesis first studies two innovative WECs. The first configuration features a multi-body WEC system comprising multiple floats and interconnected sub-structures. It is numerically analysed using the current CFD tool coupled with an external multi-body solver. The interaction force among sub-structures can be accurately captured, and the results indicate that the response mode of the individual float is strongly affected by the mechanical linking arms and the incident wave conditions, which is difficult to achieve with only the CFD solver itself. The predicted peak output is found to increase with the

decreasing of wave period and an optimal device's damping to reach a maximum power capture exists, which varies with wave period and wave height.

The second configuration involves a flexible WEC constructed of hyper-elastic material, which is analysed by coupling a Finite Element Analysis (FEA) code into the current CFD solver. A strongly nonlinear hyper-elastic material is used for the WEC, and its dynamic response under regular waves is studied. Results show that adopting hyper-elastic material has improved performance in power generation compared to linear-elastic material. Additionally, compared to conventional rigid-body WECs, the fWEC can harvest considerable wave energy within a much wider range of wave periods.

Another part of the FSI study is on FOWT, which first examines the motion response of individual supporting platforms under wave-current conditions. When considering the ocean current interaction of blunt structures, a low-frequency sway motion of the FOWT platform exists, the so-called Vortex-Induced Motion (VIM), that cannot be solved with potential flow theory and other low-fidelity methods. The dynamic response of FOWT platforms to waves and currents from different directions is studied, revealing that non-colinear interactions can intensify VIM. Present findings suggest that smaller waves may also induce significant platform motions in the presence of current.

Subsequently, it explores the performance of a fully coupled wind turbine array in the presence of waves by coupling the Actuator Line Model (ALM). This significantly reduces the time cost and complexity compared to the blade resolved method, making the simulation of FOWT farm simulation possible. The three FOWTs with different staggered layouts are simulated, and their dynamic response and wake interactions are analysed. The results indicate that the periodic motion caused by waves introduces an oscillation in the power output and thrust. It is also found that the pitch and surge motion have an opposite influence on the power output.

Publications

Journal Articles

Li, X., Xiao, Q., Wang, E., Peyrard, C. and Gonçalves, R.T., 2023. The dynamic response of floating offshore wind turbine platform in wave–current condition. *Physics of Fluids*, 35(8), https://doi.org/10.1063/5.0158917.

Li, X. and Xiao, Q., 2022. A numerical study on an oscillating water column wave energy converter with hyper-elastic material. *Energies*, 15(22), p.8345, https://doi.org/10.3390/en15228345.

Li, X., Xiao, Q., Zhou, Y., Ning, D., Incecik, A., Nicoll, R., McDonald, A. and Campbell, D., 2022. Coupled CFD-MBD numerical modelling of a mechanically coupled WEC array. *Ocean Engineering*, 256, p.111541, https://doi.org/10.1016/j.oceaneng.2022.111541.

Conference Papers

Li, X., Xiao, Q., Gonçalves, R.T. and Peyrard, C., 2022, June. A coupled wave-current-structure study for a floating offshore wind turbine platform. *In Proceedings of ASME 2022 41st International Conference on Offshore Mechanics and Arctic Engineering*. Hamburg, Germany. Paper No. OMAE2022-79016.

Li, X., Xiao, Q., Luo, Y., Moretti, G., Fontana, M. and Righi, M., 2021, September. Dynamic response of a novel flexible wave energy converter under regular waves. *In The 14th European Wave and Tidal Energy Conference* (pp. 1-7). Plymouth, UK.

Li, X., Xiao, Q., Zhou, Y., Incecik, A. and Ning, D., 2020. July. A study on wave energy array with CFD combined with multibody dynamic method. *In 7th PRIMaRE Conference*. Plymouth, UK.

Table of Contents

List of Figures

List of Tables

Nomenclature

Roman Symbols

a_c	Motion amplitudes induced by current
a_w	Motion amplitudes induced by wave
C_a	Added mass coefficient
C_p	Power coefficients
C_t	Thrust coefficients
C_t	Thrust coefficients
D	Diameter of structure
d	Water depth
f_n	Natural frequency
f_y	Dominant frequency along y direction
H	Wave height
k	Wave number
l	Characteristic length of the structure
P	Power output
r_c	Unstretched radius of the membrane
Re	Reynolds number
T	Wave period

T_n	Natural period
U	Inlet speed of fluid
u_i	Fluid velocity
V	Voltages on the membrane
V_r	Reduced velocity
x_i	Cartesian coordinates
z_{tip}	Tip displacement of the membrane

Greek Symbols

α	Volumn fraction
ε	Strain
η	Free surface elevation
θ	Angle between current and waves
λ	Tip speed ratio
μ_a	Dynamic viscosity of air
μ_w	Dynamic viscosity of water
ν	Kinematic viscosity of fluid
ρ_a	Density of air
ρ_w	Density of water
σ_U	Particle velocity amplitude in waves

σ_{eq}	Von mises equivalent stress
τ	Torque

Abbreviations

ADM	Actuator disk model
ALE	Arbitrary lagrangian-eulerian
ALM	Actuator line model
BEM	Blade element momentum
CF	Cross-flow
CFD	Computational fluid dynamic
CSD	Computational solid dynamics
DAE	Differential-algebraic equations
DE	Dielectric elastomer
DEG	Dielectric elastomer generator
DES	Detached eddy simulation
DWM	Dynamic wake meandering
ESR	Effective stress range
FEA	Finite element analysis
FFT	Fast fourier transform
FOWT	Floating offshore wind turbine

FPA	Floating-point absorber
FSI	Fluid-structure interaction
FVM	Free vortex method
fWEC	Flexible wave energy converter
HAWT	Horizontal axis wind turbines
HOBEM	Higher-order boundary element method
HOS	Higher-order spectral method
HPC	High-performance computing
IEF	Interaction effect factor
IL	In-line
LCOE	Levelized cost of energy
LES	Large eddy simulation
NREL	National renewable energy laboratory
NRIFE	National research institute of fisheries engineering
NS	Navier-stokes
OC4	Offshore code comparison collaboration, continuation
ORE	Offshore renewable energy
OWC	Oscillating water columns

PISO	Pressure implicit with splitting of operator
PTO	Power take-off
RANS	Reynolds averaged navier-stokes
RAO	Response amplitude operator
RBF	Radial basis functions
RMS	Root mean square
SIMPLE	Semi-implicit method for pressure-linked equations
SS	Semi-submersible
SWL	Static water level
TLP	Tension leg platform
TSR	Tip speed ratio
VAWT	Vertical axis wind turbines
VIM	Vortex-induced motion
VOF	Volume of fluid
WALE	Wall-adapted local eddy-viscosity
WEC	Wave energy converter

Chapter 1 Introduction

1.1 FSI in Offshore Renewable Energy

To support the modern industry, a huge amount of energy is consumed worldwide every year, most of which is conventional fossil energy (Energy Institute, 2023; Moriarty and Honnery, 2023). However, traditional energy sources are increasingly vulnerable due to unstable international conditions, including the potential for wars and financial crises in various regions. Substituting fossil fuels with renewable energy can avoid such dependency and also aligns with the objectives of the Paris Agreement to reduce emissions. Therefore, many countries have implemented policies to develop their corresponding renewable energy industry. For example, the UK government aims for renewables to contribute between 86-90% of power generation by 2035 (ESO, 2021). The EU also has a similar plan to increase the share of renewable energy to 33% by 2030 (IRENA, 2018, 2019), together with many other countries with their renewable energy policies (Martinot et al., 2007; Sen and Ganguly, 2017).

Offshore renewable energy (ORE), as a major part of renewable energy, has been rapidly developing, particularly for coastal nations with limited land availability, where floating offshore wind turbines (FOWT) and wave energy converters (WEC) are typical representatives. Unlike onshore renewable energy, complex interactions exist between fluids (such as wind and waves) and the structure of the offshore infrastructure. Thus, these ORE devices face numerous fluid-structure interaction (FSI) challenges that significantly impact their performance and reliability. For FOWTs, FSI issues can arise due to the dynamic loading from wind and waves, causing vibrations and stresses on the turbine structures. These interactions can lead to fatigue damage, reduced efficiency, and increased maintenance costs. Additionally, the motion of the floating platforms introduces additional influence on power production (Zhong et al., 2023). WECs, on the other hand, experience even more intense FSI effects due to their direct exposure to wave forces. These devices must be designed to efficiently capture wave energy while

also enduring the harsh and variable ocean environment. The constant interaction between the waves and the converter's structure can result in significant loads and potential structural failures for the mooring system if not properly addressed (Qiao et al., 2020).

Therefore, addressing FSI challenges is crucial for ORE systems like WEC and FOWT, which require advanced modelling and simulation techniques to accurately predict the behaviour of these systems under complex ocean conditions.

1.2 FSI in WECs

The FSI issue stands as one of the most crucial factors influencing WECs. This significance is underscored when considering the vast potential of wave energy globally, which is estimated to reach an impressive 32,000 TWh per year. Wave energy presents a multitude of advantages. Firstly, it has a relatively high energy density. Although it originates from solar power, its power density is 10 to 20 times the solar power per square meter (Falnes, 2007). Secondly, as mentioned, the transmission loss of wave energy is low. Finally, wave power devices have a high operational capacity, generating power up to 90% of the time, while wind and solar power devices typically have an operational time of about 20–30% (Pelc and Fujita, 2002). The wave energies are primarily concentrated in the mid-latitude regions, as shown in Figure 1.2.

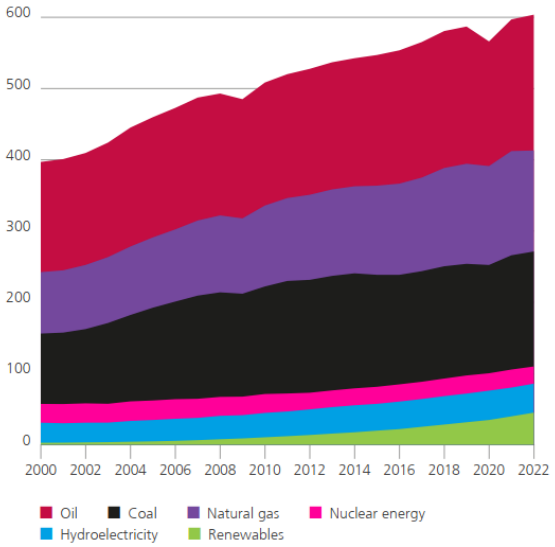

Figure 1.1 Global energy consumption by source (Energy Institute, 2023)

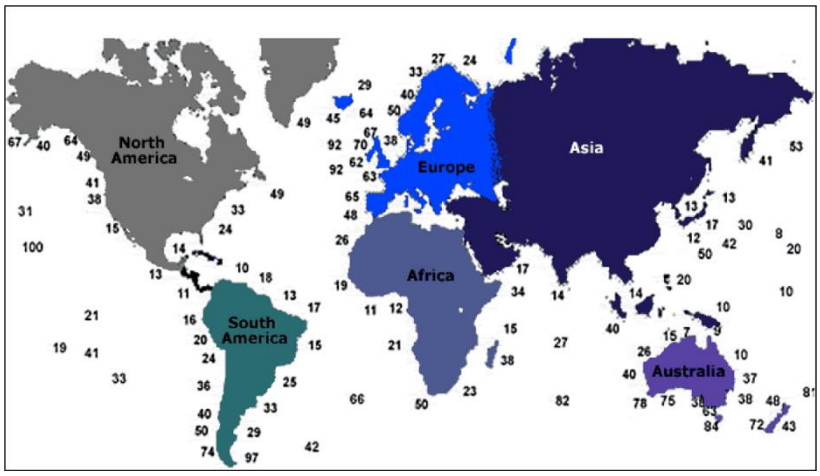

Figure 1.2 Averaged wave energy distribution (unit: kW/m)(Avilés, 2009)

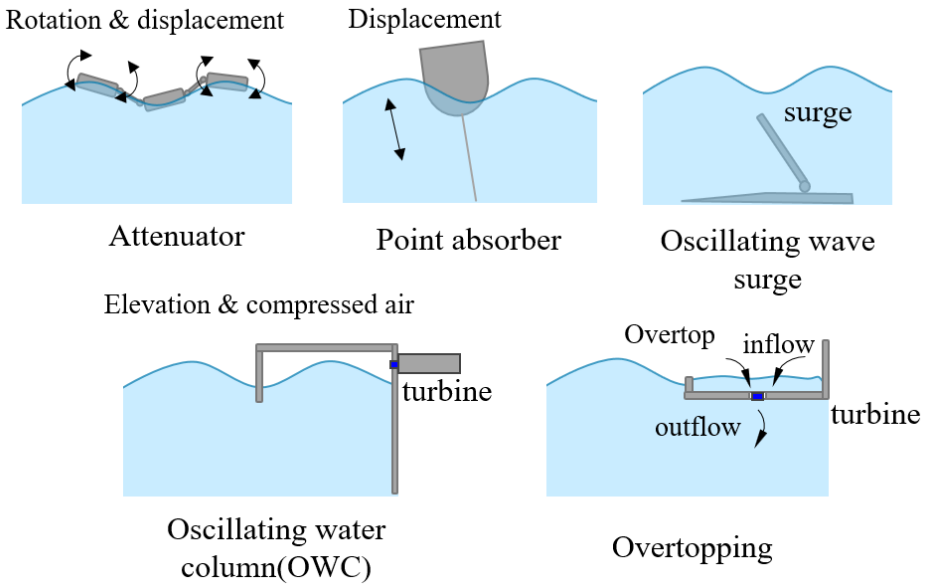

Figure 1.3 Types of WECs: Attenuators, Point Absorbers, Oscillating Wave Surge Converters, Oscillating Water Columns (OWC), and Overtopping Devices.

The FSI problems vary depending on the types of WECs, as shown in Figure 1.3. The fundamental concept behind them is to capture the energy from wave movements. Essentially, there are two primary methods for achieving this. The first involves capturing the kinetic energy of the waves and converting it into electrical energy. The second one involves utilising the gravitational potential energy of waves. In the first method, the critical components of the WEC interacting with water, known as the

working surfaces, move in sync with the wave motion. The kinetic energy from the waves is then converted into the movement of the WECs. This motion is harnessed by the Power Take-Off (PTO) system, which typically comprises either a linear or a hydraulic generator.

Among the most well-known types in this category is the Attenuator device, like Pelamis shown in Figure 1.4 (Henderson, 2006), which features a "line shape" design that flexes in accordance with the moving wave profile, harnessing power through the relative rotational movement between its segments. The FSI issue lies in addressing the coupling between complex multi-degree-of-freedom multi-body motion and fluid interaction. For the point absorber in Figure 1.5, it utilises a working surface of a single buoy, stabilised by mechanical or flexible mooring systems. As the buoy oscillates vertically with the waves, this translational motion drives a generator, producing power (Edwards and Mekhiche, 2014). For this type of WEC, the FSI problem becomes easier, with limited degrees of freedom, and only a single floating structure is considered in most scenarios. However, the nonlinearity of the free surface around the structure still needs to be investigated.

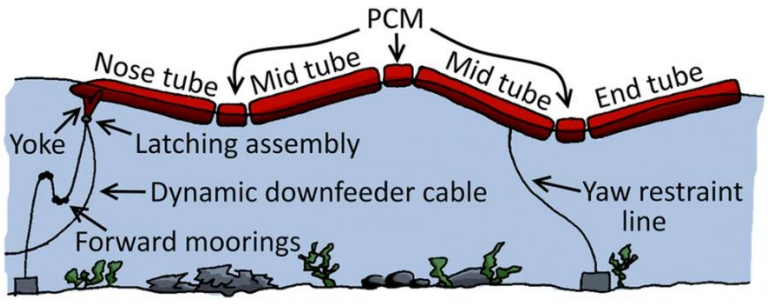

Figure 1.4 Sketch of Pelamis

The terminator has an elongated shape similar to an attenuator device but differs in its orientation, which is positioned perpendicular to the wave direction. By aligning itself parallel to the incoming wave crests, this orientation allows for enhanced energy capture by extending its length, particularly when the wave direction remains consistent. A notable example of this type is Salter's Duck. It generates power through rotation

around its long axis, parallel to the wave crest. For WECs utilising gravitational potential energy, the Oscillating Water Column (OWC) and the overtopping device are the most famous examples. For OWCs, the device's air chamber experiences a fluctuating pressure field due to incoming waves, a mechanism essential for power generation. This variable pressure difference propels a turbine connected to a generator, as depicted in Figure 1.3. The turbine's design is such that it functions effectively during both the intake and output phases of the wave's motion. Overtopping devices operate on a more straightforward principle. They collect seawater from incoming waves in an elevated reservoir and then channel it back to the sea through turbines, as depicted in Figure 1.3.

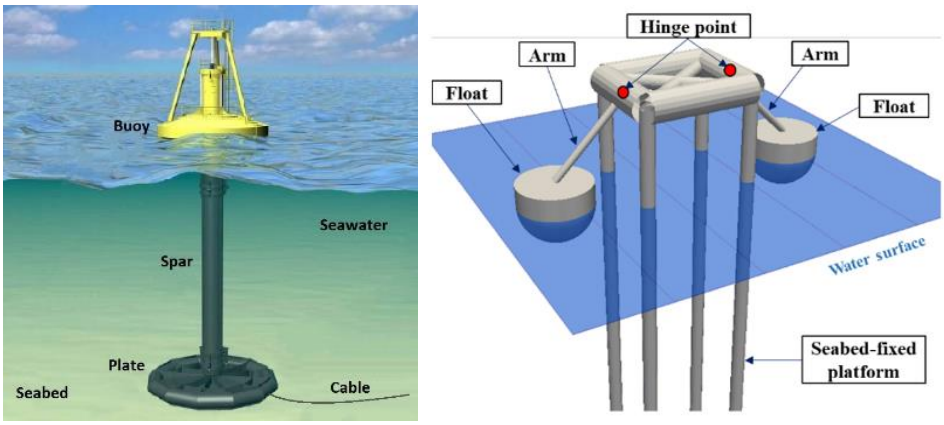

Figure 1.5 Sketch of Powerbuoy (Edwards and Mekhiche, 2014)and Wavestar WEC (Heo and Koo, 2021)

Figure 1.6 Salter's Duck String

Although with so many WEC designs, only a limited number of WECs have been commercialised, like Pelamis. Most WECs are still in the sea trial phase or are being used for demonstration purposes, like Oyster in 2005, Oceanus2 by and Offshore Pump-to-shore in 2007, Seabased in 2015 and HiWave-5/CorPower Ocean C4 WEC. Several FSI challenges are hindering the large-scale application of wave energy. The primary issue is the high cost associated with WECs. Current delicate mechanical systems are costly to build and particularly vulnerable when facing severe conditions with strong FSI. In addition, water's high density means scaling up WECs for more power leads to unmanageable loads in extreme conditions, a necessary step for commercial viability but an inherent contradiction challenge. The random feature of the ocean waves also hinders the development of WECs (Drew et al., 2016).

To overcome these issues, numerous new concepts and technologies are applied to solve the above FSI problems. For instance, from a power generation standpoint, scaling up has been a challenging issue due to larger loads. However, several initiatives have moved beyond this approach, integrating WECs with breakwaters to create a system that serves multiple purposes beyond just power generation (Zhao, et al., 2019a; 2019b). Another strategy is to arrange smaller WECs as WEC nets to enhance total power output (Carballo, Iglesias, 2013), avoiding the large wave load that may damage the devices. Additionally, the development of new flexible materials has made the creation of more adaptable WECs possible (Collins et al., 2021), which could considerably reduce costs, but it induces additional FSI problems with flexible structure interaction with fluids. These topics will be explored in greater detail later in the following literature review and analysis.

1.3 FSI in FOWT

The total potential of wind energy ranges from 19,400 TWh to 125,000 TWh annually, including onshore and offshore wind (Rogner et al., 2000). Among them, the potential for offshore wind ranges from 4,000 TWh to 37,000 TWh per year, even with this estimate considering only near-shore areas (Archer and Jacobson, 2005; Council, 1994;

Grubb and Meyer, 1993; Hoogwijk and Graus, 2008; Krewitt et al., 2009). Despite facing many additional challenges, such as higher costs from installation and operation, loads due to waves and current, transmission and storage, the benefits of offshore wind energy are evident and substantial (Esteban et al., 2011). The wind conditions offshore are generally more favourable than onshore, exhibiting more uniformity and less turbulence. The second major benefit is the availability of vast, unoccupied areas at sea suitable for large-scale wind farm installations. The remote location of these farms, far from populated areas, significantly reduces environmental concerns related to noise emissions, primarily associated with increased blade-tip speeds. These advantages have resulted in benefits that outweigh the drawbacks, leading to a marked expansion in the offshore wind energy sector in the recent decade. In 2022, the cumulated global capacity of offshore wind reached 64.3 GW, with an increase of 8.8 GW and a year-on-year growth of 16%. This upward trend is expected to persist, with an additional 30 GW capacity projected by 2026 and a further increase to 50 GW by 2030. Within the UK, there are already 36 fully commissioned wind farm projects with 11.8 GW in total by 2023, including the UK's largest existing offshore wind farm Hornsea 1& 2 (2.6Gw) (SMart Wind, 2014; ZOIA, 2022).

There are two types of onshore wind turbines: vertical axis wind turbines (VAWTs) and horizontal axis wind turbines (HAWTs), which differ in the direction of the axis in which the turbines rotate around. As shown in Figure 1.7, the VAWTs rotate around a vertical axis and are compact, making them suitable for urban or residential settings, though generally less efficient. HAWTs, however, have blades revolving around a horizontal axis. They are typically more efficient and larger, ideal for large-scale power generation. Therefore, they are primarily used in large offshore wind applications. With varying distances between the turbines and the land, different foundation strategies are required to accommodate the varied water depth. Near the shore, where the water depth is relatively shallow, wind turbines are typically fixed directly to the seabed. For these near-shore areas with water depth < 30 m, monopile foundations are commonly used owing to their simplicity and cost-effectiveness. When the water depth ranges between

25m and 50m, jacket foundations become more prevalent due to their superior structural support and stability in deeper water conditions. In deep-water scenarios, floating foundations are typically considered. These floating structures are anchored to the seabed but allow for movement and offer additional advantages, such as increased flexibility in site selection, which expands the potential deployment areas for FOWTs. Another benefit is that it can be easily deployed by assembling the entire wind turbines and their structures at ports and then towing them to the installation sites. Figure 1.8 illustrates that the capacity of fixed-bottom turbines is typically capped at 5MW. In comparison, FOWTs have shown greater capacity potential. FOWTs have readily achieved capacities between 5MW and 10MW. Recent developments include the introduction of 15MW turbines (Ma, 2022). This represents a substantial leap in the capability of FOWTs, exceeding the limitations commonly associated with fixed-bottom foundations.

Figure 1.7 Sketch of horizontal axis turbine and vertical axis turbine

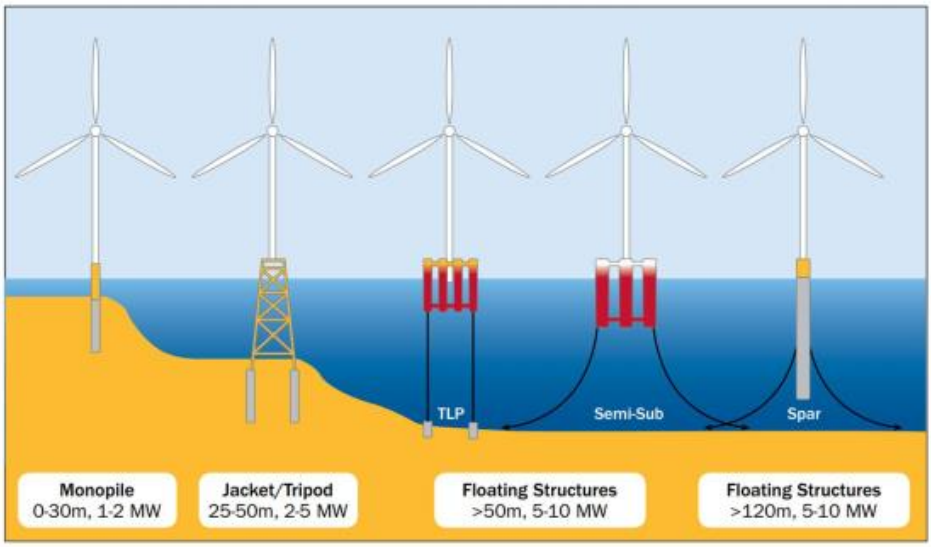

Figure 1.8 Types of offshore wind turbines supporting (EWEA, 2013)

Depending on the platform supporting the turbines, various types of FOWTs are deployed worldwide. For example, Spar platforms are commonly used in deepwater environments and are characterised by a long, cylindrical hull, as shown in Figure 1.9 (a). The platform's deep draft design makes it minimally affected by wind, waves, and currents; thus, the structure's gravity, together with its mooring lines, provides superior stability in deep water. Tension Leg Platform (TLP) is an offshore platform originally for deepwater oil and gas drilling, as shown in Figure 1.9 (b). It is typically anchored to the seabed with taut, vertical tendons. Stability is achieved by the tension applied on the tendons, minimising their heave motion and making them particularly suitable for deep water environments. While TLP foundations are considered viable for FOWTs, they are less frequently utilised than other floating foundations. One successful example of a project employing TLP is Blue H, which has a rated capacity of 80 kW (Thiagarajan and Dagher, 2014). Compared to the above-mentioned platforms, the semi-submersible (SS) platform is most frequently used recently. Its popularity stems mainly from its advantageous balance of stability and adaptability to various water depths. The SS platform is designed with multiple vertical columns interconnected, providing a stable base. Positioned centrally or atop one of these columns is the wind turbine. This

structure increases the pitch in the second moment of the waterplane, enhancing pitch stabilisation. Examples of SS platforms are the OC4 DeepCWind platform and VolturnUS. The barge platform is a simpler and cost-effective type of floating foundation. It is essentially a flat, rectangular structure that floats on the water's surface. Although it is susceptible to wave and wind motion, its manufacturing simplicity and cost-effectiveness make barge platforms a viable option for FOWTs. One representative is the BW IDEOL platform by Électricité de France, shown in Figure 1.9 (d).

(a) Hywind

(b) Blue H

(c) VolturnUS

(d) BW IDEOL

Figure 1.9 Sketch of different types of FOWT platforms (source: Wikipedia)

However, unique FSI issues were brought in with these non-stationary attributes of floating platforms. For example, these floating platforms can experience significant movement caused by waves, which becomes particularly critical with ocean currents. The transverse motion perpendicular to the current direction, typically induced by currents, is known as Vortex-induced Motion (VIM), which can be substantial. Such movements can damage the mooring system and the stability of the whole structure.

This platform motion also significantly affects FOWT's performance compared to bottom-fixed turbines. Although the motion's effect is subtle when the motion is small, a large oscillation was found for the power output with a larger motion (Tran et al., 2014; Tran and Kim, 2016a). Such fluctuation also reflects on the trust of the turbines, which may lead to fatigue issues and affect their durability. This periodic motion also leads to a periodic wake variation and faster wake recovery for the floating scenario, thus may improve the performance of the affected downstream turbines (Xu et al., 2023). It is also observed for FOWTs that the mean power output of FOWTs is higher than that of bottom-fixed turbines, though the difference is very slight (Leble and Barakos, 2017). Aerodynamics also influence platform motion, as the thrust and moment from the upper turbine cause a drift in surge motion and a change in mean pitch (Liu et al., 2017).

Another FSI problem of concern in this thesis is multiple wake interactions with FOWTs in a floating wind farm, which is deeply related to the layout of the wind farm. In practical scenarios, turbines are arranged in arrays rather than installed individually to maximise wind resource utilisation, and the optimal layout of the wind farm is important to the overall power production. Many operational offshore wind farms utilise a grid-like arrangement, featuring appropriate distances between turbines aligned with the main direction of the wind. As shown in Figure 1.10, the London Array wind farm possesses 175 turbines in the regular grid with a distance of 5.5 rotor diameters along the dominant wind direction (Glasdam et al., 2014). Similar layouts are adopted in Bard 1, Thorntonbank, and Lillgrund wind farms. These layouts bring in an important

wake issue. The blades of the turbines create a low-speed region wake region with high turbulence. The performance of the turbines located in line with this wake can be significantly affected. This wake effect can sometimes reduce the power from single downstream turbines by up to 60% and lower a whole wind farm's power by up to 54%. Therefore, understanding the wake interaction and the resulting variation in power generation of FOWTs is essential for designing floating wind farms, which will also be explored later in this thesis.

Figure 1.10 Layout of London Array offshore wind farm (Glasdam et al., 2014)

1.4 Numerical Study on the FSI Problem

The aforementioned FSI issues are pivotal to both WEC and FOWT, directly influencing their safety and power generation efficiency. Traditionally, these issues can be investigated through physical experiments. However, due to its low cost, numerical simulation has increasingly become a significant means of studying FSI problems. Three primary methods are predominantly used depending on the required level of accuracy. Morrison's equation is widely used for calculating forces on marine structures because of its fast computational speed, requiring the inertia and drag coefficients as inputs. It particularly applies to simple cylindrical fixed or slowly moving structures (Karimirad, 2013; Rainey, 1989). In ocean engineering, potential flow theory is extensively used for analysing complex structures under the assumption that the flow is both irrotational and inviscid. Consequently, the governing equation is reduced to the

Laplace equation, enabling its application. The water-air free surface equation is linearised at the time-mean surface position. The analytical method can be used for simple scenarios. For complicated cases, numerical simulation can be applied using the Boundary Element Method, like the analysis of WECs (Penalba et al., 2017; Yu Zhou et al., 2021) and floating wind platforms (Bayati et al., 2015). Many current hydrodynamic performance analysis software in both time and frequency domains are developed based on potential flow theory, including AQWA, WAMIT, FAST, TimeFloat and Orcaflex.

The Computational Fluid Dynamic (CFD) method has the highest fidelity among these methods. It is based on solving fully nonlinear Navier-Stokes equations and rapidly developed with its application in the numerical modelling of WECs (Agamloh et al., 2008; Chen et al., 2017; Devolder et al., 2018). While more time-consuming, CFD incorporates factors like fluid viscosity and vorticity, enhancing its precision, especially in complex ocean conditions. Additionally, potential flow software struggles with issues like VIM, where the interaction between platforms and flow is concerned. Thus, the CFD method is used in this paper to investigate the related FSI problems. For wider application, different models are required to be incorporated based on the specific scenarios and will be explained in detail in the literature review.

1.5 Objectives of the Thesis

In this thesis, the FSI problems associated with offshore wave and wind energy devices are studied via the CFD method based on OpenFOAM. The aim of this thesis is to further develop the existing CFD toolbox to enable it to handle various FSI problems encountered in wave and wind energy research. Despite WECs and FOWTs both featuring floating structures, their designs and functions can vary and may face different FSI problems, which include FSI with multiple rigid floating structures, FSI with flexible structures with large added mass, FSI with VIM in wave-current conditions, FSI coupling hydrodynamics and aerodynamics in FOWT. To conduct a numerical analysis of these FSI problems under a cohesive framework, multiple objectives need

to be fulfilled.

1. The FSI in closed-loop multi-body WEC net system featuring integration and complexity needs to be studied. This configuration enhances overall stability and facilitates the scalability of the WEC system. A multi-body dynamic code MBDyn needs to be coupled with CFD solver for structural solving that studies the dynamic behaviour of multiple interconnected rigid or flexible bodies and are widely used in robotics and vehicle dynamics (Eich-Soellner and Führer, 1998; Shabana, 1997). With this coupled tool, the motion responses and mechanical connection force between individual floats and linking arms can be fully resolved simultaneously.

2. The FSI problem associated with a novel flexible WEC that uses nonlinear flexible materials needs to be studied. A finite-element solver is to be integrated into the CFD code, with which the mechanical properties of flexible materials interacting with fluids can be well simulated. Using this tool, both linear elastic and hyper-elastic materials used to construct the working surface of the WEC are studied.

3. The FSI problem associated with the hydrodynamic response of the FOWT platform under wave-current conditions needs to be investigated using the CFD tool. The VIM effect, usually involving the accurate simulation of the viscosity and vortex around the floating structure, cannot be addressed by potential flow software. The motion response and vortex shedding of two different platforms are studied.

4. The FSI problem associated with the coupled aerodynamic-hydrodynamic model needs to be studied for FOWT farm. For the FOWT farms simulation, a blade-resolved simulation is not feasible due to its high computational cost. The Actuator Line Model (ALM) is to be coupled into the CFD code for aerodynamic modelling, with the aim of reducing the mesh size. This enables

the simulation of multiple FOWTs, which are fully coupled with aero and hydrodynamics. The wake interactions and the dynamic response of each FOWT can be captured.

With this work, the above FSI problems are studied regarding offshore wave and wind energy devices. A CFD code integrating multi-body dynamics, aerodynamics, wave current condition generation, and finite element analysis is further developed, which will enable more accurate simulations and analyses of complex phenomena in marine renewable energy systems, providing more reliable technical support for the development of marine energy. This tool is also valuable for researching other marine renewable energy devices or hybrid platforms, providing a useful tool in this field.

1.6 An Outline of the Thesis

The structure of this thesis is shown below:

Chapter 1 serves as the introduction and background of FSI problems in the ocean renewable energy sector, where WECs and FOWTs are focused in this study. The specific FSI problems associated with different types of devices of concern are introduced.

Chapter 2 presents a literature review. It begins by examining research on rigid WEC, focusing mainly on systems that incorporate multiple mechanical components. This is followed by an exploration of flexible WEC development, covering both prototype design and numerical simulations. The chapter then delves into studies on FOWT, encompassing aspects such as aerodynamics, hydrodynamics, fully integrated models, and layout studies of FOWT.

Chapter 3 is the numerical method, introducing the basic CFD equations, the formula in a multibody dynamic, and the formulas used in Finite Element Analysis (FEA). It then introduced the equations used for sub-models, like wave generation and absorbing theory, mooring theory and ALM theory.

Chapter 4 introduces the study of multi-body WEC net, where the hydrodynamic and power take-off performance of Albatern 12S Squid WEC net is studied. The mechanical force among sub-structures, the dynamic response, and the optimal PTO damping are studied.

Chapter 5 introduces the study of a novel flexible WEC, where hyper-elastic material is used. The impact of material and wave conditions on power efficiency is studied.

Chapter 6 introduces the study of the dynamic response of a semi-submersible platform, where different wave current conditions are included.

Chapter 7 introduces the study on the FOWT farm, where three fully coupled FOWTs are deployed in different layouts.

To summarise this thesis, conclusions and recommendations for future work are provided in Chapter 8.

Chapter 2 Literature Review

With the development of the renewable energy industry in recent decades, numerous research studies have been conducted on the FSI problems of offshore wave and wind energy devices. Experimental study is typical for this type of research in the past. With the advancing computing science, numerical modelling is becoming an important approach in the design and research stage, offering significant reductions in both time and cost. This chapter thoroughly examines the numerical studies, especially CFD studies, focused on distinct aspects potentially encountered in the FSI of WECs and FOWTs.

2.1 FSI Issues in Novel WEC Designs

One drawback of the traditional WECs mentioned in section 1.2 is their difficulty scaling up. When the size of WECs increases, the wave force on the structures increases rapidly, making them more vulnerable. One approach is to increase the number of

WECs rather than the size to create multiple WECs into a WEC net rather than enlarging individual units. Another strategy involves adopting simpler but more efficient designs, such as using flexible dielectric elastomer (DE) materials instead of complex mechanical systems, which also decreases the cost of construction and maintenance. This section reviews research efforts in both these approaches, exploring innovations in WEC design and configuration.

2.1.1 FSI Associated with WEC Net

In practical applications, deploying individual WECs as an array or matrix is expected to satisfy a large power take-off requirement. Numerical modelling methods used to uncover insights into its hydrodynamic performance and production often include various orders of accuracy. One method to study WEC is the potential flow theory-based method. Lee et al. investigated multi-body hydrodynamics for a WEC array integrated into a hybrid platform (Lee et al., 2018), with 24 individual floaters constrained on a rectangular frame, in which the interaction effect of the array configuration on the extracted power was studied. They found that the multiple array configuration increases the power capture of the WEC system, while the heave response of the platform is only slightly influenced by the PTO damping force. Ning et al. (Ning et al., 2018) studied a hybrid system consisting of an oscillating buoy WEC array and a fixed rear pontoon. It was found that the standing waves formed in front of the pontoon are not beneficial to the energy extraction of WECs, thus leading to a smaller power capture, especially in the high-frequency range. These two studies are all based on a linear potential flow theory in the frequency domain. The dynamic response is estimated by the WEC motion equation, and the output power is estimated by the linear PTO damping model.

In addition to the above frequency domain method, a time-domain analysis is also able to estimate the damping parameters of the PTO system. The latter can better predict the performance of WECs via more detailed investigations on transient/unsteady wave-structure-interaction phenomena by including the nonlinear dynamic moorings (Folley

et al., 2012). Incorporating time-domain modelling allows for the evaluation of dynamic responses at specific moments in time. Chandrasekaran and Sricharan performed a numerical study on a novel WEC with multiple floats both in frequency-domain and time-domain with a linear PTO model adopted in the software named WEC-SIM (Chandrasekaran and Sricharan, 2020). The influence of the PTO system on the power output was investigated via optimization of the damping coefficients. It was found a frequency domain analysis overestimates the results as compared to those obtained from the time domain. Rollano et.al estimated the power extracted by a Floating-Point Absorber (FPA) array with different climates using WEC-SIM (Lawson et al., 2014) (Ticona Rollano et al., 2020). In their study, the fluid-structure interaction was solved using a one-way coupling, in which only the impact of the wave on the structure was considered. The power output was found to be dependent on the wave condition in different seasons. The performance is better in winter months compared with summer months.

Due to the limitation of linearisation and potential flow hypothesis, the challenge arises in capturing an accurate flow field when the non-linear phenomena become significant, which in turn affects the accurate calculation of motion response and power capture. To overcome this issue, several nonlinear models with higher-order accuracy have been developed for WEC studies (Davidson and Costello, 2020), such as higher-order boundary element method (HOBEM) (Ning et al., 2015) and higher-order spectral method (HOS) (Van Rees et al., 2011). In addition, CFD is highly suitable for investigating WEC net problems. In the study of Chen et al. (Chen et al., 2017), the dynamic response of a point absorber WEC with a stroke control system was examined. It was revealed that the differences in the WEC behaviour predicted by a potential flow theory and a CFD simulation could be significant and vary considerably, depending on ocean wave height.

It is also worth mentioning that, in the above studies, there is no mechanical connection among individual WECs in the system. In practical applications, a single WEC is

sometimes connected with various mechanical components, such as sea trail-tested devices. One of the typical examples is Albatern Wavenet WEC, shown in Figures 2.1 (b) and (c). The multi-segments and the articulation linking arms in the design of such a device make up the WEC as a multi-body system with mechanical interactions between each section. The interconnected rigid or flexible bodies may undergo large translational and rotational displacement and motion. This specific feature of the system increases the numerical modelling challenges, which requires a powerful multi-body dynamic solver to be incorporated with a flow solver.

Many experiments have been conducted for WECs with mechanical components (Dang et al., 2019; Ning et al., 2016; Zurkinden et al., 2014). Meanwhile, numerical studies can be found focusing on the mechanical-wave-structure system issues with potential flow theory. Using a frequency domain method, Zhang et al. investigated the performance of a two-body articulated Eagle wave energy device (Chao et al., 2018). External mechanical damping was studied using a wide wave frequency range to optimise power output. The most dangerous wave angular frequency ranging from 0.2-0.5 rad/s was identified, with excessive movement occurring, causing damage to the device. Although the frequency method can obtain the dynamic response by motion equations in the post-processing process, it cannot provide more detailed time-dependent information. Yu et al. developed a module in WEC-SIM that can model a WEC's conversion of mechanical power to electrical power through its PTO (So et al., 2015). The performance of the RM3 floating point absorber with two different PTO systems was evaluated. Their results showed that the direct-drive system is more efficient as compared to the hydraulic system, but the latter can obtain smoother power output. A more complex WEC system, e.g. ALETTONE, which consists of a four-bar linkage and a floating plate, was developed in the work of Albert et al. (Albert et al., 2017). The multibody WEC was simulated using SimMechanics, and the hydrodynamic force was addressed by an impulse response function, which was calculated separately from ANSYS AQWA. The performance of WEC microarrays was examined using the AQWA-FAST simulation system, focusing on the layout's internal connections and

hydrodynamic coupling interactions(Cao et al., 2023). The study revealed that the outer microarray offers better pitch motion suppression and power output compared to the inner.

On large multibody WEC systems with mechanical connections, many studies can be found using potential flow theory. Chandrasekaran studied the performance and optimisation of a bean-shaped multi-body floating WEC using WEC-SIM (Chandrasekaran and Sricharan, 2021; Sricharan and Chandrasekaran, 2021). The performance of WEC with different numbers of components was studied, together with the PTO damping, in which a real-time simulation was achieved. It was found that WEC-SIM can obtain reasonably good results compared to CFD results with moderate sea states. However, for more extreme sea states, the linear-based results have significant errors (van Rij et al., 2019). This is because the higher-order non-linear effects are excluded in WEC-SIM. Therefore, the motion of WECs with strong resonance motion may be underestimated due to the linearised free-surface assumption. In the comparison conducted by van Rij et al., WEC-SIM results show much smaller sway drift and yaw motion than CFD results (van Rij et al., 2019). Hossein et al. integrated multiple Salter's duck WECs into a FOWT platform, making it a hybrid system that was studied using ANSYS AQWA (Yazdi et al., 2023). Various layouts with different numbers of WECs are organised into three linear groups between side columns, and it is observed that fewer WECs can even produce more power. Another research on a hybrid WEC-FOWT system using AQWA is conducted, integrating six WECs into the platform (Wu et al., 2024). The maximum total power output of the WEC array reaches 0.85 with a wave period of 7s. The platform's motion was found to have negative effects on WECs' performance.

(a) Single float

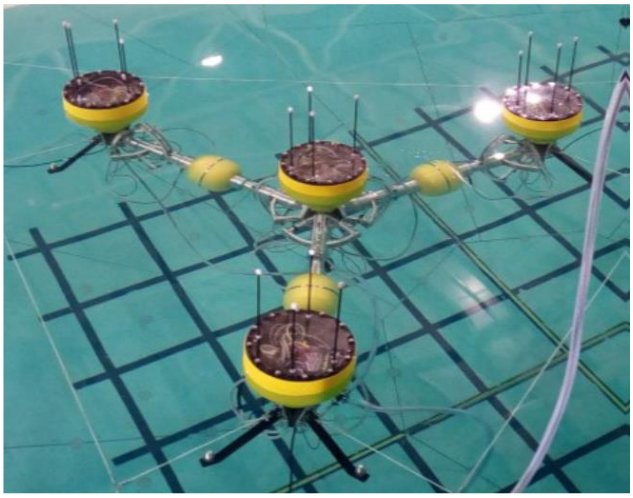

(b) Squid WEC array with sub-structures

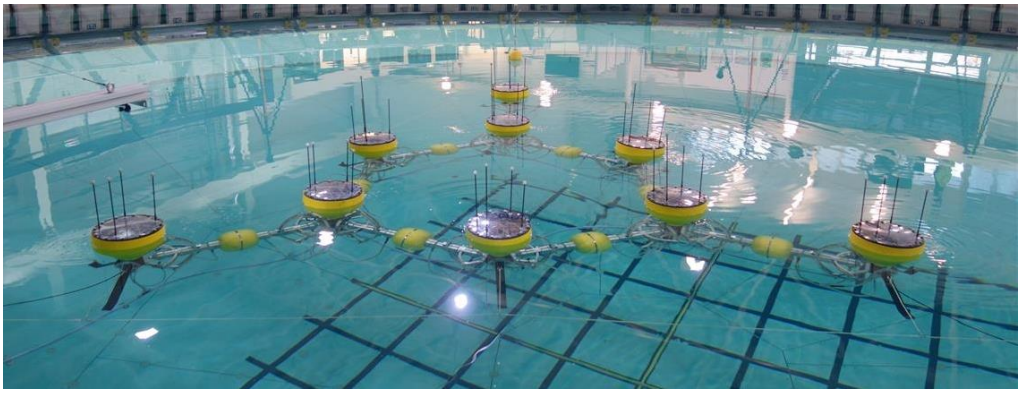

(c) Hex WEC array with sub-structures

Figure 2.1 Sketch of the Albatern squid WEC laboratory testing model (Mcdonald et al., 2017)

As far as the authors understand, none of the existing commercial CFD software packages can study the FSI problems with a rather complex mechanical system, as the wave net studied in this paper, illustrated by Figure 2.1, which comprises a great deal of mutually articulated sub-structures and restraints. For the Hex WEC system studied in this paper, shown in Figure 2.1 (c), the mechanical system includes up to eighteen mutually interacting sub-components such as floats and linking arms and articulations connecting them with Power Take-off (PTO) and mooring system.

To solve such problems, the present CFD solver is coupled with a multibody dynamic solver, MBDyn. This idea is inspired by the previous study on flexible turbines, where

the turbine deformation was solved by MBDyn, and the aerodynamic force was calculated by CFD (Liu et al., 2019). In the present study, an adapter has been established, with which the external hydrodynamic force on the WEC net derived from the CFD solver can be transferred to MBDyn, with which the motion response can be calculated. The updated motions are then transferred back to the CFD solver simultaneously.

2.1.2 FSI Associated with Flexible WEC

Apart from the aforementioned reliability and survivability issues of traditional WECs, the adaptability to the ocean wave conditions where they are installed is usually poor. For example, for OWC, the resonant phenomenon is very important for maximising power generation. This type of resonance is usually caused by the air-water free-surface interaction with a surface-piercing structure (Ning et al., 2016; Wang and Ning, 2020), which is similar to harbour oscillations or gap resonance (Yu and Chwang, 1994; Zhao et al., 2017). Those WECs can only produce a considerable amount of power under a specific range of conditions (e.g., between a narrow range of ocean wave frequencies). If these conditions are not met, the performance of the WEC will be significantly hindered and reduced.

One way to address these issues is to use flexible materials when constructing WEC. Deformable materials such as rubber and silicon elastomers can be widely used for different parts of the WEC, such as the power take-off system using dielectric elastomer materials (Moretti et.al.(Rosati Papini et al., 2018)) or the primary mover of WECs (Collins et al., 2021).

A series of studies by Moretti (Moretti et al., 2018; Moretti et al., 2020) on the utilisation of a DE material for an OWC device showed promising results and the effectiveness of constructing OWCs with DE materials. The experimental wave tank test indicated a maximum fraction of 18% of the wave energy can be converted into electricity. Based on the experimental study, a surge OWC was developed and studied numerically with a simplified hydrodynamic model, aiming to identify an optimal control strategy to

maximise the device's power production (Moretti et al., 2015). The results showed that the estimated power outputs can be as high as 1.5 MW if a 1.5m^3 elastomeric material is used.

With the recent developments of WECs utilising flexible materials, a greater understanding of how WECs are affected by hydrodynamic forces is required. For example, the forces experienced by the WEC sub-structures, the fluid-flexible structure interaction phenomena linked to the material deformation/damage, and the direct power take-off system. Currently, existing research on flexible WECs is limited, with studies using the numerical analysis tool providing limited information. These are either based on a reduced-order model or a decoupled numerical modelling for fluid flow and structural deformation. The inherent disadvantage of these models is their lack of universality, as the assumptions made in one device may not be valid for others. In addition, these simplified models might be inaccurate when the fluid nonlinearity and material nonlinearity become profound, and thus, the coupling between fluid flow and structure deformation must also be considered.

A study conducted by Michailides (Michailides and Angelides, 2015) investigated the response of a flexible structure consisting of 4 rigid plates connected by constraints. The whole structure integrates the function of the breakwater and power take-off device. The investigation was based on the potential flow theory with the hypothesis of linearisation, inviscid, and irrotational. Their results demonstrated a desirable amount of wave energy production by the WEC. Babarit et al. (Babarit et al., 2017) studied a bulge-wave WEC, i.e., SBM S3, constructed from DE material. A lumped parameter modelling system was combined with the spectral decomposition and the potential flow theory. The Anaconda WEC is a model which has been extensively studied both experimentally and numerically (Chaplin et al., 2012; Farley et al., 2012). The tube distensibility equations were utilised in the study to describe the deformation of the flexible tube. This one-dimensional model was originally developed to be tested under the simulation of the vascular system. Alongside this, a WEC rubber bag was tested

using a combination of the potential flow theory and the boundary element method (Kurniawan et al., 2017). Applying a distributed-parameter analytical approach, Renzi coupled the linear piezoelectric constitutive equations with the potential flow equations to cope with the free surface wave. A similar submerged piezoceramic plate WEC has

(a)

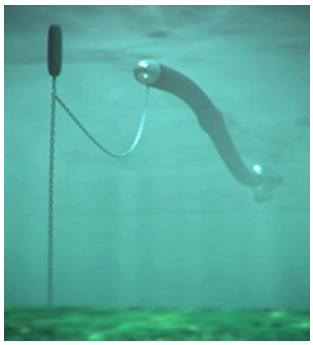

(b)

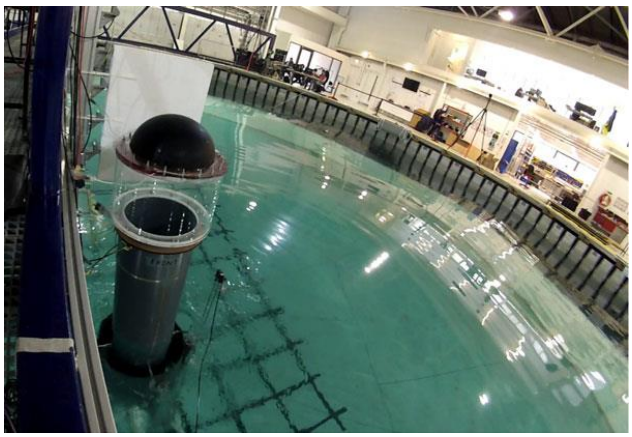

(c)

Figure 2.2 (a) The SBM S3 flexible WEC (SBM Offshore, 2021) (b) The Anaconda WEC (Checkmate Seaenergy Limited, 2013) (c) PolyWEC (Moretti et al., 2019)

also been extensively studied (Renzi, 2016). Lastly, Zheng et al. (Zheng et al., 2020) studied the characteristics of a circular plate under regular waves, investigating the effect of varying radius and edge conditions on the performance of a circular plate.

To obtain more analysable details, a high-fidelity partitioned scheme that preserves all these desired features of the flexible WEC is paramount. This partitioned scheme relies on the data transfer between the CFD solver and the computational solid dynamics (CSD) solver to solve a coupled fluid-structure interaction FSI problem. King et al.

(King et al., 2016) investigated the use of a partitioned scheme on the Bombora WEC. The CFD method was coupled with the finite element model in their study, and the simulation discovered the instability of the coupling process. For these issues to be solved, extremely small relaxation parameters are required, leading to a very large number of iterations (>100) to reach a convergent solution. The results of the coupled and uncoupled models show that the latter underestimated the results by 25% compared to the coupled method. A two-dimensional simulation on the PolyWEC (Moretti et al., 2020) was conducted with the use of a high-fidelity CFD method together with multi-body dynamics, creating a strong coupling strategy (Li et al., 2021). Even though a linear-elastic material was adopted, the nonlinear effect is overpoweringly strong and thus, the simulation is unstable, requiring 50 iterations at each timestep for a convergent solution. Three-dimensional CFD studies were conducted using the coupled CFD-FEM method, where the flow field information, fluid velocity, pressure, and structural stress distribution were obtained (Huang, Xiao, et al., 2023a, 2023b).

Aside from the aforementioned studies discussed, as far as the authors are aware, the analysis of fWEC using high-fidelity coupled tools is limited. The biggest challenge for such simulation is the numerical stability problem, as mentioned before, which is mainly affected by the added mass of the flexible structure. Through theoretical analysis, it has been discovered that as the added mass entrained by the fWEC becomes greater, the stability of both explicit and implicit coupling schemes is reduced significantly (P. Causin et al., 2005). This is just the case for the fWEC application, where the added mass might be hundreds of times the mass of the flexible structure itself and, therefore, dominates the inertia of the fWEC system.

In addition, in this study, the flexible WEC of concern is made up of hyper-elastic material, which makes the FSI problem highly nonlinear. This leads to a highly unstable numerical simulation. However, the existing MBDyn-OpenFOAM tool cannot solve such problems. For this specific FSI problem, on the structure side, a finite element solver CalculiX can resolve hyper-elastic material (Dhondt, 2004). On the coupling

scheme side, the previous coupling scheme with a constant relaxation factor is not stable enough for the present FSI problem. In this study, the coupling between the flow solver and structure solver is achieved by using the Precise Code Interaction Coupling Environment (preCICE), a coupling library for partitioned multi-physics simulations (Bungartz et al., 2016). Within preCICE, the interface quasi-Newton method with inverse Jacobian from a least-squares model (IQN-ILS) is used to stabilise the coupling and accelerate the convergence.

2.2 FSI Issues in FOWT

Simulating the entire FOWT system under one framework is complex, typically involving electrical systems, structural dynamics, aerodynamics, and hydrodynamics. Based on the present tool, additional techniques like the aerodynamic and mooring models are required depending on the specific scenarios being studied. This section offers an overview of the historical development and advancements regarding FOWTs, focusing on two key areas: the current-wave interaction with FOWT platforms and the FOWT farm simulation.

2.2.1 FSI Associated with VIM of FOWT in Wave-current Condition

FOWTs experience significant platform motion in various sea conditions, usually caused by waves and sea currents. Thus, compared to onshore wind turbines, the accurate calculation of the platform's hydrodynamics behaviour in a complex oceanic condition is essential.

Wave load, as a critical factor for floating structures, induces periodic motion responses of the FOWT platform. Potential flow theory is commonly used for wave load prediction, considering factors such as buoyancy, incident wave forces, and damping forces on marine structures. Using the TimeFloat program, the motion of a WindFloat-supported FOWT was studied and compared with that of the experiment (Cermelli et al., 2009). Another study using FAST was conducted to explore how second-order hydrodynamic effects impact the OC4-DeepCwind SS platform (Bayati et al., 2014).

Findings indicate that the natural frequencies of the platform are excited by difference-frequency second-order hydrodynamic forces. Apart from potential flow theory, CFD is frequently utilised to predict the wave load and the resulting dynamic response. It can address issues more effectively in extreme wave conditions, like wave overtopping and wave breaking, which are not adequately handled by potential flow theory. The hydrodynamic responses of the OC4-DeepCwind SS platform were studied utilising STAR-CCM+ (Tran et al., 2014). The results of their modelling were found to be in generally good agreement with the data obtained from experimental tests. Another CFD study on the same platform interaction with regular waves is conducted using OpenFOAM (Huang et al., 2021). It has been observed that the platform's movements are more sensitive to low-frequency waves compared to high-frequency waves. Similar studies have also been conducted by Burmester et al., which analyse the hydrodynamic characteristics of a semi-submersible floating platform (Burmester et al., 2017; Burmester et al., 2020).

In addition to wave-platform interaction, the current-induced motion, or VIM, is also important. This phenomenon usually occurs when a cylindrical structure or a bluff body is moored or elastically mounted in the presence of ocean currents. A typical VIM is a low-frequency, periodic sway motion perpendicular to the current direction, which is caused by the periodic vortex shedding near the structure. Its amplitude can be particularly high when the frequency of vortex shedding becomes synchronised with the structural natural frequency (Sarpkaya, 2004; Sumer, 2006). Such synchronisation is known as lock-in, and it occurs over a wide range of flow velocities. The VIM of cylinders and monocolumn platforms has been extensively studied experimentally (Bao et al., 2012; Gonçalves et al., 2013; Zhao and Cheng, 2014). It was found that the platform follows a classic 8-shaped orbital trajectory in some cases. This low-frequency response, especially in the cross-flow (CF) direction, may result in potential damage to FOWT's mooring system and cause fatigue problems (Sagrilo et al., 2009). The in-line (IL) motion is relatively small compared to that in the CF direction. The interaction between current and FOWT platforms tends to receive less focus during the design

phase, partly due to the typically low current speeds encountered in many common operating environments. The speed of tidal is usually large, whose maximum value can be as large as 4.5 m/s as observed in some channel areas (Liu et al., 2021), with a water depth ranging from 40-110 m, but this velocity is much smaller in the deep, open ocean. Away from these shallow water areas, the surface current caused by wind has a characteristic speed of 0.05 to 0.5 m/s, which is much less than tidal, which is also lower than the minimal threshold required for VIM to occur. However, in certain locations, such as the Gulf Stream, the current velocity at the free surface can exceed 2m/s, which is sufficiently large to induce VIM for a floating platform having cylinders, such as SPAR (Cueva et al., 2006; Gonçalves et al., 2010, 2012). The SS platform, on the other hand, has a smaller aspect ratio (draft/characteristic length), which has been investigated by Gonçalves et al. (Gonçalves et al., 2012, 2021). Their experimental findings confirmed that VIM occurs even at a relatively low current speed for two SS platforms with different geometric dimensions. Other research regarding VIM of different platforms has also been conducted recently (Du et al., 2022; Fujarra et al., 2022). Due to the inherent disadvantage of potential-flow theory in which fluid is assumed to be irrotational and non-viscous, numerical analysis involving offshore structure-fluid interaction has been conducted using CFD method, that considers viscosity of fluid directly by solving Navier-stokes equation with turbulence models (Huang and Chen, 2020; Huang et al., 2022; Liu et al., 2023; Liu et al., 2020; Vinayan et al., 2015). In their studies, the formation and shedding of the vortices due to VIM were clearly observed.

In the presence of both waves and current, a combined colinear wave-current interaction with four square columns platform is studied experimentally (Gonçalves et al., 2013, 2020). The findings indicated that the addition of wave sometimes tends to have little impact on VIM while mitigating VIM entirely in other cases. This is further observed in the studies of (Maximiano et al., 2017) and (Li, Xiao, Gonçalves, et al., 2022). A detailed examination of the fluid flow vorticity field indicated that the reduced amplitude of VIM is caused by the wave interaction with the current and platform,

changing the vortex shedding pattern and, thus, the vortex shedding frequency. While VIM mitigation by waves has been observed in past studies, most of the existing investigations are focused on the flow condition where wave and current are aligned. In reality, it is very likely the angle between the wave and current can vary in different sea states. For instance, in the project of LIFE50+ for a 10MW wind turbine, the wave and current inter-angle ranges from 82.5 to 150 degrees at three deployment sites with a water depth of over 50m (Bayati et al., 2016). It is, therefore, critical to understand the wave-current-structure-interaction under various angles and flow conditions. In this study, the dynamic response of the floating platform in complex sea conditions is numerically studied using OpenFOAM. Both waves and currents are generated in different directions, where the wave-only, current-only conditions are examined as comparisons.

2.2.2 FSI Associated with FOWT Farm

2.2.2.1 Fully coupled FOWT

To study the FOWTs considering both aerodynamics and hydrodynamics, an aerodynamic model needs to be incorporated into the present tool. The most classic theory on the aerodynamics of wind turbines is the Blade Element Momentum (BEM) theory, which was initially proposed to calculate the load on propellers (Glauert, 1935) and then applied in the study of the aerodynamics of wind turbines (Wilson and Lissaman, 2018). In their theory, the blade is divided radially into discrete elements, simplifying the complex flow around the blade into a two-dimensional airfoil problem. By integrating one-dimensional momentum theory, the induced velocities at various radial positions on wind turbine blades can be calculated. Then, the two-dimensional airfoil data with lift and drag coefficients in relation to the angle of attack is used to calculate aerodynamic loads on individual blade elements. This enables the calculation of the loads on the wind turbines and then the power output.

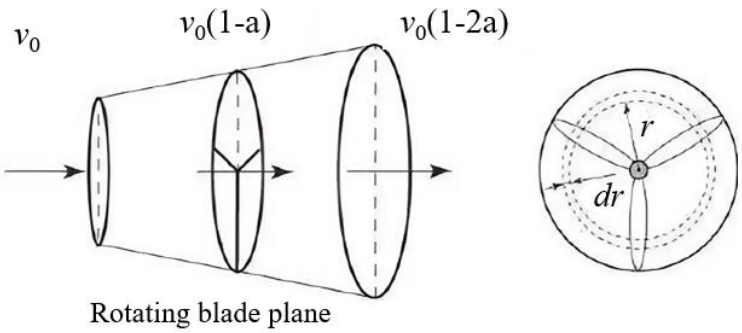

Figure 2.3 Schematic diagram of momentum theory (Wang et al., 2014)

The key to utilising BEM theory is access to existing airfoil data, which hinders its application in the design and analysis of the latest turbines. Nevertheless, due to its computational efficiency and simplicity, it is widely used by many engineering software such as FAST (Fatigue, Aerodynamics, Structures, and Turbulence) by National Renewable Energy Laboratory (NREL) and Bladed by Det Norske Veritas (DNV). The drawback of BEM is obvious due to its simplification. Wind turbine blades are theoretically assumed to be infinite in number. To rectify this assumption, various scholars have proposed different correction models (Glauert, 1935; Shen et al., 2005; Vries, 1979), aiming to correct for the finite number of blades in actual turbines, improving the accuracy of BEM's predictions. It also faces limitations in accurately predicting the aerodynamic performance of wind turbines under complex inflow conditions, although various correction methods have been proposed (Holierhoek et al., 2013). This uncertainty brings challenges in its application for FOWTs, where complex inflow conditions are more prevalent. The vortex method is another method for wind turbine modelling, which was previously used for estimating the loads and wake of the rotors of helicopters (Landgrebe, 1969, 1972). It was then introduced to the research on the wind turbine (Kocurek, 1987). Based on that, the Free Vortex Method (FVM) was proposed, which is suitable for solving wind turbine wake problems (Xu et al., 2018). It is assumed that the flow field is incompressible and potential. The rotor blades are depicted through lifting lines or surfaces, which effectively represent the trailing and shed vorticity in the turbine's wake. This approach allows for a detailed simulation of

the 3D airflow and vortex patterns generated by the movement of the blades, which is used in many wind turbine studies (Farrugia et al., 2014; Jeon et al., 2014; Qiu et al., 2014). Although the FVM can predict the aerodynamic performance of wind turbines under complex conditions, it also has limitations. It does not accurately account for viscous effects and the impact of wake roll-up on wake development. Additionally, it cannot capture details like pressure on the blade surfaces and flow separation. Consequently, the accuracy of the FVM in forecasting the unsteady wake characteristics of FOWT needs further improvement.

Compared to the FVM and BEM theory, CFD offers more detailed and accurate simulation. It doesn't simplify the turbine geometry and doesn't rely on input airfoil data. It also provides a comprehensive analysis, considering the full geometry of the turbine and accounting for complex fluid dynamics, which is essential for optimising design and performance in various conditions. For example, it can be used to obtain the airfoil data needed for other commercial software (Petrilli et al., 2013). With advancements in computational capabilities, the focus of CFD studies on turbines has progressively shifted from two-dimensional to three-dimensional analyses. CFD was initially applied to wind turbine aerodynamics using the k-ω SST turbulence model to close the RANS (Reynolds Averaged Navier-Stokes) equations (Sorensen and Hansen, 1998). The flow fields for both single and three-blade configurations are both simulated. In the simulations of the NREL Phase VI wind turbine, both RANS and Detached Eddy Simulation (DES) methods were applied for comparison. It was found that the aerodynamic loads calculated by both approaches were quite similar (Johansen et al., 2002).

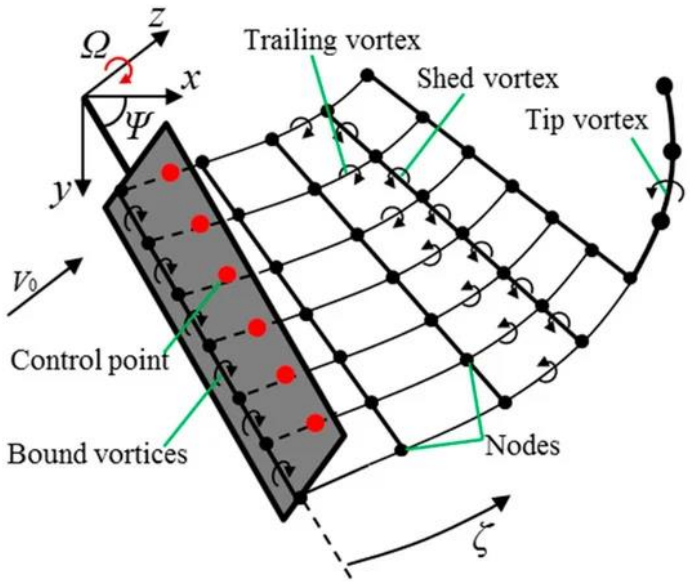

Figure 2.4 Schematic diagram of the blade model and the vortex wake model(Xu et al., 2018)

Since the direct simulation of three-dimensional wind turbines is quite time-consuming, especially for wind farm studies with more than one turbine, many researchers turn to the body force model based on the CFD method. The fundamental concept of the volume force model is to substitute real wind turbine blades with virtual surfaces, lines, or points exerting volume forces. This approach eliminates the need to mesh the actual blade structure, significantly reducing the number of meshes without solving the boundary flow of the turbines, consequently conserving computational resources. The most commonly used body force models are the Actuator Disk Model (ADM) and ALM. In ADM, the wind turbine's rotor is represented by a disk with an equivalent swept area. This model combines BEM to compute the aerodynamic Loads on the turbine, which are then projected into the flow field (Leclerc et al., 1999; Wu and Porté-Agel, 2011, 2015). It's important to note that the ADM, which uses a symmetric flow assumption, has significant limitations in simulating the complex wake of wind turbines. To represent the 3D rotational characteristics of wind turbine wakes more accurately, ALM was developed that uses virtual lines exerting volume forces to replace turbine blades, effectively simulating the rotational motion of the blades (Sorensen and Shen, 2002).

This approach enhances the model's ability to reflect the complex aerodynamic behaviours of wind turbines. Using ALM, a simulation of the wake of a three-blade turbine was conducted, and the results were compared with experimental data (Troldborg et al., 2007). Tandem wind turbine wake interaction was studied using ALM (Yu et al., 2018). Findings indicated that the optimal turbine performance at a wind speed of 8 m/s for two aligned turbines is achieved with 7D, which is ideal for mitigating wake effects on downstream turbines.

In addition to the above aerodynamic models, it is essential to couple different models into a unified system, enabling data feedback between different models. Many commercial and open-sourced software are able to simulate FOWT already, like FAST (Jonkman and Jonkman, 2016), Bladed (Beardsell et al., 2018), HAWC2 (Bose, 2010) and Qblade (Bergua et al., 2022). All of them are based on potential flow theory/Morison's equation + BEM theory, which are listed in Table 2.1. These tools offer acceptable computational speeds, making them ideal for the early stages of design, where simulation of numerous cases is required. Numerical simulation was conducted on a barge FOWT using the FAST, focusing on calculating its load characteristics and dynamic response under extreme sea conditions, followed by an analysis of its stability (Jonkman, 2007). Qblade is used to study FOWT loads on three different types of platforms in realistic environmental conditions and compare its results with those from OpenFAST (Papi et al., 2023). It was observed that OpenFAST tended to overestimate lifetime damage equivalent loads by as much as 14%. 3Dfloat was also used for both FOWT simulations, and the results were compared with SIMO (Nygaard et al., 2016).

While the aforementioned software is useful, the accuracy of their low-fidelity or reduced-order models cannot be fully assured. Consequently, for more in-depth analysis of FOWT beyond the initial design phase, more dependable tools are required. In this context, CFD emerges as one of the viable options. Traditionally, the CFD method was primarily employed for blade analysis, airfoil studies, and simulations of fixed turbines.

Table 2.1 Typical coupled aero-hydrodynamic simulation tool for FOWTs. The acronyms refer to various modelling techniques. (BEM: Blade Element Momentum; GDW: Generalized Dynamic Wake; DS: Dynamic Stall; Airy: Linear wave theory; ME: Morison Equation; PF: Potential Flow; QSCE: Quasi-static Catenary Equations; UDFD: User-Defined Force-Displacement Relationships; MBS: Multi-body Simulation; FEM: Finite Element Method; ALM: Actuator Line Model; CFD: Computational Fluid Dynamics)

Software/Tool	Developer	Aerodynamic Model	Hydrodynamic Model	Mooring System
FAST	NREL	BEM/GDW+DS	Airy+ME, Airy+PF+ME	QSCE
GH Bladed	DNV GL	BEM+DS	Airy+ME	UDFD
ADAMS	MSC+NREL+LUH	BEM+DS	Airy+ME, Airy+PF+ME	QSCE, UDFD
HAWC2	Risø-DTU	BEM+DS	Airy+ME, Airy+PF+ME	QSCE, UDFD
AeroDyn/SIMO/RIFLEX	NTNU	BEM	Airy+ME	QSCE, MBS
SESAM.SIMA	DNVS	BEM	Airy+ME, Airy+PF+ME	QSCE, FEM
3Dfloat	IFE-UMB	BEM	Airy+ME	FEM, UDFD
DARwind	UNew+SJTU	BEM	PF+ME	QSCE, FEM
SLOW	Uni. Stuttgart	BEM	PF+ME	QSCE
SIMPACK/HydroDyn	SIMPACK	BEM/GDW	PF+ME	QSCE
Qblade	Qblade	BEM+DS+GDW	PF+ME	QSCE
FOWT-UALM-SJTU	SJTU	ALM/CFD	CFD	QSCE/FEM

However, with the growth of the FOWT industry and advancements in high-performance computing (HPC), an increasing number of researchers have begun utilising CFD for FOWT studies. A blade-resolved CFD study using STAR CCM+ was conducted on the NREL 5-MW turbine, considering the surge and pitch motion (Lin et

al., 2018). The prescribed platform motion, as input, was derived from the results from OpenFAST. It was found that the motion of the platform significantly impacts the unsteady aerodynamic performance of the wind turbine rotor, which has higher power and thrust than the OpenFAST result. Using OpenFOAM, another study with prescribed-surge motion is conducted focusing on the aerodynamic behaviour during the rotor's transition into the propeller state (Kyle and Früh, 2022).

Although with many studies on blade-resolved simulation with prescribed motion (Fu et al., 2023; Kyle et al., 2020; Yao et al., 2023), a method that fully couples aerodynamic and hydrodynamic models is closer to reality and can more accurately reflect the interaction between these two aspects. Tran and Kim used STAR-CCM+ to model an OC4 FOWT with integrated aero-hydrodynamics (Tran and Kim, 2016b) with an overset moving grid technique. The motion response generally matched FAST data, but they found significant differences: the CFD predicted up to four times higher maximum wind turbine power, highlighting the restriction for the BEM model. Based on OpenFOAM, a CFD solver was developed. The coupling effects between different components of the OC4 semi-submersible FOWT model are investigated (Liu et al., 2017). The blade deformation was then considered in the study, combining moving mesh and sliding mesh techniques, where the deformation of the blade and the motion of the system were solved by MBDyn (Liu et al., 2019). Further investigation was conducted on the FOWT's performance under extreme wave conditions (Zhou et al., 2019; Yang Zhou et al., 2021). The type and steepness of waves appear to have minimal effect on the aerodynamic performance of the turbine, as indicated by the consistent thrust and power predictions across various incident wave conditions.

However, the blade-resolved CFD demands an extensive number of computational resources because of the dense mesh required near the blades. Incorporating actuator modelling methods provides a solution to this issue. A fully coupled tool with ALM, called FOWT-UALM-SJTU, is used for the study of two spar FOWTs (Huang et al., 2023), which enables a faster simulation of multiple FOWT interactions. The analysis

shows that both platform motions and wake interactions significantly increase the variation range of inflow wind speed, thereby destabilising the aerodynamic loads of the downstream FOWT. Additionally, platform motions enhance turbulence intensity in the wake region, accelerating wake velocity recovery and broadening the wake width.

2.2.2.2 FOWT farm

As mentioned, the interaction between the wakes of adjacent wind turbines may deeply affect their performance. Many studies have been done on tandem arrangements. Rezaeiha and Micallef (Rezaeiha and Micallef, 2021) studied the interactions between two FOWTs using CFD with an ADM. They analysed how the upstream rotor's prescribed surge motion impacts a downstream fixed rotor. They found that surge motion slightly increases the average power of both rotors and enhances flow mixing in the wake. Their results also suggest that the standard deviation in power output of the downstream rotor is minimally affected by the surging motion of the upstream rotor. However, with advanced ALM instead of ADM in their following research (Arabgolarcheh et al., 2022; Arabgolarcheh, Micallef, Rezaeiha, et al., 2023b; Arabgolarcheh, Rouhollahi, et al., 2023), which has a higher fidelity, they found that upstream rotor's motion has a significant influence on the downstream turbine. It was found that the pitch motion also affects the load fluctuations and power output downstream. The mean values of the power coefficient and thrust coefficient are also influenced as the amplitude of the upstream platform's motion increases. Both increased by 4.97%. Tandem turbines, both with prescribed surge motion and with various phase lags, were studied (Arabgolarcheh, Micallef, and Benini, 2023). It was found that the amplitude of loads and power is sensitive to phase alignment, and a 72% increase in amplitude was observed for the thrust coefficient. Significant increases in load amplitude are observed when the phase lag between the rotors is not aligned, highlighting the importance of synchronised rotor motions for reducing fatigue effects. Huang et al. investigated two FOWTs using the ALM method, which coupled the hydrodynamic model and aerodynamic model (Huang, Zhao, et al., 2023). It was found that platform motion heightens turbulence in the wake area, which speeds up the

recovery of wake velocity and leads to a broader wake. Different layouts of the two turbines are studied. Compared to the tandem layout, the staggered arrangement results in a larger fluctuation amplitude of aerodynamic loads on the downstream rotor. Zhang et al. studied interactions between two FOWTs of staggered and tandem layouts using blade-resolved CFD. The levelized cost of energy (LCOE) for each case is calculated, and it is concluded that tandem layout with a distance of $9.25D$ is the practical optimal parameter choice (Zhang et al., 2022). In tandem arrangement with more than two FOWTs, the CFD mesh can be very large; Kheirabadi and Nagamune developed a low-fidelity dynamic wind farm model for FOWT farm simulation (Kheirabadi and Nagamune, 2021). Three FOWTs are studied with a distance of $7D$. This method assumes that the free stream wind velocity is uniform throughout the wind farm, with steady-state turbine aerodynamics and mooring line model. The platform's motion is assumed to be two-dimensional. Dynamic phenomena in floating wind farms, including the movement of wakes, the variability of wind speed and direction, and the motion of floating platforms, can be seen and are consistent with logical, physical understanding and intuition. Xue et al. studied two tandem FOWTs using FAST.Farm based on dynamic wake meandering (DWM) model(Xue et al., 2022).

However, above studies on two FOWTs are not enough to account for the wake interactions between FOWTs as well as their dynamic response. In an operating wind farm, one FOWT might be affected by more than one turbine ahead of it along the wind direction. This multiple wake effects should be considered by studying the areas influenced by the shadowed cones of the upstream wind turbine (González-Longatt et al., 2012), as shown in Figure 2.5.

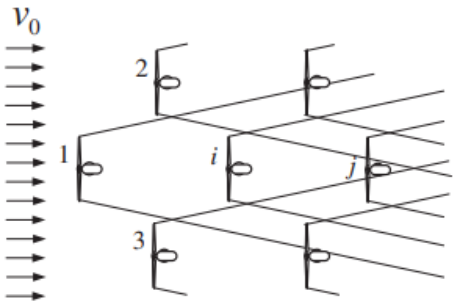

Figure 2.5 Illustration of multiple wake interaction and the shaded area behind turbines (González-Longatt et al., 2012)

This multiple-wake interaction may happen in different scenarios. For example, changes in wind direction while operating lead to changes in the varied shadowed zone of the turbine, making it possibly affected by more upstream turbines (Qian and Ishihara, 2021), as shown in Figure 2.6 (a). A wind turbine operating with a nacelle yaw offset deflects the downstream path of the generated wake in the crosswind direction, which may also increase the number of turbines affecting the downstream turbine (Jiménez et al., 2010; Wagenaar et al., 2012).

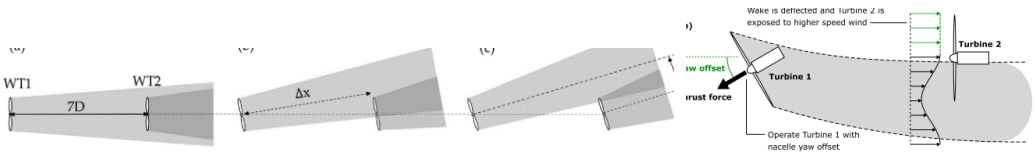

Figure 2.6 (a)Wake changed by wind direction (Qian and Ishihara, 2021) (b) Wake deflected by rotor's yaw (A. C. Kheirabadi and R. Nagamune, 2019)

Repositioning of the turbine may also lead to this scenario. Fleming et al. found that in a two-turbine array, repositioning the downstream turbine along the perpendicular direction to the wind direction leads to a significant change in its load and power efficiency (Fleming et al., 2015). Moving the downstream turbine over a full rotor diameter off the upstream turbine's axis significantly boosts power, with up to a 41% increase. Load changes on the downstream turbine are minor for slight shifts, more pronounced with partial overlap, and plateau when moved by a rotor diameter. Many

studies aiming at boosting the power output are Inspired by this idea, with actively or passively adjusting the position of each FOWT in a wind farm (Mahfouz and Cheng, 2022; Rodrigues et al., 2015). By adjusting the mooring line properties for individual turbines in an array, the passive control of FOWTs is performed, and the overall 13.3GWh output increase can be achieved annually.

Other than the gridded layout, another layout might be applied in a wind farm, which could lead to multiple wake effects. In the optimisation of the wind farm, wake models were used to estimate yearly power production and optimisation algorithms were employed to identify the optimal position of turbines to maximise the wind farm's annual energy production (Shakoor et al., 2016). The updated wind farm layout usually possesses irregular features, as shown in Figure 2.7. A series of optimisation methods based on the wake model are used to optimise the wind farm layout (Fan et al., 2023; Froese et al., 2022; Han and Nagamune, 2016; Kheirabadi and Nagamune, 2019; Kheirabadi and Nagamune, 2020). Meanwhile, yaw and de-rated control was used for each FOWT to reach their optimised position. It is found that the optimised layout generates 2.4% more energy than the regular layout for specific 6*6 FOWT arrays. After optimisation, the staggered and random layout may also lead to a multiple wake interaction between turbines.

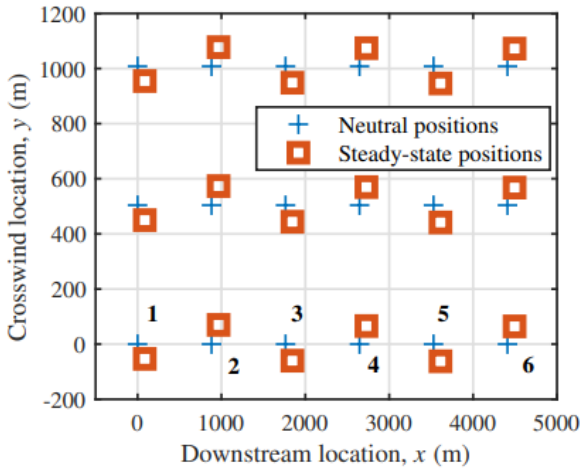

Figure 2.7 Position change of the optimised FOWTs (Kheirabadi and Nagamune, 2019)

Despite the above practical scenarios on multiple wake effects for FOWT farms, limited research can be found. This may be due to the absence of wind farm simulation tools capable of incorporating non-stationary wind turbines (A. C. Kheirabadi and R. Nagamune, 2019). For CFD study, a blade-resolved method can only study a single FOWT with an overset mesh scheme. For multiple turbine studies, there will be extremely large computational costs. Limited studies with more than two FOWTs can be found to the authors' knowledge. In this study, the interaction between platform motion and the multiple wake effects has been studied. Since simulating the entire FOWT farm is infeasible due to computational limits, an array consisting of three FOWTs with varying arrangements is studied. This is the minimum number of turbines required to investigate multiple wake interactions. To deal with this FSI problem, the ALM model is used to solve the aerodynamics of the turbines. Since both aerodynamic and hydrodynamic solvers are OpenFOAM-based, the FSI problem can be solved simultaneously in the same computational domain. The turbine force and moment calculated by ALM are added as an external force to the rigid platforms during each iteration, which is then used for motion solving by six degrees of freedom solver.

2.3 Concluding Remarks

This chapter provides an in-depth review of numerical studies on specific aspects of the FSI of WECs and FOWTs, including the WEC net, flexible WEC, wave-current interactions with FOWT, and the interactions between multiple FOWTs. From this review, several gaps in the literature have been found and need to be resolved in this thesis.

1. Research on WECs mainly focuses on individual WECs or multiple WECs without connections in between. The WEC net with an interconnected multibody system has been limitedly investigated using the CFD method.

2. Research on flexible WECs usually uses experimental analysis or a reduced-order

numerical model. Studies using the partitioned CFD-CSD method are limited and incomplete, especially for numerical studies on WECs utilising hyper-elastic material. Parametric studies on hyper-elastic WECs are necessary.

3. The ocean current effects on the FOWT platforms have been studied extensively. However, there is not much research on VIM under wave-current conditions. In a few studies on wave-current interaction with platforms, the waves and current are in the same direction. Related research is scarce regarding the platform's VIM response under conditions of differing wave and current directions.

4. The CFD studied on fully coupled FOWT mainly focused on individuals. Parametric studies using the CFD method with more than two FOWTs are limited. It is necessary to clarify the influence of layout on wake interactions among FOWTs. This study specifically examines three FOWTs, although the methodology developed is capable of handling more than that.

Chapter 3 Numerical Method

Depending on specific FSI issues, different numerical strategies are needed, as shown in Figure 3.1. For flow field solving, the CFD solver is used with customized boundary conditions for wave absorbing and generation. Also, an in-house code has been integrated to solve the mooring system. All forces calculated by these solvers are considered as external solvers and are transferred to the structural solver in an iterative manner. For the FSI problems with the multibody system in Chapter 4, MBDyn is coupled. For FSI problems with flexible hyper-elastic structures in Chapter 5, CalculiX is coupled. For FSI problems in FOWT, six degrees of freedom motion solver built in OpenFOAM is used to solve rigid body motion problems.

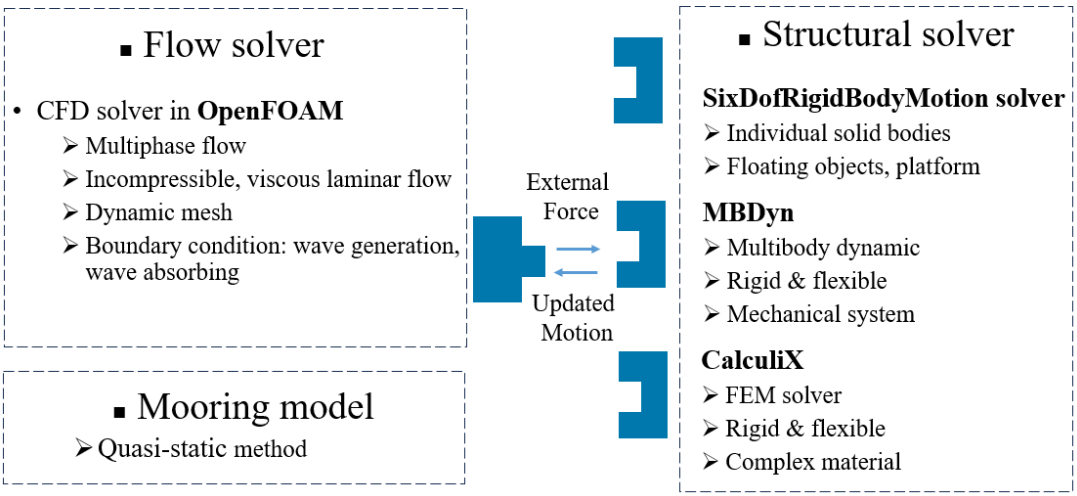

Figure 3.1 Structure of the fully coupled FSI analysis tool

Field Solving

3.1.1 Governing Equations of Fluid Flow

The solution to the fluid dynamics issue is performed using the open-source CFD code OpenFOAM. The current solver utilised is developed from the inherent solver InterFOAM and designed for multi-phase flow solving. In this model, the flow is governed by incompressible Navier-Stokes (NS) equations. Since moving mesh is utilised, the Arbitrary Lagrangian-Eulerian (ALE) form of NS equations is adopted:

$$\frac{\partial u_i}{\partial x_i} = 0 \tag{3.1}$$

$$\frac{\partial \rho u_i}{\partial t} + \frac{\partial}{\partial x_j}\left(\rho u_i \left(u_j - \hat{u}_j\right)\right) = -\frac{\partial p}{\partial x_i} + \frac{\partial}{\partial x_j}\left[\mu_{eff}\left(\frac{\partial u_i}{\partial x_j} + \frac{\partial u_j}{\partial x_i}\right)\right] + \rho g_i + f_{\sigma i} + f_{\varepsilon i} \tag{3.2}$$

where x_i is the Cartesian coordinate, and the subscript I represents the i_{th} component. The index i=1 denotes the x direction, while i=2 and 3 indicate the y and z direction, respectively. u_{i} is the fluid velocity; $\widehat{u_i}$ is the speed of the moving mesh grid; t is the time; ρ is the fluid density; p denotes dynamic pressure; $\mu_{\text{eff}} = \rho\,(v + v_t)$ denotes the effective dynamic viscosity of the fluid, in which v and v_t are the kinematic and eddy viscosity, respectively; g_i is the gravity acceleration; $f_{\sigma i}$ represent the surface tension; $f_{\varepsilon i}$ denotes the body force from the wind turbine if the ALM model is enabled.

3.1.2 Turbulence Modelling

For a fluid problem, the Reynolds number $Re = \mathbf{u}l/v$ is one non-dimensional parameter to differentiate between laminar and turbulent flows, where l is the characteristic length of the structure. In this study, different scenarios are involved. For studying the WEC interacting with waves in Chapters 4 and 5, the laminar flow is assumed. This assumption is widely accepted by researchers because it was found that there is no apparent discrepancy between the results obtained from turbulence or laminar models when the flow is mainly dominated by wave rather than current (Finnegan and Goggins, 2012; Wang et al., 2021).

In the VIM study of platforms in Chapter 6, the *Re* ranges from 8000 to 40000 for current-only cases. In these studies, vortex shedding and flow fields surrounding structures are essential components. As such, it's crucial to capture a precise structure of the vortex, a task which is normally not optimally accomplished by utilising the standard RANS model due to its highly numerical dissipation. In the present study, the Large Eddy Simulation (LES) wall-adapted local eddy-viscosity (WALE) model is used (Nicoud and Ducros, 1999). In addition, it is also applied in the FOWTs study in

Chapter 7 for the same reason. In LES, the largest, most energy-containing turbulent structures (large eddies) are explicitly resolved on the computational grid, while the smaller, more isotropic structures (small eddies or sub-grid scales) are modelled. After filtering turbulence using a filter function $G(\mathbf{x}, \mathbf{x}')$, the flow field variable ϕ can be decomposed into the filtered one $\bar{\phi}_i$ representing the large-scale eddies, and the subgrid-scale one ϕ^{sgs}

$$\bar{\phi}(\boldsymbol{x}) = \int_{Domain} \phi(\boldsymbol{x}')G(\boldsymbol{x}, \boldsymbol{x}')d\boldsymbol{x}' \tag{3.3}$$

$$G(\boldsymbol{x}, \boldsymbol{x}') = \begin{cases} 1/V, & \boldsymbol{x}' \in V \\ 0, & \boldsymbol{x}' \notin V \end{cases} \tag{3.4}$$

where V is the control volume. The filtered Naiver-Stokes equations are as follows:

$$\frac{\partial}{\partial t}(\rho\bar{u}_i) + \frac{\partial}{\partial x_j}\left(\rho\bar{u}_i(\bar{u}_j - \hat{u}_j)\right) = -\frac{\partial\bar{p}}{\partial x_i} + \frac{\partial}{\partial x_j}\left[\mu_{eff}\left(\frac{\partial\bar{u}_i}{\partial x_j} + \frac{\partial\bar{u}_j}{\partial x_i}\right)\right] + \rho g_i + \bar{f}_{\sigma i} + \bar{f}_{\varepsilon i} - \frac{\partial\tau_{ij}^{sgs}}{\partial x_j}$$

(3.5)

$$\tau_{ij}^{sgs} = \rho\overline{u_i u_j} - \rho\bar{u}_i\bar{u}_j \tag{3.6}$$

The subgrid-scale stresses resulting from the filtering operation are unknown. Thus, the Boussinesq hypothesis is applied to compute the subgrid-scale stress:

$$\tau_{ij}^{sgs} - \frac{1}{3}\delta_{ij}\tau_{kk}^{sgs} = -2\nu_{sgs}\bar{S}_{ij} \tag{3.7}$$

where

$$\nu_{sgs} = (C_w\Delta)^2 \frac{\left(S_{ij}^d S_{ij}^d\right)^{3/2}}{\left(\bar{S}_{ij}\bar{S}_{ij}\right)^{5/2} + \left(S_{ij}^d S_{ij}^d\right)^{5/4}} \tag{3.8}$$

where C_w is the model constant. The filter width Δ is taken as the local grid size. The tensor S_{ij}^d can be rewritten in terms of the strain rate and vorticity tensors:

$$S_{ij}^{d}=\frac{1}{2}\left(\bar{g}_{ij}^{2}+\bar{g}_{ji}^{2}\right)-\frac{1}{3}\delta_{ij}\bar{g}_{kk}^{2},\ \bar{g}_{ij}=\frac{\partial\bar{u}_{i}}{\partial x_{j}} \tag{3.9}$$

The benefit of employing the WALE model lies in its invariance to coordinate translation or rotation and its reliance solely on local information, making it highly suitable for LES applications in complex geometries. This model facilitates more precise estimations of velocity gradients and shear stresses near walls, offering robust performance and straightforward implementation.

For the near-wall treatment in the LES cases, the turbulence models are modified to enable the viscosity-affected region to be directly resolved with a mesh all the way to the wall, which is normally termed the near-wall modelling approach. To ensure sufficiently fine meshing in the near-wall region, the mesh with wall $y+ \leq 1$ is used in the related study.

3.1.3 Free Surface Modelling

In FSI problems with free-surface, two types of fluid, air and water, should both be simulated. Thus, the Volume of Fluid (VOF) method (Hirt and Nichols, 1981) is used to capture the free surface. The volume fraction α for each cell is defined to govern the interface of air and water, which represents the percentage of the cell occupied by the water. α=1 means the whole cell is occupied by water, while α=0 it is filled with air. A value between 1 and 0 means that the cell is located at the free surface. The following transport equations govern the volume fraction:

$$\frac{\partial\alpha}{\partial t}+\frac{\partial}{\partial x_{j}}\left(\left(u_{i}-\hat{u}_{i}\right)\alpha\right)+\frac{\partial}{\partial x_{j}}\left(u_{ri}\left(1-\alpha\right)\alpha\right)=0 \tag{3.10}$$

$$\begin{cases}\alpha=0 & air\\ \alpha=1 & water\\ 0<\alpha<1 & free\ surface\end{cases} \tag{3.11}$$

To better capture an accurate interface, it is crucial to maintain a sharp interface and ensure that the α remains conservative and bounded between 0 and 1. To achieve this,

OpenFOAM utilises an artificial compression term $\frac{\partial}{\partial x_j}\left(u_{ri}\left(1-\alpha\right)\alpha\right)$, where u_{ri} is the velocity field used to compress the interface and only functions near the free surface (Rusche, 2003). For the present water-air problem, fluid density and viscosity can be written as a mixture of water and air:

$$\rho = \alpha\rho_w + \left(1-\alpha\right)\rho_\alpha \tag{3.12}$$

$$\mu = \alpha\mu_w + \left(1-\alpha\right)\mu_\alpha \tag{3.13}$$

where ρ_w and ρ_a denote the density of water and air, μ_w and μ_a denote their dynamic viscosity.

3.1.4 Wave and Current Modelling

Based on the above model, a numerical wave tank is developed, with wave generation and absorption being the most important part. The incident waves are produced by specifying velocity and wave elevation at the inlet boundary. In this study, Stokes 2nd order wave theory is applied to represent the incident wave, where free-surface elevation can be defined as:

$$\eta = \frac{H}{2}\cos\theta + \frac{H}{8}\left(\frac{\pi H}{L}\right)\frac{\cos kd}{\sinh^3 kd}\left(\cos 2kd + 2\right)\cos 2\theta \tag{3.14}$$

$$\theta = kx + \omega t \tag{3.15}$$

where H and T denote the wave height and wave period, k and d denote wave number and water depth. The fluid velocity along the x and z axis given at the inlet boundary can be written as:

$$u = \frac{\pi H}{T}\frac{\cosh k\left(z+d\right)}{\sinh kd}\cos\theta + \frac{3\pi H}{4T}\left(\frac{\pi H}{L}\right)\frac{\cosh 2k\left(z+d\right)}{\sinh^4 kd}\cos 2\theta \tag{3.16}$$

$$w=\frac{\pi H}{T}\frac{\sinh k\left(z+d\right)}{\sinh kd}\sin\theta+\frac{3\pi H}{4T}\left(\frac{\pi H}{L}\right)\frac{\sinh 2k\left(z+d\right)}{\sinh^4 kd}\sin 2\theta \tag{3.17}$$

In the wave-current combined condition, a constant current velocity $\mathbf{U}_c$ should be applied on top of the wave velocity. This wave generation boundary is achieved by an in-house code developed on OpenFOAM, which has been proven to be very effective in previous studies (Liu et al., 2017). Also, to reduce wave reflection at the outlet boundary, a passive wave absorbing model is applied (Wang et al., 2021), in which the sponge layer is used to damp waves and takes effect by adding an additional artificial viscous term as a source term to equation 3.2, which is defined as

$$\mathbf{f}_s=-\rho\mu_s\mathbf{U} \tag{3.18}$$

Where μ_s is the artificial viscosity coefficient calculated by the following equation:

$$\mu_s\left(x\right)=\begin{cases}\alpha_s\left(\dfrac{x-x_0}{L_s}\right)^2, x>x_0\\ 0\qquad\qquad\quad, x\le x_0\end{cases} \tag{3.19}$$

where α_s defines the damping strength for the sponge layer, x_0 and L represent the start position and length of the sponge layer.

The above passive wave absorbing scheme is applied in Chapter 4. Although passive wave absorption remains effective and straightforward to apply, this method requires extending the domain at least 1 - 2 wavelengths to obtain an acceptable performance. This leads to far more additional computational domains in the relaxation zone, increasing the computational cost, especially when the wavelength is large (Wei and Kirby, 1995). After Chapter 5, an active wave absorbing scheme is utilised, with the waves directly absorbed at the outlet boundary without relaxation zones (Higuera, 2020). This can significantly reduce the computational domain size required by the relaxation zone (Li, Xiao, Zhou, et al., 2022). The primary concept is to produce waves with a phase opposite to that of the incident waves but with the same characteristics at

the outlet boundary. The corrected velocity at the outlet boundary is described by:

$$\Delta u = -\Delta\eta \frac{\pi H}{T} \frac{\cosh k\left(z+d\right)}{\sinh kd} \tag{3.21}$$

where $\Delta\eta$ is the difference of the surface elevation η due to reflected waves.

3.1.5 Actuator Line Model

In the FOWT study, to calculate the forces and power of the wind turbines, as well as the interaction with the surrounding flow field, the ALM, as a high-fidelity aerodynamic modelling approach, is used in our present CFD solver. The ALM is rooted in BEM theory but incorporates the spatial resolution of forces along the blade span. The lift and drag forces exerted by each blade element are calculated using blade element theory, which relates the lift and drag coefficients to the local angle of attack and the Reynolds number, which are then used to calculate the forces based on the relative wind velocity. These forces are then applied back to the flow field, allowing the simulated wake to develop naturally and interact with the rotor and the environment. In this study, the traditional ALM is modified, incorporating the platform's motion. To implement an ALM in the CFD, many steps are required.

The first step is discretisation, where the turbine blades are firstly discretised into a series of spanwise line segments or actuator lines, as shown in 0. These lines represent the blade's centre of pressure or a specified percentage of the chord from the leading edge, typically at 25%.

The second step is the calculation of local flow conditions. For each line segment, the local flow conditions, including the angle of attack α and local relative wind speed $\mathbf{U}_{rel}$, are needed for the force calculation. These are determined by the interaction of the incident wind with the rotational motion of the rotor and any additional motions of the turbine platform, for example, wave or current-induced motion for a FOWT.

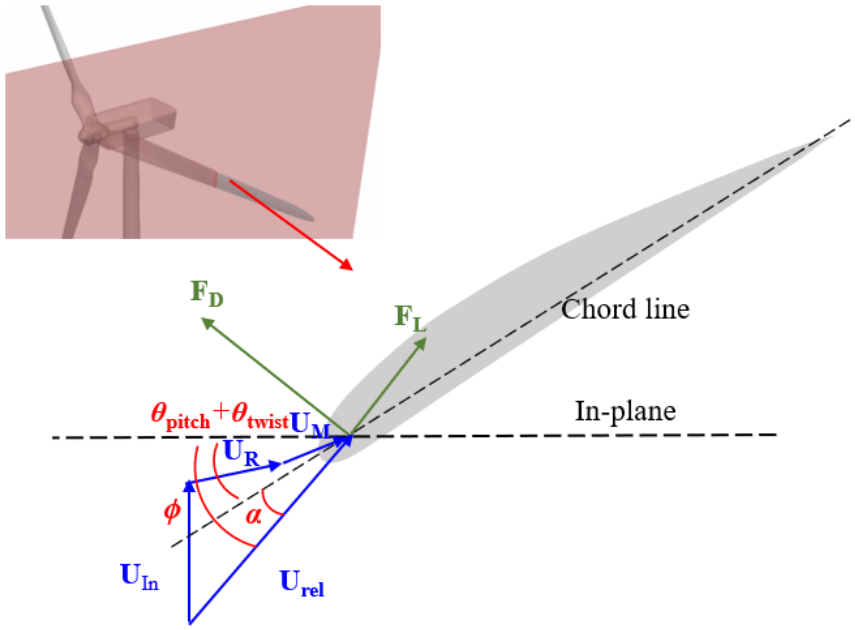

Figure 3.2 Sketch of the velocity components at the blade section

The interplay between the velocity vectors can be expressed as follows:

$$\mathbf{U}_{\text{rel}} = \mathbf{U}_{\text{In}} + \mathbf{U}_{\text{R}} + \mathbf{U}_{\text{M}} = \mathbf{U}_{\text{In}} + \boldsymbol{\Omega} \times \mathbf{r} + \mathbf{U}_{\text{M}} \tag{3.22}$$

where $\mathbf{U}_{\text{In}}$ is the velocity of the incoming wind velocity in the blade-aligned coordinate system, $\mathbf{U}_{\text{R}}$ is the velocity induced by the rotor's rotation, $\boldsymbol{\Omega}$ is the rotor's angular velocity, $\mathbf{r}$ is the vector that extends from the blade root to the concerned actuator point, and $\mathbf{U}_{\text{M}}$ is the platform-induced velocity. $\mathbf{U}_{\text{M}}$ is translated to the motion of blades since the influence of $\mathbf{U}_{\text{M}}$ on aerodynamic performance is significant. The translated position $\mathbf{X}_{\text{M}}$ and velocity $\mathbf{U}_{\text{M}}$ of specific actuator point are:

$$\mathbf{X}_{\text{M}} = \boldsymbol{\eta}_1 + \boldsymbol{\eta}_2 \left(\mathbf{x}_j - \mathbf{x}_c \right) \tag{3.23}$$

$$\mathbf{U}_{\text{M}} = \dot{\boldsymbol{\eta}}_1 + \dot{\boldsymbol{\eta}}_2 \left(\mathbf{x}_j - \mathbf{x}_c \right) \tag{3.24}$$

where $\mathbf{x}_j$ is the points' position without considering the platform's motion, and $\mathbf{x}_c$ is the initial platform's centre of rotation. $\boldsymbol{\eta}_1$ and $\boldsymbol{\eta}_2$ are the displacement and rotation of the platform. The local angle of attack α is calculated based on the $\boldsymbol{U}_{\text{ref}}$:

$$\alpha = \phi - \left(\theta_{\text{pitch}} + \theta_{\text{twist}} \right) \tag{3.25}$$

$$\phi = \arctan\left(\frac{U_{\text{rel},x}}{U_{\text{rel},y}}\right) \tag{3.26}$$

where ϕ is the inflow angle, θ_{pitch} is the local pitch angle, and θ_{twist} is the section twist angle. ϕ can be calculated by the x and y components of $\mathbf{U}_{\text{rel}}$ ($U_{\text{rel},x}$, $U_{\text{rel},y}$, $U_{\text{rel},z}$).

Figure 3.3 Discretized elements of the blades.

Based on the above local flow conditions, the aerodynamic forces are computed using airfoil data. These forces are broken down into lift and drag components per segment and are functions of the local angle of attack, the relative wind speed, and the chord length of the blade segment. This force can be determined by the following equation:

$$f = \left(\mathbf{F}_{\text{L}}, \mathbf{F}_{\text{D}}\right) = 0.5\rho\left|\mathbf{U}_{\text{rel}}\right|^2 c\left(c_{\text{l}}\mathbf{e}_{\text{l}} + c_{\text{d}}\mathbf{e}_{\text{d}}\right) \tag{3.27}$$

where $\mathbf{F}_{\text{L}}$ and $\mathbf{F}_{\text{D}}$ are lift and drag forces, respectively. $\boldsymbol{e}_{\text{l}}$ and $\boldsymbol{e}_{\text{d}}$ are the unit vectors of lift and drag forces, respectively. c_l and c_d are the lift and drag coefficients. ρ is the air density, and c is the chord length. These coefficients can be found in the airfoil data as given properties for specific turbines.

When calculating the aerodynamic loads on wind turbine blades using blade element theory, it's crucial to account for the effects of vortex shedding from both the blade tip and root. These effects lead to modifications in the aerodynamic load predictions, necessitating the application of specific correction factors. The tip and root loss factor,

$F_{\text{tip and}}\ F_{\text{root,}}$ are introduced to adjust for the reduced aerodynamic efficiency in these areas due to the vortex shedding:

$$F_{\text{tip}} = \frac{2}{\pi}\cos^{-1} e^{-\frac{N_b}{2}\frac{R_{\text{rotor}}-r}{r\sin\phi}} \tag{3.28}$$

$$F_{\text{root}} = \frac{2}{\pi}\cos^{-1} e^{-\frac{N_b}{2}\frac{r-R_{\text{hub}}}{r\sin\phi}} \tag{3.29}$$

where R_{rotor} and R_{hub} are the radius of the rotor and hub, respectively. N_{b} is the number of blades. The corrected loads on the turbines f' are then corrected by:

$$f' = f \cdot F_{tip} \cdot F_{root} \tag{3.30}$$

By integrating the loads along the blade's spanwise direction, the power output P and thrust F_{T} can be calculated:

$$\mathbf{F}_{\text{T}} = \sum_{i=1}^{N_{\text{b}}}\sum_{j=1}^{N_{\text{p}}}\mathbf{F}_{\text{D}ij} \tag{3.31}$$

$$\mathbf{M}_{\text{e}} = \sum_{i=1}^{N_{\text{p}}}\mathbf{F}_{\text{L}i}\times\mathbf{r}_i \tag{3.32}$$

$$P = \sum_{i=1}^{N_{\text{b}}}\mathbf{M}_{\text{e}i}\cdot\boldsymbol{\Omega} \tag{3.33}$$

where $\mathbf{F}_{\text{L}i\ \text{and}}\ \mathbf{F}_{\text{D}i}$ are the lift and drag force of the i^{th} element, N_{p} is the number of elements, N_{b} is the number of blades, and $\mathbf{M}_{\text{e}}$ is the torque. The calculated forces are then projected onto the flow field using a body force projection. This step ensures the forces are smoothly distributed over the CFD mesh, preventing numerical instabilities. To project the body forces, a regularisation kernel function η is used:

$$\eta\left(d_j\right) = \frac{1}{\varepsilon^3\pi^{\frac{3}{2}}}\exp\left[-\left(\frac{d_j}{\varepsilon}\right)^2\right] \tag{3.34}$$

where d_j is the distance between the gird node and the actuator point. The constant parameter ε decides the width of the projection region and has significant effects on the computation results. It is recommended to set it to twice the minimum mesh size to ensure a stable numerical solution(Troldborg et al., 2010). It can be seen that this function only influences the cells near the element. The force projected to the cells is then calculated by:

$$f_\varepsilon\left(x,y,z,t\right)=\sum_{j=1}^{N_p} f\left(x_j,y_j,z_j,t\right)\eta_\varepsilon\left(d_j\right) \tag{3.35}$$

After the force projection, the modified flow field equations, now including the body forces from the actuator lines, are solved using CFD techniques to capture the resulting flow field, like the velocity and the pressure, which is used for the aerodynamic force's calculation.

3.2 Structural Solving

3.2.1 Multibody Dynamics Model

Generally, a multibody system is defined as a complex system consisting of more than one rigid body, where each body can interact with others. This is exactly the same situation as for the WEC net in Chapter 4, where the floats are the main components, and the linking arms are sub-structures that connect them. There are articulations at the connection points between the two floats, imposing constraints where rotation mode is permitted while translation is prevented. At the articulations, damping or stiffness can be applied if the electric damping of the joint is numerically modelled. The mooring lines are involved as a practical solution to restrain the WEC system from drifting caused by the wave and current. In the present study, the dynamic of such a complex system is solved by MBDyn (Ghiringhelli et al., 2000).

MBDyn adopts a Lagrange multiplier or redundant coordinate set formulation for a multi-body system. Compared to the reduced coordinate set method, where only minimum numbers of degrees of freedom (DoFs) are used to describe the motion of the

system, a redundant formulation which allows 6 DoFs motion for each body and constraints are enforced by Lagrange multipliers (Masarati and Sitaraman, 2011).

For each body of the system, Newton-Euler equations of motion are established in the differential-algebraic form as a set of first-order equations together with the constraint equation, resulting in a system of Differential-Algebraic Equations (DAE) as follows:

$$\mathbf{M}\dot{\mathbf{x}} = \mathbf{p} \tag{3.36}$$

$$\dot{\mathbf{p}} + \phi_{\mathrm{x}}^{\mathrm{T}}\boldsymbol{\lambda} = \mathbf{f}\left(\mathbf{x}, \dot{\mathbf{x}}, t\right) \tag{3.37}$$

$$\phi\left(\mathbf{x}, t\right) = 0 \tag{3.38}$$

where **M** denotes the inertia matrix of the rigid body, **x** denotes the translational and rotational parameters in the global reference frame. **p** refers to the momentum of the body. $\boldsymbol{\lambda}$ denotes the vector of the Lagrange multipliers for the constraints; **f** is the external force and moment vector exerted upon the body, which might be related to its displacement and velocity as well as time. ϕ is a set of kinematic constraints applied to the body and $\phi_{\mathrm{x}}^{\mathrm{T}}$ is the Jacobian of ϕ with respect to the generalised coordinates. At the conjunction of the arm and float, the constraint should be applied, acting as a spherical joint, which is shown in 0. The joint connects two objects like a hinge; each object has six degrees of freedom and moves freely, but their relative translational displacement is restrained. Only relative rotation is allowed.

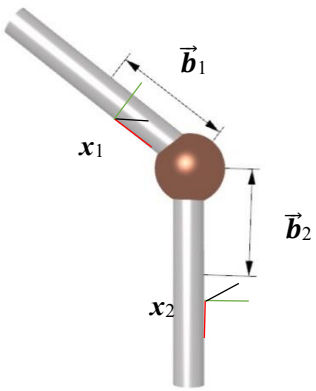

Figure 3.4 Sketch of the spherical joint

Constraint equations ϕ are as follows:

$$\phi\left(\mathbf{x}(t)\right)=\left(\mathbf{x}_2+\mathbf{b}_2\right)-\left(\mathbf{x}_1+\mathbf{b}_1\right) \tag{3.39}$$

$$\mathbf{b}_1=\mathbf{R}_1\vec{\mathbf{b}}_1,\mathbf{b}_2=\mathbf{R}_2\vec{\mathbf{b}}_2 \tag{3.40}$$

where $\vec{\mathbf{b}}_1$ and $\vec{\mathbf{b}}_2$ are the offsets of connection points from structures 1 and 2 in the structure reference, respectively. $\mathbf{R}_1$ and $\mathbf{R}_2$ are the orientations of the structures.

When electric damping is applied to the spherical joint in Chapter 4, it creates a damping torque τ_i; this can be quantified by equation 3.41, where *i* denotes the number of the floats, β denotes the electric damping, and ω denotes the rotational angular velocity. The total power output of the WEC net can be estimated by equation 3.42.

$$\tau_i(t)=\beta\omega(t) \tag{3.41}$$

$$P(t)=\sum_{i=1}^{9}\tau_i(t)\cdot\omega(t) \tag{3.42}$$

To simplify the complexity of the system, the mooring which controls the drifting motion is substituted with a force between two points. The mass of ropes is neglected in our model, reducing the simulation time significantly. The force of the rope depends on the relative distance between the two points, which follows the following constitutive law:

$$f=\begin{cases}k_{\mathrm{r}}\cdot\varepsilon_{\mathrm{r}}\left(\varepsilon_{\mathrm{r}}>0\right)\\0\left(\varepsilon_{\mathrm{r}}<0\right)\end{cases} \tag{3.43}$$

where k_{r} is the stiffness of the ropes, ε is the strain of the ropes. The force only exists when the ropes are elongated $\left(\varepsilon_{\mathrm{r}}>0\right)$.

3.2.2 Finite Element Model

For the solving of flexible structures in Chapter 5, in order to consider different material

properties, the deformation of the flexible structure is solved by an open-sourced FEA code CalculiX (Dhondt, 2004). This code has been successfully coupled with our in-house flow solver and is widely used for a variety of biomimetic fish swimming problems involving passive flexible material deformation (Luo, Xiao, Shi, et al., 2020; Luo, Xiao, Zhu, et al., 2020; Luo et al., 2021). The governing equation of the structure solver is the weak form of the balance of momentum and is written in the differential form as

$$\rho_s \frac{D^2\mathbf{S}}{Dt^2} = \nabla \cdot \mathbf{P}_s + \mathbf{f}_s \tag{3.44}$$

where the acceleration of the material point is obtained by the second derivatives of displacement vector **S** of the structure and surface forces are modelled by the second Piola–Kirchoff stress tensor $\mathbf{P}_s$ and external force such as gravity and hydrodynamic force, which is represented by $\mathbf{f}_s$.

A constitutive equation describing the relation between the stress and the strain is used to close equation 3.44. Specifically, for a Saint Venant–Kirchhoff material, the second Piola–Kirchoff stress tensor P_s is obtained by

$$\mathbf{P_s} = \mathbf{C} : \mathbf{E}, \mathbf{E} = 1/2\left(\mathbf{F}^{\mathrm{T}}\mathbf{F} - \boldsymbol{\delta}\right) \tag{3.45}$$

where **C** is the elasticity tensor, **E** represents the Green–Lagrange strain tensor, the deformation gradient is characterised by **F,** and **δ** is the unit tensor. The governing equation of the structure equation is discretised using the finite element method. With the application of the virtual work method, a linear algebraic equation system by the discretisation in the complete solid domain is obtained:

$$\mathbf{KS} + \mathbf{M}\frac{D^2}{Dt^2}\mathbf{S} = \mathbf{F} \tag{3.46}$$

where **K** is the global stiffness matrix, **M** is the global matrix, and **F** is the global force vector, respectively. The time domain is discretised using the α method (Dhondt, 2004).

3.2.3 Rigid Body Motion Model

In the study of FOWTs in Chapters 6 and 7, the platform can be considered as an individual rigid body with no mechanical interactions between adjacent platforms. In this case, the sixDoFRigidBodyMotion solver is applied to solve the six degrees of freedom (6-DoF) motion of the platform. The governing equation is:

$$m_s \frac{D^2\mathbf{S}}{Dt^2} = \mathbf{f}_s \tag{3.47}$$

where m_s is the mass of the platform, $\mathbf{f}_s$ is the external force acting on the Platform, which includes the gravity, the hydrodynamic force, the aerodynamic force from the turbine, and the mooring force.

3.2.4 Mooring Model

The mooring model is applied for FOWT simulations in Chapters 6 and 7 using an in-house code (Liu et al., 2017). In the current research, the solver models the mooring lines in a quasi-static manner. This model breaks down the mooring line into several equal-length segments; only the tension and the buoyant weight are considered while ignoring hydrodynamic impacts from currents and waves. Static equilibrium equations are applied to each segment, considering both horizontal and vertical forces, as shown in Figure 3.5, where each mooring line is assumed to be two-dimensional.

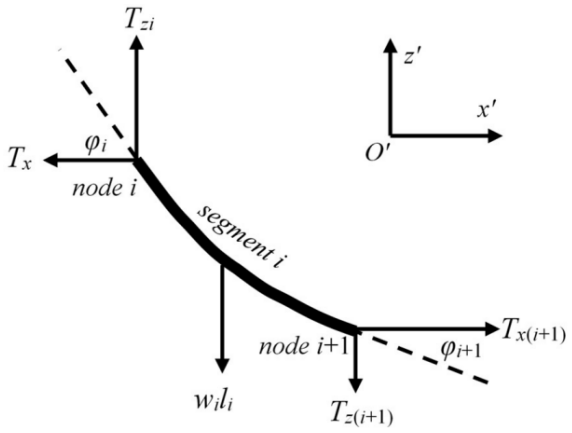

Figure 3.5 Sketch illustrating force balance for segment *i* within the quasi-static analysis model for mooring lines.

Static equilibrium equations are formulated for both horizontal and vertical components:

$$\begin{cases} T_{x(i+1)} = T_{xi} \\ T_{z(i+1)} = T_{zi} + w_i dl \end{cases} \tag{3.48}$$

where T_x and T_z denote the horizontal and vertical tension forces at the two nodes (i and i+1) linked by segment i. w_i represents the weight per unit length of the segment in water, effectively excluding the buoyancy effects present in air. l_i refers to the unstretched or original length of the segment. Considering the stretch of the mooring line, the stretched length s_i is calculated by:

$$s_i = l_i \left(1 + \frac{T_i}{E_i A_i} \right) \tag{3.49}$$

where T_i is the total tension force at the i_{th} node, E_i and A_i is the Young's modulus and the section area of the i_{th} node, respectively. Additionally, there are geometric constraints relating the coordinates of the nodes to the length of the stretched segment:

$$\begin{cases} s_i \cos\varphi_i = x'_{i+1} - x'_i = \Delta x' \\ s_i \sin\varphi_i = z'_{i+1} - z'_i = \Delta z' \end{cases} \tag{3.50}$$

Where ϕ_i represents the included angle between the total tension T_i and its horizontal component T_{xi}. The variables x' and z' denote the horizontal and vertical coordinates of the node within the local mooring line reference frame. Furthermore, $\Delta x'$ and $\Delta z'$ indicate the absolute differences between adjacent nodes along the x' and z' directions, respectively. The solving procedure is shown in Figure 3.6, where the initial T_{x0} and T_{z0} are assumed for initialisation at the fairlead node $\boldsymbol{x}_0'$. Based on equation 3.47, the tension force at the adjacent point $\boldsymbol{x}_1'$ can be calculated, as well as the position of $\boldsymbol{x}_1'$ based on equation 3.49. By iterating from the fairlead node to the anchor node, the tension force and position of each node can be calculated. The total positional error of the anchor point, termed *errTotal*, will be assessed to determine if it meets the convergence standards, typically requiring around 40 iterations. The final tension force

at the fairlead points is then applied to the floating structures as external mooring loads. For a mooring line with parts of it resting on the seabed, the current model uses a simplified kinematic constraint to manage the line-seabed interaction. In simulations, if a node's predicted position is below the seabed level, z_i' is set equal to the seabed level. Additionally, the vertical tension force T_{zi} at this node, and any subsequent nodes, is set to zero.

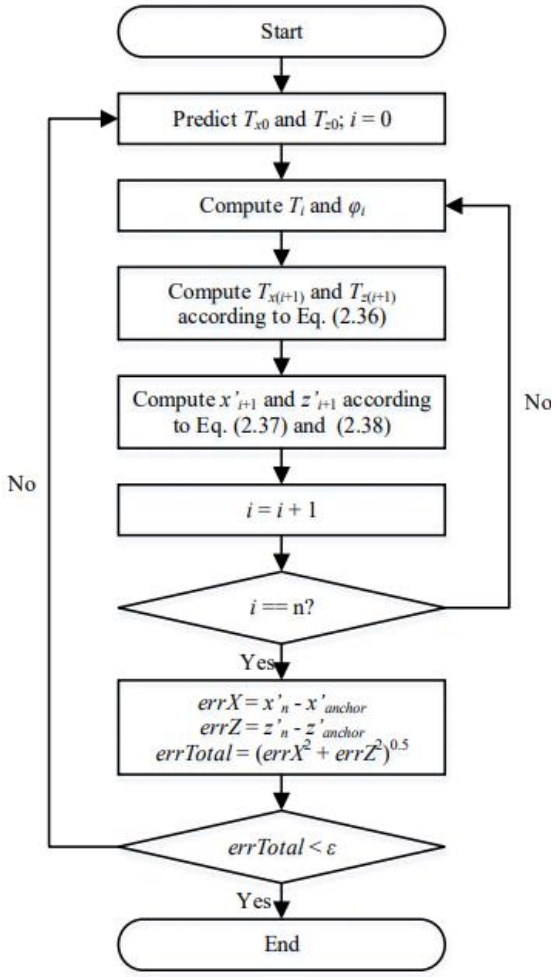

Figure 3.6 The workflow of the mooring line analysis

3.3 Coupling Scheme

Aside from the multi-physical field solving, data transfer between each solver is necessary for weak coupling. In the present framework, coupling between CFD and computational structural dynamics CSD solvers involves different solvers. For flexible

structures, FEA solvers should be coupled, while a multi-body solver should be coupled when a multi-body structure exists.

For multi-body systems, after receiving the dynamic response of the structures, the data should be transferred back to the CFD solver. The coupling method between the CFD solver and MBDyn software was previously implemented and utilised to solve a flexible wind turbine blade analysis, in which the blade was simplified as a beam-like structure in the structural solver (Liu et al., 2019). The coupling strategy performed in the present study for a WEC net is shown in Figure 3.7. The CFD solver and the structural solver run simultaneously at separate computer processes, and the data exchange is achieved with the help of TCP/IP protocol. At the very beginning of the simulation, MBDyn uses a TCP/IP socket for two-way communication to exchange information with the CFD solver. The hydrodynamic force on the components calculated from the CFD solver is transferred into the multi-body system solver, MBDyn. By accepting the force data, MBDyn predicts the dynamic response of the WEC system and then feeds the updated position data back into the CFD solver. The CFD mesh is then updated, followed by an update of the entire flow field. The communication between the two solvers is completed at each iteration in each time step so that strong coupling is achieved with a robust and fast convergence.

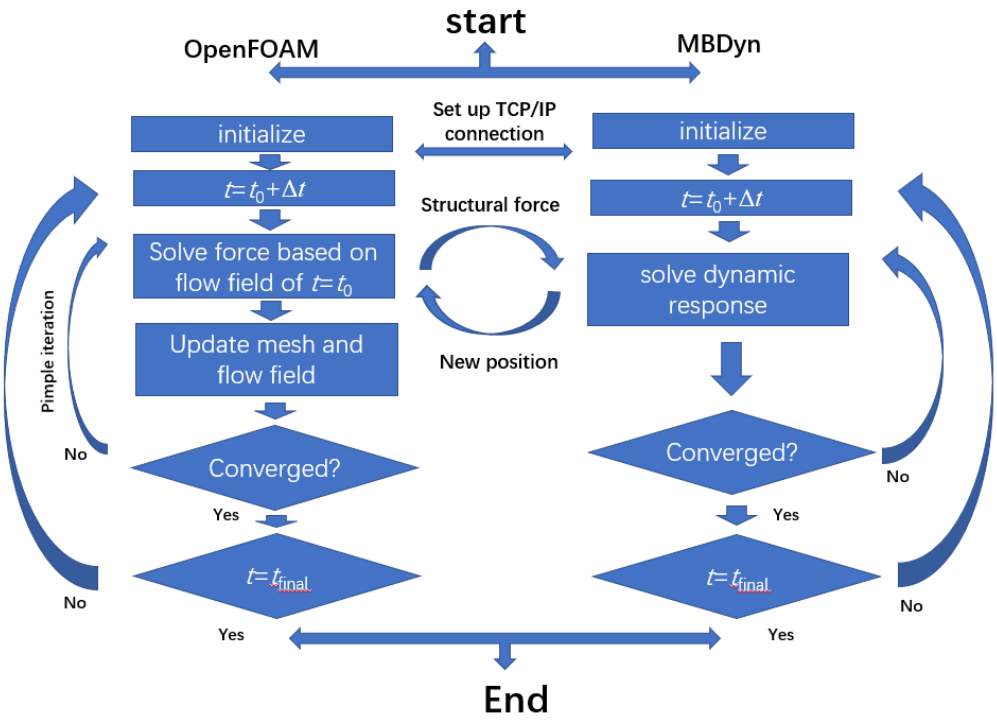

Figure 3.7 The workflow of the CFD-MBD coupling strategy

For FEA coupling, an open-sourced code preCICE, which functions as a general framework for partitioned method studies, is utilized for coupling, as shown in Figure 3.8 (Chourdakis et al., 2021; Dhondt, 2004). It provides a tool which minimises the effort of adapting the original computation code when coupling two solvers, as well as several schemes to accelerate and stabilise the coupling process. It is very challenging to solve strongly coupled FSI problems, where numerical instabilities may cause divergence, especially when the fluid has a similar density to the solid structure (Paola Causin et al., 2005). This problem is especially serious when the nonlinearity is strong, such as for the hyper-elastic material study with highly nonlinear features. In order to achieve numerical stability and convergence within this framework, a sub-iteration is added during each time step in an implicit scheme. In addition, the interface quasi-Newton method with inverse Jacobian from a least-squares model (IQN-ILS) (Degroote et al., 2009; Haelterman et al., 2016) implemented in preCICE is used to stabilise the coupling and accelerate the convergence. It is a Newton–Raphson scheme that tries to find the root of the residual equations of displacements and fluid forces at the interface.

Since the fluid and structural grids are non-conformal, an interpolation between the two is needed to map the data at the interface. In this work, the radial basis functions (RBF) based interpolation (Lindner et al., 2017) is utilised, which is a data mapping method used in multi-physics coupling with a second-order method to transfer forces from the fluid solver to the structural solver and the deformation in turn.

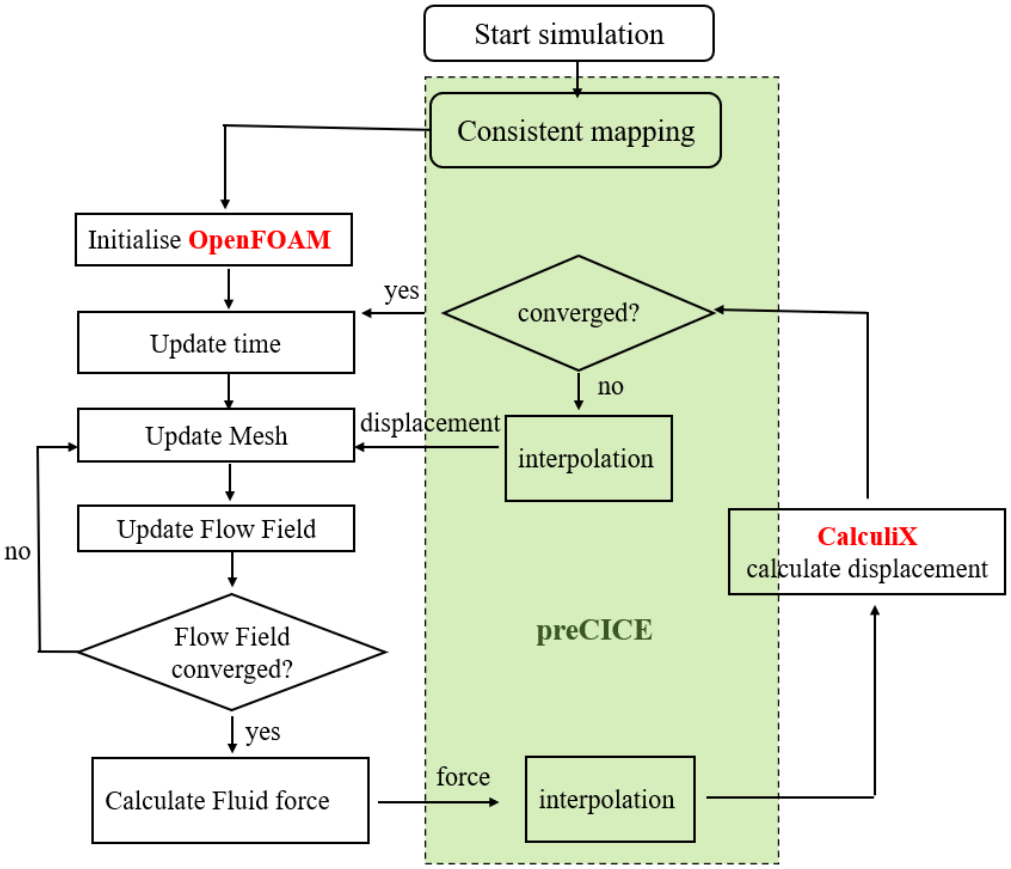

Figure 3.8 The workflow of the CFD-FEA coupling strategy

Chapter 4 Mechanically Interconnected WEC Net

In this chapter, the complex mechanical system interaction with waves is studied. The high-fidelity CFD solver is fully coupled with a multibody dynamics tool MBDyn. The latter method studies the dynamic behaviour of multiple interconnected rigid or flexible bodies and is widely used in robotics and vehicle dynamics (Eich-Soellner and Führer, 1998; Shabana, 1997). With this tool, the motion responses and mechanical connection force between individual floats and linking arms can be fully resolved simultaneously with any arbitrary topological complexity. The detailed data provided can be used to predict the weakest mechanical component in the WEC net, where the peak mechanical force may occur and thus become the most vulnerable part of the system.

4.1 Problem Description

4.1.1 Model Parameters

The Squid WEC array in this study is a geometrically simplified version of the Squid WEC system from Albatern Ltd. (Mcdonald et al., 2017). Two WEC arrays are examined in this study, one consisting of four floats and another having nine floats, as displayed in Figure 2.1 (b) and (c). The Squid model is a 1:18 Froude-scaled physical model which was tested in the FloWave Ocean Energy Research Facility in Edinburgh. The hull of each float comprises upper and lower cylinders, with a cone-shaped transition in the middle (see Figure 2.1(a)). These floats are connected by several linking arms to form a WEC net. A smaller buoy is installed at the centre of each arm to offset its weight. The angle between the arms is 120 degrees. At the connection points between the arms and the floats, articulations are installed, which can be equivalent to universal joints, allowing the free rotation of each node. The energy conversion is achieved via the relative rotational motion between the floats and linking arms. A constant stiffness mooring grid is used at the outer loop of the array to control the system's drift.

4.1.2 Parameters for Numerical Simulation

4.1.2.1 CFD model configuration

To reduce the complexity of the system from the perspective of CFD simulation, the model described above is simplified in the CFD model shown in Figure 4.1. The geometrical dimensions of the array are as follows: the height of the single float is 9.0m, the diameter of the upper and lower cylinder is 6.5m and 1.6m. The floats and the linking arms are rigid bodies; thus, no deformation is allowed. Since the arms' weight are mostly balanced by buoyancy and has minimum effect on the system, to reduce the complexity of the simulation, the arms are not meshed in the CFD domain, which means the hydrodynamic force is neglected. In the MBDyn solver, the arms are modelled as long cylinders, and a neglectable small mass is adopted. Neither the hydrodynamic forces on the arms are calculated. The articulations at the arms' ends are achieved using a spherical joint constraint, as described in section 3.2.1. The mooring grid is simplified without considering the circular grid at the outer loop. The grid is modelled as a linear force with constant stiffness, with its far ends anchored in space. The incident waves come from the left, and the static water depth d=63m.

Table 4.1 Geometric parameters of the WEC net

Node Properties	
The mass of each node	1.17×10^5 kg
Centre of mass	-2.93 m
Pitch inertia about the centre of mass	1.46×10^6 kgm^2
Yaw inertia about the centre of mass	1.46×10^6 kgm^2
Roll inertia about the centre of mass	1.46×10^6 kgm^2
Length of linking arm	20.754 m
Mooring grid parameters	
Number of mooring lines	9
The angle between adjacent lines	120 degrees
Stiffness	4×10^5 Nm

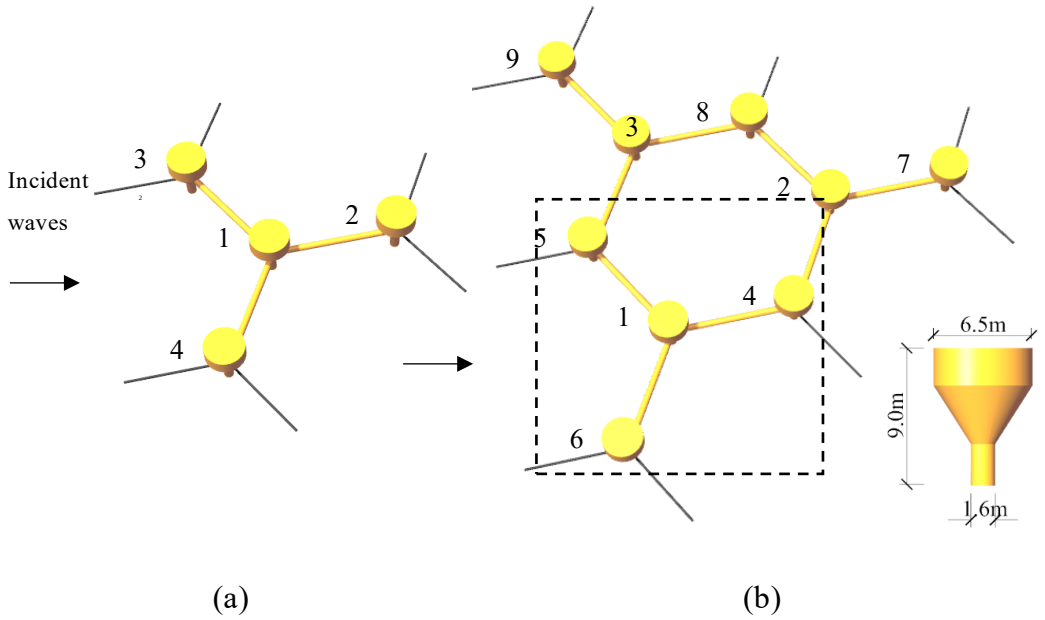

(a) (b)

Figure 4.1 Sketch of the CFD model for (a) 4-node array and (b) 9-node array

The boundary conditions and dimensions of the computational domain are shown in Figure 4.2. At the inlet boundary, the flow field is prescribed based on the Stokes 2nd-order wave theory. The pressure gradient is set to zero. The outlet boundary is treated as a zero-gradient boundary for the pressure, while the velocity is fixed as zero when the relaxation zone is applied. The top boundary is treated as a constant pressure inlet/outlet, which represents the atmosphere. Both the bottom and side boundaries are set as wall boundary conditions. On the hull of the nodes, a non-slip wall boundary condition with zero pressure gradient is defined. The dimension of the domain of the full-scaled model is -150m≤X≤200m, -70m≤Y≤70m, -63m≤Z≤33m. The origin of the coordinate system is located on the static water level at the horizontal centre of the array. The side boundary is set far enough from the structures to avoid the impacts of walls. The relaxation zone is set close to the outlet boundary with a length of about one wavelength. Although it is recommended to use a relaxation zone of two wavelengths, in our numerical wake tank testing, we found that one wavelength is sufficient to suppress the free surface. To reduce the overall computational cost, one wavelength relaxation zone is adopted. To model WEC hydrodynamic responses, laminar flow is assumed in this study. This is widely accepted by researchers because

it was found that there is no apparent disparity between the results obtained from turbulence or laminar models when the flow is mainly dominated by wave rather than current (Finnegan and Goggins, 2012; Wang et al., 2021).

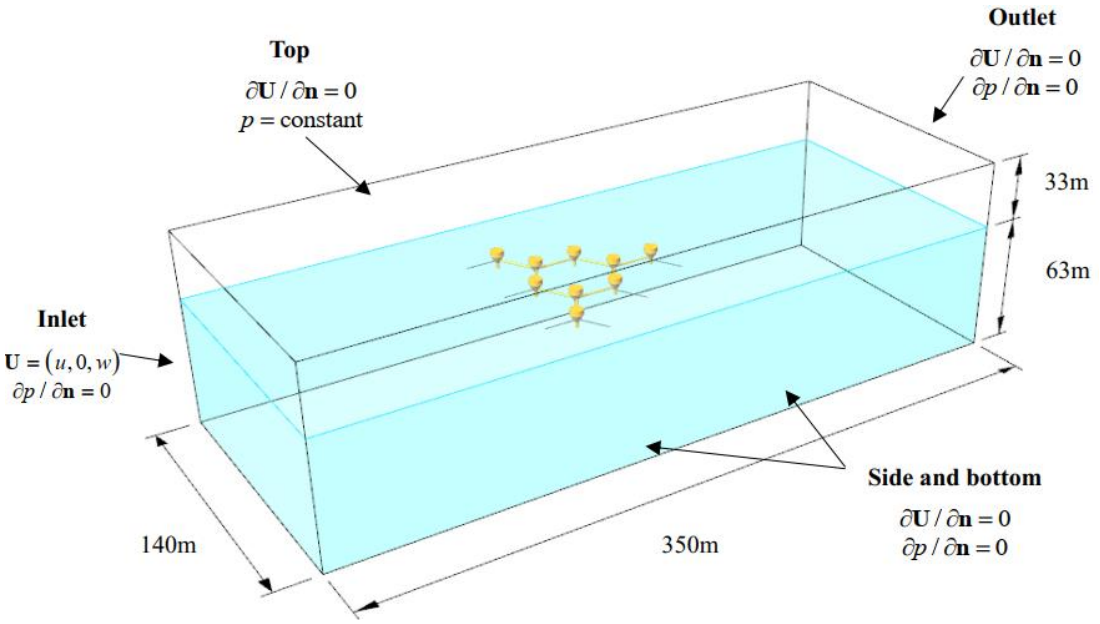

Figure 4.2 Dimensions and boundary conditions for the WECs simulation

Because the structures are not fixed and the position of WEC may change with time, moving CFD mesh is required. Three-dimensional unstructured meshes consisting of hexahedra (hex) and split-hexahedra (split-hex) elements are generated with the built-in meshing tool SnappyHexMesh in OpenFOAM. The mesh refinement is achieved near the free surface, as shown in Figure 4.3 (a). According to the Stokes wave theory, the wave motion only affects the fluid near the free surface. Therefore, the size of the background mesh, which is far from the surface layer, can be larger to speed up overall computation. The cell size of the background mesh is 8m. Meanwhile, the free surface region within a height of one wave height (H) should be refined to achieve accurate results. In this study, the cell size around the surface layer satisfies $\triangle z=H/8=0.125$m, where the wave height H =1.0 m is based on the smallest one among all cases. Along the x-direction, the grid size satisfies $\triangle x \leqslant \lambda/60$, where λ is the wavelength. Apart from the free-surface area, the mesh around the WEC nodes is also refined, as plotted in

Figure 4.3 (b). Also, the surface mesh near the structure is also refined with a cell length of 0.125m

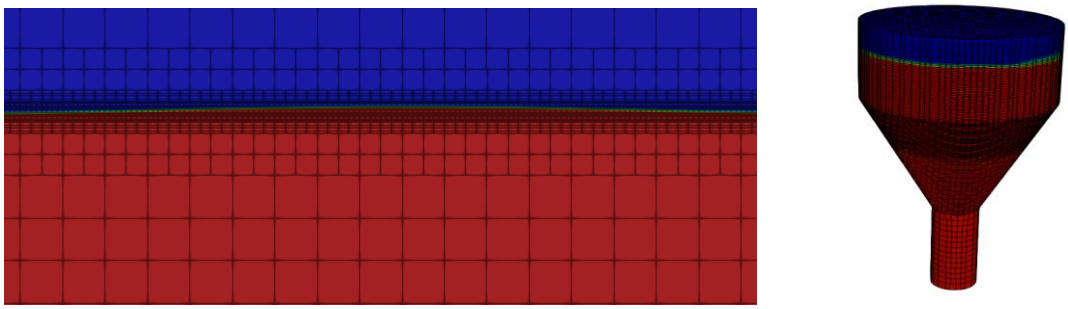

(a) (b)

Figure 4.3 Mesh refinement (a) near the free surface (b) on the WEC node

In the present study, the PIMPLE (a combination of Pressure Implicit with Splitting of Operator (PISO) and Semi-Implicit Method for Pressure-Linked Equations (SIMPLE)) algorithm is utilised to solve the pressure-velocity coupling. A second-order Crank-Nicolson scheme is used for temporal discretisation. A second-order upwind scheme is adopted for convective terms. Gradient terms are handled via a second-order cell-limited Gauss linear scheme (Mcdonald et al., 2017). Four multistep integration schemes can be chosen in MBDyn, among which the Crank-Nicolson method is used in this study. For the computation of linear systems and nonlinear problems, a linear solver called “umfpack” and a Newton Raphson scheme is chosen, respectively (Masarati, 2017). The timestep must be set in the same way as that in the CFD solver for data transfer.

4.1.3 Mesh and Time-step Dependency Study

The developed CFD approach is first compared with the experimental testing results for validation (Mcdonald et al., 2017) on a 4-node WEC array. The wave parameters used in the simulation are shown in Table 4.2. In the experiment, the joints connecting the arms and floats are not ideal, leading to the large friction and resistance appearance at the joint, thus moderating the amplitude of rotation significantly. A numerical test on the influence of friction on the dynamic motion of WEC shows that it can lower the pitch amplitude significantly in some conditions. The linear friction coefficient was

obtained in the experimental test, where the maximum torque caused by the friction is 283kNm. Therefore, this linear coefficient is directly used in the numerical study to simulate the contribution of friction.

A sensitivity study of mesh density and the unsteady time step is conducted. Figure 4.4 shows the time history of wave amplitude in the middle of Node 3 and Node 4 with different mesh densities and time steps. The number of cells is 2.6 million (fine mesh), 1.9 million (intermediate mesh), and 1.0 million (coarse mesh). For the results with different time steps, the predicted wave amplitude hardly changes when $\triangle t$<0.005s. Considering the cost of computational time, a time step of $\triangle t$=0.005s is chosen for the CFD modelling in this study. Similarly, a mesh of intermediate density is chosen. In a 9-node case, the intermediate mesh consists of 2.4M cells and a time step of $\triangle$t=0.005s is chosen. Simulations are performed on the Cirrus UK National Tier-2 HPC facility at EPCC with three compute nodes, each of which contains two 2.1 GHz, 18-core Intel Xeon E5-2695 (Broadwell) series processors. The overall time for a typical 4-node case is approximately 23 hours, which may increase for a 9-node case.

Table 4.2 Wave parameters for cases 1-4

	Wave height *H*/m	**Wave period *T*/s**	**Water depth *d*/m**
Case 1	1.5	9.5	63
Case 2	1.5	10.5	63
Case 3	1.0	9.5	63
Case 4	1.0	10.5	63

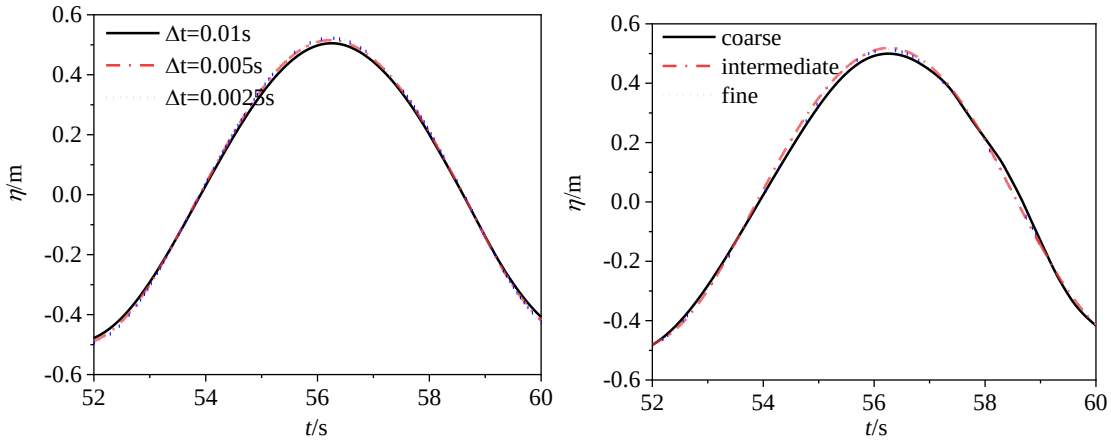

(a) (b)

Figure 4.4Time history of surface elevation in the middle of node 3 and 4 for Case 1 of different (a) mesh density (b) time step

4.1.4 Validation Test

Figure 4.5 shows a typical free surface elevation variation for case 1 between *t*=110s to 120s within one wave period. The figure shows that the floats' clear dynamic motion response is well captured with the incident wave propagates. In addition, the diffraction and wave run-ups can be observed around each float. It is noted that the dominant motion mode comes from pitch, and the motion trajectory is very similar for all three nodes both in CFD and experimental results. Thus, only the result of node 2 is compared with experimental data in Figure 4.6. The six blue points in Figure 4.6 (a) are the instantaneous time indicated in Figure 4.5.

As we can see from Figure 4.6, the two results appear similar in terms of phase and amplitude, although the CFD results display more smooth results than the experimental results, especially at the trough of curves. This may be due to the simplified details of our CFD model. For instance, the articulation attached to the nodes is simply represented as the joint with certain damping values and stiffness without physical presence. As such, their blockage effect on the fluid flow is absent in our simulation. In addition, simplifying the linking arms can be another possible reason.

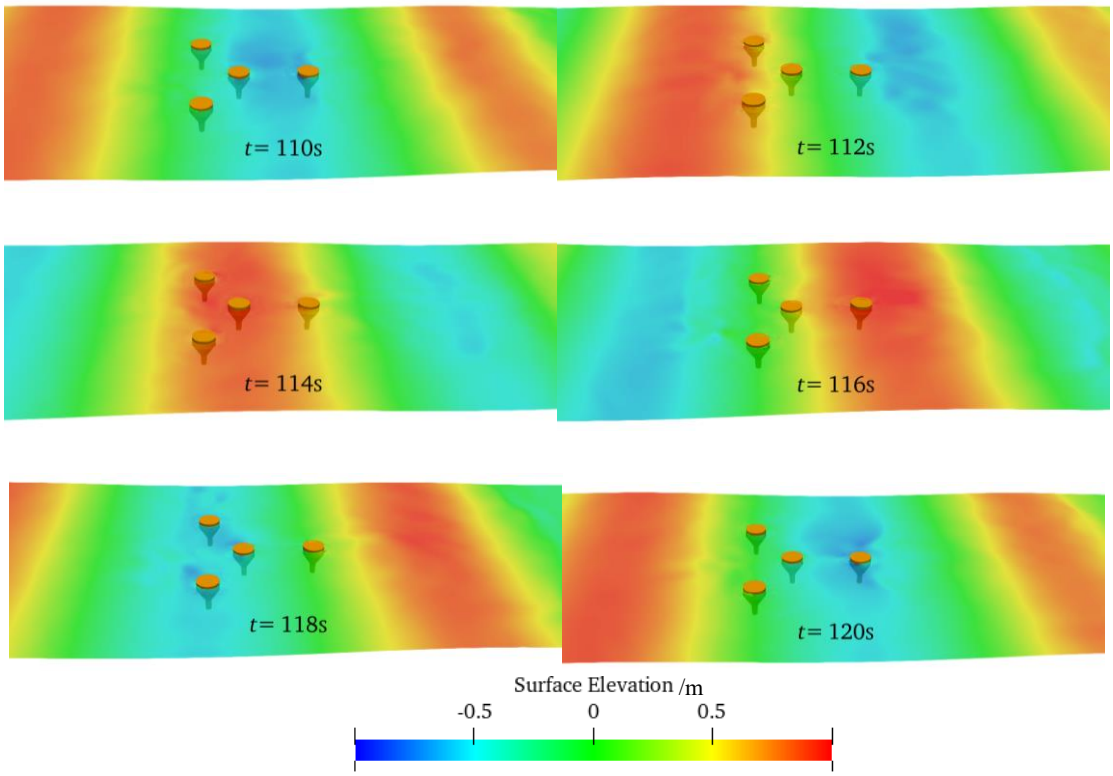

Figure 4.5 Contour of the free surface elevation from t=110s-120s with H=1.5m and T=9.5s

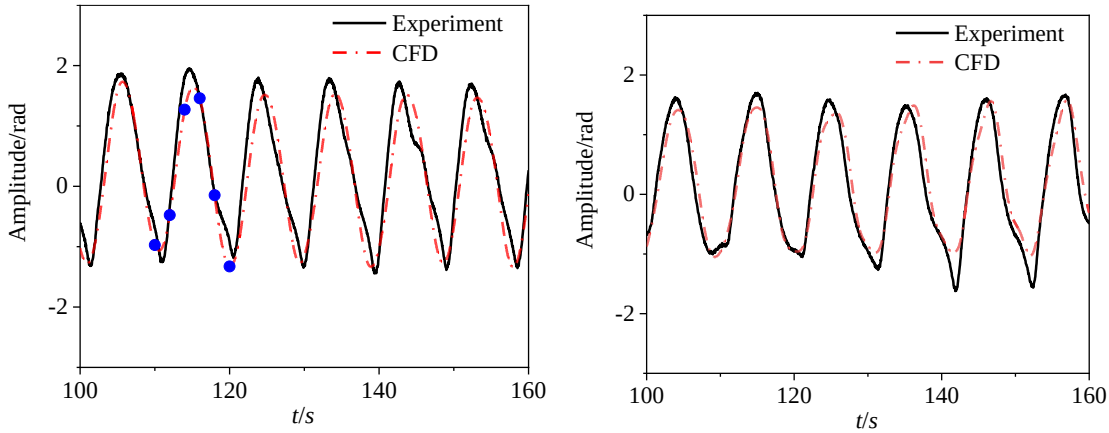

(a) (b)

Figure 4.6 Pitch motion of node 2 for (a) case 1 (b) case 2. Blue labels are the sampling time shown in Figure 8.

4.2 Results and Discussions

A more complicated WEC array consisting of 9 nodes is investigated, as displayed in Figure 4.1 (b). The 9-node array in this case contains far more components and has a

centered closed loop, with which the topological complexity and the constraints limiting the individual float degree of freedom motion increase as compared to an open-loop system for 4-node WEC. The study is focused on Case 3, as summarised in Table 4.2. With the numerical modelling tool developed, either a systematic study of the whole WEC net or a localised analysis of a specific single sub-structure/component is possible. To better demonstrate the above features, we will present our results, starting with a description of the global motion of the WEC net, followed by the interactions between specific substructures.

4.2.1 Global Motion Response of WEC Net

Figure 4.7 shows the free surface elevation from a top view of the WEC net within a wave time period, specifically from t_1=82s to t_6=92s, including the mechanical linking arms and mooring grids. The colour of the arms denotes the CFD-predicted axial force along the arms, and the contour legend is included in the figure. Only tensile force is allowed for the moorings since a mooring grid cannot sustain a compression motion. The 'shadow nodes', i.e. the black circles plotted underneath each node, represent the floats' location at the last sampling time. For ease of description, we define three phases from t_1 to t_3. Phase 1 is named the 'wave trough phase', during which the wave trough is just passing through the WEC array. Phase 2 is called the 'transition phase', when a wave trough (or wave crest) has passed the array. However, the next wave crest (or wave trough) has yet to arrive. Phase 3 is referred to 'wave crest phase', meaning a wave crest has passed the array completely.

As shown in Figure 4.7, t_1 is in the 'wave trough phase'; the WEC array is moving backwards against the wave propagating, indicated by the plot that each node is moving along the negative x-direction. At this moment, the tensile force of the side mooring reaches its maximum to 'drag back' the array to its previous location. Afterwards, WEC develops into the 'transition phase' at t_2. It can be inferred from the 'shadow nodes' that all nodes hardly change their positions along the x-direction. The axial force of the arm is eased. In the last stage of the 'wave crest phase' at t_3, the WEC array drifts towards

the wave propagation direction, and the axial force of arms reaches the negative peaks, indicating these linking arms are stretched. The above phase variations appear periodically within one wave period. It is reasonable to conclude that the compression of the mechanical arms results in the movement of the array backwards, which is associated with the 'wave trough phase'. The situation is observed vice versa in the 'wave crest phase'.

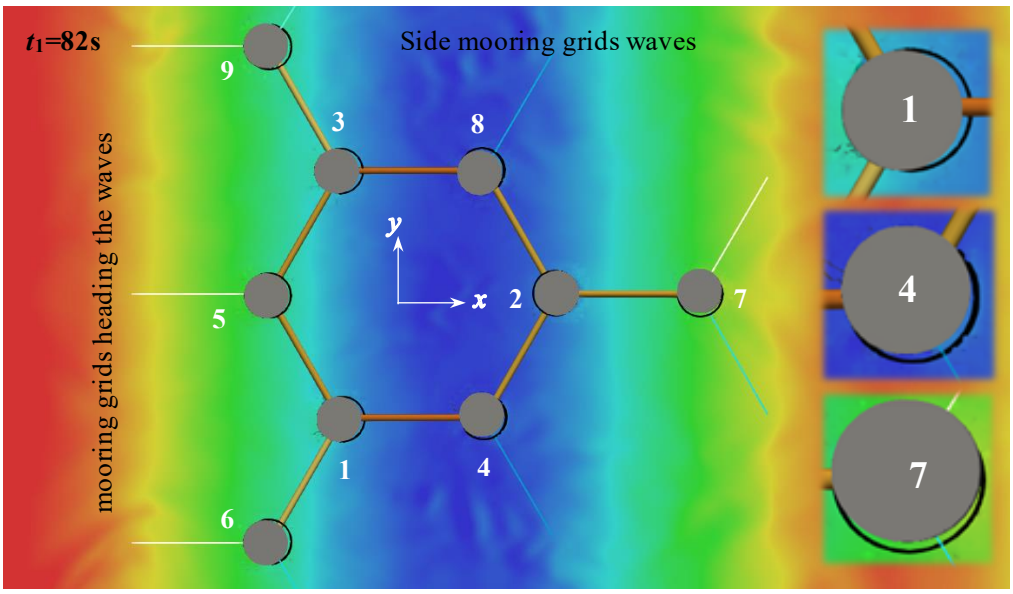

(a) t_1=82s

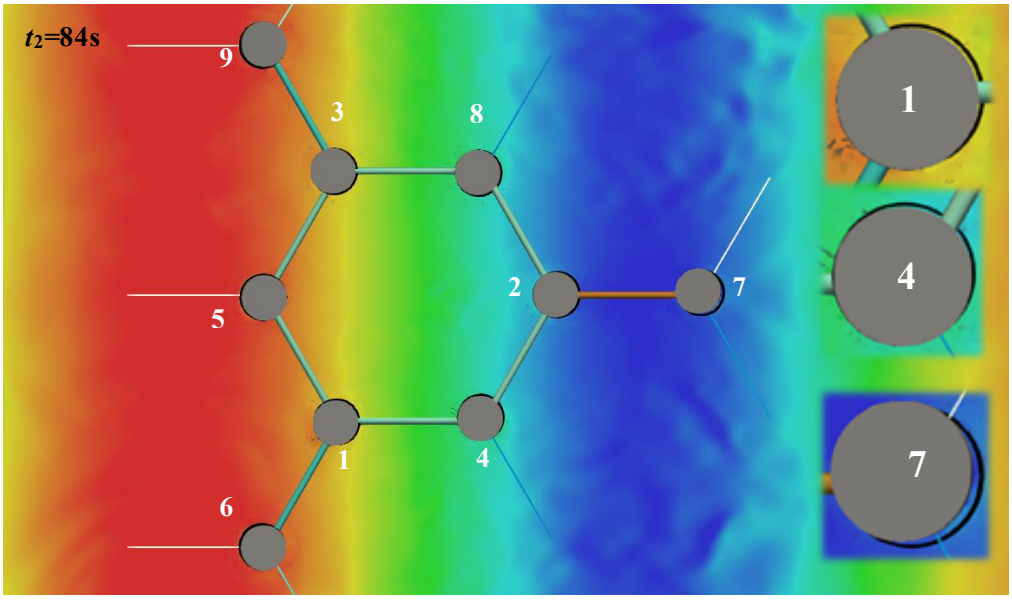

(b) t_2=84s

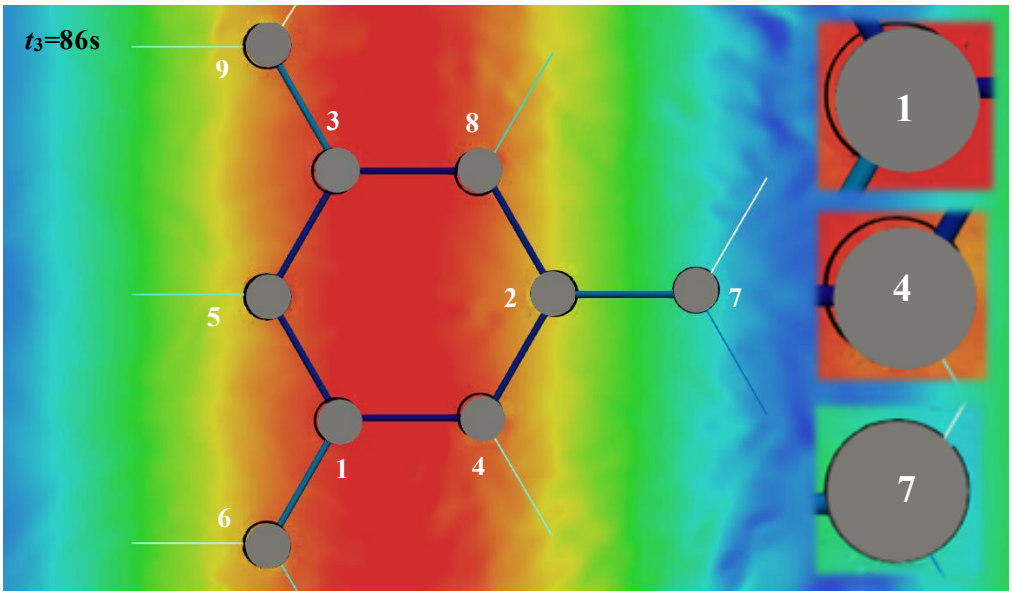

(c) t_3=86s

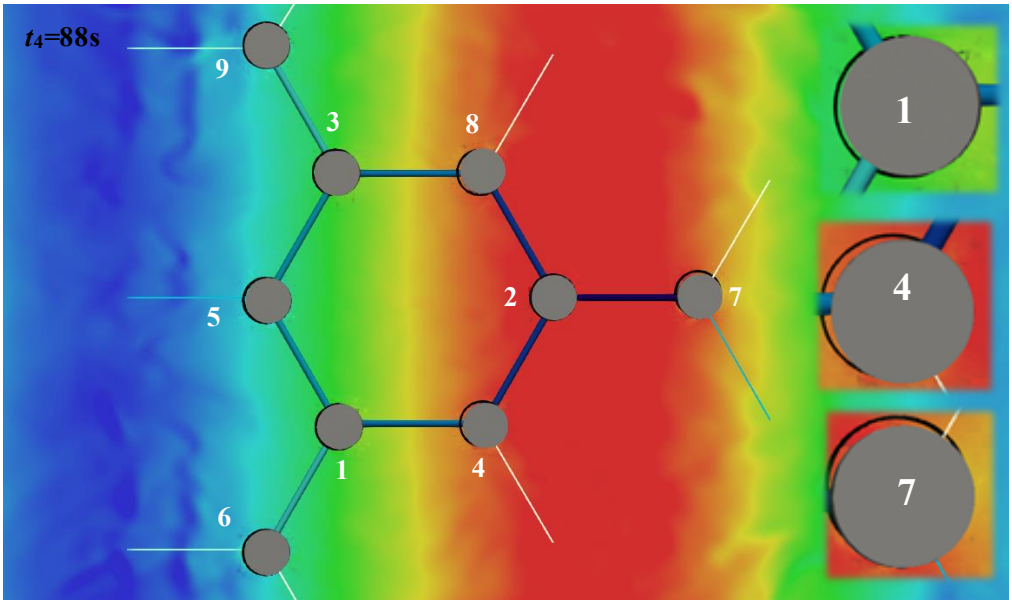

(d) t_4=88s

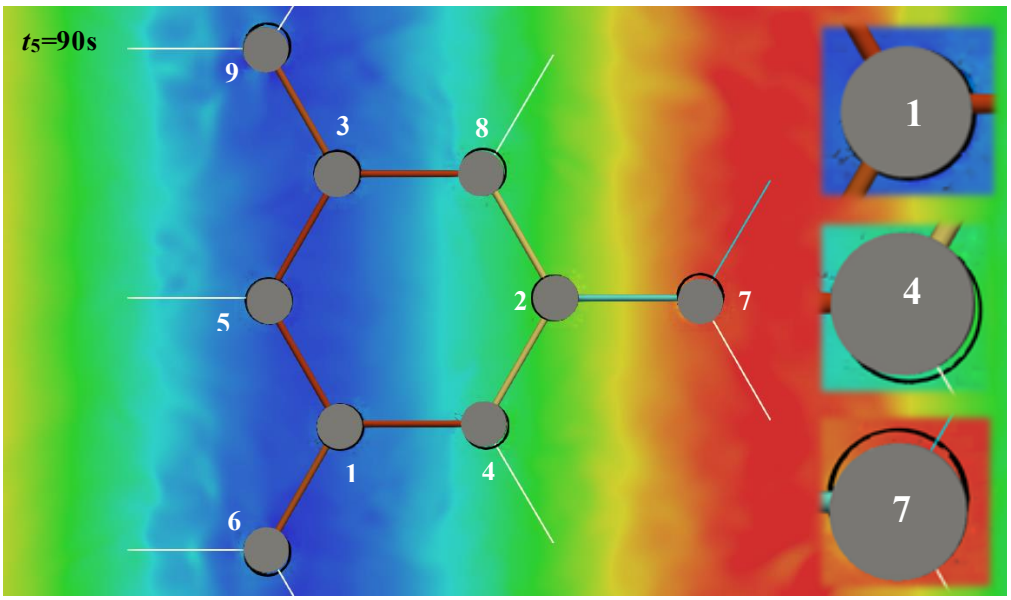

(e) t_5=90s

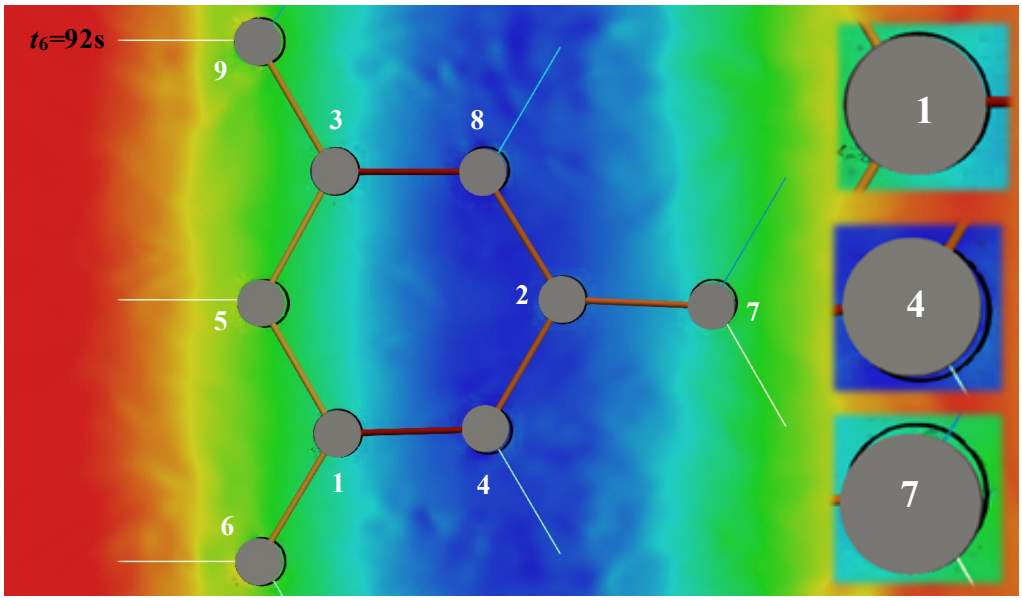

(f) t_6=92s

Figure 4.7 Free surface elevation for 9-node WEC from t_1~t_6 from the top view. The contour on the linking arms and moorings denotes the axial force, and the enlarged figures around node 1, 4 and 7 denote their new position compared to their old position in the last sampling time (black shadow)

4.2.2 Translational Mode Response

Apart from the above observations on the global motion of the WEC array, the dynamic response of individual node, i.e. Nodes 1,2,4 and 7 in the net, is discussed in this section. The aim is to demonstrate that the individual nodes behavior and their interaction have impact on the response of WEC net.

The motion trajectories of various nodes in the *x*-*z* plane are displayed in Figure 4.8, derived from two sampling wave periods. The trajectory of floats follows approximately closed ellipses, with a similar maximum displacement of 0.8 m in *x* and 1.0 m in the *z*-direction, respectively. A further examination of Figure 4.8 suggests that the trajectories for Node 1 and Node 2 are very similar, i.e., the ellipses lean backwards in the negative *x*-direction, while they appear to be in the positive *x*-direction for Node 4 and 7. This clearly indicates that the motion response for individual float is diverse, depending on their actual position and connection in the WEC net, which is actually

induced by the mechanical force generated in the linking arm, discussed in the next part.

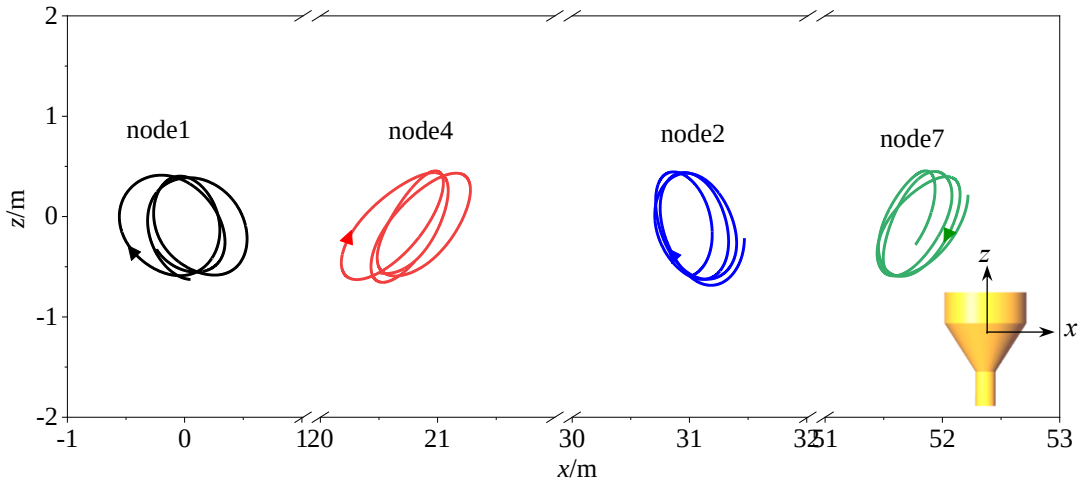

Figure 4.8 Motion trajectories of an individual node in an *x*-*z* plane within two wave periods

Figure 4.9 shows the velocity of floats in *x*-direction v_x, the mechanical force acting on the floats along x-axis F_{mx} provided by linking arms and mooring grids, and the total resultant force acting on floats along x-axis F_{tx}. One observation is that F_{tx} is of the same magnitude as F_{mx}, implying that the mechanical components, such as linking arms herein, play a significant role in the motion response of floats. It is known that in this WEC system, the response of mode is determined by a combined input from both hydrodynamic pressure force and the mechanical force generated via mechanically coupled linking arms. Given node 1 and 2 as examples, as shown from an enlarged plot in Figure 4.9, the F_{mx} variation is almost coincident with v_x within a wave cycle, indicating that the velocity and mechanical force are pointing in the same direction. However, for Node 4 and 7, the F_{mx} and the v_x are pointing in two opposite directions. The above force and velocity relation lead to two entirely different motion trajectories for Nodes 2,4, and Nodes 4,7, shown in Figure 4.8.

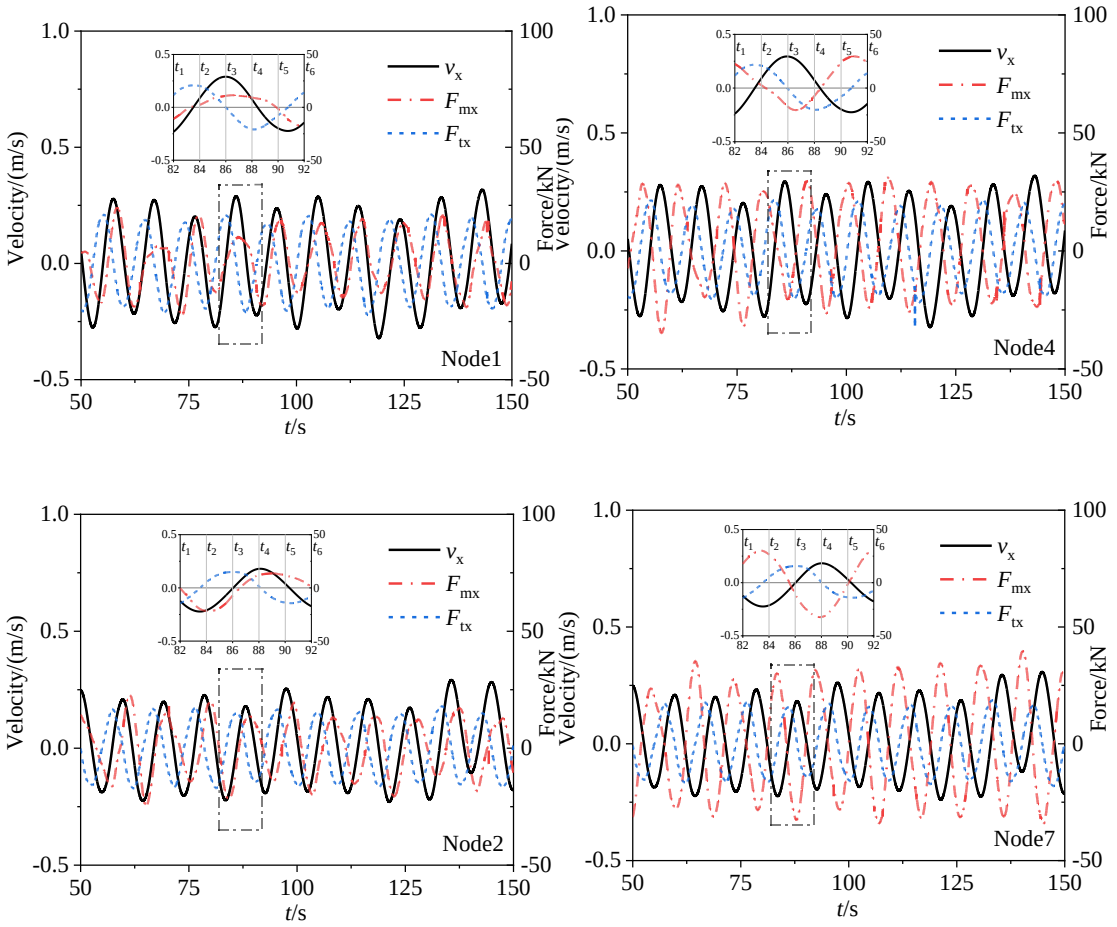

Figure 4.9 Velocity v_x, mechanical force $F_{mx,}$ and total forces F_{tx} along the x-axis for Node 1,4,2 and 7

The motion in the *z*-direction, namely the heave response history, is shown in Figure 4.10. Each float heaves up and down with the wave period. The motion amplitude is around 1 m, almost the same as the wave height. It can be observed that the linking arms hardly influence the float's motion in the heave direction. This is because the displacement at the two ends of the arm is very small (the maximum relative displacement is 0.5 m), which is immaterial compared to the arm length (20.754 m), thus resulting in a tiny component force in the z-direction.

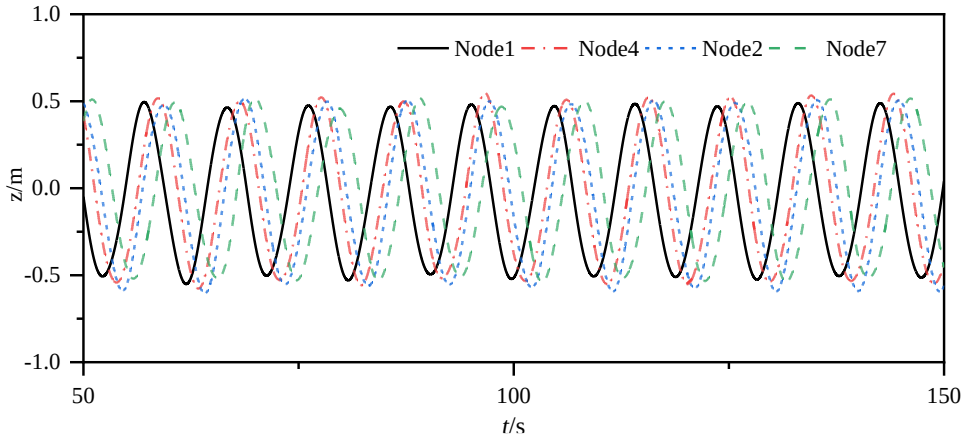

Figure 4.10 Heave amplitude for individual floats

4.2.3 Rotational Mode Response

The lateral view of the float's rotational motion at t_1-t_6 is shown in Figure 4.11. The colour of the floats denotes the surface dynamic pressure distribution. The 'shadow' underneath each node represents their positions at the last sampling time. It can be seen that the magnitude of the force depends on the wave elevation. The higher the surface elevation is, the larger the magnitude of the force. The distributed pressure on floats leads to the heave and rotational motion responses.

The pitch motion response is plotted in Figure 4.12. Since both Node 1 and Node 2 are well restrained by three linking arms, their pitch responses are larger than Node 4 and Node 7. For the latter two nodes, the motion is only constrained by two and one arm, respectively. Figure 4.13 summarises the time-average heave and pitch peak values associated with different wave periods in the present study. It can be seen that the wave state change has little impact on the time-mean heave response with tested wave frequency, while it influences pitch mode. With a reduction of wave period, closer to the natural frequency of floats, which is 5.1s, via experimental test, the wave becomes steeper and the pitch amplitude increases.

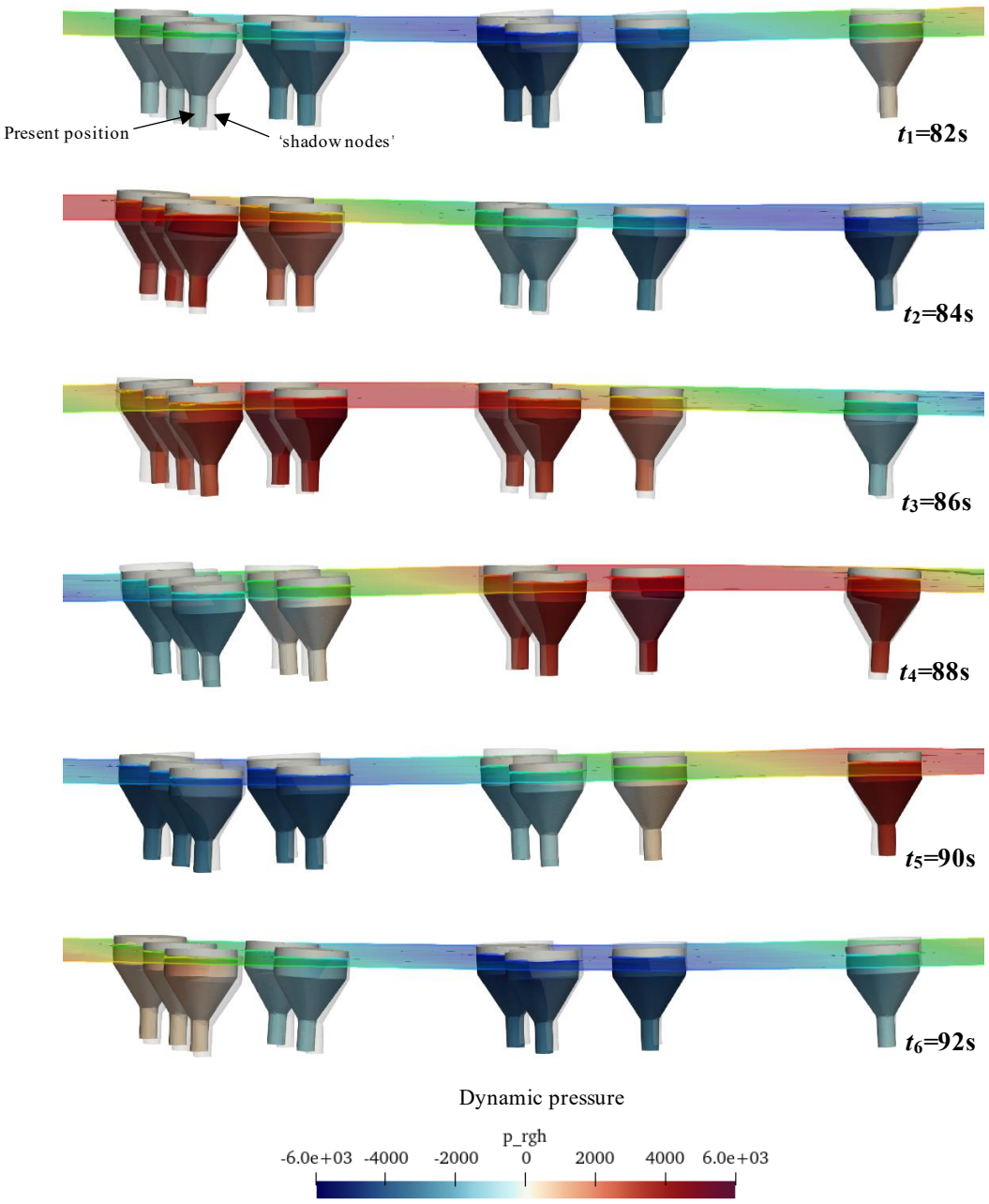

Figure 4.11 Free surface around the floats and rotational motion of each float from t_1-t_6

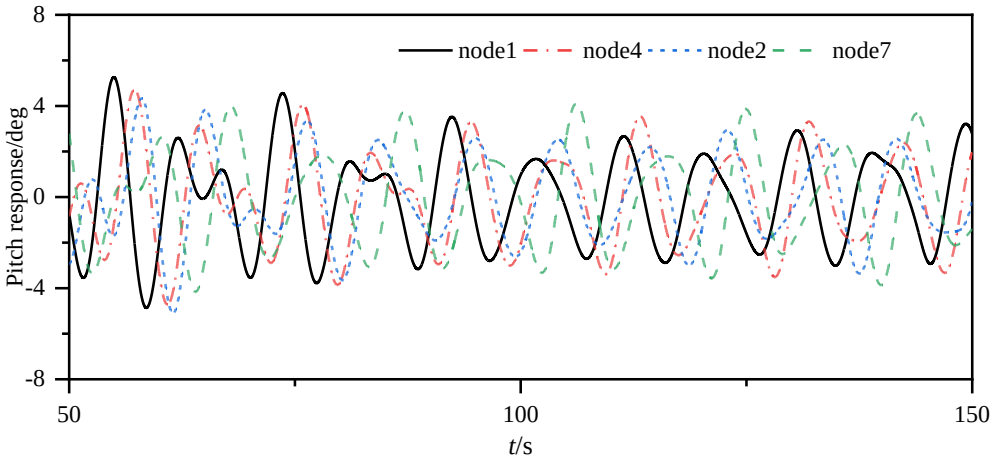

Figure 4.12 Time history of pitch mode response for individual float

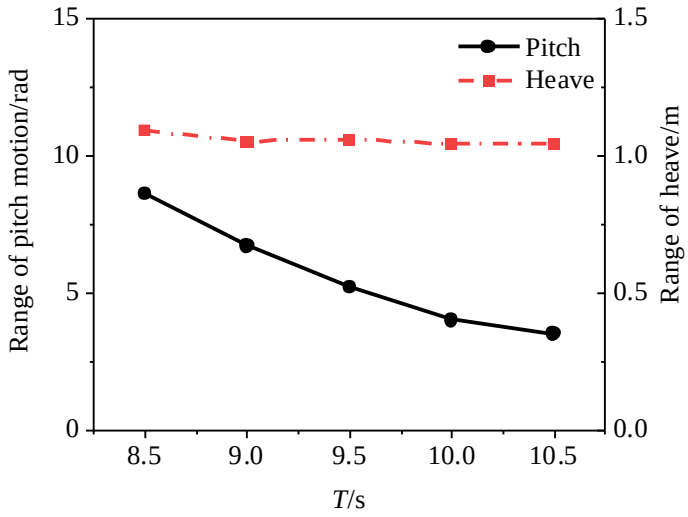

Figure 4.13 Time-average pitch and heave amplitude for different wave periods

4.2.4 Optimal Parameters for Torque and Power Output

A critical attribute of a WEC system is how much power it can achieve. This will be discussed in this section. This calculation of power output can refer to equations 3.41 and 3.42.

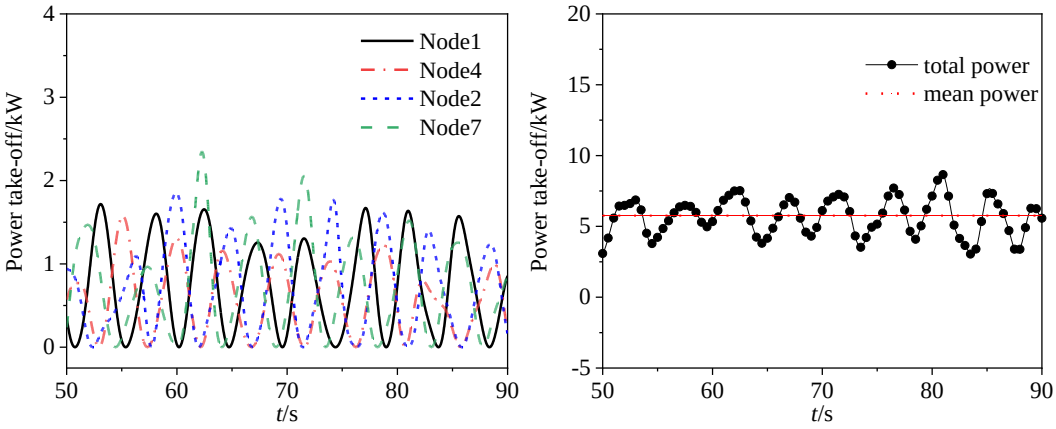

Figure 4.14 Power capture of (a)each float and (b) the whole system

Figure 4.14 shows the power capture of individual float in the WEC net at a wave condition of H=1.5m, T=9.5s. It can be seen that the instantaneous peak power capture of individual float varies between 1-1.5kW. Because of their difference in positions in the wave net and the impact received from linking arms, the time-variation of power capture for individual float is not synchronised. This NetandArm configuration allows the overall energy output to become more stable. Also, the formation of the net structure reduces the complexity of both device construction and mooring systems. Here, the factors which may influence the power capture are investigated. According to equations 3.41 and 3.42, power capture is controlled by the electric damping and rotational angular velocity, the latter is also influenced by the hydrodynamic force acting on floats.

The influence of electric damping is studied first. Node 2 is selected for the convenience of the study. The time-averaged torque induced by the fluid pressure, the torque due to the electric damping and the angular velocity are presented in Figure 4.15. The expected outcome of the study is that the angular velocity decreases with an increase in the electric damping. We also observed that the hydrodynamic force increases gradually. When the wave acts on a fixed offshore structure, the induced hydrodynamic force is usually larger than that acting on the same floating structure. The free degree of motion of a floating structure can reduce the hydrodynamic force experienced by it. That's the reason why the torque increases when the float's motion gets weak, as a result of large damping. It can also be observed that both the hydrodynamic and the mechanical torque

approach a unified constant when the damping increases once the motion of a WEC is eventually stopped by the large damping. Since the power capture is estimated by velocity and torque, an increase in damping leads to an enlarged torque but a reduced velocity. Therefore, it is reasonable to deduce that optimal damping should exist to achieve the maximum power capture. This is well reflected in Figure 18 (b), where this damping equals 2000 kNs/m.

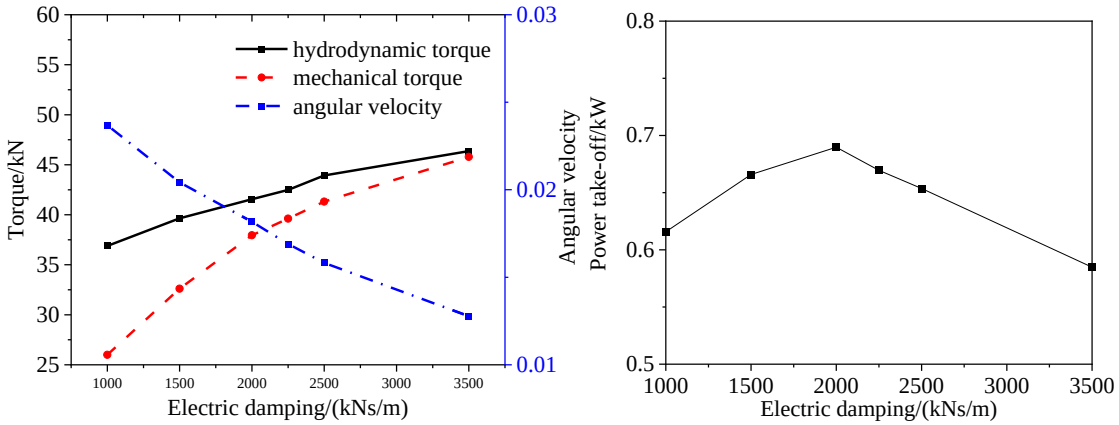

Figure 4.15 (a)Torque and its angular velocity (b) Power capture with different electric damping of Node 2

Except for electric damping, hydrodynamic force, which is strongly related to the interaction between wave and floating structure, also affects power capture, as mentioned earlier. As shown in Figure 4.16 (a), the power capture increases dramatically with the decrease of the wave period. Given the same wave period, there's always a peak power capture. However, the matching damping varies with different wave periods. It can be found from Figure 4.16 (b) that the peak electric damping decreases linearly with the wave period. In fact, by shortening the wave period from 10.5s to 8.5s, the optimal power capture increases from 4.5 kW to 15 kW.

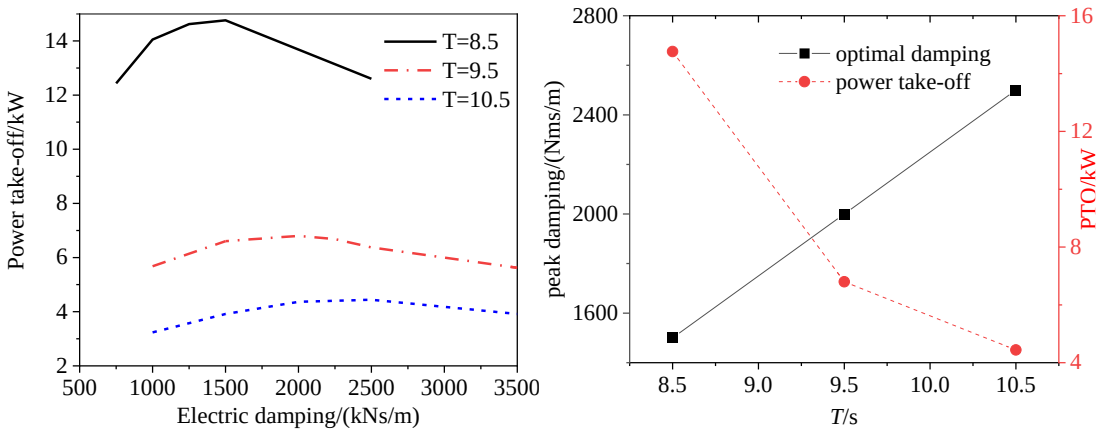

Figure 4.16 (a) Power capture under different wave periods (b) Optimal power capture and match damping

4.3 Conclusion Remarks

This study aims to use a coupled CFD-MBD numerical modelling tool to study complicated WEC net problems. OpenFOAM is utilised as the fluid solver, and a multibody dynamic code is selected to solve structural parts. An adapter is established to exchange data between the above two solvers. On the Albatern squid WEC net, we demonstrate the success of this integrated numerical modelling tool. A comparison between the CFD predicted results against the nonlinear Morison model results shows that our CFD-MBD framework can better capture high nonlinear effect, which is persistent in the problem associated with a strong wave-structure interaction. The computational time cost of a nonlinear Morison model study is about 1/10 of that of a CFD simulation. With this tool, a WEC net with nine floats is examined, covering a series of varying wave conditions. We found that the force and moment generated via the connecting mechanical elements, such as the linking arms herein, play a significant role in the dynamic motion responses of individual float and the WEC net as a whole. The level of such impact also depends on the wave conditions and the specific location of the float in the WEC net. By applying electric damping to the joints, we estimated the device power capture. We found that the power capture damping and wave period are the two most important parameters for the power output. Given a specific wave period, an optimal electric damping force exists at which the maximum power can be

captured. As expected, the power increases with the decrease in the wave period. For instance, the optimal power capture increases from 4.5kW to 15kW when the wave period decreases from 10.5s to 8.5s. This tool has demonstrated its powerful capability to solve such a complex WEC net problem.

Chapter 5 Novel Flexible WEC

In this chapter, the flexible WEC performance with linear-elastic and hyper-elastic material in regular wave conditions is studied. It is demonstrated that the use of hyper-elastic material can significantly improve the performance of an fWEC. Because the FSI induced by the hyper-elastic material is highly nonlinear, which makes convergence more difficult, previously used tools such as the multi-body dynamic tool and the coupling scheme (Li et al., 2021) are non-applicable to this study. A more versatile finite element method is introduced in this study to solve this problem. The coupling between the flow solver and structure solver is achieved by using the Precise Code Interaction Coupling Environment (preCICE), a coupling library for partitioned multi-physics simulations (Bungartz et al., 2016). With this tool, the material selection and its influence on the fWEC performance with different ocean wave conditions are examined, and the approximated fWEC's power output is estimated.

5.1 Problem Description

5.1.1 Model Parameters

The fWEC model studied is inspired by the PolyWEC device by Giacomo et al. (Moretti et al., 2020). The three-dimensional fWEC holds a symmetric geometry, whose section along the y-axis is shown in Figure 5.1, where the origin is in the centre of the initial membrane position. x points to the wave direction and z opposites to the direction of gravity. The whole device is submerged under water, where the membrane, made up of DE material, is the main element that functions as the PTO to convert the wave energy into electricity. The membrane is placed in the centre of the device as an interface to separate the top water and bottom air chambers. The air pressure is almost constant and equal to the atmospheric pressure in the air chamber. A collector is attached at the top of the membrane, which aims to increase the added mass of the fWEC system. When the wave comes over, the pressure difference between the top and bottom surfaces of the membrane causes it to deform continuously like a balloon. In this process, the

membrane is stretched, thus leading to a change in the thickness. The DE membrane holds stretchable electrodes on both faces and functions as a variable capacitor. Deformations induced by the hydrodynamic pressure cause a variation in the membrane surface and thickness, hence leading to variations in the Dielectric Elastomer Generator (DEG) capacitance. Properly modulating the voltage applied on the DEG as a function of the current deformation (e.g., allowing a charge on the DEG during the phases in which its capacitance decreases and keeping it uncharged while its capacitance is increasing) allows converting part of the input mechanical energy into electrical energy (Moretti et al., 2020).

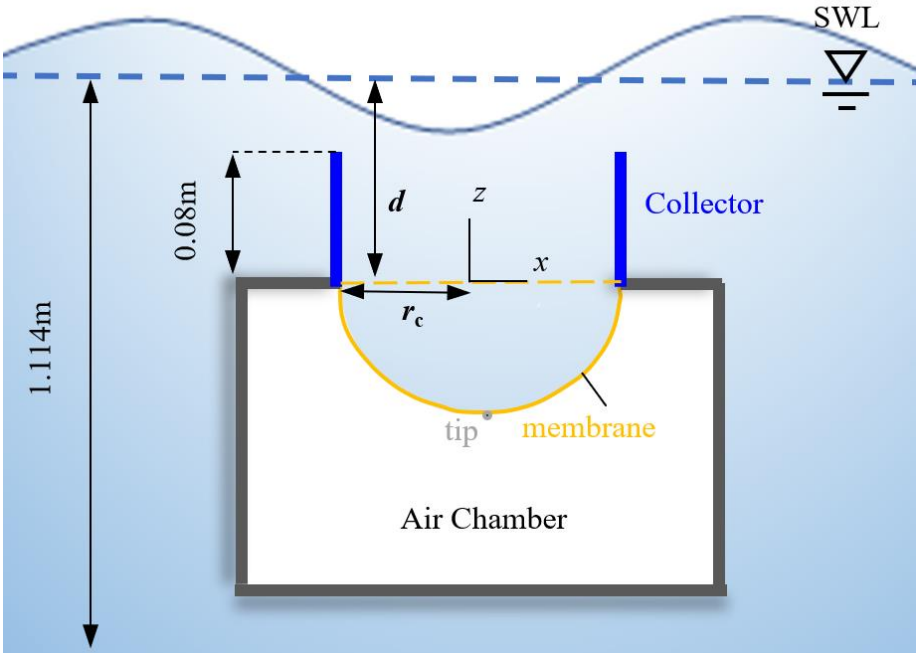

Figure 5.1 Sketch of the fWEC model. The plates in blue colour are given the name of the collector to create a water column above the membrane. The yellow solid line denotes the membrane, which functions as the PTO. The yellow dashed line denotes the initial position of the membrane (unstretched).

A preliminary test shows that for three-dimensional numerical modelling, because of its highly nonlinear feature, a time step as small as 0.006% of the wave period is needed to ensure the stability of the simulation, which is very computationally expensive. To

reduce the overall computational cost, the fWEC in this study is simplified as two dimensions.

5.1.2 Parameters for Numerical Simulation

In our numerical study, the geometric dimensions of the above device are the same as those in the experiment (Moretti et al., 2020), in which the model is a scaled-down version of a scale factor of 1:40/1:50. At the beginning, the membrane is unstretched with a radius of r_c=0.065m, and its initial position is shown in Figure 5.1. Once it starts deforming, we monitor the tip displacement of the membrane z_{tip}, which is directly linked to the energy conversion. The distance between the position of the unstretched membrane and the static water level (SWL) is defined as the water height d.

The numerical wave is generated using Stokes second-order waves, with wave height H = 0.1 m. The wave period ranges from 0.8 s to 1.8 s, corresponding to an unscaled fWEC operating with a wave period of 5.6 s to 12.6 s for the real sea states.

The CFD mesh is presented in Figure 5.2 with a total number of cells of around 68000. As shown in Figure 5.2 (a) and (b), the mesh is refined around the free surface and inside the collector to better capture the wave profile and the flow details. The boundary condition of the membrane is set up as a non-slip wall boundary for fluid velocity and a zero gradient for pressure. The velocity and pressure at the inlet boundary are prescribed by regular wave theory, and both are set to be zero gradients at the outlet boundary.

To solve this time-dependent problem, the time step for all cases is fixed to 5×10^{-5} s, which is 0.006% T when T=0.8 s. The pressure-velocity coupling is achieved through the PIMPLE algorithm. A second-order Crank-Nicolson scheme is used for temporal discretisation. A second-order upwind scheme is adopted for convective terms. Gradient terms are handled via a second-order cell-limited Gauss linear scheme.

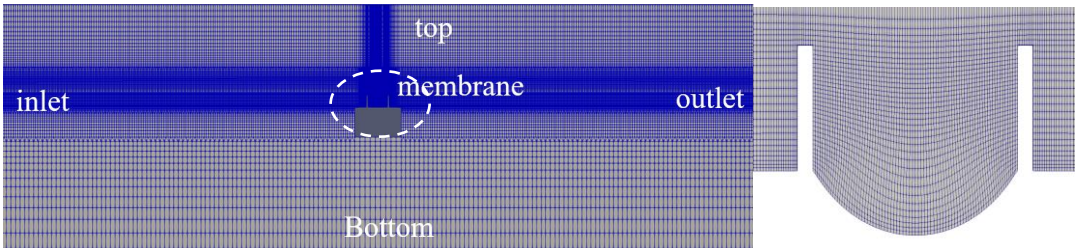

(a) (b)

Figure 5.2 CFD mesh (a) of whole wave tank (b) inside the collector with deformed membrane.

5.1.3 Mesh and Time-step Dependency Study

A sensitivity study of mesh density and the unsteady time step is conducted for an fWEC with d=0.18 m, H=0.1 m and T=0.8 s. Figure 5.3 shows the time history of tip displacement of the membrane zip with different mesh densities and time steps. The surface mesh size of the base mesh is 1.25% of the characteristic length L (length of the membrane), which is 0.75% and 2% for fine and coarse mesh, respectively. As indicated by Figure 5.3, the results from the base and fine mesh are very close to each other. Therefore, the base mesh is selected to reduce the computational cost. As to the time step, no obvious difference was observed. However, a large time step may cause the simulation to be divergent; a comprising time step of 5e-5 s is finally chosen for the rest of the simulation in this work.

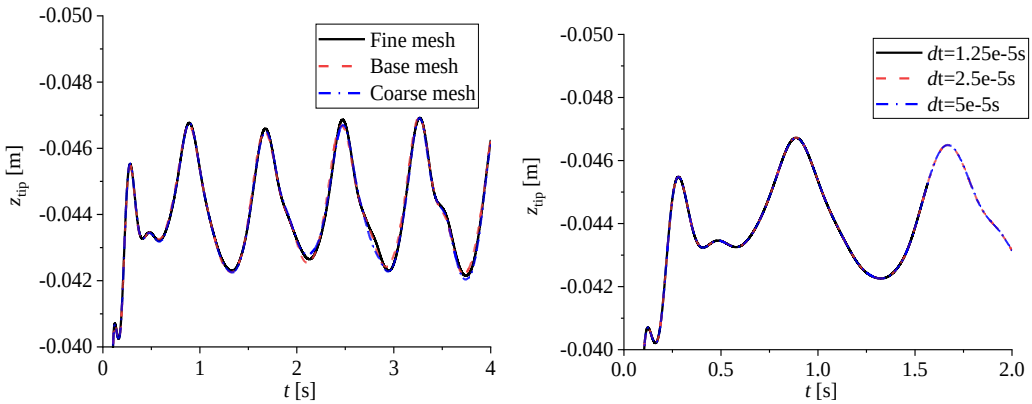

(a) (b)

Figure 5.3 Time histories of the tip displacement with different (a) mesh density (b) time steps for a case of d=0.18m, H=0.1m and T=0.8s.

5.1.4 Validation Test

A flow across a flexible cantilever plate behind a square cylinder is validated to conduct a numerical method validation. This is used to validate our developed tool for the fluid-flexible structure interaction, which is one of the key elements for this fWEC analysis. This case consists of a fixed square bluff body, behind which the Von Karman vortex street shedding occurs and excites a periodic deformation of the elastic cantilever, as seen in Figure 5.4 (a). Typical parameters are the Reynold number Re =330, the mass ratio m^*=1.27, the non-dimensional bending stiffness K=0.23, and the Poisson's ratio v =0.35. The predicted time-dependent displacement of the tip of the beam is shown in Figure 5.4 (b). The frequency is estimated as 3.137 Hz, and the amplitude of the oscillation is 1.071 cm, which is consistent with the other results summarised in Table 5.1.

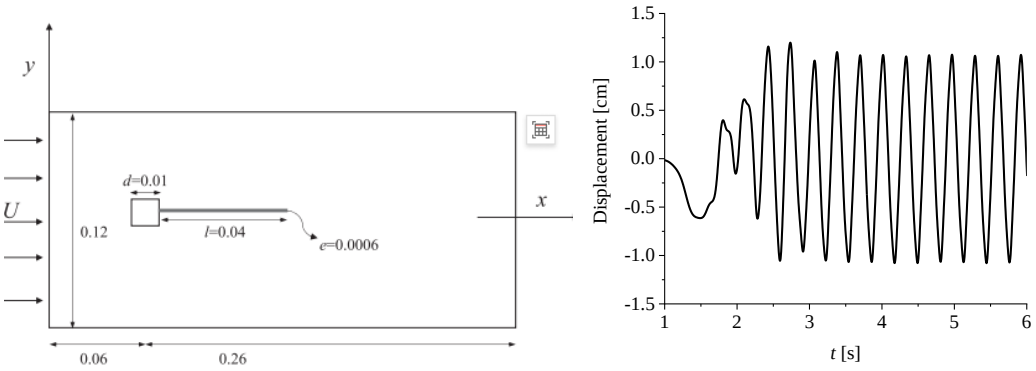

(a) (b)

Figure 5.4 (a) The layout of the computational domain (b) Displacement of the tip of the cantilever beam.

5.2 Results and Discussions

In this study, the free surface is initially still, and the membrane starts from a flat configuration. There are two phases of the motion response of the membrane. In phase one, the waves have not reached the device, and the membrane deforms due to hydrostatic pressure. After a while, the membrane reaches its equilibrium configuration

and stops moving at a position of δ_{static}, see Figure 5.5. In phase two, the membrane deforms periodically because of the waves that pass by, induced by the hydrodynamic pressure. Within one wave period, the membrane oscillates with an amplitude of $\delta_{dynamic}$. Since the magnitude of $\delta_{dynamic}$ is directly linked to the energy conversion, it is desirable to achieve a large value of $\delta_{dynamic}$. Obviously, the fWEC system structural natural frequency is determined by the material characteristics and the hydrostatic pressure, which is mainly contributed by the added mass of water inside the collector and, thus, the water height (d in Figure 5.1). However, in Phase Two, the wave states also control the dynamic motion of the membrane.

Table 5.1 Comparison of present results with open literature

Author	***f*[*Hz*]**	**Displacement [cm]**
Matthies and Steindorf (Matthies & Steindorf, 2003)	3.13	1.18
Wood et al. (Wood et al., 2010)	2.77-3.125	1.10-1.20
Walhorn et al. (Walhorn et al., 2002)	3.14	1.02
Habchi et al.(Habchi et al., 2013)	3.25	1.02
Present	3.137	1.07

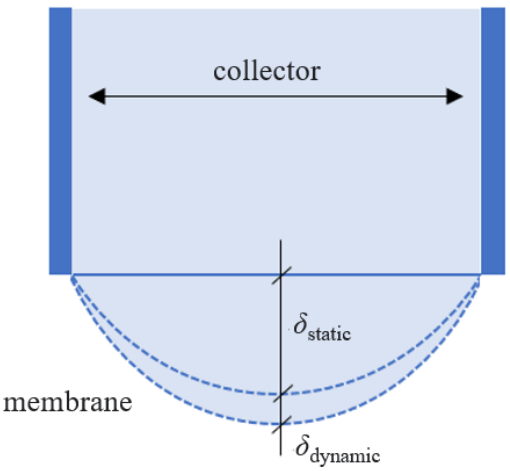

Figure 5.5 Membrane deformation under static pressure and dynamic pressure

5.2.1 Response of Membrane Deformation under Hydrostatic Pressure

In this section, the membrane deformation under a range of hydrostatic pressures is first examined to identify the system's natural frequency, followed by an investigation of the material characteristics and wave conditions' impact on fWEC.

The tip displacement of the membrane under constant hydrostatic pressure, i.e., a constant d=0.18 m, is illustrated in Figure 5.6, with the material properties summarised in Table 5.2. The material's hyper-elastic characteristics are described by the following strain energy potential equations (Martins et al., 2006), inspired by the rubber used in fWEC:

$$E = \sum_{i=1}^{N} C_{i0}\left(\bar{I}_1 - 3\right)^i + \sum_{i=1}^{N} \frac{1}{D_i}\left(J-1\right)^{2i} \tag{5.1}$$

where I_1 is the Cauchy-Green deformation tensors, C_i and D_i are material constants. From Figure 5.6, the hyper-elastic membrane holds a larger displacement (z_{tip}) and a smaller frequency of motion than that of a linear-elastic material. The final equilibrium position of the membrane is z_{tip}= -0.041 m and z_{tip}= -0.045 m for a linear-elastic and a higher-elastic material, respectively.

Table 5.2 Parameters for membrane materials.

	Young's modulus	**Poisson's ratio**	
Linear	6.5e5	0.35	
	(YEOH) C10	**C20**	**C30**
Hyper-elastic	2.5e5	-1.3e5	5e4

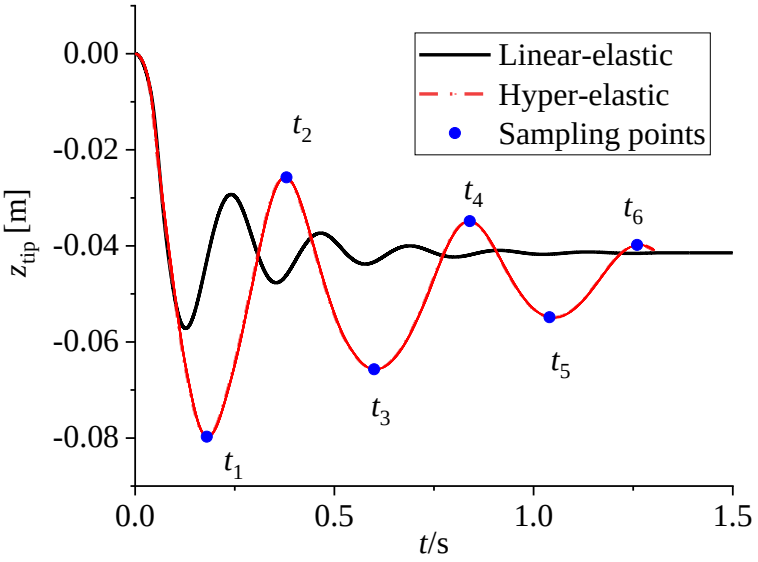

Figure 5.6 Tip displacement of the membrane with linear and hyper-elastic material (d=0.18m)

The flow velocity field distributions inside the water collector with a hyper-elastic material at each sampling time from t_1 to t_6 are shown in Figure 5.7. As revealed from those two figures, under a static pressure generated by a water height d =0.18 m, at t=t_1, the membrane deforms downwards from a flat configuration and reaches its maximum displacement of z_{tip}. Afterwards, it bounces back at t=t_2. The process repeats from t=t_1 to t=t_6 until the membrane reaches its final stationary position. A pair of symmetric eddies can be observed in the water chamber and grow with time.

As mentioned earlier, the system's natural frequency is dependent on the water column height d, i.e., the added mass of fWEC. A series of cases are tested with variable d. The selection of d is based on the water height d_0 and the wave amplitude A of 0.05m in an experimental model (Moretti et al., 2020), resulting in a range of d=$d_0 \pm A$ in this study. Figure 5.8 (a) and (b) show the FFT analysis distributions for the tip displacement with the variable d for a linear-elastic and a hyper-elastic material, respectively. Their quantitative values are plotted in Figure 5.8 (c). As seen from Figure 5.8 (a) and (b), given the same range of d variation, the dominant frequency of a linear-elastic material system occurs at 4.5 *Hz*. In comparison, those for a hyper-elastic material system spread out between 2.25 and 4.25 *Hz*. In addition, a 2nd order low frequency is also excited

with large *d*. This might be caused by the strong nonlinearity associated with large *d*. All the natural frequencies of fWEC are higher than the wave frequency (f=0.65Hz to 1.25Hz), which will be further discussed in Section 4.3.

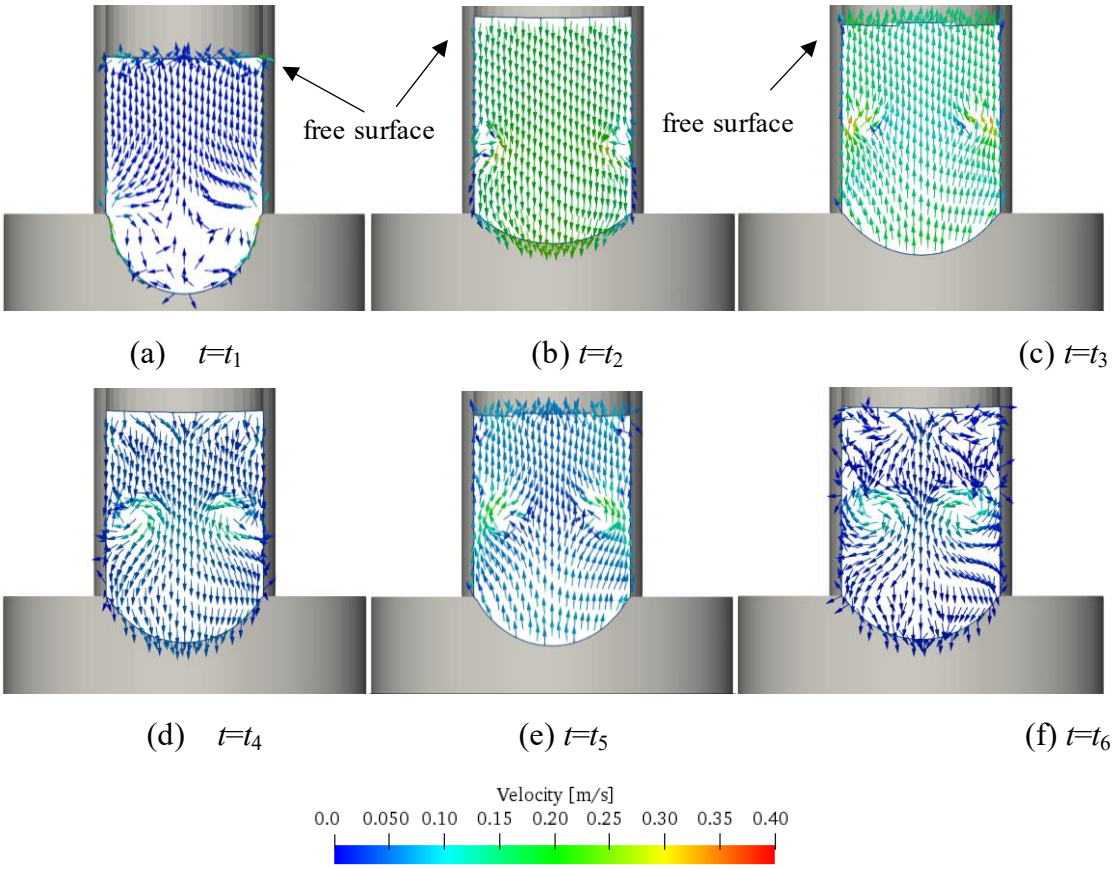

Figure 5.7 Development of the membrane deformation and the flow velocity vector inside the water chamber with a hyper-elastic material (d = 0.18m).

Figure 5.8 (a) also indicates that the larger the added mass is, represented by larger *d*, the smaller the fWEC structural natural frequency is. Given the same added mass, the fWEC with hyper-elastic material presences a wider range of natural frequency than its counterpart of linear-elastic material. This is consistent with the classic natural frequency, defined as $\omega_n = \sqrt{k/m}$, where *k* is the stiffness and *m* is the mass. The tip displacement z_{tip} dependence on *d* is plotted in Figure 5.9. It shows that a hyper-elastic fWEC is easier to deform than a linear-elastic material, especially at large *d*.

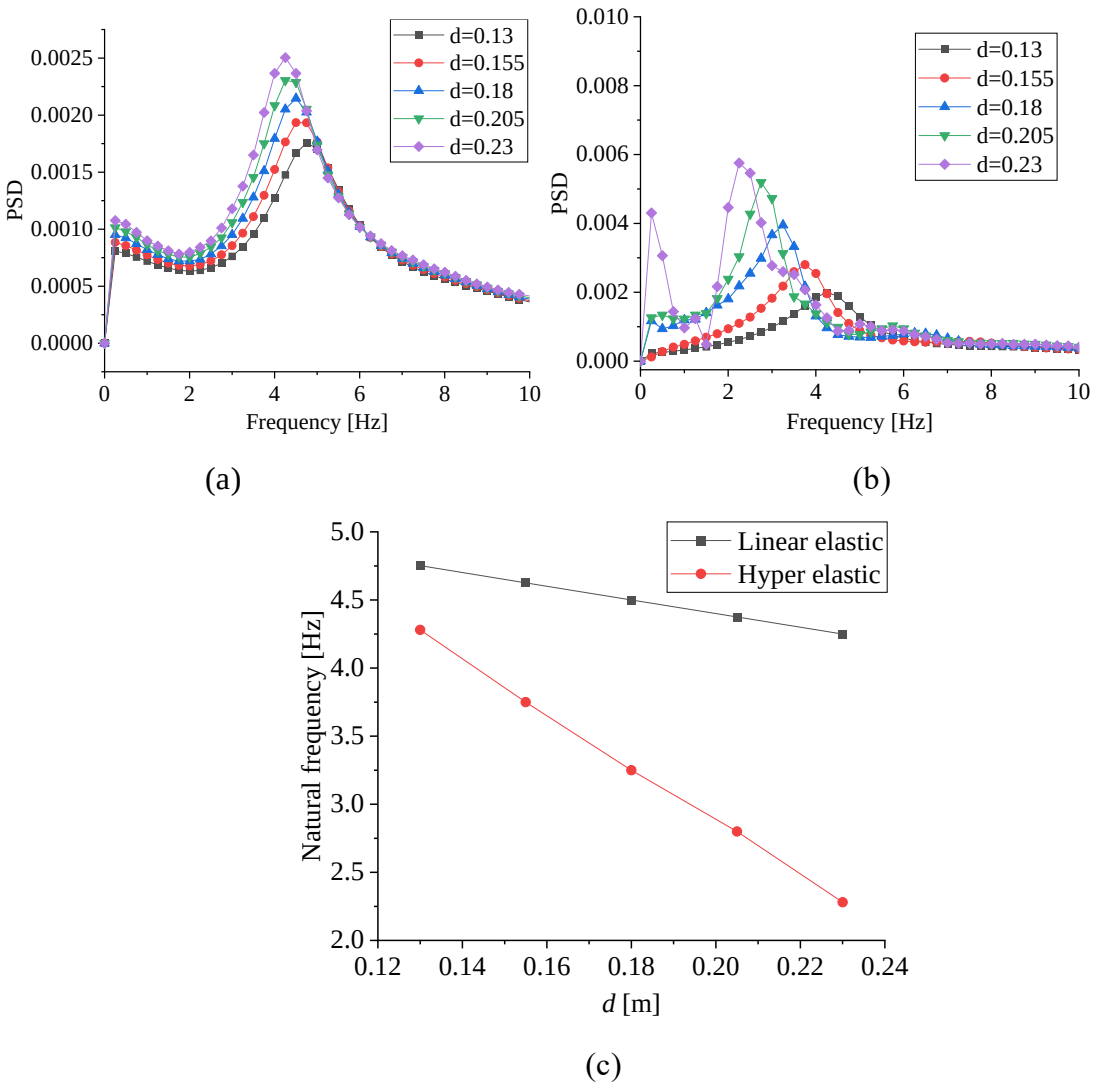

Figure 5.8 FFT analysis of the displacement with different d (a)linear-elastic material (b) hyper-elastic material (c) The natural frequencies via FFT analysis.

5.2.2 Response of Membrane Deformation under Hydrodynamic Pressure – Material Impact

This section discusses the dynamic response of fWEC with different materials under regular waves. For the convenience of analysis, the wave height is fixed at H=0.1m, and the wave period is T=0.8s. In addition to the two materials discussed in the last section, the linear-elastic and hyper-elastic M3, a softer hyper-elastic material, M4, is also included. Their mechanical characteristic properties are listed in Table 5.3 below.

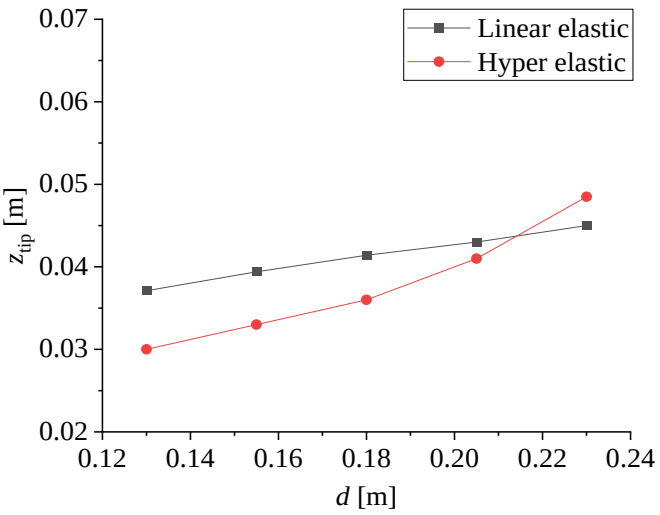

Figure 5.9 Tip displacement with different d for linear-elastic and hyper-elastic material

Table 5.3 Parameters for hyper-elastic materials.

	(YEOH) C10	C20	C30
M3	2.5e5	-1.3e5	5e4
M4	2.14e5	-1.14e5	4.29e4

The stress-strain relationship of the two materials in a uniaxial tensile test is shown in Figure 5.10, where the stress is represented by the Von Mises equivalent stress σ_{eq}. The curve is certainly linear for a linear-elastic material. For the hyper-elastic materials, the curves are divided into three sections with two inflection points at the strain ε of 0.3 and 0.9, respectively. The materials appear to have small stiffness between $0.3<\varepsilon<0.9$ while having large stiffness beyond this range, indicated by the large stress-strain curve slops. For an fWEC in this study, it is obvious that the section between ε=0.3 to ε=0.9 is desirable to achieve a large deformation of the membrane to maximise the energy conversion.

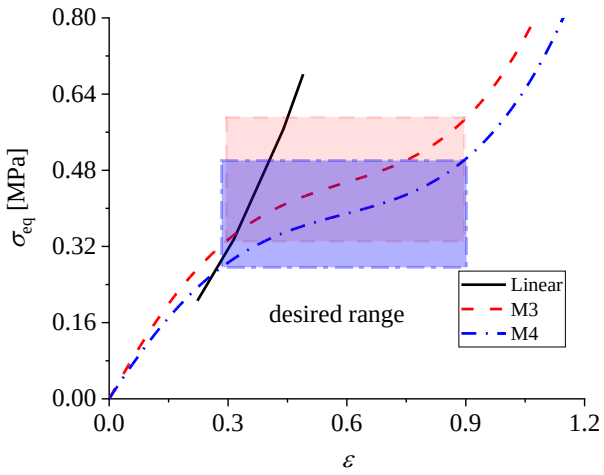

Figure 5.10 The stress-strain relationship of linear-elastic, hyper-elastic model M3 & M4.

Figure 5.11 shows the evolution of the waves and the dynamic response of fWEC within half a wave period. The wave crest propagates from the left and reaches the device at t=3.85 s. The water particle velocity magnitude increases and points to the surface in the normal direction of the membrane. This leads to an increase in momentum and thus accelerates the deformation. Once the wave moves closer to the fWEC, the wave steepness increases and the plunging wave breaks afterwards, which is a typical phenomenon associated with a wave propagating with a sudden depth change. With a short delay, the deformation reaches its maximum at t=3.95 s. As the wave further propagates, the velocity gradually changes its direction upwards. The wave, though, arrives at t=4.25 s, and the membrane bounces back to its highest position, with minimum deformation.

The time history of the tip displacement for linear-elastic, hyper-elastic M3, and M4 is shown in Figure 5.12. For a linear-elastic membrane and a hyper-elastic M3, their initial equilibrium position (δ_{static}) is similar under hydrostatic pressure. When waves propagate, although all three oscillate periodically with the same period as waves, the motion of the M4 is the largest among the three. The typical amplitudes are 0.0025 m for a linear-elastic, 0.01m for M3 and 0.0156 m for M4.

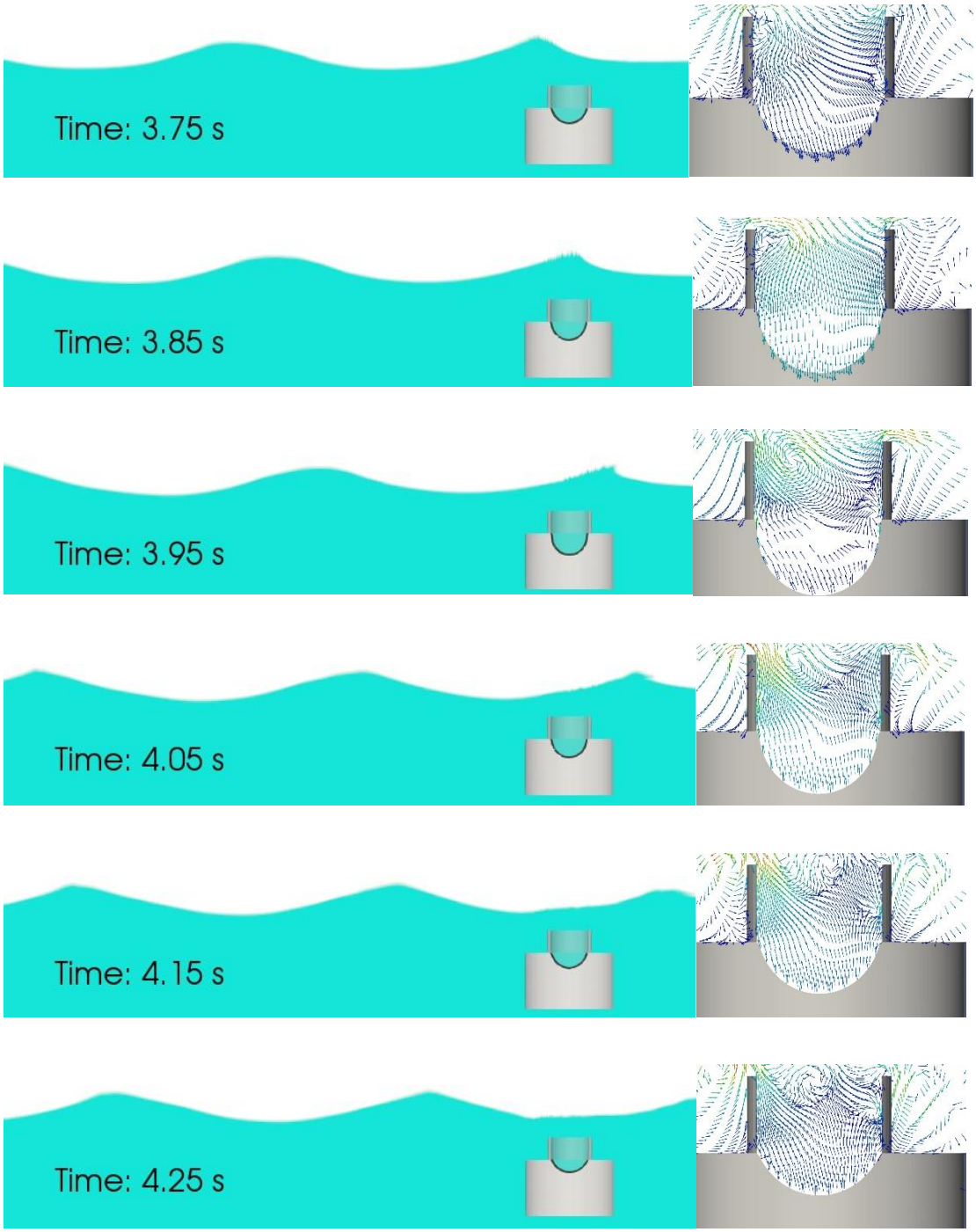

Figure 5.11 The evolution of the waves and fWEC response at different sampling times for M4. Wave elevation (Left) and zoom-in view around the fWEC with velocity vectors (Right).

It is worth mentioning that, from our previous study on a linear-elastic material, a reduction of material stiffness only changes the initial equilibrium position δ_{static} but does not influence the motion oscillating amplitude significantly (Li et al., 2021). In contrast, the present results show that a decrease in hyper-elastic material stiffness can achieve a profound increase in motion amplitude, indicating a distinct material characteristic between a linear-elastic and hyper-elastic material. In this regard, a hyper-elastic material provides a greater potential for deformation in contrast to a linear-elastic material.

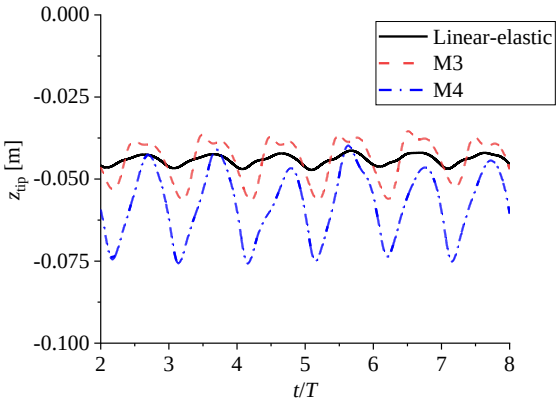

Figure 5.12. Tip displacement of the membrane with different materials (H=0.1 m, T=0.8 s and d=0.18 m).

Figure 5.13 shows the dynamic pressure contour around the fWEC. It can be seen the dynamic pressure reaches its maximum and minimum at the crest and wave trough. Inside the water chamber, the pressure is much larger than outside with wave crest passing. The opposite is true when the wave trough passes over.

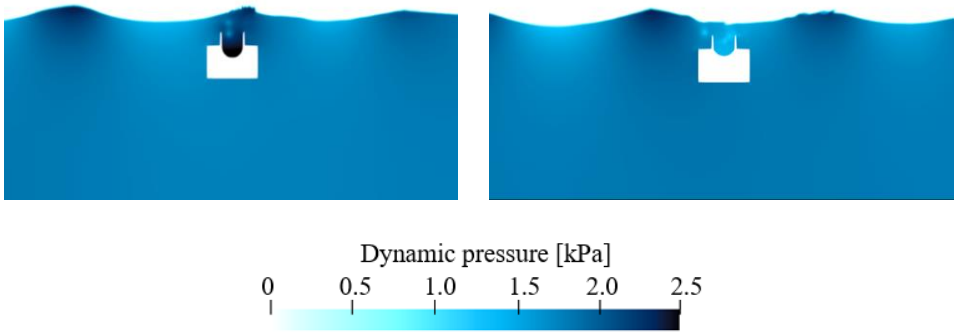

Figure 5.13. Dynamic pressure contour inside and outside the water chamber when the maximum (left) and the minimum (right) deformation is reached.

To better understand the membrane deformation in relation to the material stress induced by the hydrodynamic pressure, Figure 5.14 plots the instantaneous stress distribution along the membrane as well as the maximum and minimum membrane displacements. A comparison between a linear-elastic and a hyper-elastic M3 displayed in Figure 5.14 (a) and (b) indicates that M3 has a larger deformation than a linear-elastic one, although their stress varies in the same range of σ_{eq} =0.21-0.41. This observation highlights the superior feature of using a hyper-elastic material over using a linear-elastic material if a large displacement is desirable. Again, this is proved by a much softer material of M4, as shown in Figure 5.14 (c). The time-dependent stress and strain variation at the tip of the membrane is shown in Figures 5.15 (a) and (b). They confirm the above findings from Figure 5.14 with some additional information added as to the appearance of non-linearity of material associated with a hyper-elastic material M4.

Another important feature that can be observed from Figure 5.14 is that the stress is non-uniformly distributed along the membrane. As expected, the maximal stress occurs both at the tip of the membrane and the far ends of the membrane, and the non-uniformity increases with softer material from M3 to M4. This impairs the durability of the membrane, which may be caused by the device structure fatigue.

As discussed earlier, in the design phase of fWEC, a large motion amplitude is expected to get better performance by selecting different materials. Figure 5.16 demonstrates the effective deformation ability (the amplitude of the deformation rather than total deformation) associated with material properties. The boxes are the effective stress range (ESR), representing the actual stress ranges and strain variation during an operation. It can be seen that the ESR of linear-elastic material is very small, while hyper-elastic gets a larger value. This provides the evidence to conclude the superiority of hyper-elastic materials over linear elastic materials.

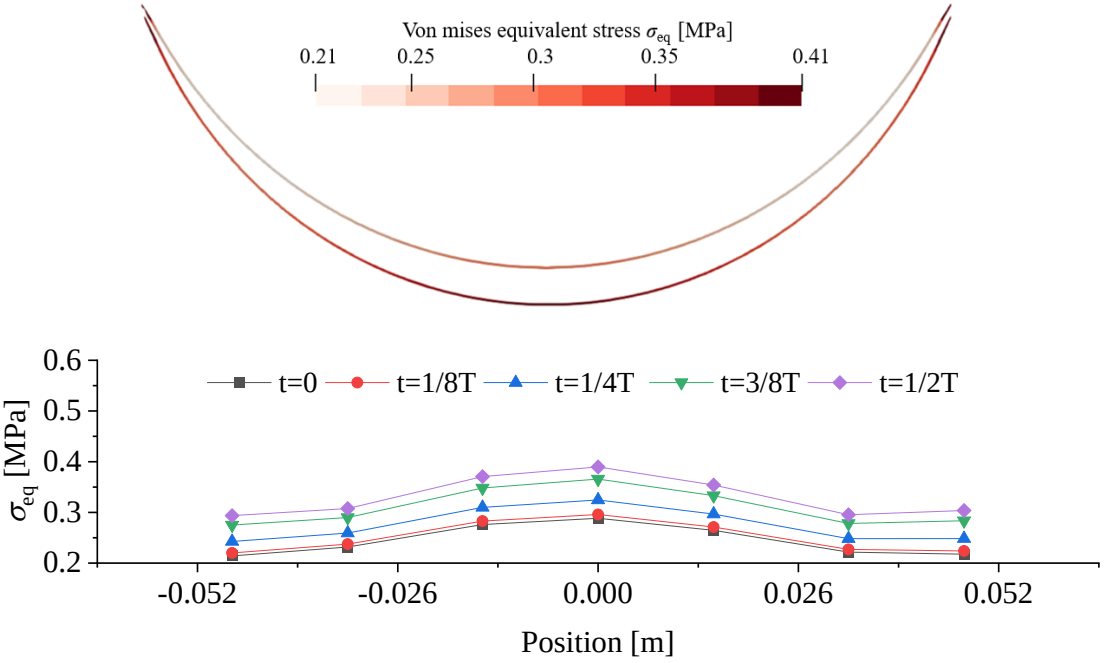

(a) Linear elastic

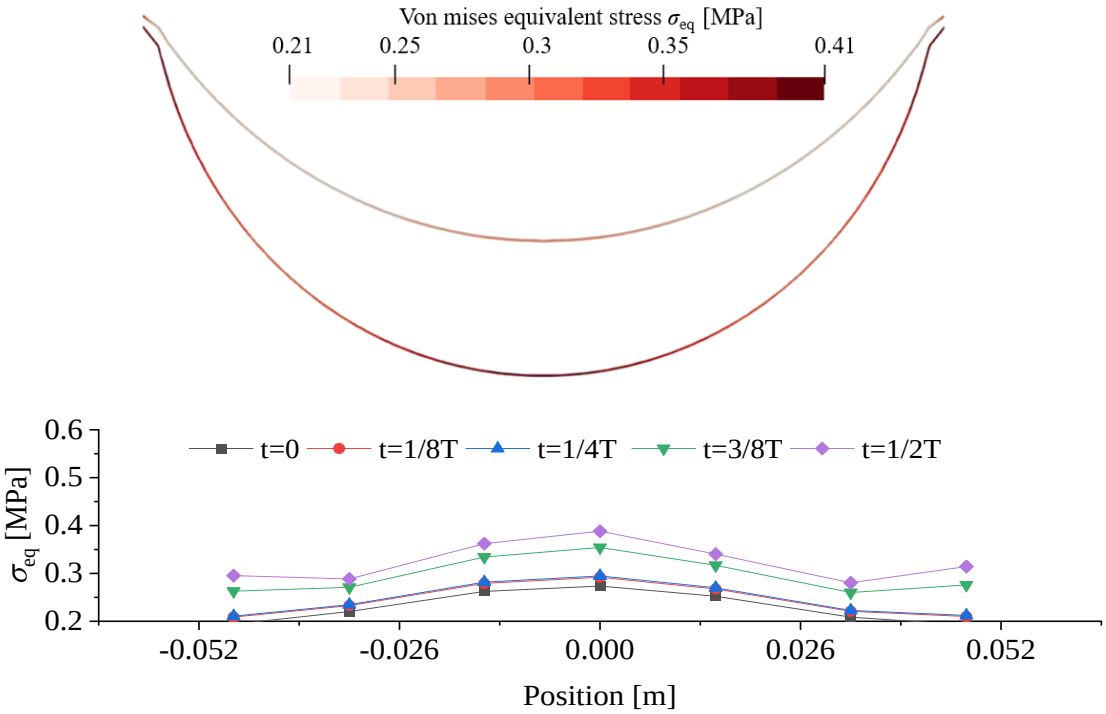

(b) Hyper-elastic M3

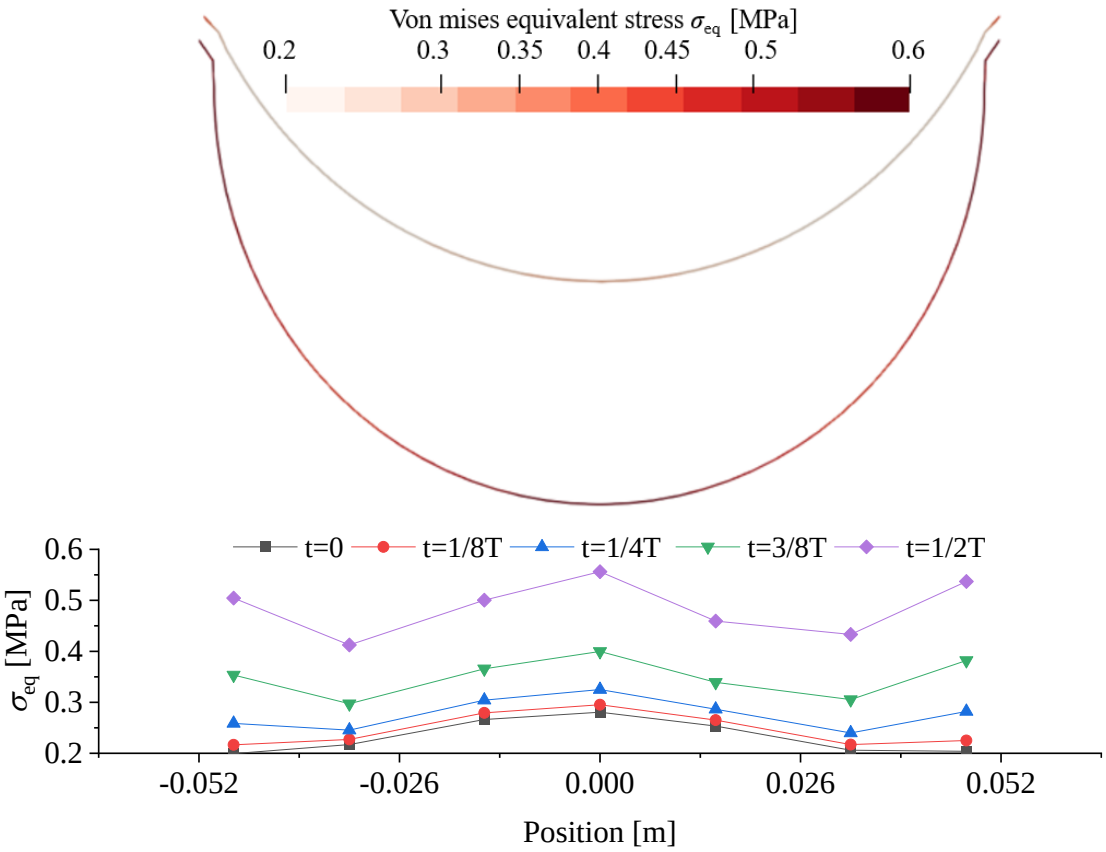

(c) hyper-elastic M4

Figure 5.14 The maximum and minimum deformation of the membrane and the distribution of equivalent stress σ_{eq} along the membrane. (a) linear-elastic (b) hyper-elastic M3 (c) hyper-elastic M4.

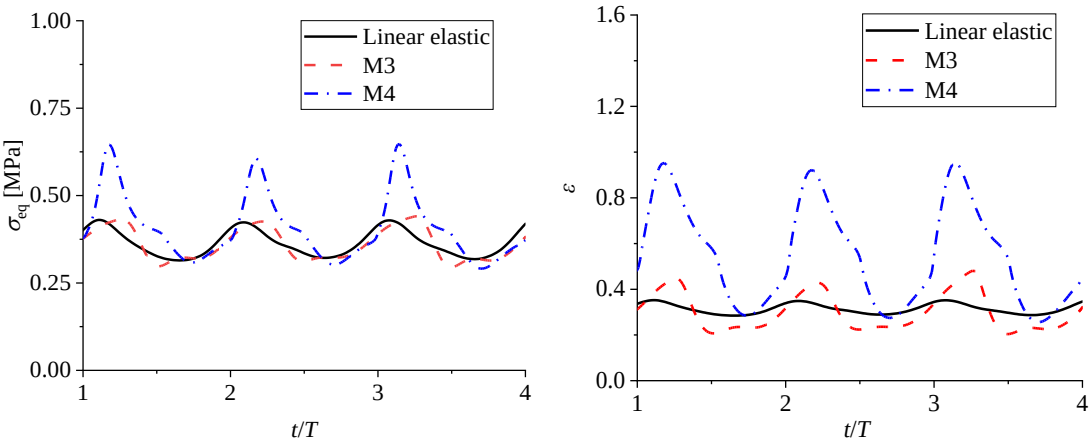

Figure 5.15 Time history of stress σ_{eq} and strain τ of the tip for different materials

When the stiffness of M3 is reduced, the stress-strain curve translates downward, as illustrated by the zoom-in figure on the top right. This makes the ESR adapt more to the stress variation induced by waves, thus obtaining a larger strain range and deformation. In the aspect of the practical application of material selection, if the desired deformation is pre-determined, with this figure, the strain range can be estimated; thus, the material's mechanical property and the stress-strain relationship can be obtained.

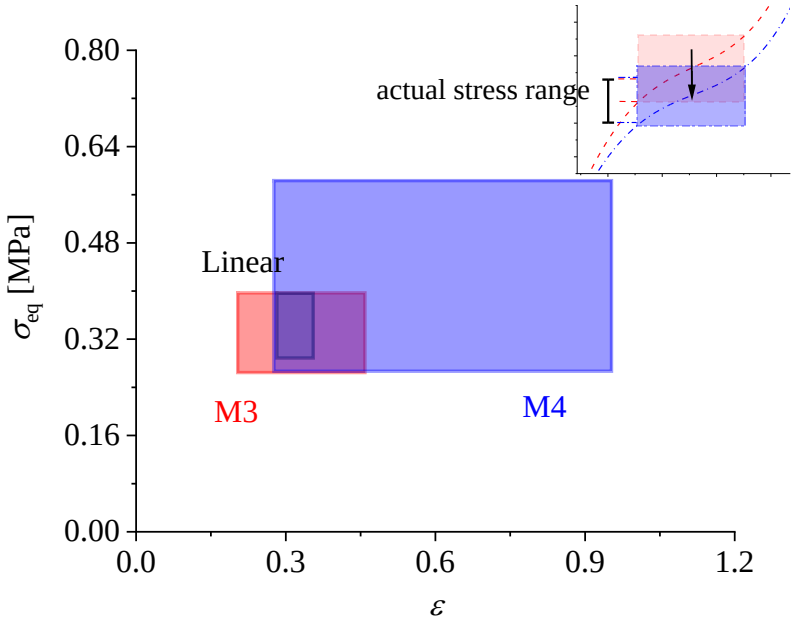

Figure 5.16 ESR of the fWEC. The rectangles represent the ESR of the WEC device during operation. The larger the rectangle is, the better the performance is for this material (which means a larger deformation can be achieved).

5.2.3 Response of Membrane Deformation under Hydrodynamic Pressure – Wave Period Impact

The effect of the wave periods on the fWEC is studied in this section with a constant d=0.18 m. The wave height is fixed as 0.1 m and the wave period ranges from T=0.8 s to T=1.6 s, corresponding to the wave period of 5.6 s-12.6 s at the device full-scale level. The time histories for the tip displacement of the membrane are presented in Figure 5.17, along with the FFT analysis. Large wave periods generally lead to a more vigorous

motion of the membrane, indicated by the large amplitudes. For a linear-elastic material, the curve appears to be a smooth variation, though some nonlinear features can be observed with T increasing. However, given a hyper-elastic material, significant differences can be seen for T=0.8 s and T=1.6 s. In fact, with a large wave period, the motion is more unstable, and wavelets at the wave trough and crest can be observed, implying higher-order components are excited, which is clearly illustrated by the FFT analysis. In particular, only 1st and 2nd order harmonic components are excited for a linear-elastic material, while for the hyper-elastic material M3 and M4, a 3rd-order and even higher-order components are added in, caused by the non-linearity of material mechanical characteristics.

The internal flow field can be examined easily through the CFD results. The vortex variation inside the collector is shown in Figure 5.18 and Figure 5.19 for T=0.8 s to T=1.6 s, respectively. With a wave period of T=0.8 s, the clockwise and anti-clockwise vortices are generated alternately at the top left of the collector. The anti-clockwise vortex forms because of the backward flow caused by the propagating wave trough. This anti-clockwise vortex then moves downwards over the fWEC with waves passing from left to right. Meanwhile, the clockwise vortex forms due to the wave crest propagating into the water chamber. Only a clockwise vortex remains in the chamber. With a large wave period of T=1.6 s, the clockwise vortex generates at the top left, and only part of the vortex goes into the chamber. The vortex field is more chaotic than that of T=0.8 s, and the anti-clockwise vortex remains inside. Meanwhile, the clockwise vortex generated at the left top of the chamber becomes larger. This contributes to the excitation of higher-order components, which partly explains why the wave with a larger period and with a smaller wave steepness shows higher nonlinearity.

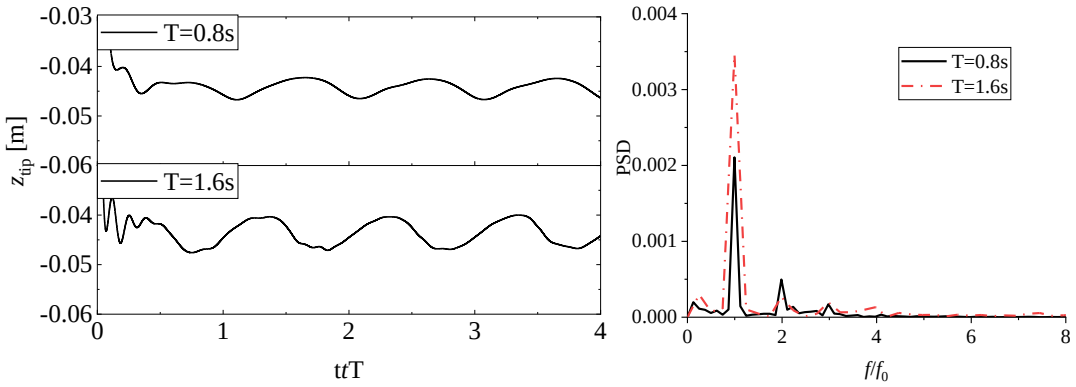

(a) Linear

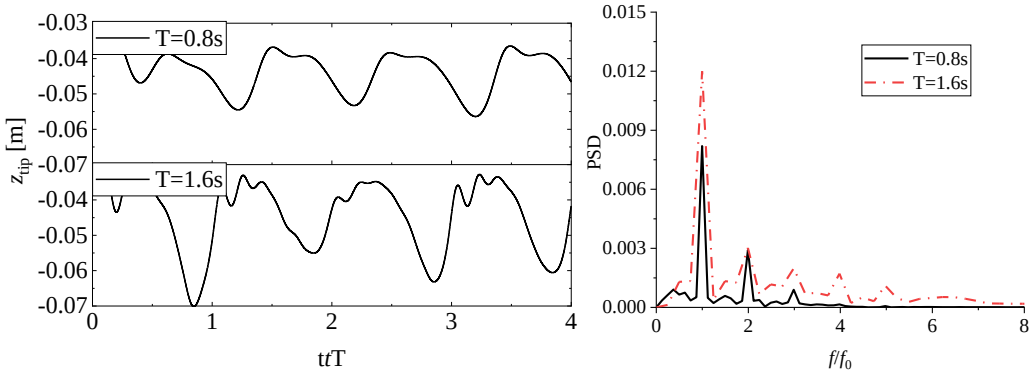

(b) M3

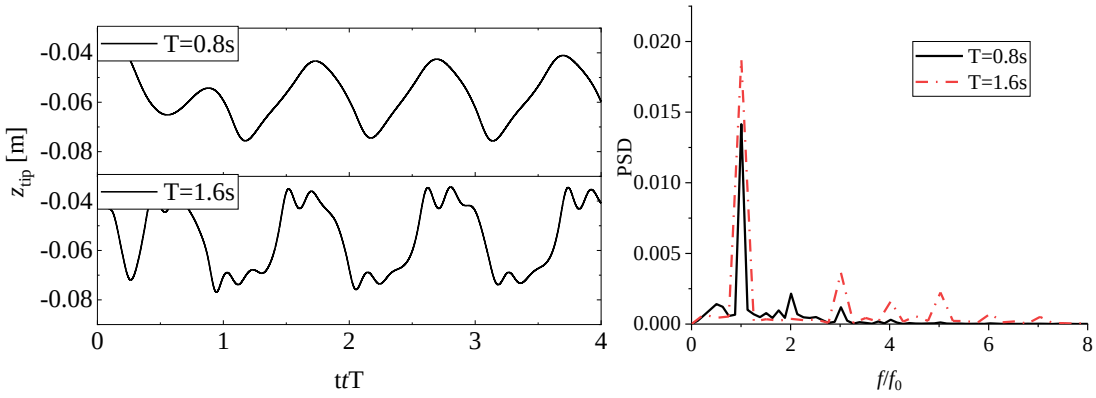

(c) M4

Figure 5.17 Time histories of the displacement of membrane tip (left) and the FFT results (right), with different materials (H=0.1 m, d=0.18 m for T=0.8 s and 1.6 s).

The time-averaged membrane displacements with various wave periods are compared in Figure 5.20 Again, the hyper-elastic material has a much larger amplitude than the linear-elastic one, regardless of wave periods, indicating the advantage of using hyper-elastic material over linear material for all wave conditions. Although a subtle peak

appears between T=1.4 s and T=1.6 s, its magnitude is not significantly larger than that of other wave conditions. This is an advantage of flexible WEC compared to traditional rigid WEC. Traditional WEC, such as point absorber or oscillating water column, usually works favourably for a specific wave period. The efficiency of the device decreases significantly, even does not produce any energy, if the sea state is too far from the design condition. This is not observed in the present fWEC, which has no preference for wave conditions. As discussed in section 4.3, the natural frequency of the system is far away from the wave periods, thus there's almost no resonance occurring. However, by using a hyper-elastic material and adjusting the material parameters, a large amplitude can also be achieved without resonance, thus obtaining a large power output.

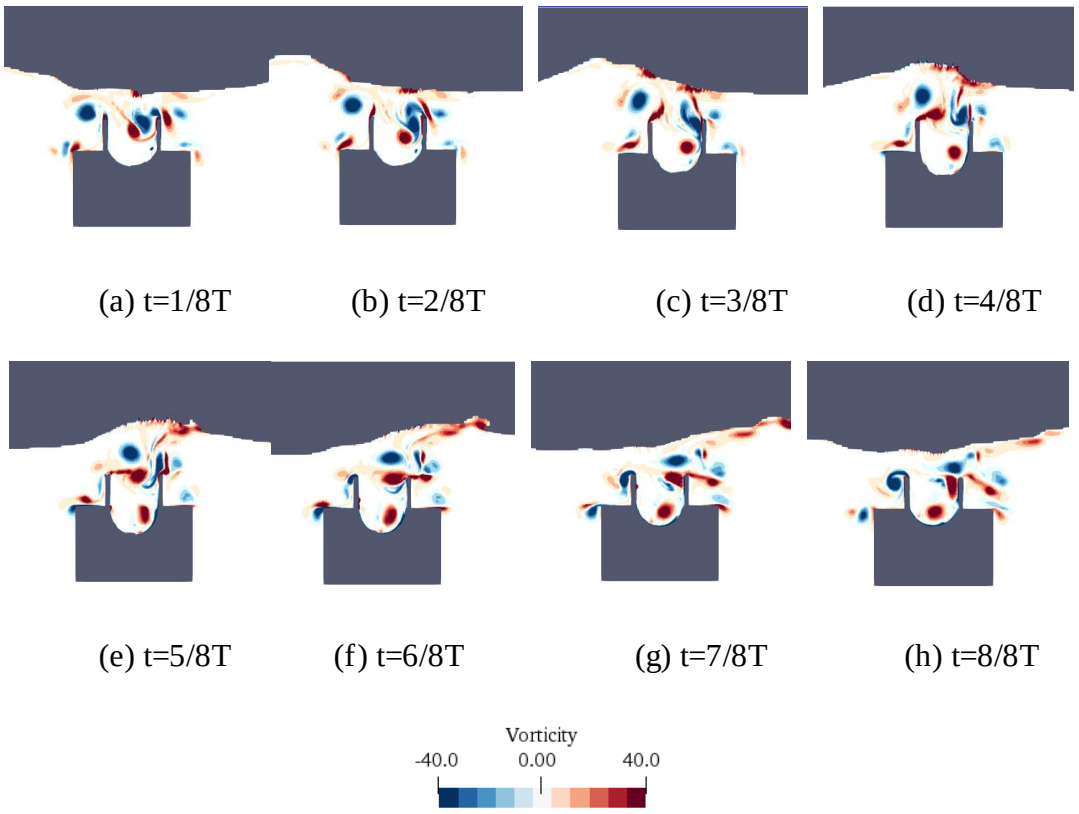

(a) t=1/8T (b) t=2/8T (c) t=3/8T (d) t=4/8T

(e) t=5/8T (f) t=6/8T (g) t=7/8T (h) t=8/8T

Figure 5.18 The instantaneous vorticity contour for T=0.8 s in one wave period (H=0.1 m, d=0.18 m).

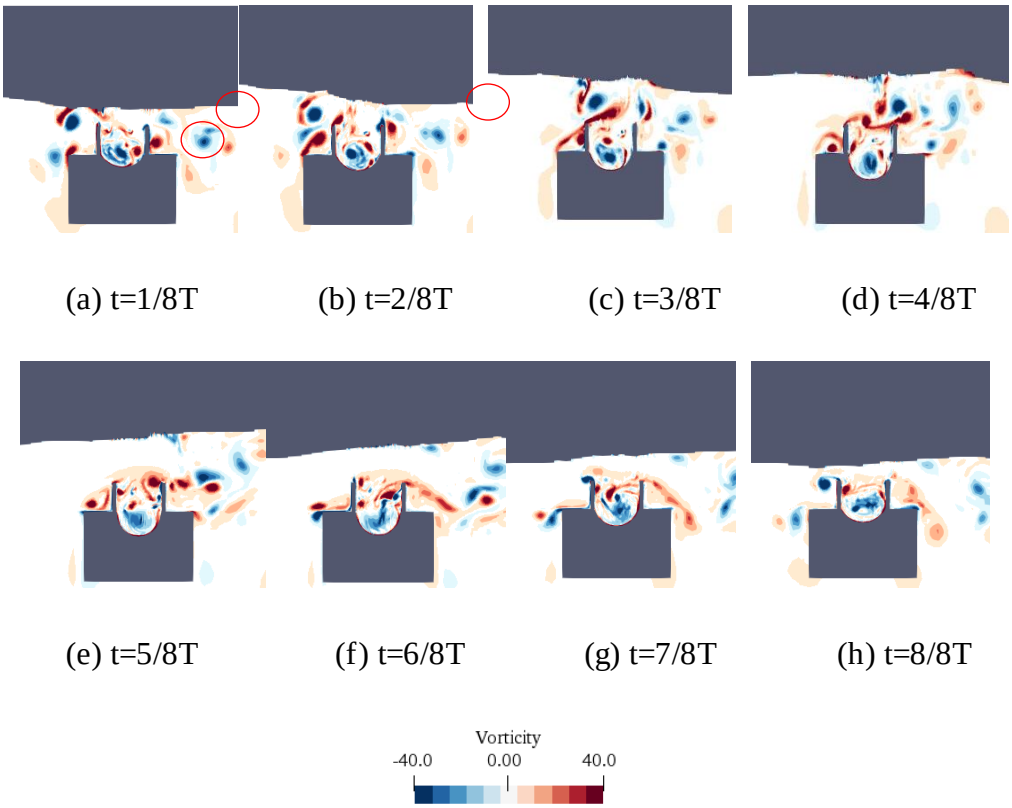

Figure 5.19 The instantaneous vorticity contour for T=1.6 s in one wave period (H=0.1 m, d=0.18 m).

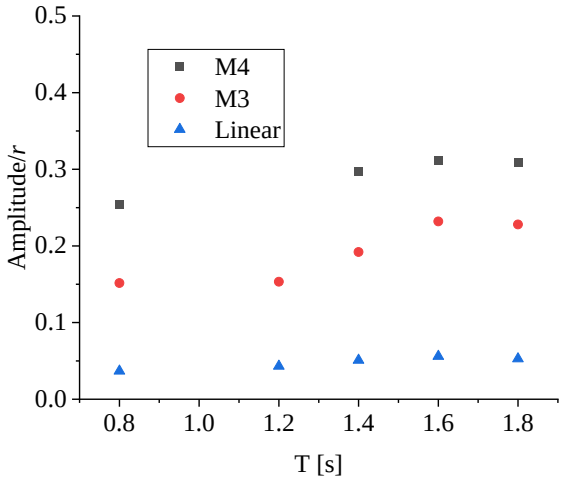

Figure 5.20 The amplitude of the motion for different materials versus wave period. The amplitude is non-nondimensionalized by r_c.

The power output of the fWEC on a full scale is calculated via a post-process procedure using the data from CFD-FEA results. The details of the power calculation can be

referred to (Moretti et al., 2019; Rosati Papini et al., 2018). The electrical energy produced in one wave period can be estimated by the energy harvested from the fWEC during the charging and discharging processes.

$$E = 0.5\left(C_a + C_B\right)V_B^2 - 0.5\left(C_a + C_A\right)V_A^2 \tag{5.2}$$

where C_a is the additional in-parallel capacitance. V_A and V_B are the voltages immediately after electric priming and before discharging respectively. The corresponding capacitance is C_A and C_B, which are related to the deformation of the membrane, i.e., the average thickness of the membrane t_A and t_B obtained from the simulation. The capacitance is then evaluated by the capacity equation $C_A = \varepsilon * \varepsilon_0 S/t_A$. ε and ε_0 are the relative dielectric constant and permittivity of vacuum, respectively. S is the area of the membrane.

V_A and V_B can be estimated by the following equation:

$$C_A = C_a\left(\frac{V_0}{V_A} - 1\right) \tag{5.3}$$

where V_0 is the priming voltage to charge the fWEC, which is 7500V in this paper. The calculated power output based on the above equations is summarised in Table 5.4. It can be concluded that the power output of the fWEC is at the level of tens of kilowatts. The performance of fWEC is significantly improved by substituting linear-elastic material with hyper-elastic material. The maximum power generating capacity of M4 can be up to 112 kW. In addition, such fWEC can effectively avoid its sensitivity to wave conditions. Indeed, as previous studies revealed, the efficiency of a conventional rigid WEC can drop significantly from 0.8 to 0.1 when the wave conditions, in particular the wave periods, are changed (Ning et al., 2016)). However, for this fWEC, the reduction of power is much less than rigid WEC, as indicated by min/max power generation of 7.4/10.6 and 58.5/112.5 for linear-elastic and hyper-elastic materials, respectively. It is worth mentioning that since the electro-mechanical model is not included in this study, the estimated power might be larger than the real values.

Table 5.4 Power estimation in full-scale versus varied wave period. (Unit in kW).

T [s]	5.6	8.4	9.8	11.2	12.6	**mean**
Linear	10.6	8.2	8.7	8.7	7.4	**8.7**
M3	40.0	32.6	29.4	32.1	22.6	**31.4**
M4	112.5	81.1	79.2	72.9	58.5	**80.8**

5.2.4 Discussion between 2D and 3D results

A three-dimensional simulation is conducted with H=0.1m and T=0.8s, with a hyper-elastic material. The deformation, along with the pressure contour and velocity vectors, are shown in Figure 5.21(a). The time-dependent tip displacements are compared in Figure 5.22. Although the displacement for a 2D and a 3D simulation seem very similar, the differences in the material properties are observed as shown in Figure 5.22. The structural model constraints conditions are different. For a 2D model, the constraints are applied at the two ends of the membrane, see Figure 5.21(b). However, for a 3D model, the constraints are applied along the circumference of the membrane. Therefore, it is expected to achieve a larger deformation from a 2D model than that from a 3D model, if the same material is applied. Therefore, it is necessary to conduct research on a 3D fWEC to explore additional features in the future.

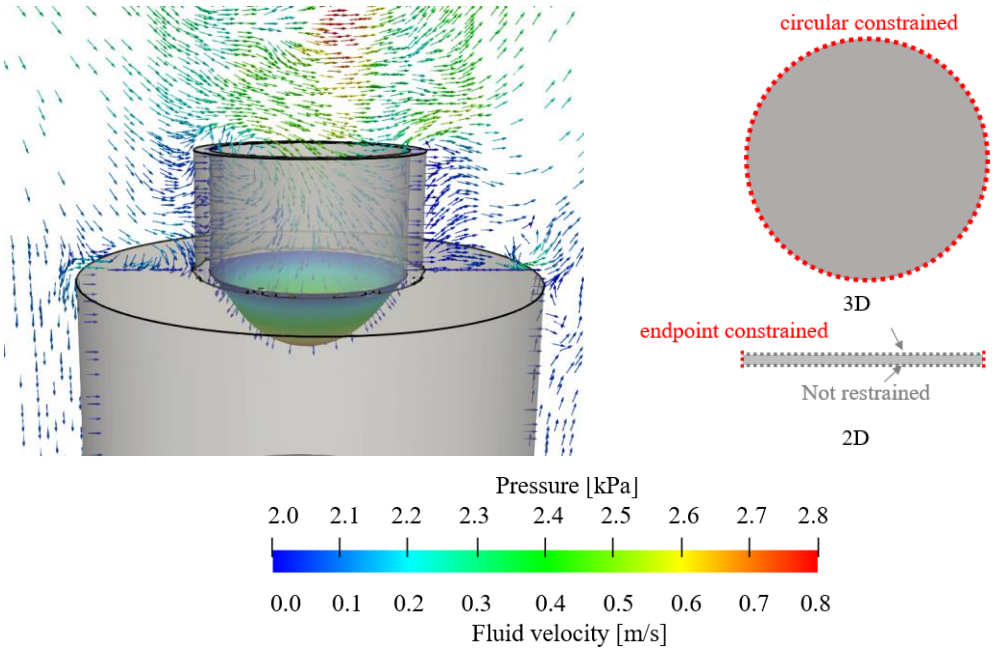

Figure 5.21 (a) Deformation of a 3D fWEC at a maximum tip displacement (b) Constraints for 3D and 2D models

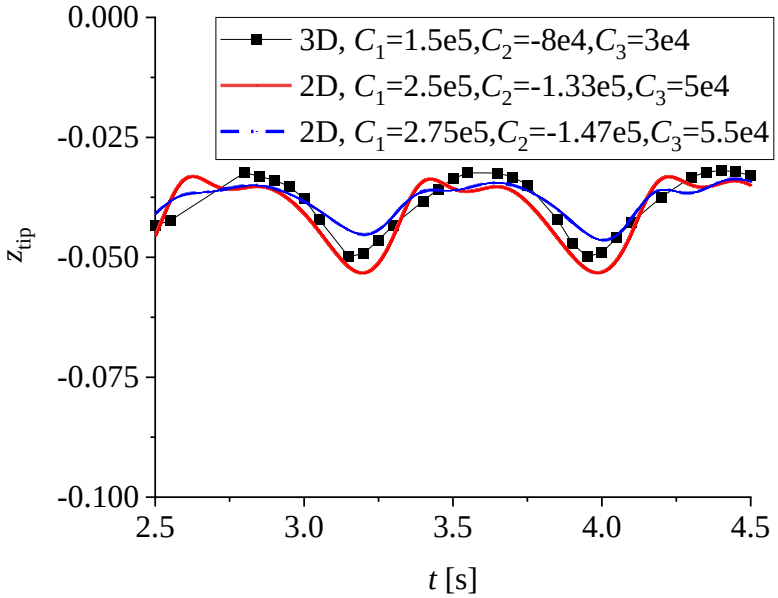

Figure 5.22 Tip displacement of the membrane for 2D and 3D models with different materials for H=0.1m, T=0.8s, and d=0.18

5.3 Concluding Remarks

This chapter aims to study an FSI problem of the hyper-elastic fWEC using a coupled CFD-FEA numerical tool. OpenFOAM is utilised as the fluid solver, and CalculiX is

selected to solve the deformation of flexible structures. Because the study is highly nonlinear, a coupling library for multi-physics simulation (PreCICE) was implemented for a robust coupling and to allow the data transfer between the two solvers. With this tool, the flexible WEC with different materials used in constructing an fWEC can be examined, covering a series of varying wave conditions.

The water height (d) above the PTO membrane is found to have a significant effect on the natural frequency of the fWEC. The natural frequency of hyper-elastic fWEC is more sensitive to d than the linear-elastic one. Resonance at the fundamental frequency is avoided at all stages in any case.

A positive correlation exists between d and the deformability of the hyper-elastic fWEC, as d increases, so does the deformation of the hyper-elastic fWEC. The linear elastic material is seen to do the opposite of this phenomenon with the deformability getting poorer when increasing the water height d.

A further investigation of fWECs constructed with different materials indicates that the stiffness of this hyper-elastic material becomes smaller within a certain stress range. The hyper-elastic material becomes significantly less stiff. This range is given the name the effective stress range. If the actual stress variation caused by the simulated waves matches the ESR, a larger level of deformability can be observed and, consequently, a greater motion amplitude. By selecting the hyper-elastic material, the dynamic motion of an fWEC can be three times larger than a linear one. Adjusting the hyper-elastic mechanical parameters can increase this ratio up to six times for the hyper-elastic material. Despite this, the stress distribution experienced along the hyper-elastic membrane is distributed unequally compared to the linear-elastic material. This makes it more vulnerable to fatigue at the tip and both ends of the membrane.

A study on how varying wave periods influence the fWEC shows that second-order components are excited about T=0.8 s. As T increases, a greater number of higher-order components, up to five, are excited. Although a peak period corresponding to a

maximum motion amplitude exists, the difference under a wide range of wave periods is insignificant. This suggests that this fWEC has strong adaptability to the sea state rather than requiring preferring a particular wave parameter to perform optimally.

Chapter 6 VIM of FOWT Platforms in Wave-Current Conditions

In this chapter, the VIM of the floating platform in complex sea conditions is numerically studied using a high-fidelity CFD tool. We aim to illustrate the underlying mechanisms related to this FSI problem using this tool. The wave-only and current-only scenarios are studied for both the OC4 DeepCwind platform by the NREL and the BW IDEOL platform with Électricité de France. Then, the combined wave-current conditions are studied for the OC4 platform at various angles and wave current parameters.

6.1 Problem Description

6.1.1 Model Parameters

The two platforms studied are the OC4 semi-submersible platform and a barge IDEOL platform, as shown in Figure 6.1. The OC4 semi-submersible platform model is based on a 1:73 model test performed at the University of Tokyo by Gonçalves et al. (Gonçalves et al., 2021). The platform comprises four columns: one central column with a smaller diameter and three offset columns with larger diameters. Columns are connected by crossbars in between. There are base columns attached below the side columns. In the experiment, the model was restrained by four perpendicular mooring lines. The main parameters, including the equivalent stiffness of the mooring system, are summarised in Table 6.1. The natural frequencies of the platform in IL and CF directions are 9.4 s and 9.6 s, respectively, which were obtained via free decay tests.

The barge IDEOL platform is a 1:50 model, which was experimentally tested in the National Research Institute of Fisheries Engineering (NRIFE) wave tank in Japan (Kosasih et al., 2019), shown in Figure 6.1 (b). The width of the barge semi-submersible platform is 0.82m, with a draught of 0.14m. The skirt with 0.055m width is attached at the bottom to reduce the dynamic motion response. Compared to the OC4 platform, this

barge platform has a simpler geometry and is easier to construct, with a larger area of water plane and smaller draft. To constrain the platform, three catenary mooring lines are applied. The nominal diameter of these studless chains is 3mm with a total length of 8m. The geometric parameters of the platform can be found in Figure 6.1 and Table 6.1.

Table 6.1 Geometric parameters and the mooring parameters

OC4 Platform		**IDEOL Platform**	
Central column diameter	D_c=0.09m	Thickness of the Skirt plate	d_s=0.004m
Offset Column diameter	D_s=0.165m	Skirt plate width	W_S=0.055 m
Base column diameter	D_B=0.33m	Width	W_B=0.82m
Height of base column	d_B=0.083m	Height	H_B=0.19m
Platform draft	d=0.27m	Platform draft	d=0.14m
Distance between offset columns	L=0.688m		
Inertia properties			
Mass of the Platform	m=36.7kg	Mass of the Platform	m=62.31kg
Centre of mass	z_c=-0.134m	Centre of mass	z_c=0.03m
Mooring parameters			
Stiffness in *x* direction	k_x=27.5N/m	Type	Studless
Stiffness in *y* direction	k_y=28.1N/m	Weight in water	0.067kg/m

In ocean engineering, the geometry of a platform significantly influences its motion response, particularly in interaction with water currents. The above two platforms exhibit distinct geometries, primarily differentiated by their waterplane area. The IDEOL barge platform, akin to a hollowed-out box, has a substantially larger waterplane area than the SS platform. This expands the waterplane area, resulting in a shallower draft and a reduced aspect ratio (defined as draft/characteristic length). In a VIM study, a lower aspect ratio typically exhibits enhanced three-dimensional

characteristics at the platform's bottom edge, subsequently altering the motion amplitude.

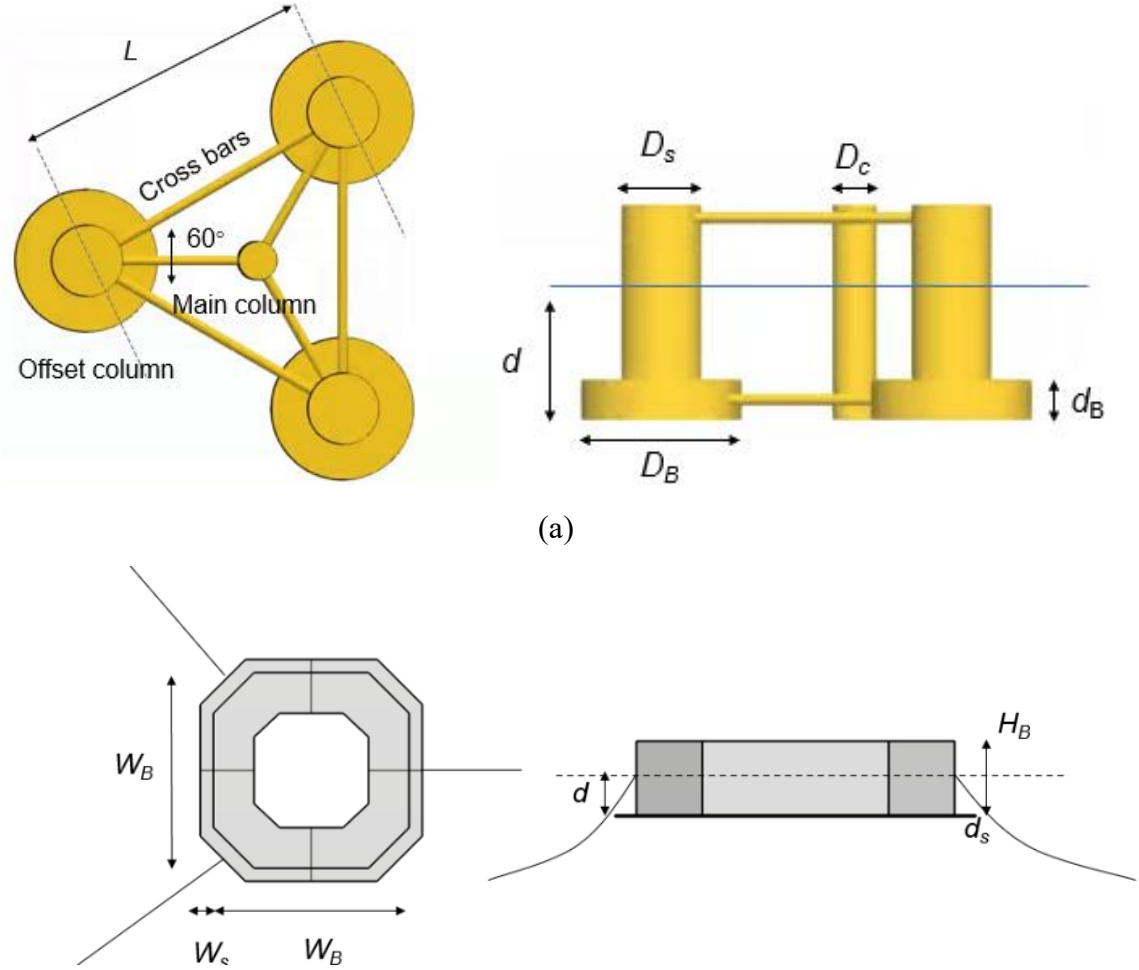

Figure 6.1 Sketch of the scale-down model for (a) OC4 Platform and (b) IDEOL platform

6.1.2 Parameters for Numerical Simulation

The computational domain is shown in Figure 6.2 with top and side views. The boundary conditions are set as follows: the zero-gradient pressure condition is applied at the inlet and outlet boundaries with the air speed equal to zero, while the fluid velocity is given by a build-in boundary based on the wave theory, for the generation of inflow wave-current condition and wave absorbing. For those cases with oblique incident waves, the front boundary is imposed by the same settings as the inlet boundary

condition for wave generating. A non-slip wall boundary condition is applied to the bottom.

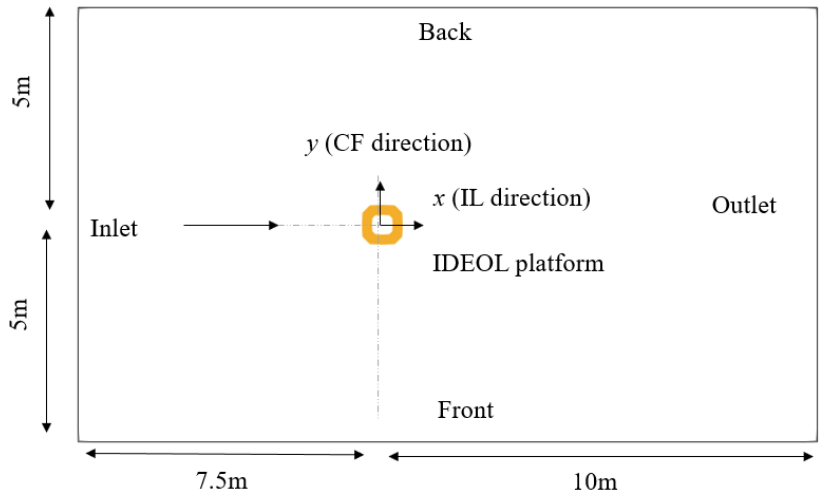

(a) Top view

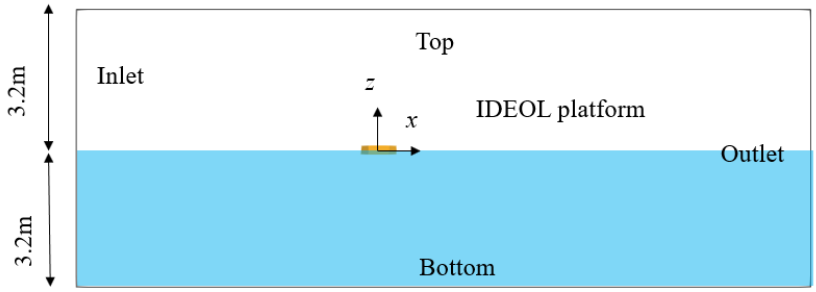

(b) Side view

Figure 6.2 (a)Top view (b)Side view of the numerical wave tank for IDEOL platform

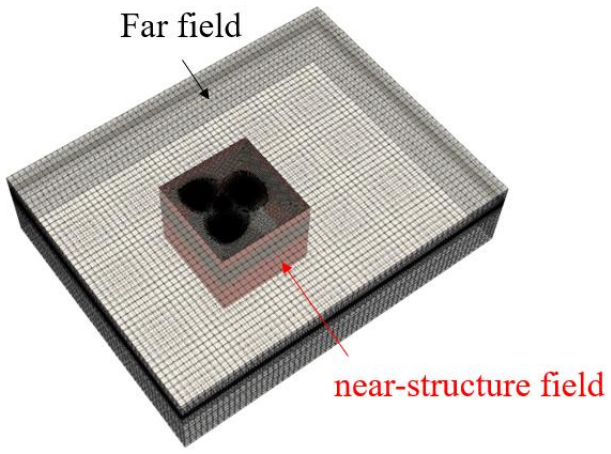

Figure 6.3 Computational mesh for the OC4 platform; the inner red zone is a structured mesh to capture high-quality boundary layers, and the outside is the unstructured far-field mesh, where the mesh is only refined near the water-air surface.

To accurately model the motion of the platform under both wave and current conditions, it is essential to ensure that the mesh resolution meets different mesh density requirements. For instance, to capture VIM, the separation of the boundary layer around the structure and the vortex street downstream should be accurately modelled. Therefore, CFD mesh is refined at the near wall field region as well as the wake region. To reduce the overall cell numbers of the computational domain, a hybrid mesh is used, which is made up of the near-field structured mesh (red one) and the far-field unstructured mesh, as shown in Figure 6.3. Within the boundary layer, the thickness of the mesh is set so that the $y+$ around the platforms ranges from 1.0 to 4.0. The surface cell on the platform is 1/100 of the characteristic length D. At the near field of the structure, the average cell size is 1/50 D. In the far field region, to ensure the accuracy of numerical wave generation, the cells near air-water-free surfaces are refined. In particular, the cell length of $H/8$ is used along the z-direction for all cases, and the cell length along the x and y directions is $\lambda/160$.

6.1.3 Mesh and Time-step Dependency Study

The convergence test of the numerical simulation is conducted, and the results are shown in Table 6.2. Three mesh sets with different cell counts are used, with which the normalised IL and CF motion (A_x/D and A_y/D) are compared, as well as the frequency of the cross-flow oscillation f/f_n. The disparity between the Medium and Fine cases is less significant than between the intermediate and coarse cases. This suggests that the intermediate grid is sufficiently fine for the current research. Similarly, for the sensitivity study with different time steps, the predicted motion hardly changes when $U\Delta t/D$ <0.002. Considering the computational time cost, a time step of $U\Delta t/D$ =0.002 is chosen for the CFD modelling in this study.

PIMPLE algorithm is utilised to solve the pressure-velocity coupling. A second-order Crank-Nicolson scheme is used for temporal discretisation. The second-order upwind scheme is adopted for convective terms. Gradient terms are handled via a second-order cell-limited Gauss linear scheme. The total number of cells in the simulation is around

350 million for both platforms. The computations are made in parallel with five nodes (180 cores) for each case on Cirrus HPC (http://www.cirrus.ac.uk). The average simulation time is $3T_n$ per day, which may vary depending on the specific cases.

Table 6.2 Sensitivity study for computational mesh and unsteady time step for OC4 platform with $V_r = 8.1$

Mesh	Cell count	$U\Delta t/D$	A_x/D	A_y/D	f/f_n
Coarse	2,650k	0.002	0.050	0.424	0.990
Intermediate	3,510k	0.001	0.055	0.403	0.959
		0.002	0.059	0.410	0.958
		0.004	0.077	0.421	0.932
Fine	5,400k	0.002	0.061	0.402	0.959

6.2 Results and Discussions

6.2.1 Response of Different Platforms with Current-only and Wave-only Conditions

When waves and currents coexist, their respective motions become coupled. To decouple this effect, we start with a comparative study on the FSI problem, either induced by wave or current separately for both OC4 and IDEOL platforms. Because of their different geometric characteristics, it is expected to observe different dynamic motion responses.

6.2.1.1 OC4 Platform

Either current or wave interaction with the OC4 platform is first studied, and the flow conditions are listed in Table 6.3. Figure 6.4 displays the amplitude of the motion

response in the current-only scenario along with the experimental data, in which the IL component (A_{cx}) and CF component (A_{cy}) are plotted against flow velocities. They are calculated by multiplying the root mean square (RMS) displacement by $\sqrt{2}$, and then normalised with the characteristic length, which is D_s for OC4 platform and W_B for IDEOL platform.

Table 6.3 Wave and current parameters for OC4 Platform testing

Wave Parameters

H[m] Scaled 1:73	0.02	0.04	0.07	0.09	0.116	T[s] Scaled 1:73	1.5	2.0	2.63
H[m] Full-scale	1.45	2.91	5.09	6.54	8.44	T[s] Full-Scale	12.78	17.04	22.4

Current parameters

U [m/s] Scaled 1:73	0.05	0.08	0.11	0.14	0.17	0.20	0.24
U [m/s] Full-scale	0.43	0.68	0.94	1.20	1.45	1.70	2.05
Vr	2.30	3.7	4.6	8.1	9.9	11.6	14.3

In VIM analysis, the freestream velocity is commonly normalised using the natural frequency of the system (f_n). The reduced velocity is defined as $V_r=U/f_nD$, where U and D are the structure's flow velocity and characteristic length. It can be rewritten as $V_r=UT_n/D$, where T_n is the natural frequency of the structure. From a physical perspective, the numerator can be considered as the distance that the constant fluid flows over the structure in one natural vibration period. Thus, V_r indicates the ratio

between this distance and the structural dimension. In this study, cases with different V_r are achieved by only varying the flow velocity; meanwhile, the Re number is also synchronised with V_r since they are both representative of the flow velocity.

The plot indicates that the CFD predictions agree with the experiments. The IL motion is significantly smaller than that of CF motion, with A_{cx}/D being less than 0.1, indicating that the IL movement of the platform is not dominant. However, the CF motion response shown in Figure 6.4 (b) reveals a very typical current-structure-interaction VIM phenomenon. In particular, the lock-in region ranges from V_r =5 to 10, in which the maximum A_{cy}/D characterised by VIM reaches a value of 0.41 at V_r =8.1. At real sea conditions, the full-scale current velocity in the lock-in region can vary from 1.0 to 1.45 m/s. Therefore, it is expected to observe significant platform motion within this velocity range.

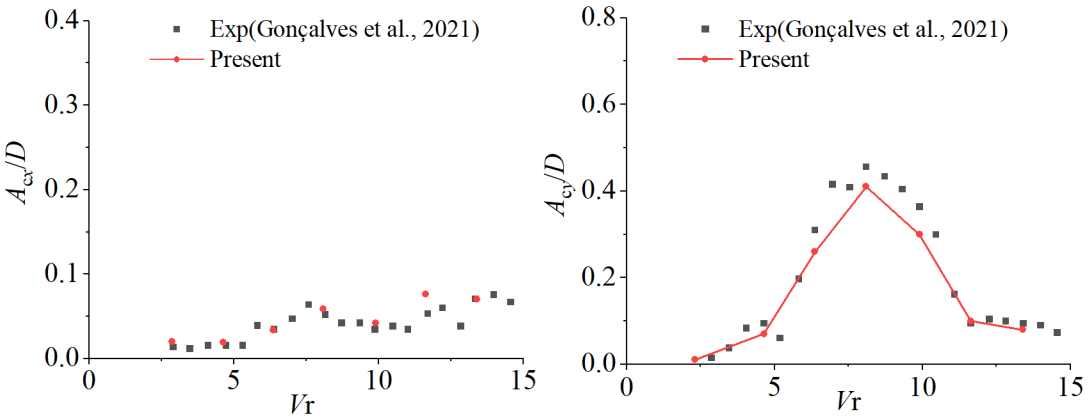

(a) (b)

Figure 6.4 Variation of the motion response amplitude with V_r in (a) IL direction and (b) CF direction for OC4 platform with current-only condition

The added mass coefficient in the CF direction (C_a) also agrees well with the experiment as shown in Figure 6.5, which is defined as $C_a = -R\left\{\frac{fft[F_y(t)]}{fft[\ddot{y}(t)]}\right\}/m$ where $F_y(t)$, y are the hydrodynamic force and displacement in CF direction, respectively. $R()$ represents the real part of the complex number, and fft represents the FFT operator. The large and positive values of C_a with V_r <9.9 denote the synchronisation with the

vortex shedding frequency. As the velocity increases, C_a decreases and becomes negative after $V_r > 9.9$, indicating the end of resonance.

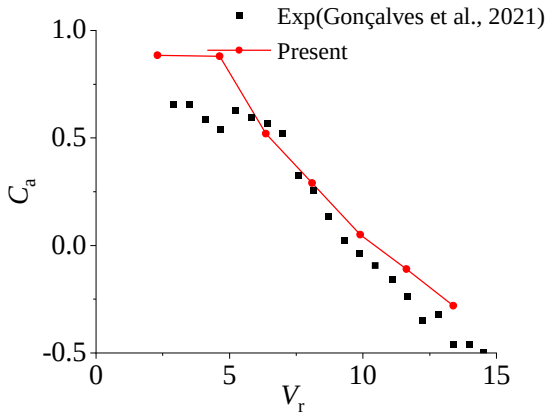

Figure 6.5 Variation of added mass coefficient with V_r in CF direction for OC4 platform with current-only condition

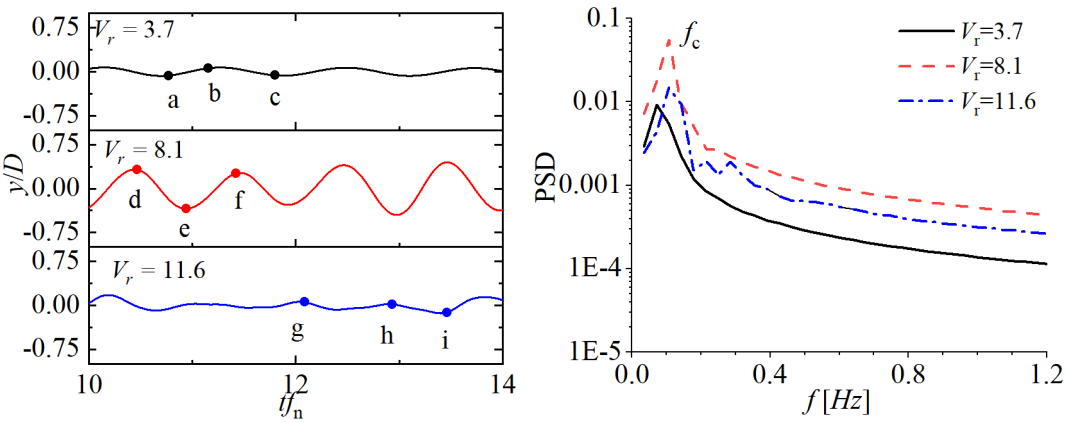

Figure 6.6 Time-series and FFT analysis of CF motion response for V_r = 3.7, 8.1 and 11.6 for OC4 platform with current-only condition

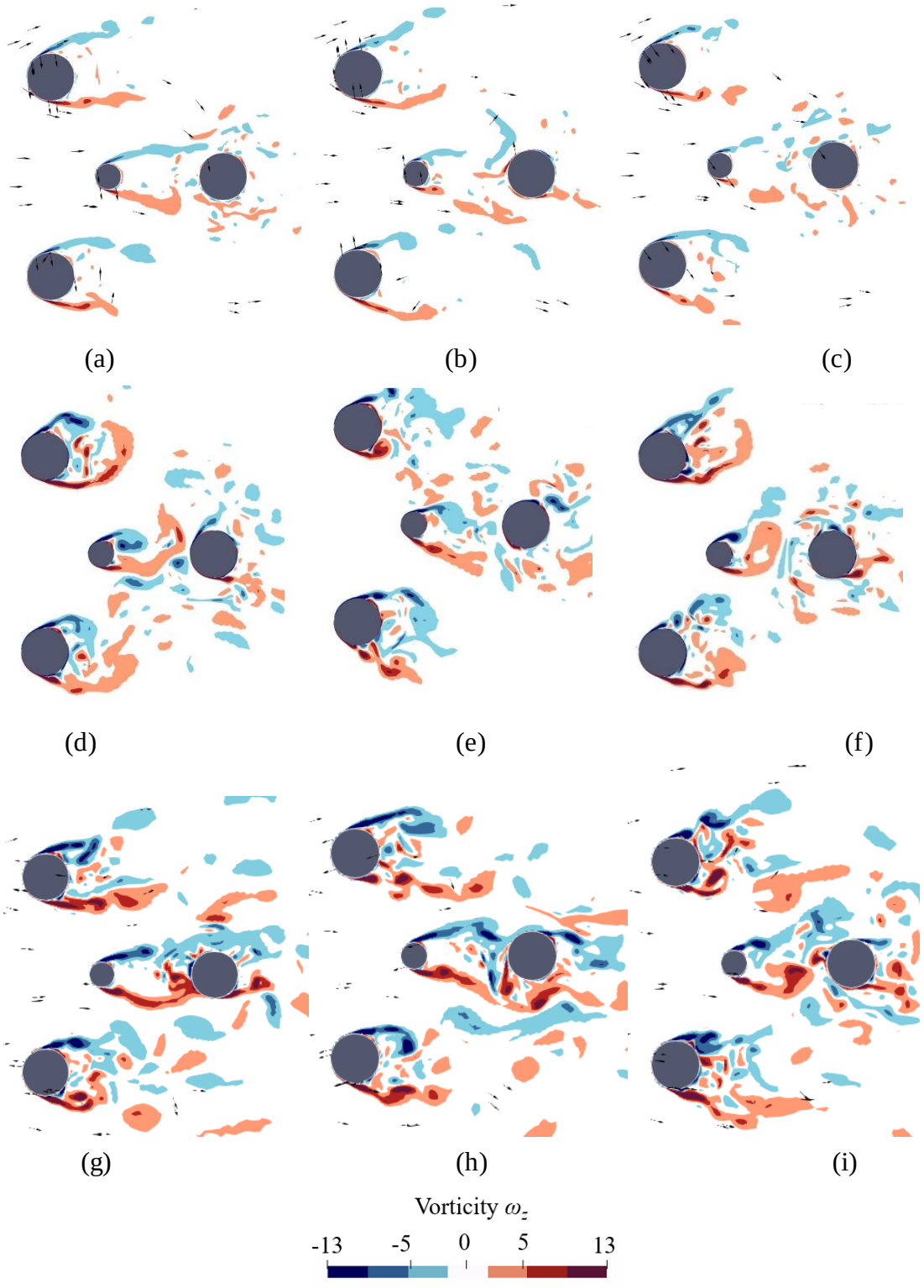

Figure 6.7 Contours of spanwise vorticity ω_z at the section with z=-0.1m at the time instants shown in Figure 6.6 at V_r=3.7 (a)-(c), V_r=8.1 (d)-(f) V_r=11.6 (g)-(i) for OC4 platform with current-only condition.

The resonance in lock-in region is also reflected by the time-series and the

corresponding FFT analysis shown in Figure 6.6, where a dominant VIM motion can be observed at V_r = 8.1 in lock-in region. With a smaller V_r = 3.7, the periodic motion exists but has a lower frequency and smaller amplitude. At larger V_r beyond the lock-in region, the amplitude is small but has higher-order frequency components.

The vorticity field is plotted and examined in Figure 6.7 to reflect the typical vortex shedding associated with the VIM phenomenon. It is seen that with the increase of V_r, the vorticity becomes stronger, and the flow field becomes more irregular. Within the lock-in region at V_r=8.1 (Figure 6.7 (d)-(f)), the vortices generate alternately from both sides of the column and then shed from either side of the column at a frequency equal to the lock-in frequency f_n. An anti-clockwise vortex is observed when the platform reaches y_{min} in Figure 6.6 (e), and another anti-clockwise vortex is observed while a clockwise vortex is shed when y_{max} at (f), revealing a typical 2P mode for the wake in VIM. At V_r = 3.7, no obvious vortex shedding is observed, which is associated with a smaller motion in the CF direction.

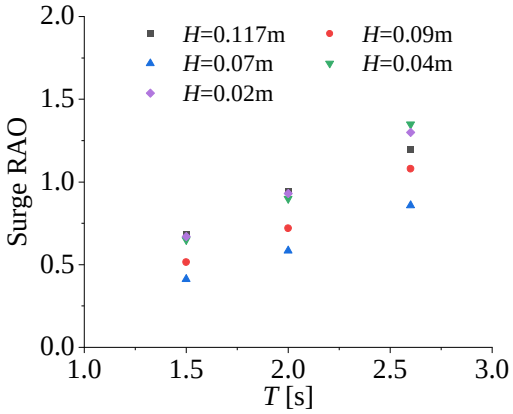

Figure 6.8 Variation of surge RAOs with wave periods of OC4 platform for wave-only condition

In addition to the above current-only condition, the wave-only condition is also examined for OC4 to set up a baseline model for the subsequent wave-current investigations. Figure 6.8 shows the predicted surge RAO with various wave heights H and wave periods T. It is seen that the RAO increases with T, as the platform's structure

natural period aligns more closely with it, increasing the motion response. The response amplitude operator (RAO) relationship with H is rather complex due to enhanced mooring forces with increasing H, as well as the higher nonlinearity with larger H. Therefore, the variation follows a nonlinear trend.

6.2.1.2 IDEOL Platform

The IDEOL platform is analysed starting with the current-only scenarios. The response amplitudes in IL and CF directions are shown in Figure 6.9, with the parameters summarised in Table 6.4. It is seen that the barge-type platform has an even smaller IL motion compared with the OC4 platform. The motion in the CF direction is also relatively smaller. For the largest reduced velocity of V_r=9.6 (U=2.3 m/s at full-scale), the maximum A_{cy}/D is less than 0.2. Only at this largest V_r, the periodic platform motion characterised by VIM becomes notable, as shown in the time-series plots in Figure 6.10.

Compared to the OC4 platform, the VIM phenomena are less profound compared to its dimension, which might be due to several reasons. Firstly, the most pronounced VIM for the SS platform occurs around V_r=8.1. Comparatively, for the IDEOL platform to experience significant VIM, it requires a much higher reduced velocity of at least 10.0 or even higher, as can be seen in Figure 6.9. Thus, the VIM of the IDEOL platform is not obvious. In addition, the aspect ratio of the IDEOL platform is 0.17, which is much smaller than that of 1.64 for the OC4 platform. This finding agrees with the research by Goncalves et al. that the response of CF motion of a cylinder weakens as its aspect ratio decreases. The VIM could be even negligible if the aspect ratio is less than 0.3 (Gonçalves et al., 2013).

Table 6.4 Wave and current parameters for IDEOL platform testing

Wave parameters						**Current parameters**			
T[s] Scaled 1:50	1.6	1.8	2	2.2	2.4	U [m/s] Scaled 1:50	0.20	0.26	0.32
T[s] Full-Scale	11.3	12.7	14.1	15.6	17.0	U [m/s] Full-scale	1.4	1.8	2.3
						Vr	6.1	8.0	9.6

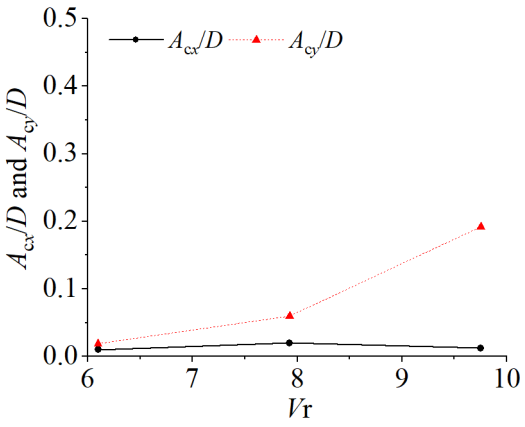

Figure 6.9 CF and IL motion amplitude versus reduced velocity for IDEOL platform with current-only condition

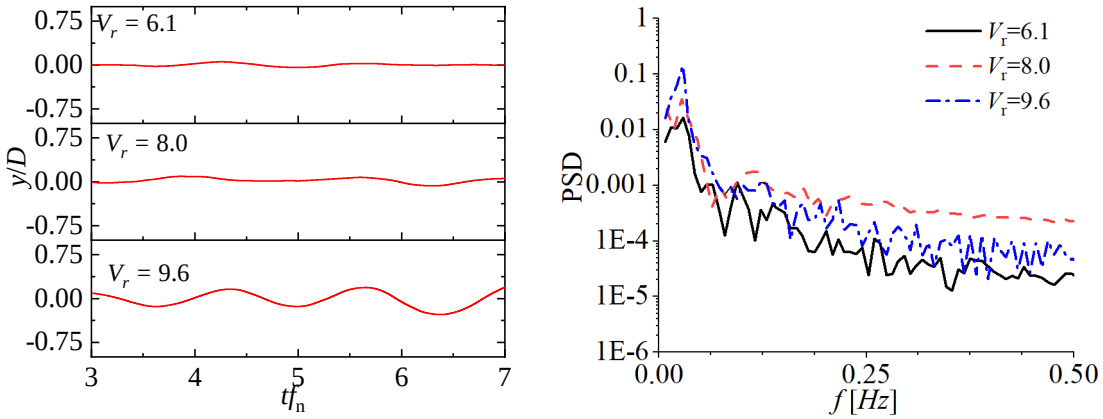

Figure 6.10 Time-series and FFT analysis of CF motion response for V_r = 6.1, 8.0 and 9.6 for IDEOL platform with current-only condition

Then, the dynamic response of the IDEOL platform for the wave-only conditions is studied for a series of wave periods (Table 6.4). In the experiment, the wave heights varied from 2.5 m to 7.5 m. In this validation, an intermediate wave height of H=5 m is chosen. Figure 6.11 shows the predicted RAOs in comparison with the experiment (EXP) and numerical modelling (SIM) data. In the SIM studies, the potential-flow-based method is used, the hydrodynamic coefficient is obtained by Ansys Aqwa software and the dynamic response is calculated using DNV-GL's Bladed software package to couple the hydrodynamic loads. The RAOs are normalised by the wave amplitude for heave and surge motions, while the pitch response is normalised by $kH/2$

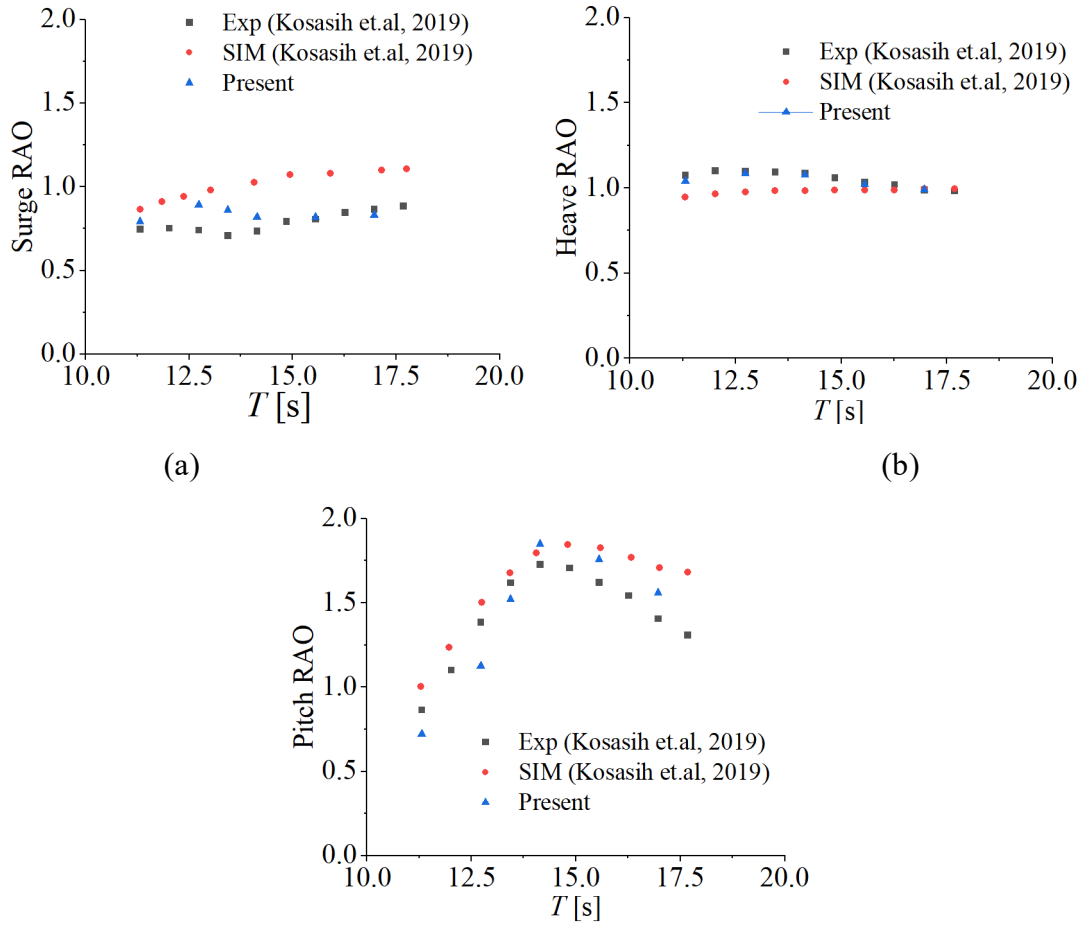

Figure 6.11 Variation of RAOs with wave periods with H=5 m for (a) surge (b) pitch (c) heave for IDEOL platform with wave-only condition

Figure 6.12 Wetted surface changes on the IDEOL platform at different sampling time (a) t/T=3.5 and (b) t/T =4.0 with H=5 m and T=14.1 s

For the wave periods studied, an averaged RAO for the surge and heave are typically

0.84 and 1.0, respectively, from CFD and EXP. However, the pitch RAO reveals an initial increasing and then decreasing trend. The peak RAO occurs at T=14.1s. It is evident that better agreement between the present CFD predictions and the experimental data has been reached than the results obtained from the potential-flow-based tool (SIM). One explanation for the improved accuracy of CFD modelling over the potential theory method is that the latter linearises the wave-air free-surface equation at the time-averaged positions. Therefore, the nonlinear effect of fluid-structure interaction, represented by the changing wetted surfaces, is not very well captured. As shown in Figure 6.12, the green water can be observed clearly, showing the changing wetted surface. Also, for the CFD modelling, tuning the viscous damping to fit the experiments is not required, which is usually needed for a viscous-modified potential flow model.

6.2.2 VIM in Both Waves and Current at Different Angles

To concentrate on the influence of waves on VIM, the following studies will be focused on the OC4 semi-submersible platform.

It is well known that in a real sea state, current and wave do not always exist alone, and the extreme loading condition for a FOWT platform may occur with specific combinations of wave and current. In the study on a colinear wave-current condition, it was found that the current-induced CF motion can be mitigated with the addition of waves, depending on V_r under investigation. This conclusion is consistent with others' findings. Some other studies also found that if the wave and current were non-colinear, the mitigation became less obvious (Finnigan et al., 2005; Saito et al., 2012). To investigate this phenomenon, this section is dedicated to examining the impact of the angle of the flow direction between current and wave (θ) on the platform's dynamic responses. Three angles varying from θ=0° to 90° are selected. Typical wave period and wave height are T =2.0 s, H=0.09 m. The current speed varies from 0.05 to 0.20 m/s, leading to the reduced velocity V_r ranging from 2.3 to 11.6, as shown in Table 6.5.

Table 6.5 Current parameters for wave-current interaction with OC4 platform on the effect of angles

U [m/s] Scaled 1:73	0.05	0.08	0.11	0.14	0.17	0.20
U [m/s] Full-scale	0.43	0.68	0.94	1.20	1.45	1.70
Vr	2.30	3.7	4.6	8.1	9.9	11.6

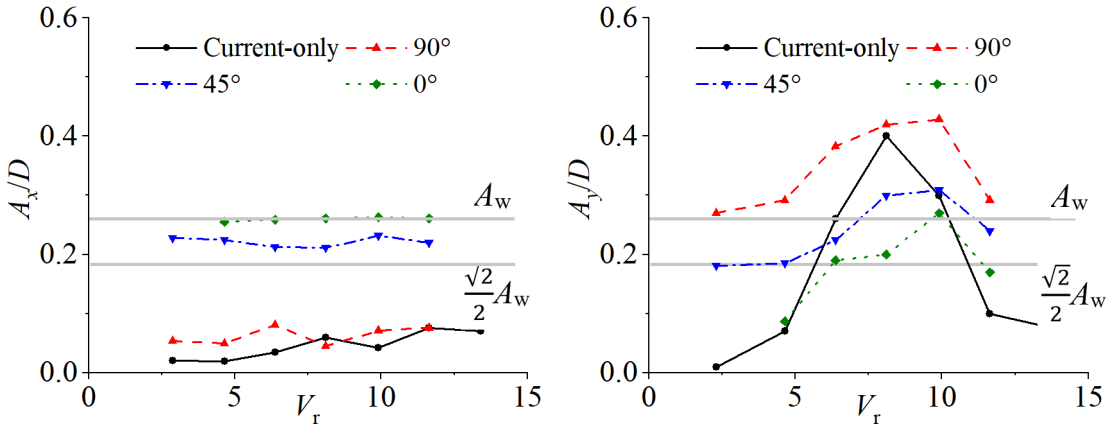

(a) (b)

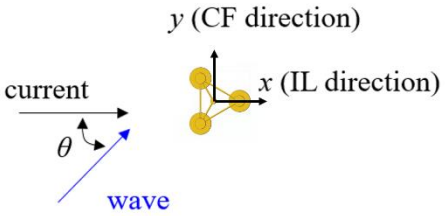

(c)

Figure 6.13 Variation of motion response in wave-current condition with V_r and θ (H=0.09m and T=2.0s) (a) IL direction and (b) CF direction (c) is the sketch of the direction of current and wave. The horizontal line (A_w) is the amplitude shown in Figure 6.8 for the wave-only test, and $\sqrt{2}/2A_w$ denotes the motion components at θ=45°

The responses of the platform are shown in Figure 6.13 with different angles. Given a combined wave-current condition, the IL motion varies a little with reduced velocity, indicating that varying current speed does not affect IL motion significantly, as shown

in Figure 6.13 (a). However, the IL motion is noticeably impacted by angle variation (θ). In fact, with $\theta = 0°$, A_x/D is the largest and close to A_w in the wave-only cases, while $\theta = 90°$, A_x/D is the smallest and close to that in the current-only cases. Unlike the above IL response, CF motion varies significantly with reduced velocity and the peak values can be clearly captured (Figure 6.13 (b)). As the angle θ increases, A_y/D increases across all V_r. Therefore, for safety design purposes, it is recommended to pay more attention to those cases with $\theta = 90°$. Beyond the lock-in region, with $\theta > 0°$, A_y/D are greater than those observed in the current-only cases and close to A_w. However, within the lock-in region, with increasing θ to 90°, A_y/D is always larger than that of either wave-only or current-only. The large CF motion in this wave-current condition is induced by a non-zero wave-current angle. As the velocity components along the y-axis increase with the angle, CF response increases due to the enlarged inertia wave force acting on the platform. In addition, the flow field and VIM are altered with a combined wave-current interaction.

To examine the individual effect of current and wave on the motion response, the above CF motion (A_y/D) is decomposed:

$$a_c = \left|Y\left(f_c\right)\right| \quad \text{and} \quad a_w = \left|Y\left(f_w\right)\right| \tag{6.1}$$

where $|Y(f)|$ is the FFT of CF motion. a_c and a_w are the motion amplitudes induced by current and wave, f_c and f_w are the peak frequency corresponding to VIM and the wave. The decomposed a_w and a_c for $\theta = 45°$ and 90° are shown in Figure 6.14 (a) and (b). For both angles, a_w almost remains unchanged with V_r. As a result, the contribution of the wave to the total response is nearly constant with varying V_r.

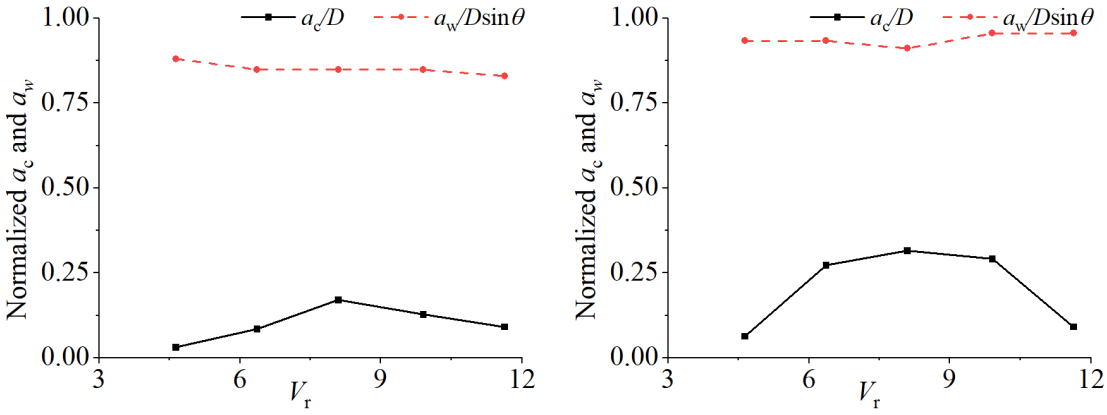

Figure 6.14 Variation of decomposed CF motion excited by current (a_c) and waves (a_w) (H=0.09m and T=2.0s) at angles of (a) 45° and (b) 90°, a_c is normalised by characteristic dimension D and a_w is normalised by wave amplitude multiplied by $\sin(\theta)$

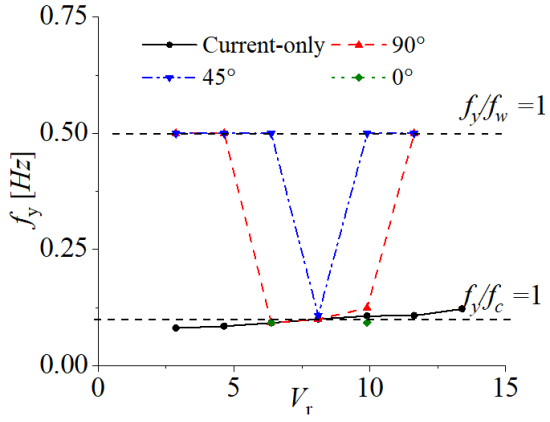

Figure 6.15 Variation of dominant frequency with V_r (H=0.09m and T=2.0s)

However, the variation of a_c with V_r resembles the pattern of current-only cases, with the peak amplitude occurring at V_r=8.1 and decreasing beyond this V_r. This indicates that the VIM effect still exists even with waves. Hence, the response peaks in the wave-current cases depicted in Figure 6.13 are primarily due to the current's contribution within the lock-in region. A comparison between Figure 6.14 (a) and (b) indicates that larger θ leads to an amplified VIM. It is also worthwhile to note that with a larger angle, the a_c near the peak value at Vr=8.1 also increases, which means the VIM becomes significant for a wider range of reduced velocities with the addition of waves.

The effects of angle are also reflected in dominant frequencies, as analysed in Figure 6.15. For current-only cases, the dominant frequency along y direction f_y increases with V_r and locks onto fc in the lock-in region, leading to a large motion response. For cases with $\theta=0^o$, f_y is the same as that of current-only. However, for those with $0^o<\theta<90^o$, outside the lock-in region, f_y is close to f_w, indicating the platform's motion is dominated by waves. Within the lock-in region $f_y=f_c$, the resonance occurs. With an increasing θ, the lock-in region becomes wider, revealing a more vulnerable platform due to large-scale motions under a wide range of current velocity. The time-series distribution of y/D and their FFT analysis displayed in Figure 6.16 reinforce the above observations. In fact, two dominant frequencies appear in relation to f_c and f_w. Outside the lock-in region, the low-frequency components are not as prominent compared to the high-frequency components. Within the lock-in region, the low-frequency component is substantially large and increases with angles. In addition to the above dominant frequencies, other spikes are also noted, which might be caused by the nonlinear coupling between the vibration of the platform and fluid flow. The difference frequency $f_{diff}=f_w-f_c$ and sum frequency $f_{sum}=f_w+f_c$ exist, although with a relatively small magnitude, which is also noticeable in the cases with 90° with their magnitudes increasing with angle.

Figure 6.17 to Figure 6.18 present the vorticity field under the combined waves and current conditions for $\theta=0^o$ and $\theta=90^o$ at $V_r=8.1$. Unlike the current-only cases, the fluid field with waves for $\theta=0°$ in Figure 6.17 becomes chaotic, and its precise pattern is hard to discern. It displays the characteristics of cylindrical structures interacting with both steady and oscillatory flow. The steady flow leads to a typical VIV vortex shedding, while the oscillatory flow leads to a different shedding pattern. The specific appearance of the pattern highly replies to the Keulegan-Carpenter number (KC number) (Sarpkaya, 1986), which describes the relative importance of the drag forces over inertia forces in an oscillatory flow. In a pure oscillatory flow scenario, VIM only occurs at a large KC, by the hydrodynamic lift force in the CF direction.

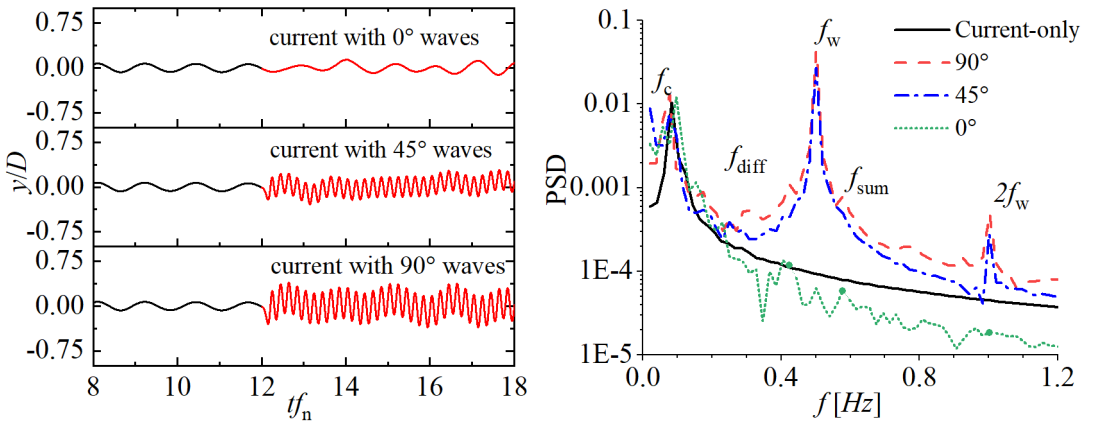

(a)

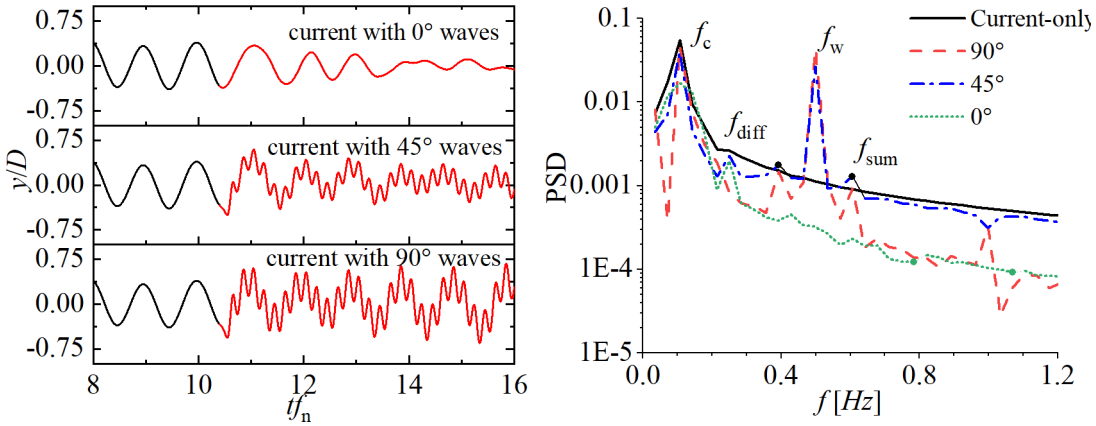

(b)

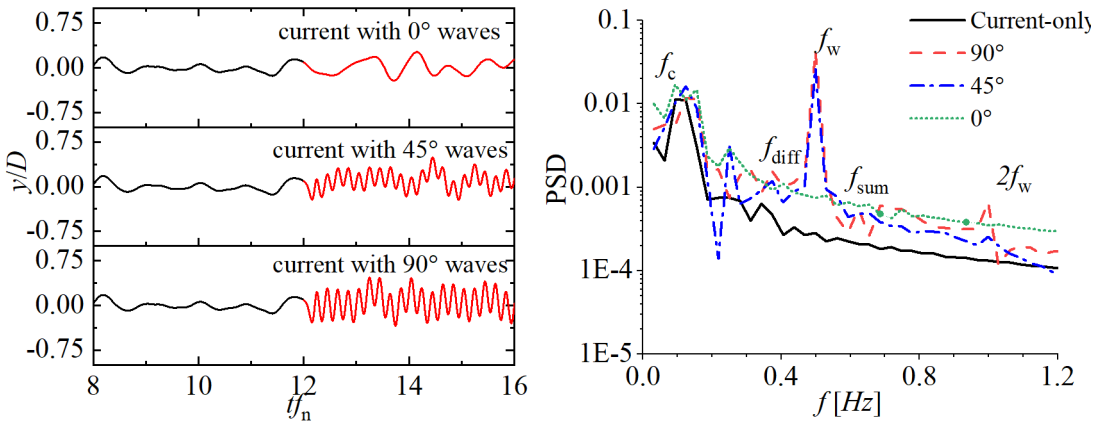

(c)

Figure 6.16 Time-series and FFT analysis of CF motion response in wave-current condition (H=0.09m and T=2.0s) of (a) V_r=4.6 (b) V_r=8.1 (c) V_r=11.6. In the time series, the black line represents the response caused by the current only, while the red line indicates the addition of waves to the current.

$$KC = \frac{U_M}{f_w D} \tag{6.2}$$

where U_M is the maximum flow velocity in the IL direction. At time instants of (c) to (e), the vortices are shed from both sides of offset columns (the larger columns) and move downstream, having a symmetric pattern. The vortex shedding frequency of this process is 1/2 seconds, much smaller than the lock-in frequency, but is identical to the wave frequency f_w, indicating that the symmetric vortex pair is dominated by oscillatory flow/waves. When oscillatory flow passes a cylinder at a small KC number between 1.6-4.0, the vortex separation begins to occur as a pair of symmetrically attached vortices (Sumer, 2006), as also observed for an offset column with KC=2.1. Two vortex pairs are generated in one cycle, one from the previous half period where flow passes in one direction. Another pair is generated from the second half period when the oscillatory direction reverses. In the present case for wave-steady current, only one vortex pair generates within one cycle and is flushed downstream, showing a 2T mode (Figure 6. 17 (b)), where three vortices are seen to be shed from the lower offset column. This mode was also observed in Zhao's study of steady and oscillatory currents around a cylinder (Zhao et al., 2013). The 2T mode is observed when the motion displacement reaches its maximum at the steady flow-dominated frequency. Away from this time period, the double pair mode dominates (Figure 6.17 (a) and (d)). For the central smaller column, the vortex shedding is also dominated by waves but with a different pattern than the offset column. The KC number for the central column is 3.8, and the vortex is seen shed alternatively from one side of the column with an asymmetric pattern. Typically, this pattern occurs for a pure oscillatory with a cylinder when KC > 4.0 (Sumer, 2006). However, in cases where a steady flow is present, this pattern is also observed at a smaller KC number.

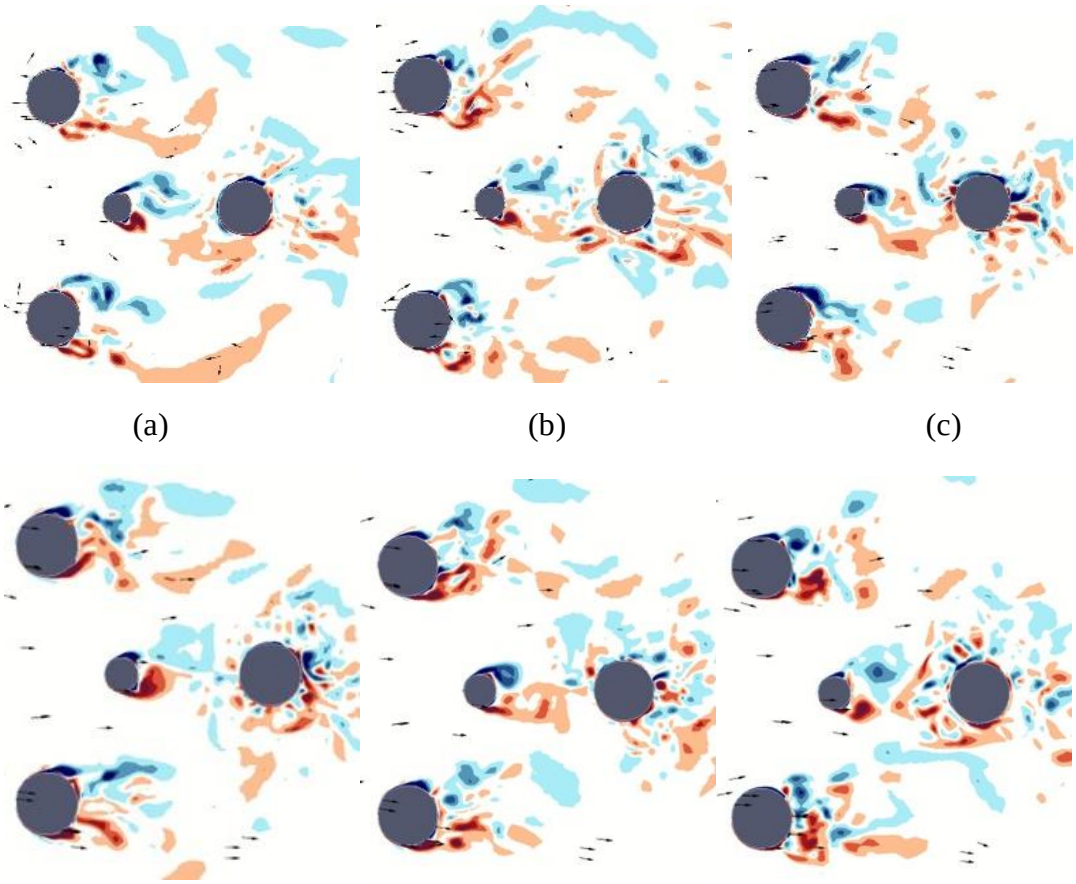

Figure 6.17 Contours of spanwise vorticity ω_z at the section with z=-0.1 m and θ=0° in wave-current condition (H=0.09 m and T=2.0 s) at different time instants at V_r=8.1 for (a) to (f), (g) is the corresponding time series, on top of which is the sketch of the angle between wave and current

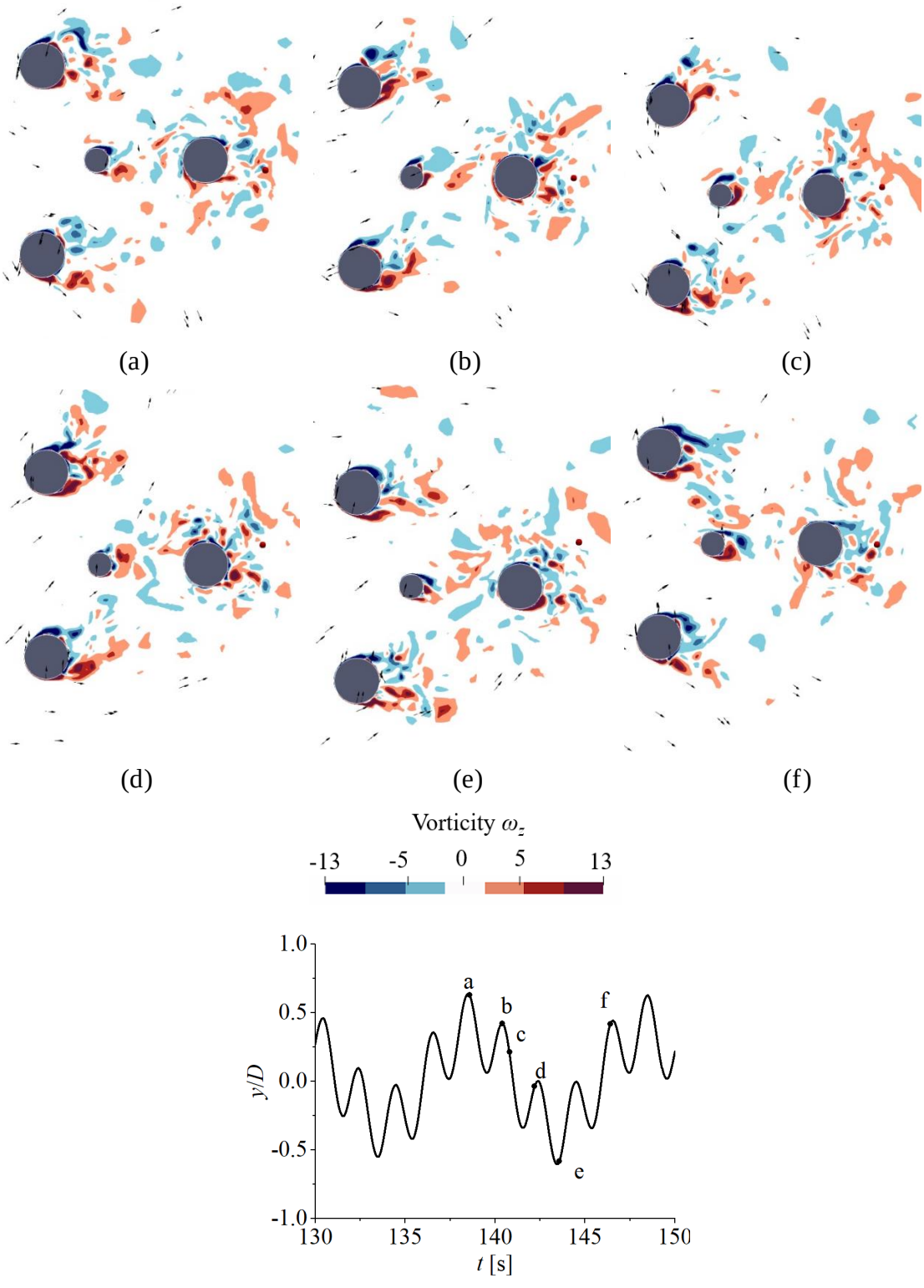

Figure 6.18 Contours of spanwise vorticity ω_z at the section with z=-0.1m and θ= 90° in wave-current condition (H=0.09 m and T=2.0 s) at different time instants from (a) to (f), at V_r=8.1, (g) is the corresponding time series, on top of which is the sketch of the angle between wave and current

It should be noted that the symmetric vortex pair doesn't provide net force along the CF direction, but it interferes with the vortex formed by the steady flow. Moreover, the flow in the -x direction caused by the waves mitigates the generation of a complete vortex due to a steady current, leading to a possible reduction in crossflow motion.

Compared to the cases with θ=0°, the vortex field for θ=90° in Figure 6.18 shows more asymmetric characteristics. Since the waves propagate along the y-axis, the flow along the x-axis is less affected. As a result, when a vortex forms, it is periodically stretched and carried by oscillatory flow in the CF direction, causing it to split into smaller vortices. At $(y/D)_{max}$ and $(y/D)_{min}$ in Figure 6.18 (a) and (e), a large vortex is generated on one side of the offset column but breaks down into small eddies. The vortex from the central small column presents a 2S mode with one clockwise and one counter-clockwise vortex detaching from the central column within one cycle. Moreover, the shed vortex not only moves downstream but also along CF direction, bringing it closer to the platform and increasing the chances of encountering between the clockwise and counter-clockwise vortices, thereby changing the motion frequency. This is clearly depicted in Figure 6.18 (b) to (c), where V_y is positive, while V_y is negative in Figure 6. 18 (f). It is clearly indicated that when the wave and current are colinear, oscillatory flow mitigates the generation of a complete vortex due to the current. Thus, the VIM is mitigated. The disturbed vortex field by the symmetric vortex from the oscillatory flow contributes to this trend.

The platform motion trajectory with different θ and V_r is shown in Figure 6.19. For current-only cases, the platform experiences significant motion displacement within lock-in region at V_r=8.1. The predominant motion is along y-axis and the movement along x-axis is limited. This pattern of movement is similar to that in the study on a four-square column semi-submersible platform, where a typical eight-shaped trajectory is not found (Gonçalves et al., 2012).

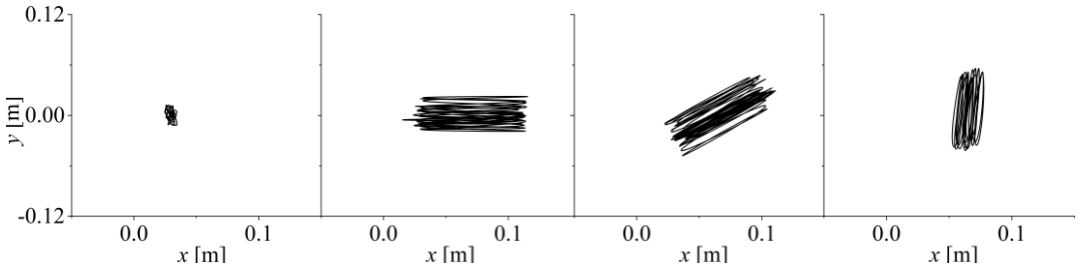

(a)

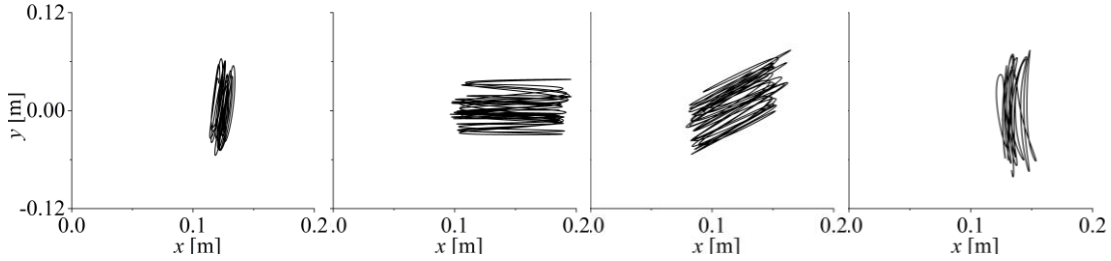

(b)

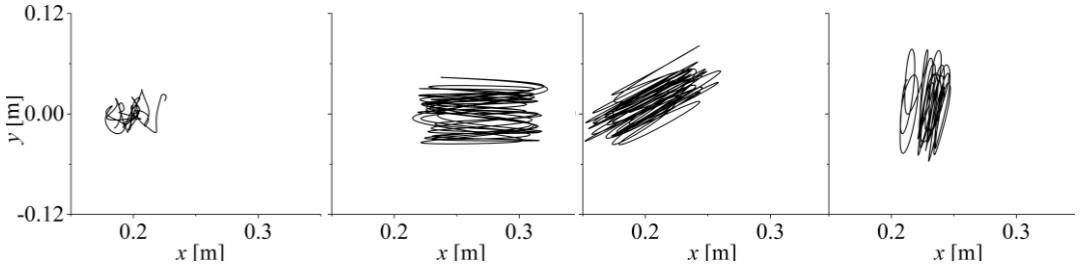

(c)

Figure 6.19 The trajectory of the platform with current-only, wave-current condition (H=0.09m and T=2.0s) with θ=0°, 45° and 90° at (a) Vr=4.4 (b) Vr=8.1 (c) Vr=11.6

6.2.3 Response for θ=90° with different wave parameters

Previous studies on colinear wave-current-structure interaction indicated that the CF response was not only affected by the reduced velocity but also influenced by the wave parameters, i.e., the wave height and wave period (Gonçalves et al., 2013, 2020). In addition, our findings from Section C for various θ values reveal that the largest CF motion occurs at θ=90°. In this section, the investigation is focused on the study of wave-current-platform interaction at θ=90° for a series of wave heights and wave periods (Table 6.6). The reduced velocity is fixed at V_r=8.1, where the strongest VIM occurs.

The effect of wave parameters on the platform's response is shown in Figure 6.20. It is seen that IL motion is relatively small compared with the large platform dimensions. The overall CF motion is larger than that observed in the current-only cases and increases with wave period T. The motion response is also influenced by wave height H. As H increases, A_y/D approaches that of wave-only cases. A_y/D decreases monotonically with H for T=1.5s. However, peaks are observed for T=2.0s and T=2.6s; the peak A_y/D is seen at H=0.04m and 0.07m, respectively. This concludes an important finding, e.g. waves with small wave height may also lead to large platform motion under wave-current conditions.

Table 6.6 Parameters for wave-current-platform interaction with OC4 platform on the effect of wave conditions with θ=90°

Wave height H [m] Scaled 1:73	0.116	0.09	0.07	0.04	0.02	Wave period T [s] Scaled 1:73	1.5	2.0	2.63
H [m] Full-scale	8.4	6.5	5.1	3.0	1.5	T [s] Full-scale	12.8	17.6	22.6

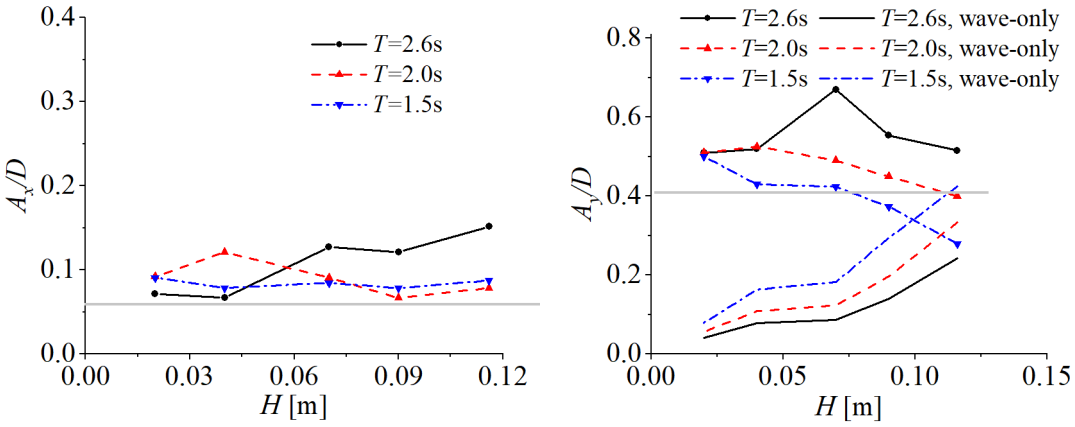

(a) (b)

Figure 6.20 Response amplitude in wave-current condition with different wave heights and periods along (a) IL direction and (b) CF direction, with θ=90°. The grey

line indicates the motion amplitude with current-only.

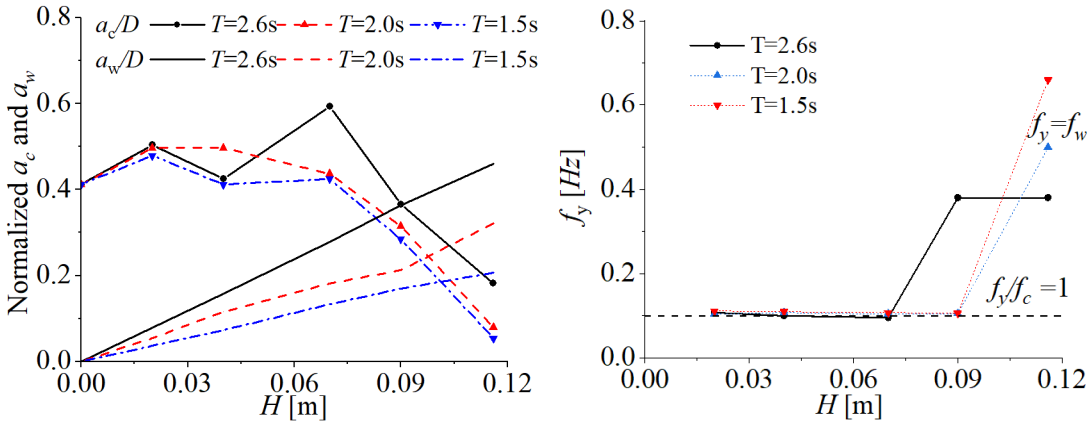

Figure 6.21 (a) Decomposed motion amplitude excited by current and waves (b) Dominant frequencies at V_r=8.1 with different wave parameters

This can be further inferred by decomposing the motion amplitude shown in Figure 6. 21 (a). For cases with small H <0.06m, the motion induced by current, indicated by a_c, varies between $0.4 < a_c/D < 0.5$, which is larger than that observed in current-only cases, indicating an enhanced VIM effect. However, for H>0.06m, a_c decreases significantly with increasing H, indicating a mitigated VIM effect by waves. Meanwhile, a_w becomes dominant after H>0.11m, and the motion is locked onto f_w rather than f_c, as shown in Figure 6.21 (b). The shift in the predominant influence from currents to waves can also be observed from the time histories of y/D and FFT plots in Figure 6.22. As H increases, the low-frequency motion induced by the current becomes less prominent. The FFT analysis indicates the appearance of difference frequency and sum frequency components, especially for θ=90°. These frequencies are only excited when the contribution of current and wave to the system's energy is roughly equivalent. As H increases, the energy at f_c weakens, causing the above two frequencies to become less significant.

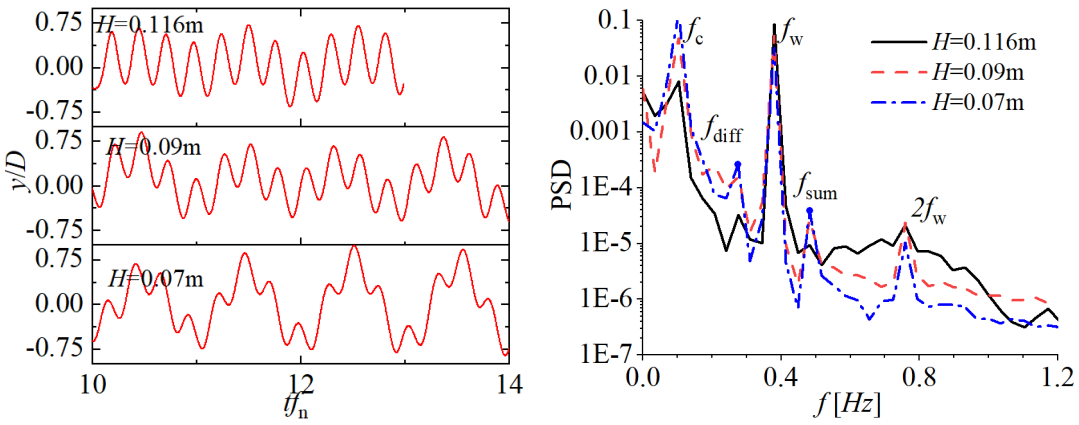

(a)

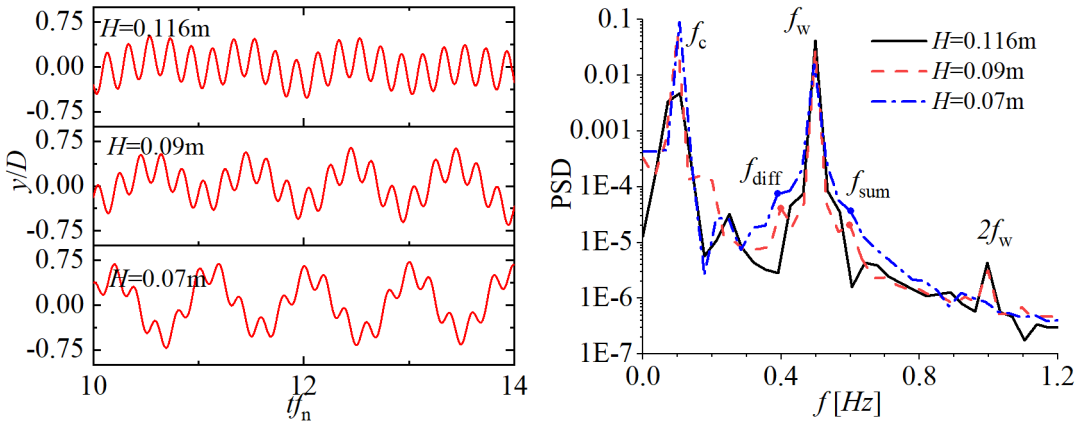

(b)

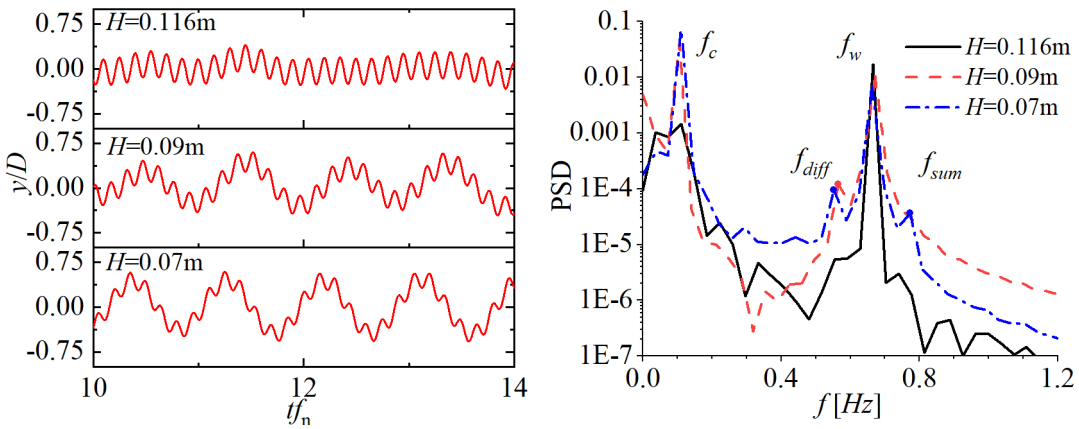

(c)

Figure 6.22 Time-series and FFT analysis of CF motion response in wave-current condition with θ=90° at V_r=8.1 with (a) T=2.6s (b) T=2.0s (c) T=1.5s.

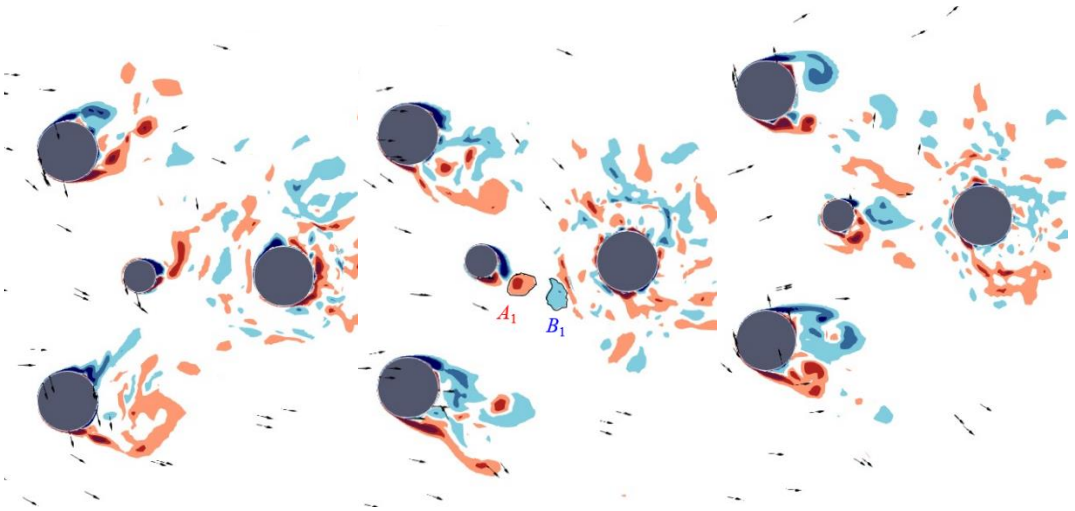

(a) (b) (c)

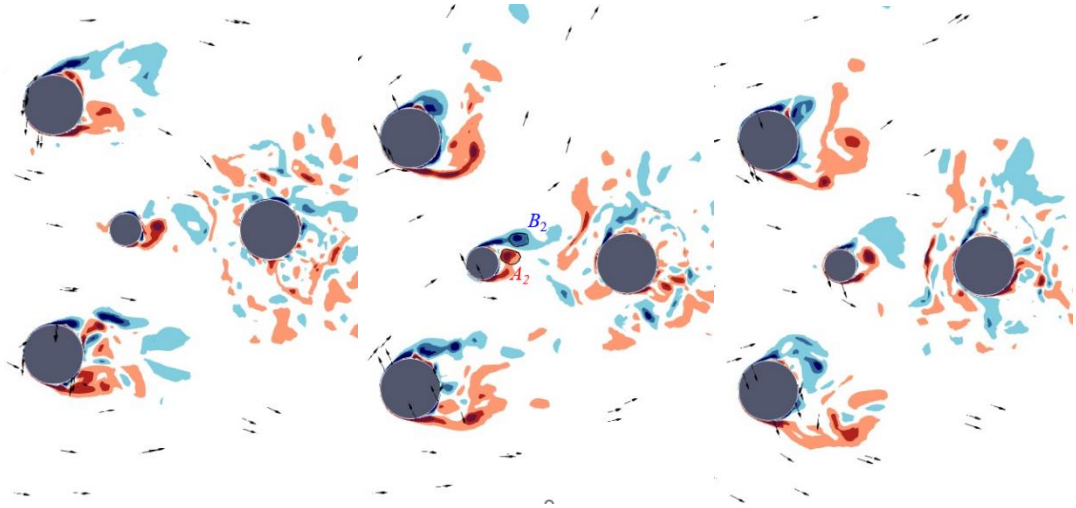

(d) (e) (f)

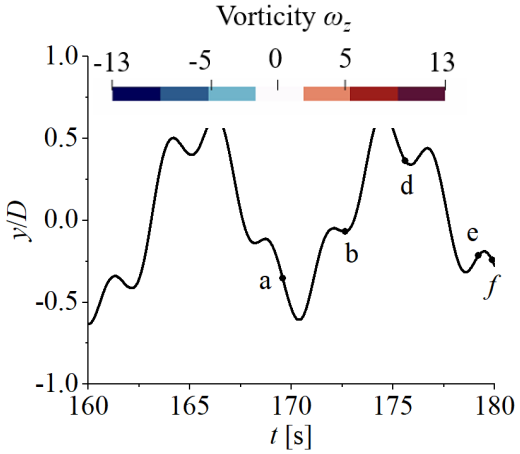

(g)

Figure 6.23 Contours of spanwise vorticity ω_z at the section with z=-0.1m with T=2.6s and H=0.04m in wave-current condition with θ=90° at V_r=8.1, at different time instants from (a) to (f), (g) is the corresponding time series

The differences in wave parameters are also reflected in the vorticity field shown in Figure 6.23 for H=0.04m. Compared with larger H=0.09m in Figure 6.18, the vortex herein is less disturbed by waves, thus leading to a larger CF motion response. The vortex shedding appears in a 2P mode, with two pairs of vortices shed in one cycle, such as the vortex A_1 and B_1 at instant b and A_2 and B_2 at instant e. As the wave period decreases, the vortex flow exhibits greater levels of turbulence and disorder, as seen in Figure 6. 24 (a) and (c). Additionally, the vortex motion is observed to occur in close proximity to the structure with a smaller T.

According to Iwagaki and Asano (Iwagaki and Asano, 1984), velocity ratio can be an important parameter in the study of a combined wave-current environment. It is defined as:

$$\alpha' = \frac{\sigma_U}{\sigma_U + U} \tag{6.3}$$

where U and σ_U are the current velocities and the particle velocity amplitude in waves. With this definition, α' quantifies whether a flow is viscous or inertial dominant, and thus α'=1 and 0 represent a wave-only or a current-only scenario, respectively. A previous study by Gonçalves et al. (Gonçalves et al., 2012, 2013) for a semi-sub platform revealed that VIM is governed by both viscous and inertia forces. The threshold between the viscous and inertia zones can be quantified by:

$$KC = \frac{1 + C_a}{C_D} \pi(\alpha')^2 \tag{6.4}$$

where C_a and C_d is the added mass and drag coefficient, which are 0.63 and 0.61 for OC4 Deepcwind platform respectively (Robertson et al., 2014).

Figure 6.25 plots velocity ratio (α') as a function of KC number with θ=90°. For the wave parameters examined, most cases are within a regime where VIM is obvious, thus associate with a large CF motion. For those falls into inertia force regime, the response is mainly wave-dominant.

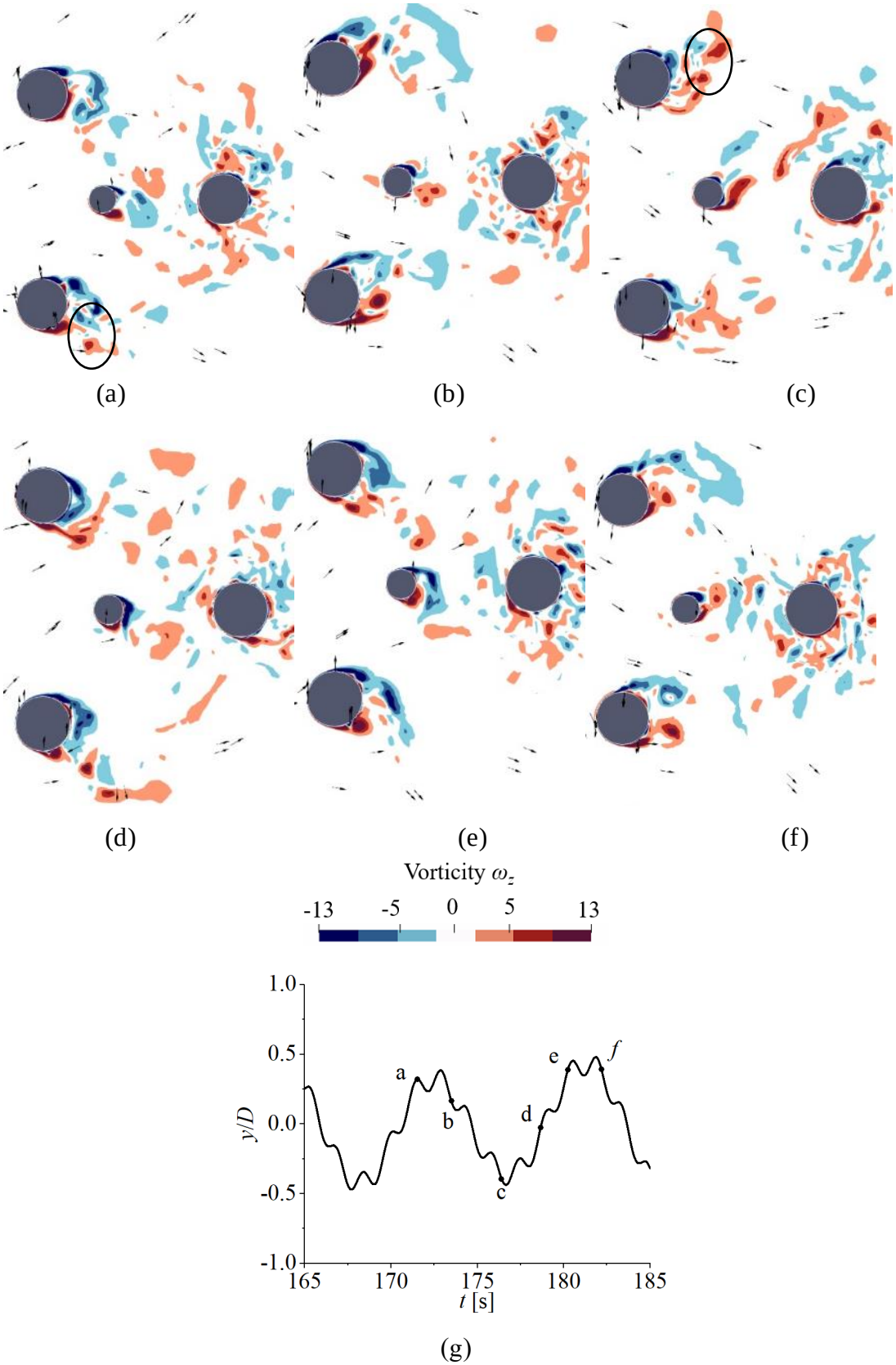

Figure 6.24 Contours of spanwise vorticity ω_z at the section with z=-0.1m with T=1.5s and H=0.04m in wave-current condition with θ=90° at V_r=8.1, at different time instants from (*a*) to (*f*), (g) is the corresponding time series

It should be noted that falling in the drag zone does not correspond to larger motion. For instance, the cases with a V_r beyond the lock-in region have a very small velocity ratio, and should be located in the drag zone. However, the absence of resonance leads to a smaller VIM amplitude. The interaction effect factor (*IEF*) is normally used to which is defined as

$$IEF = \frac{stddev(y_{wc})}{stddev(y_w) + stddev(y_c)} \tag{6.5}$$

where y_{wc} is the CF motion in a wave-current combined environment, y_w and y_c are the CF motion in wave and current independently, and *stddev* means the standard deviation function. *IEF* can be viewed as the ratio between the amplitude of y_{wc} and y_w+y_c. For larger H and smaller T, the IEF becomes lower than 0.75, as shown in Table 6.7, suggesting that the interaction of waves and current mitigated the sum of their original motion. For small H and large T, the *IEF* is the largest and close to 1, which means the motion can be considered as the sum of the motion in waves and current alone. For some cases, the *IEF* exceeds 1 and reaches 1.35 when H=0.07 m and T=2.6 s, indicating that the motion is enhanced by the wave-current interaction. Special attention should be paid to those cases when the extreme conditions for the platform are considered during the design process.

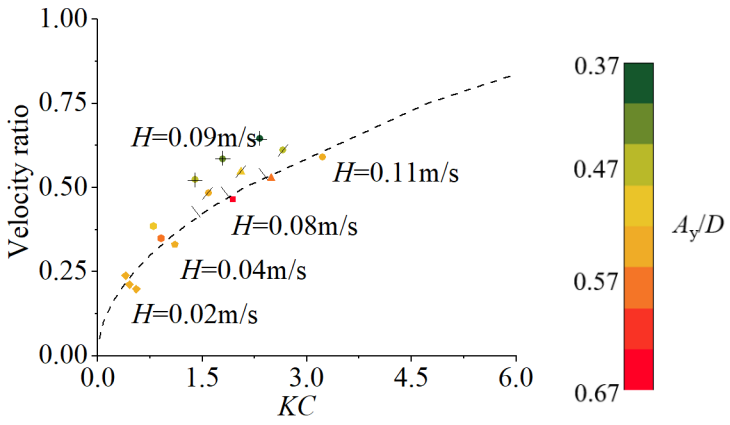

Figure 6.25 *α'-KC* plot with θ=90° denoting predominant region of either drag or inertia force in wave-current condition for OC4 platform. The point with colour denotes CF motion response. The black line denotes the threshold between the drag range and the inertia range.

Table 6.7 *IEF* with different wave parameters for θ=90° and V_r=8.1

H[m]/*T*[s]	1.5	2	2.6
0.02	1.02	1.09	1.13
0.04	0.75	1.01	1.06
0.07	0.72	0.92	1.35
0.09	0.53	0.74	1.01
0.116	0.34	0.54	0.79

6.3 Concluding Remarks

This chapter explores the fluid-structure interaction of floating offshore wind turbines under various scenarios, including wave-only, current-only, and wave-current conditions, in which the motion response is one of the main concerns. A comparison study shows that a semi-submersible platform has a larger aspect ratio, exhibits a larger cross-flow motion and experiences the lock-in phenomenon for the reduced velocities considered. Conversely, a barge platform, with a larger cross-surface area and low aspect ratio, shows a much smaller motion. Obvious VIM is not seen with selected V_r, indicating there is little chance for a floating barge platform undergoing a lock-in phenomenon.

The angle between the directions of the wave and current significantly affects the platform's CF motion, with a mitigated VIM and small CF motion being observed when the wave and current are colinear or have a small angle. Increasing the angle from 0° to 90° leads to a more significant VIM and larger CF motion, with the oscillation frequency being more synchronised with the system's natural frequency. The motion displacement reaches its maximum at the angle of 90°, where the motion induced by wave and current are in the same direction and coupled nonlinearly. A combination of the largest wave height and the most significant VIM does not result in the largest CF motion. The motion can be even larger for smaller wave heights in some cases. The study of Keulegan-Carpenter number (*KC* numbers) and velocity ratio shows that the motion is mitigated if the problem is inertia-force dominant, whereas motion will be

enhanced if it is drag-force dominated.

The interaction effect factor (*IEF*), which represents the motion ratio in wave-current conditions compared to the sum motion in wave and current conditions separately, is evaluated. For large wave height and small wave period, the ratio is lower than 0.75, suggesting that the interaction of wave and current mitigates the sum of their individual motion. However, the most extreme motion does not necessarily occur with the largest wave height. With a smaller wave height, the ratio may be larger than 1.0. Remarkably, wave and current interaction could sometimes amplify the IEF to values as high as 1.35. At the design stage of floating offshore wind turbine platforms, these coupling effects have generally not been accounted for, though it is sometimes critical, as we illustrated. Therefore, our findings offer valuable insights for engineers considering the installation of wind turbines in regions where currents and waves coexist, potentially leading to more efficient and safer designs.

Chapter 7 Fully Coupled FOWT Array in Regular Wave Conditions

Besides the hydrodynamics of FOWT, aerodynamics plays a crucial role in determining both power output and thrust. The interactions between hydrodynamic and aerodynamic necessitate the development of a fully coupled model, which is introduced in this chapter. The ALM is incorporated into the current tool to study the FSI of FOWT, eliminating the need for meshing blade geometry and conserving computational resources, making FOWT farm simulation feasible. This chapter studies the dynamic response, aerodynamic performance, and wake interaction of three FOWTs in regular wave conditions.

7.1 Validation

Before the specific research, the present tool is validated for different scenarios. The hydrodynamics model has already been validated in previous chapters. Therefore, in this chapter, the aerodynamic model, i.e. ALM, is validated. Specifically, the aerodynamic performance of a single wind turbine is first validated in section 7.1.1. Secondly, to ensure the accurate capture of wake interaction between turbines, tandem wind turbines wake interaction is validated in section 7.1.2. Finally, to ensure the wake interaction of turbines is accurate with platform motion, tandem wind turbines with surge motion are studied in section 7.1.3.

7.1.1 Single Bottom-fixed Turbine

CFD results of the single bottom-fixed turbine are validated against the "Blind test" data on wind turbine wake modelling organised jointly by Nowitech and Norcowe in Bergen in October 2011 (Krogstad and Eriksen, 2013), as shown in Figure 7.1 (a). The turbine model is designed to be simple, and the same airfoil NREL S826, 14% thick, was used throughout the span. The blades were made of aluminium, and the maximum load on each blade was estimated to be about 15 N. The turbine model was characterised by a rotor diameter of D =0.894m, with wind speeds subjected to it at U_∞ =10m/s. The

height of the rotor is 0.817m. Furthermore, its rated Tip Speed Ratio (TSR, representing the ratio between the wind speed and the speed of the tips of the wind turbine） was set at λ=6.0. For more details about the turbine, readers can refer to the reference (Krogstad et al., 2011). This study explores five distinct cases, each marked by $\lambda = 2$, 4, 6, 8, and 10, which is achieved by altering the rotor's speed. The sketch of the numerical wind tunnel is shown in Figure 7.1 (b). The dimension of the computational domain is $11D \times 4D \times 2D$. The turbine is $5D$ from the inlet and $6D$ from the outlet boundary. The boundary conditions are also annotated in Figure 7.1 (b). A constant wind velocity U_∞ along the x-axis is applied on the inlet boundary, while a constant pressure outlet $p = 0$ is defined. A symmetry boundary condition is used for the other four side walls. The length of the background cell is 0.063m, while the length of the cell near the turbine and wake zone is 25% of the background cell length. The total cell count is 5.15 million for the whole domain.

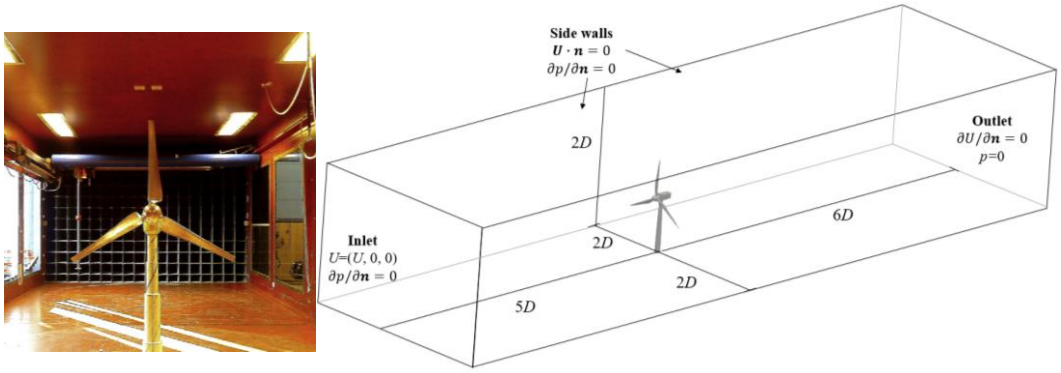

(a) (b)

Figure 7.1 Sketch of the single turbine model in the (a) experiment (Krogstad and Eriksen, 2013) (b) computational domain with specific dimensions and boundary conditions

Figure 7.2 provides the power and thrust coefficients C_p and C_t, which are defined by equation 7.1:

$$C_p = \frac{P}{0.5\rho S v^3} \quad \text{and} \quad C_t = \frac{P}{0.5\rho_{air} S U^2} \tag{7.1}$$

where P is the power output, and S is the swept area of the turbine blades. The results are validated against experimental data and other numerical results. The left graph depicting power coefficient C_p reveals a bell-curve trend for the experimental data, with the peak power coefficient observed around λ=6. Among the various simulation methods, the present data closely aligns with the experimental results within a wider TSR range from 2 to 10. The thrust coefficient C_t shows an increasing trend in the experiment. Again, the present simulation data aligns closely with this trend, underscoring its accuracy.

In Figure 7.3, the power output and thrust variation with time can be seen. The fluctuations can be found, whose periods increase with the TSR. The fluctuation frequency matches thrice the rotor's frequency, equating to the blade-passing frequency, given the turbine has three blades. This pattern could come from varying wind conditions encountered by each blade during rotation. As the blades move, they experience shifts in wind velocity and angle, leading to a cyclical variation in power generation. Although the amplitude of the fluctuations increases with TSR, it can be neglected compared to their time-averaged value.

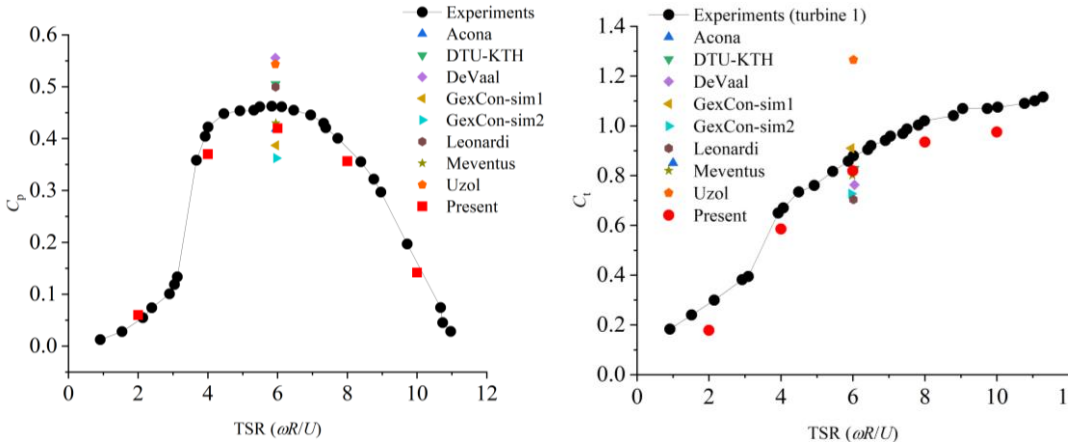

Figure 7.2 Power and thrust coefficients C_p and C_t of the single turbine versus experimental data (Krogstad and Eriksen, 2013)

The wake velocity of the single turbine is also compared in Figure 7.4. The velocity along a horizontal line at the hub height is sampled; each of them is time-averaged and

normalised by the incident wind speed U_∞ = 10 m/s. The position is normalised by the rotor's radius D. It can be seen the present study aligns well with experimental measurements, evidencing a strong correlation in wake behaviour. Despite some discrepancies, the pronounced central velocity deficit and its attenuation downstream are captured accurately.

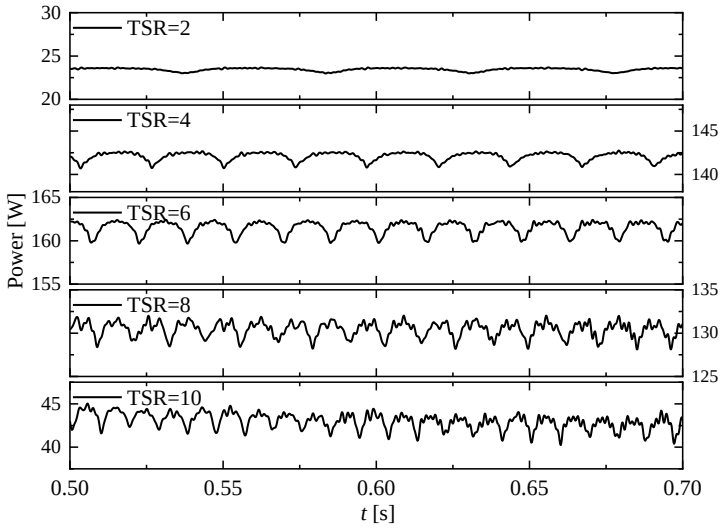

(a)

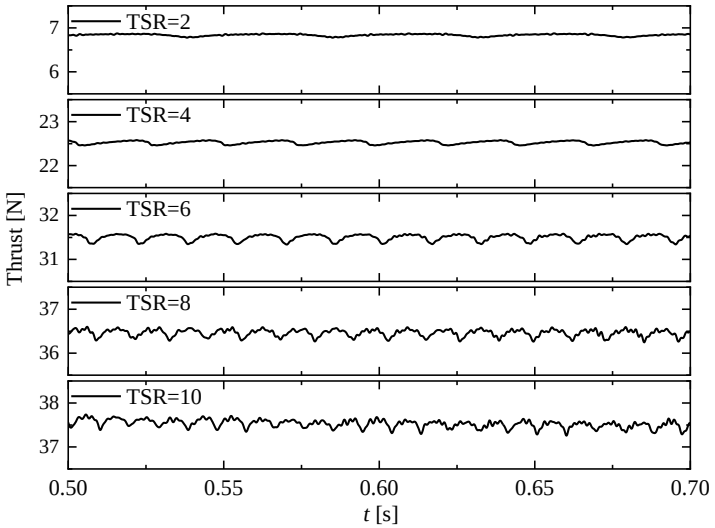

(b)

Figure 7.3 Time series of (a) power output and (b) thrust with different TSR

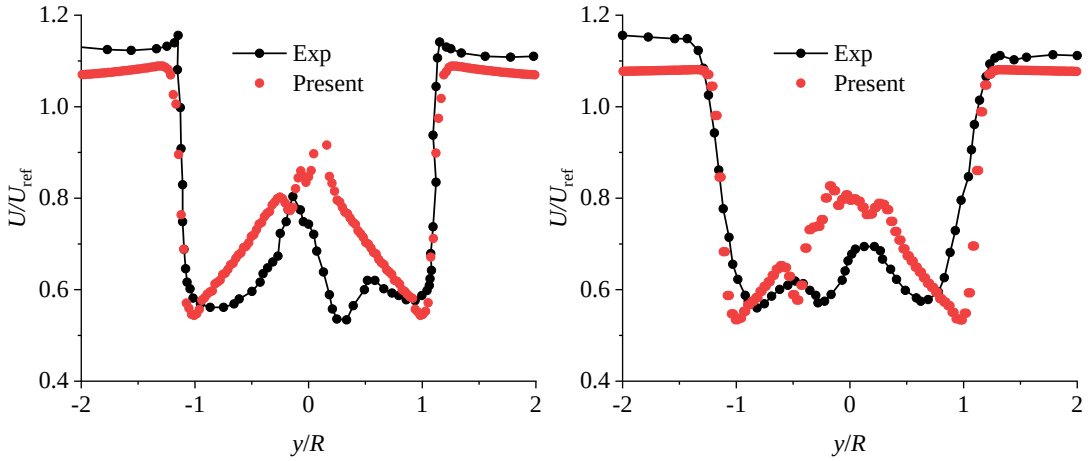

Figure 7.4 Mean velocity profiles along the horizontal line with TSR = 6 at a distance of (a) 1*D* (b) 3*D* along the downstream direction

7.1.2 Tandem Bottom-fixed Turbines

This section is to validate the accurary regarding performance changes caused by the wake interference between turbines (Pierella et al., 2014). A second turbine is deployed downstream the upstream turbine discussed in section 7.1.1. It has a slightly larger rotor diameter of 0.944 m and a rated TSR of 4.0. The distance between the two turbines is 3*D*. Since ALM doesn't need meshing the turbine geometry in the computational domain, the mesh for single turbine validation is re-used. For this setup, three distinct cases were examined:

Case A, where the TSR for the downstream turbine is set at the standard value of 4; Case B, an optional high-speed scenario with the downstream turbine at a TSR of 7; Case C, an optional low-speed case where the downstream turbine has a TSR of 2.5. To better understand the setup, the layout of the two turbines is shown in Figure 7.5. In Figure 7.6, C_p and C_t for the downstream turbine are compared against the experimental data across a range of TSRs. The present results consistently follow the experimental trend, especially in the crucial mid-range TSR values. It can be seen that the performance of the downstream turbines is weakened due to the low-velocity wake region created by the upstream turbines with high-turbulence, leading to a significant

drop in power output. A peak in the power coefficient can be observed near a TSR of 4, and it is seen that the current model closely reflects these experimental values.

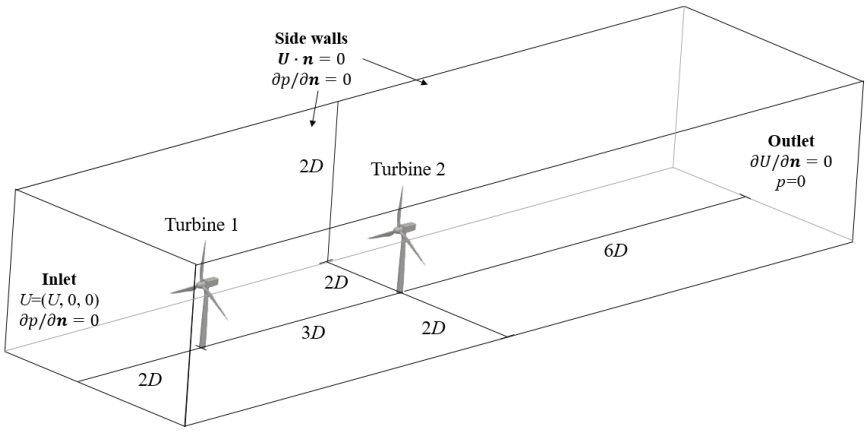

Figure 7.5 Dimensions and boundary conditions for the computational domain of tandem bottom-fixed turbines.

In Figure 7.7, the time series of power output and thrust are displayed for three distinct TSRs. The stability and periodic behaviour of both coefficients over time provide insights into the system's dynamic response. Both power and thrust coefficients demonstrate stable oscillations, suggesting a consistent turbine response over time for each TSR circle. The wake velocity profile shown in Figure 7.8 also shows good agreement for different TSRs. In summary, the presented data for tandem bottom-fixed turbines indicates that the current modelling approach not only aligns closely with experimental results but also provides stable and consistent outputs across various TSR values, reinforcing the model's robustness and reliability.

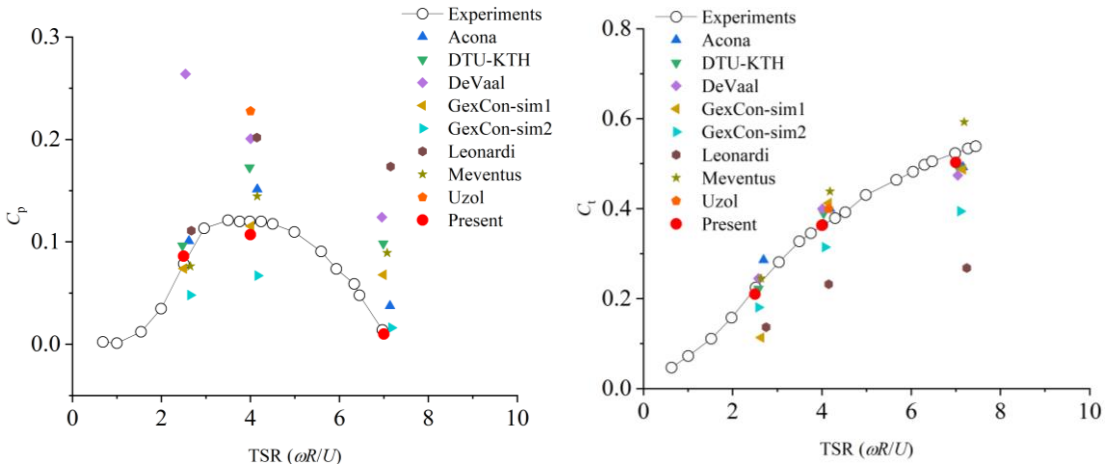

Figure 7.6 power and thrust coefficients C_p and C_t for T_2 against experimental data (Pierella et al., 2014)

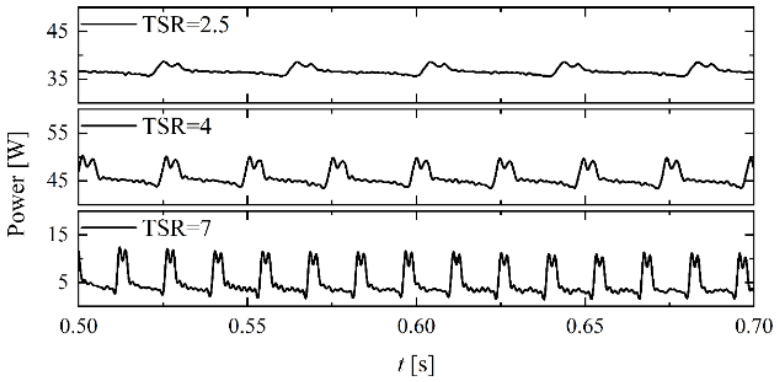

(a)

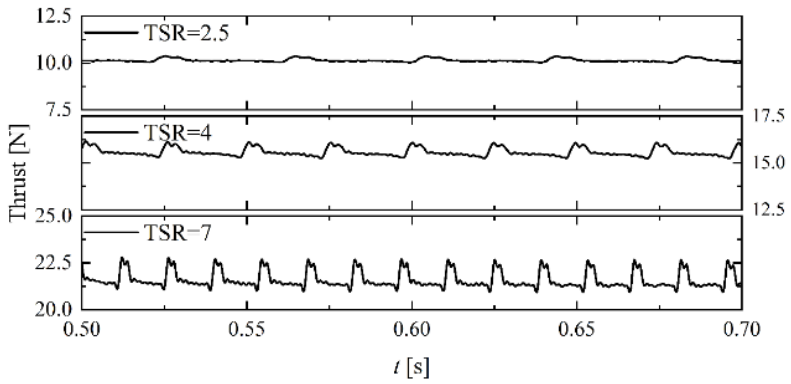

(b)

Figure 7.7 Time series of power output and thrust of the downstream turbine with different TSR

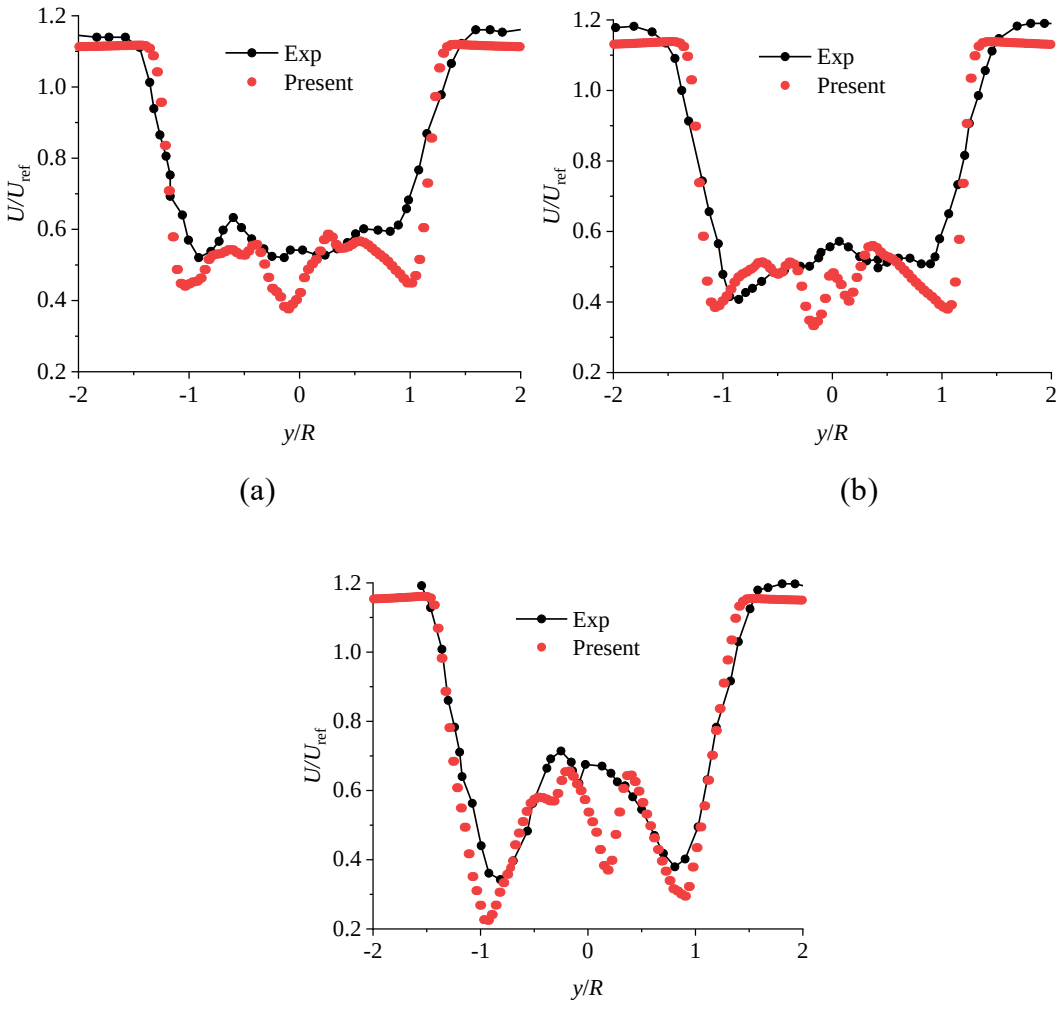

Figure 7.8 Mean velocity profiles along the horizontal line at a distance of 1D of the downstream turbine with TSR of (a) 2.5 (b) 4.0 (c) 7.0

7.1.3 Tandem Turbines with Surge Motion

To validate the influence of platform motions on the performance of wake interaction, a simulation was conducted in which the upstream turbine was subjected to a prescribed surge motion while the downstream turbine remained bottom-fixed. The specifications for both turbines were based on the NREL 5MW blades shown in Table 7.1, with a given TSR of 7.0 for the upstream turbine and 9.62 for the downstream turbine. They were spaced at a distance of 3D, as shown in Figure 7.9.

Three different scenarios were tested, each characterised by a unique surge motion for

the upstream turbine shown in equation 7.2:

$$x = A_s \sin\left(\frac{2\pi}{T_s} t\right) \tag{7.2}$$

where A_s is the amplitude of the prescribed surge motion. A_s = 1.02 m in case 1, 2.04 m in case 2 and 3.06 m in case 3. T_s is the constant surge period, which remains T_s = 9 s in all three cases. Each case aimed to discern how varying surge amplitudes impact the performance metrics of the turbines. The mesh setup follows the same rule as bottom-fixed ones. The results are compared with the single-phase CFD simulation results (Arabgolarcheh, Micallef, Rezaeiha, et al., 2023a). The boundary condition can be seen in Figure 7.9, where the bottom boundary is set to a non-slip boundary. The uniform wind velocity is set above the free surface at the inlet boundary.

Figure 7.10 presents the normalised power coefficients (normalised by the averaged power) for the upstream and downstream turbines. For the upstream turbine, a close examination reveals that the temporal evolution of C_p for all three cases exhibits a periodic fluctuation with the same period as T_s. Unlike bottom fixed cases, this fluctuation is significant, and the amplitude increases with the motion amplitude and reaches 0.4 of the time-averaged power output with A_s = 3.06m. For the downstream turbine, although it is bottom-fixed, the power output also has a periodic variation with the same period, although with a much smaller amplitude than the upstream turbine. This indicates the influence of the upstream turbine on the performance of the downstream turbine. Both results show good agreement between the two results, showing the accuracy of the present method. Figure 7.11 illustrates the normalised thrust coefficient C_t, which also shows a similar trend and agrees well with the referenced data.

Table 7.1 Properties of the FOWT

Wind Turbine Properties	
Wind regime	IEC Class 1A
Rotor orientation	Upwind
Number of blades	3
Rotor diameter	126 m
Hub diameter and height	3 and 90 m
Cut-in/out wind speed	4/25 m/s
Rated wind speed	11.4 m/s
Rated rotor speed	5.0MW
Rated power	90 m/s
Gross Properties	
Total mass	1.414×10^7 kg
Pitch inertia about centre of mass	1.315×10^{10} kgm^2
Yaw inertia about centre of mass	1.906×10^{10} kgm^2
Roll inertia about centre of mass	1.315×10^{10} kgm^2
Displacement	1.399×10^4 m^3
Mooring parameters	
Number of mooring lines	3
Angle between adjacent lines	120 degrees
Radius to anchors from centre of rotation	837.6 m
Mooring line diameter	0.0766 m
Unit mass	113.35 kg/m
Unit mass under water	108.63 kg/m

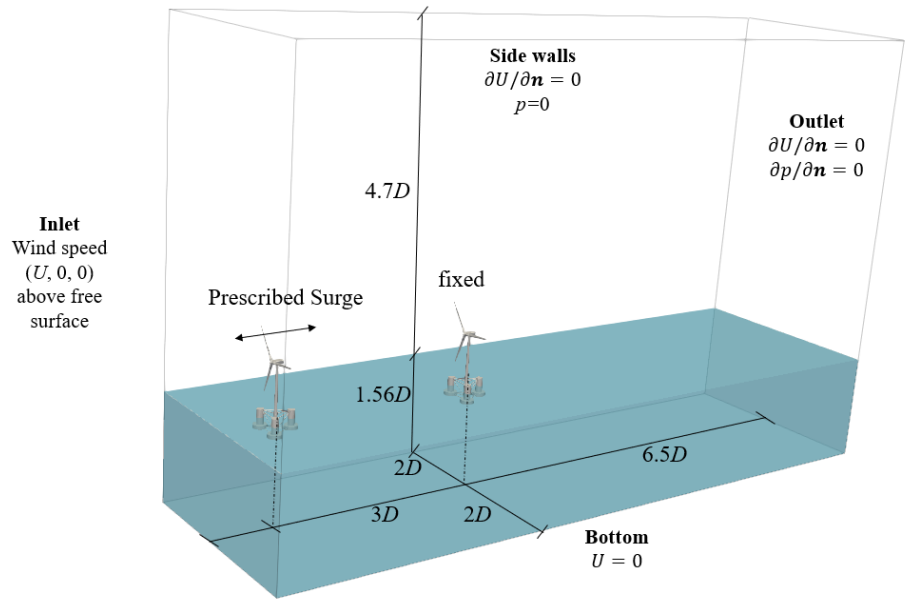

Figure 7.9 Sketch of the computational domain with tandem turbines

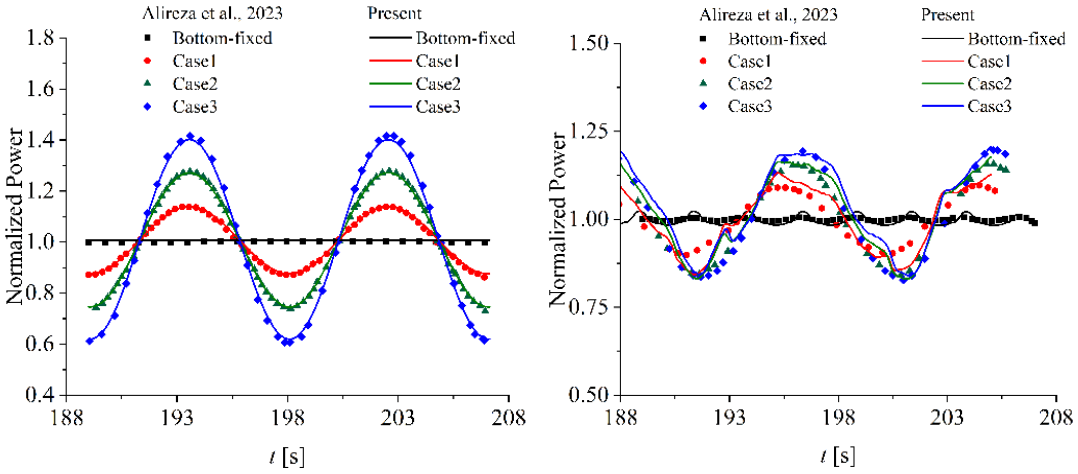

Figure 7.10 Normalized C_p coefficients for the (a) upstream turbine (b) downstream turbine for case A, B and C within two prescribed motion cycles

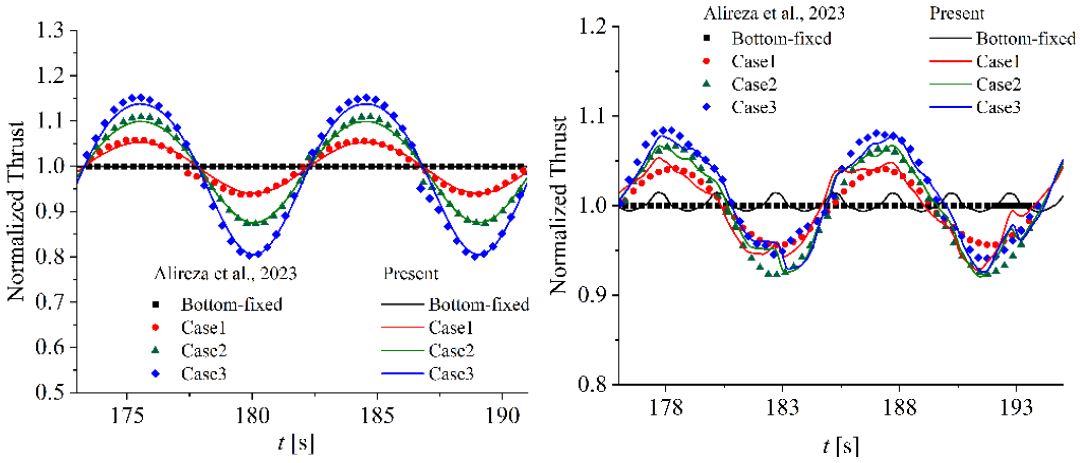

Figure 7.11 Normalized C_t coefficients for the (a) upstream turbine (b) downstream turbine for case A, B and C within two prescribed motion cycles

7.2 Model Parameters

To study the wake interactions in the FOWT farm, three FOWTs with the same properties are studied in this chapter, where NREL 5 MW wind turbines are adopted, supported by OC4 DeepCwind semi-submersible platforms. The 5MW wind turbine consists of three blades, and its properties are shown in Table 7.1. The scaled model of the OC4 platform has been introduced in Chapter 6. In this section, a full-scale model is studied, and its gross properties, including turbine and tower, are shown in Table 7.1. Each FOWT is constrained by three mooring lines anchored on the seabed, the properties of which are also shown in Table 7.1.

7.3 Parameters for Numerical Simulation

The setup of the computational domain of the numerical simulation is shown in Figure 7.12. The dimension of the computational domain is $11D\times 6D\times 6.27D$. The distance between each turbine along the x direction is $3D$ from the inlet boundary. The boundary conditions are also annotated in Figure 7.12. At the upper part of the inlet boundary, which is above the static water level, a constant wind velocity U along the x-axis is applied. For the lower part, a prescribed wave generation velocity is applied. At the side walls and the upper part of the outlet boundary, the Neumann boundary condition is

assumed for both velocity and pressure. The lower part of the outlet boundary is set as an active wave-absorbing boundary. The bottom boundary is set to a non-slip boundary.

The computational mesh is shown in Figure 7.13. To guarantee the accuracy of the simulation and to maintain an acceptable cell count, different levels of refinement are applied. The cells near the free surface are refined along the z direction, keeping the cell length along the z direction is 1/8 of the wave height. The mesh is also refined near the platforms' surface to accurately capture the hydraulic force. To capture the wake interaction, the wake zone behind the first turbine is also refined where the cell size is 2 m. This cell size has been proven to be adequate for ALM simulation of the NREL 5MW turbines (Huang, Zhao, et al., 2023).

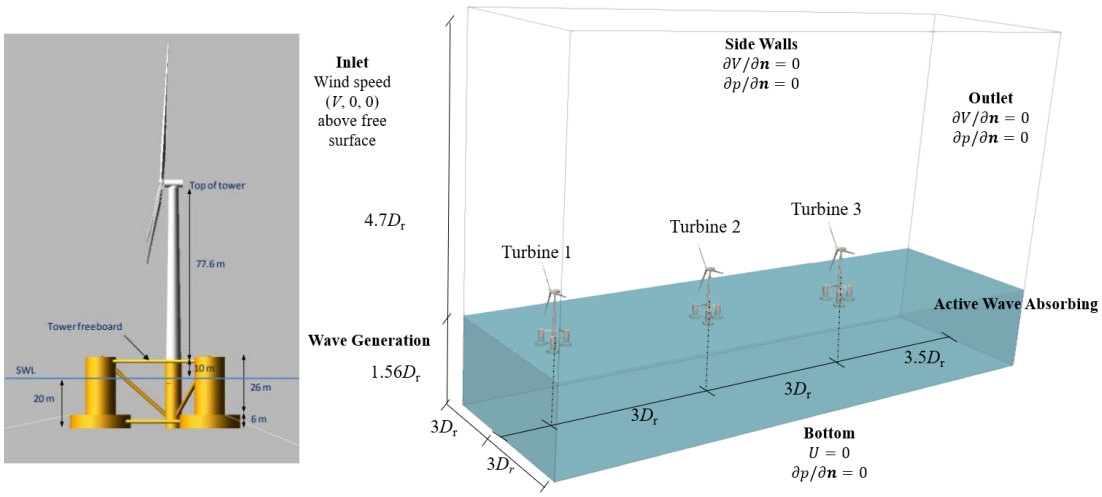

Figure 7.12 Sketch of (a) DeepCwind FOWT system (b) the computational domain with three turbines

The PIMPLE algorithm is used to solve the pressure-velocity coupling. A second-order Crank-Nicolson scheme is used for temporal discretisation. A second-order upwind scheme is adopted for convective terms. Gradient terms are handled via a second-order cell-limited Gauss linear scheme.

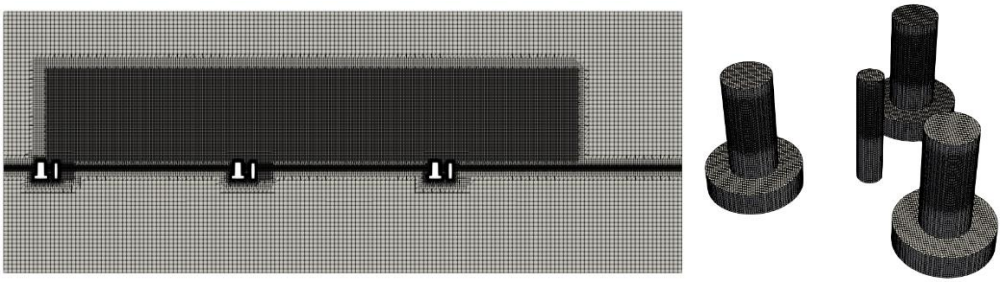

Figure 7.13 Mesh of the domain and the platform

7.4 Layout of the FOWT

To study the wake interaction within a wind farm for different scenarios, three turbines with different arrangements are studied, which are derived from the gridded and staggered layouts. The scenarios of these derived layouts may come from the optimisation of basic layouts and possess irregular features (Shakoor et al., 2016), or the position change due to the platform motion. For these novel layouts, the mechanism of the multiple wake interaction would be complicated and important (Fan et al., 2023; Froese et al., 2022; Han and Nagamune, 2016; Kheirabadi and Nagamune, 2019; Kheirabadi and Nagamune, 2020). The 1st and 2nd FOWTs are deployed either in a gridded layout (cases 1-3) or a staggered layout (cases 4-6), both are commonly used layouts for wind farms, as in Figure 7.14. The position of the 3rd turbine varies within the wake region of the other two turbines, which is shown in Figure 7.15 and Table 7.2. The spacing between each turbine along the x-axis, Δx is fixed as $3D$ for all cases, which is the same as that in the validation part for comparison (Arabgolarcheh, Micallef, and Benini, 2023; Arabgolarcheh, Micallef, Rezaeiha, et al., 2023). The main difference between these cases is their spacing along the y-axis Δy, where the subscripts in Δy_{12} mean the spacing between the 2nd and 1st turbine. In order to decouple and analyze the contribution of platform motion, six special cases 1b-6b are studies where the 3rd turbine is set to be bottom-fixed.

Table 7.2 Different layouts of the FOWTs

		Δy_{12}	Δy_{13}	3rd FOWT condition
Gridded layout	Case 1 Case 1b	0	0	Floating Bottom-fixed
	Case 2 Case 2b	0	0.5D	Floating Bottom-fixed
	Case 3 Case 3b	0	1.0D	Floating Bottom-fixed
Staggered layout	Case 4 Case 4b	1.5 D	0	Floating Bottom-fixed
	Case 5 Case 5b	1.5 D	0.75D	Floating Bottom-fixed
	Case 6 Case 6b	1.5 D	1.5D	Floating Bottom-fixed

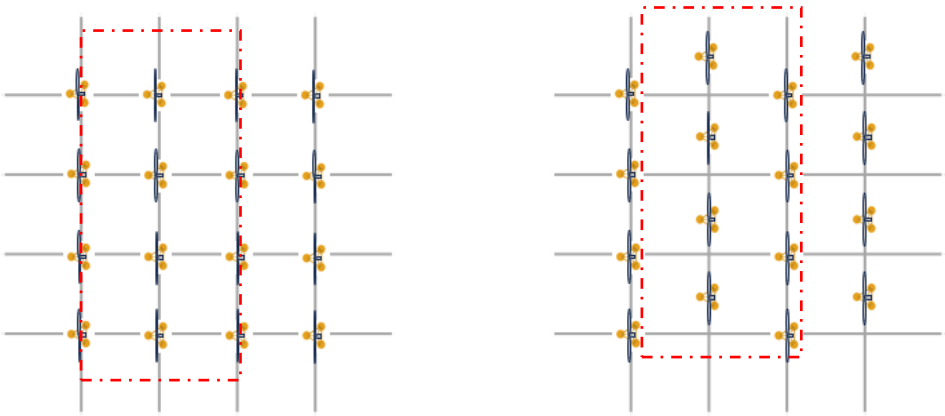

Figure 7.14 Sketch of gridded and staggered layout in a wind farm

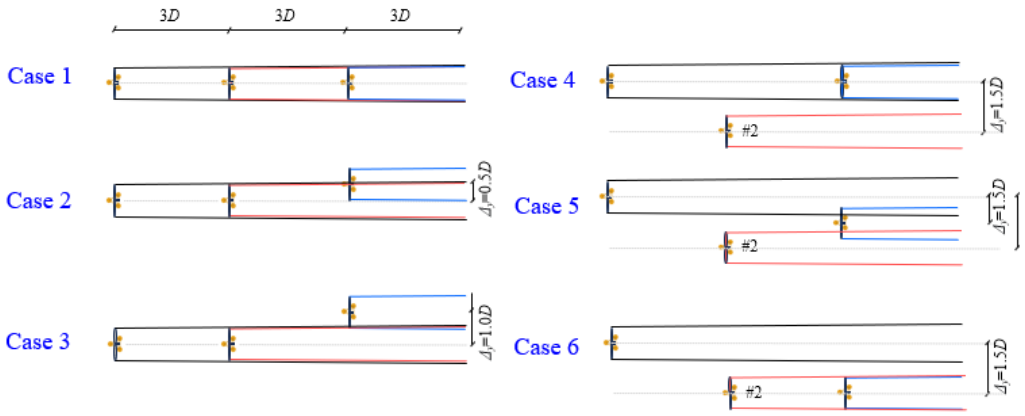

Figure 7.15 Position of the FOWT and its wake zone. The black, red, and blue lines represent the wake zones of turbines 1, 2, and 3, respectively.

Table 7.3 Sensitivity study for computational mesh and unsteady time step for case 1.

		Power [MW]		Thrust [kN]	
		Turbine 2	Turbine 3	Turbine 2	Turbine 3
coarse		1.659	0.983	428.483	261.861
intermediate	Δt=0.0125s	1.670	1.069	428.475	260.475
	Δt=0.010s	1.663	1.012	428.744	264.913
	Δt=0.0075s	1.665	1.025	428.731	265.896
fine		1.667	1.033	429.044	259.881

7.5 Mesh and Time-Step Dependence Test

To investigate the impact of mesh resolution and time step sensitivity, various configurations involving different mesh sizes and time steps were implemented. For the mesh sensitivity analysis, Case 1 utilises three different mesh arrangements on bottom-fixed platforms. The mesh configurations varied by cell length in the wake region: 1.5m for the coarse mesh, 2.0m for the intermediate mesh, and 2.5m for the fine mesh. As shown in Table 7.3. the variations in mesh size result in discrepancies of less than 1% for turbine 2 and less than 3% for turbine 3. Thus, the intermediate mesh was selected for this study. Additionally, time steps of 0.0125 s, 0.01s, and 0.0075 s were examined for the convergence test. The results show closer alignment between the time steps of

0.01 s and 0.0075 s, compared to the larger gap observed between 0.0125 s and 0.01 s. Consequently, a time step of 0.01 s was chosen to balance accuracy with computational efficiency. The total cell of the simulation is around 900 million, with a slight variance depending on the specific layouts. The computations are made in parallel with 5 nodes (180 cores) for each case on Cirrus HPC (http://www.cirrus.ac.uk). The average simulation time is 3 - 4 wave periods per day, which may vary depending on the specific cases.

7.6 Results

This section studies both gridded and staggered layouts in Figure 7.15. It analyses the power output and thrust of turbines in different positions and their spectral characteristics. In these studies, the third turbine located downstream is implemented as stationary or mobile for comparative analysis. The hydrodynamics and aerodynamics are both studied for different FOWTs.

7.6.1 Gridded Layouts

To analyse the FOWTs in gridded layouts, this section is divided into three subsections. The hydrodynamics of the FOWTs, focusing on the motion response of FOWTs in the array is firstly studied. It then examines the aerodynamic performance of the wind farm and the wake interactions among the FOWTs. Since the above two aspects are correlated, the influence of the platform motion on aerodynamics and wake characteristics is investigated. To achieve this goal, cases 1b to 3b are conducted, where the 3rd turbine is set as bottom fixed. By comparing them with the floating cases, the effect of platform motion is isolated.

Among cases 1-3, the 1st and 2nd turbines are in tandem arrangement. For the 3rd turbine, different offsets from the x-axis Δy_{13} are selected, with Δy_{13} ranging from 0 to D, as indicated in Table 7.2.

Figure 7.16 shows the dynamic response of each FOWT, which is deeply related to the wake interaction in two aspects. Firstly, the motion of each FOWT in a given case

differs due to wake interaction between upstream and downstream turbines. Secondly, the position of the 3rd FOWT varies in cases 1-3, which also affects the wake interaction. For the first aspect, take case 1 as an example, the 1st upstream turbine experiences uniform wind conditions and exhibits the largest surge and pitch motion. The 2nd turbine, located in the wake of the first one, displays a decreased motion amplitude. Meanwhile, the 3rd turbine decreases its motion further, influenced by the complex turbulent wake of the above two upstream turbines. The primary reason for the sequentially decreased motion is that the velocity deficit in the downstream wakes decreases the thrust of downstream turbines, thus lowering the load on the platforms in both surge and pitch directions. This will be further addressed in following discussion where the aerodynamics analysis will be focused. For the second aspect, as the offset Δy_{13} increases from case 1 to case 3, the third turbine shifts further from the wake zone of the upstream turbines, resulting in a significant increase in the mean surge and pitch in Figure 7.16 (c) and (d), where the mean pitch of the 3rd turbine is 3.6 times greater than in case 1, almost approaching the level of the first upstream turbine. This is because the swept area of the wind turbines is less influenced by the low-speed zone in the wake from case 1 to case 2. The motion amplitude is also seen to be increased in Figure 7.16 (a) and (b). When the third turbine is fully within the wake zone of the two upstream turbines, the turbulent wake with higher frequencies interferes with the turbine's periodic motion. The resulting irregular loads result in more complex dynamic responses, causing the turbine to experience a broader range of motion frequencies and amplitudes, further diminishing the dominance of its primary periodic motion. However, when the turbine moves out of the wake zone, this interference decreases, and the amplitude of its motion response increases. This will also be confirmed in the following section.

Another finding is that the surge and pitch motion are opposite in phase for present cases, as indicated by Figure 7.17, where the time-dependent surge and pitch motion are shown. This implies that for the present combination of turbine and floating platform, the relative wind velocity variation caused by pitch and surge are coupled and

opposite, which is also confirmed in other OC4 platform studies (Huang et al., 2021; Liu et al., 2017). In other words, the pitch motion compensates for the relative wind speed caused by the surge motion. Therefore, instead of studying a single degree of freedom of platform, a coupled simulation that considers multiple degrees of freedom is necessary for accurate results.

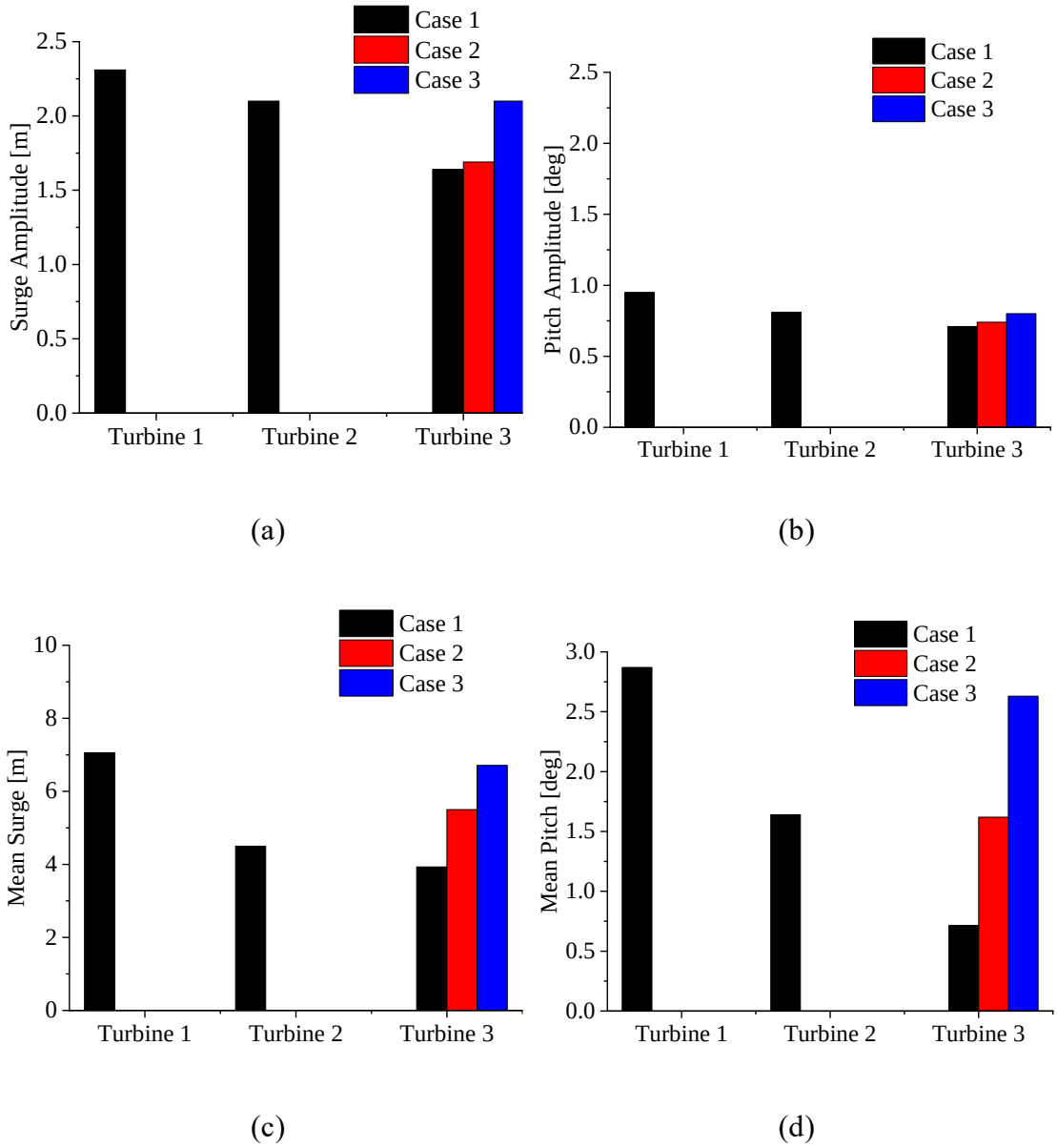

Figure 7.16 (a) Surge and (b) pitch motion amplitude, time-averaged (c) surge and (d) pitch of different FOWTs

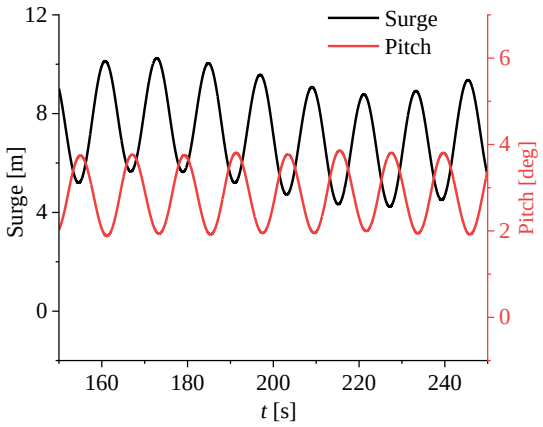

Figure 7.17 Surge and pitch time series of the third turbine in Case 1.

The time-mean power output of the 3rd turbine shown in Figure 7.18 indicates that the two upstream turbines remain unaffected by the existence of 3rd turbine. Hence, the power output of the 1st and 2nd turbines remains constant across cases 1-3. When Δy_{13} = 0 in case 1, the 3rd turbine is aligned with the two upstream turbines, having a minimum power output among the three turbines of about 1 MW. With Δy_{13} increasing from 0 to D, the power output increases significantly to around 4.8 MW but still less than the first turbine, which means the wake interaction still affects the turbines' efficiency. This significant increase shows the turbine position has a profound effect on its power output.

Another key element of aerodynamic performance is the fluctuation of the power output, which can be induced by both the wake interaction and the motion of the platform. The amplitude of the power output, estimated by its standard deviation multiplied by $\sqrt{2}$, indicates it gets smaller with the increase of Δy_{13} in Figure 7.18. For the 1st turbine, the amplitude is mainly caused by the periodic motion of the platform induced by waves, reaching a maximum of 0.75 MW. However, for the 2nd and 3rd turbines, they are under the combined influence of the unsteady varied wake and the periodic platform motion, the amplitude gradually decreases as reflected in Figure 7.18 (a). The dominant factor varies depending on the case, which will be further explained in detail in the following discussion.

The thrust of the 3rd turbine is summarized in Figure 7.18, shows a similar trend to the power output. Among different FOWTs in case 1, the thrust decreases sequentially from turbine 1 to 3, which confirms the hypothesis in Figure 7.16 that the progressive wake decreases the thrust of downstream turbines and leads to a smaller motion response.

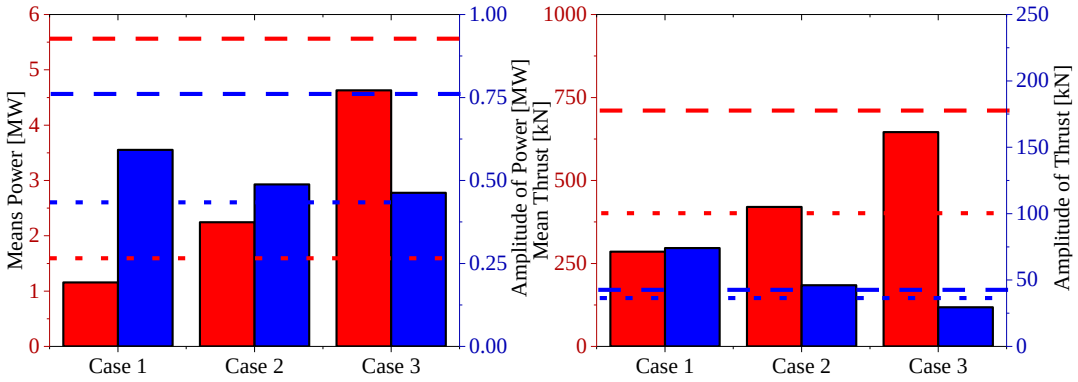

(a) (b)

Figure 7.18 (a) Time-averaged power output and amplitude of the power (b) Time-averaged thrust and amplitude of the thrust of the third turbine. The dashed lines denote the physical quantities of the first FOWT, while the dotted lines denote the physical quantities of the second FOWT.

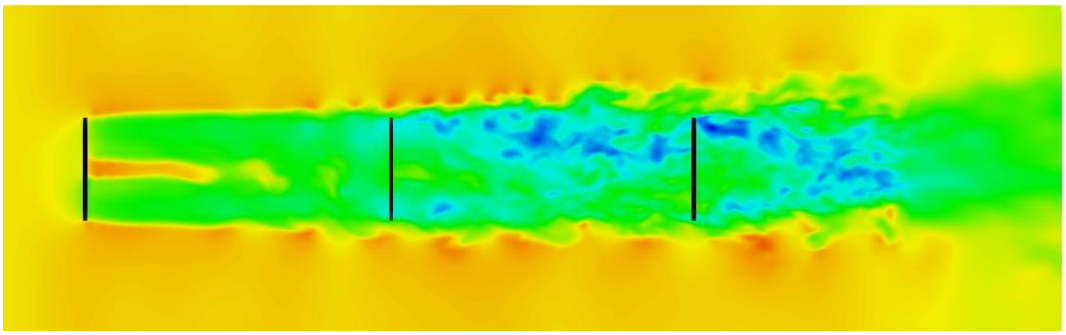

(a_1)

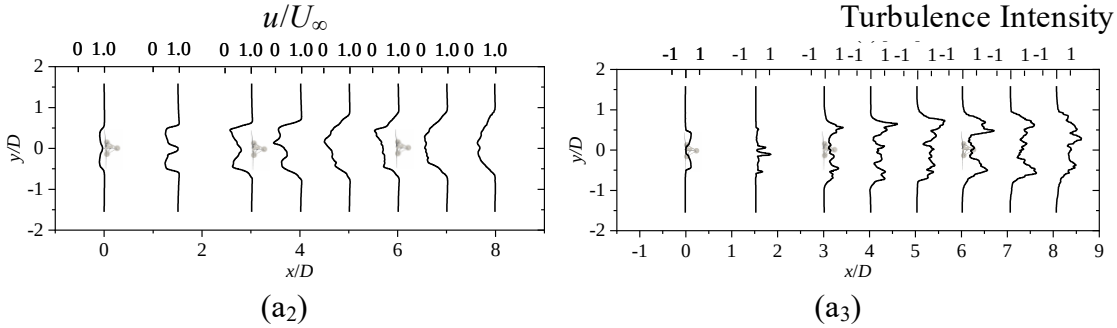

(a_2) (a_3)

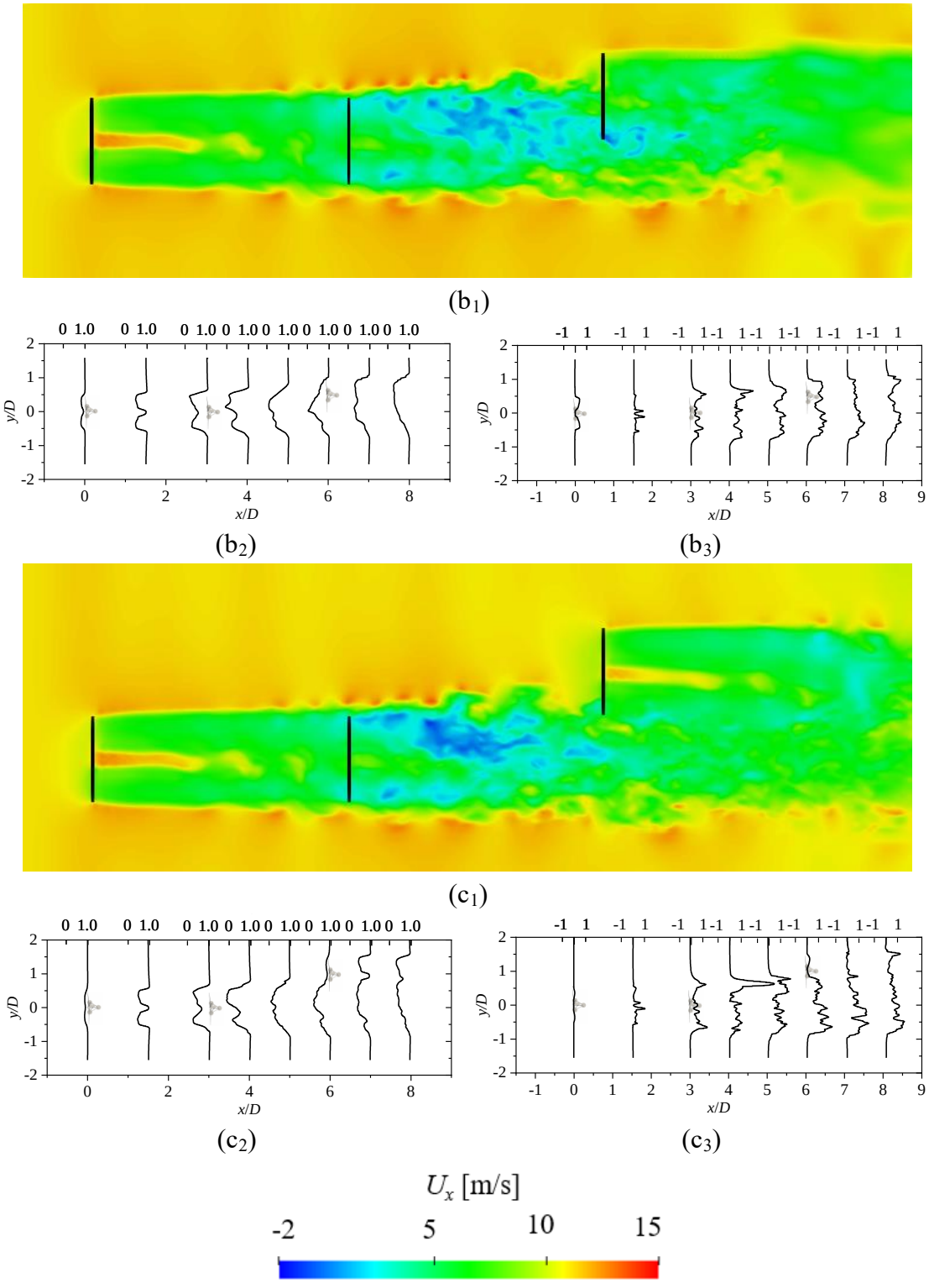

Figure 7.19 (a_1) - (c_1) Contours of spanwise velocity at hub height for at t=200 s (a_2)-(c_2) denotes the time-averaged velocity profile u/U_∞ at different cross sections in the horizontal plane at hub height. (a_3)-(c_3) denotes the corresponding time-averaged turbulence intensity profile. The subscripts denote the case number.

To observe how the velocity changes and how it affects the aerodynamic performance, the velocity field at a specific time instant t=200 s is shown in Figure 7.19 along with time-averaged velocity and the turbulence intensity at the hub height.

From Figure 7.19 (a_1), a distinct low-speed wake region can be observed behind the 1st turbine and an even lower speed zone can be found behind the 2nd turbine, which causes the power reduction for the downstream turbines, as confirmed in Figure 7.18. As the 3rd turbine gradually repositions along the y-axis from Figure 7.19 (a_1) – (c_1) and moves out of the wake area, the inflow conditions improve, resulting in a recovery of its power output. This velocity recovery is evident from Figure 7.19 (a_2) – (c_2), where the time-averaged velocity distribution behind the first turbine exhibits a bell-shaped form, which is essentially symmetrical. Behind the 2nd turbine, a more noticeable velocity deficit can be found, and the maximum velocity reduction occurs at the axial position and gradually decreases along the y-direction. For the 3rd turbine, the velocity deficit affects it most in Case 1, and the influence of this wake decreases as the position offset Δy increases, leading to a gradual increase in power.

From Figure 7.19 (a_3) – (c_3), the turbulence intensity can be analysed. Behind the 1st turbine, the increase in turbulent intensity is not significant. Therefore, the power fluctuation of the 2nd turbine is not greatly affected by the turbulent intensity but is primarily dominated by the platform motion. When the two wakes interact and propagate to the third turbine, the air from the center and edges of the rotor plane is thoroughly mixed, maximizing turbulence intensity. At this point, the turbine's power fluctuation is more influenced by the turbulence of the wind field rather than platform motion. This will be further demonstrated in following discussions.

The vortex structures shown in Figure 7.20 is presented by the Q-criterion, which is coloured by the velocity. The free surface is also shown with its colour denoting the surface elevation. For Case 1 in Figure 7.20 (a), the vortices can be seen symmetrically shed from the tip of the 1st wind turbine's blades and grow progressively larger with increasing distance. 3D helical wakes form downstream of the trailing edge, with the

spacing between the generated vortex rings increasing with propagation distance, which might be caused by the velocity recovery along the propagating path: the velocity recovers gradually with larger spacing, allowing the rings to move at a higher speed, increasing the intervals. As these vortices pass the 2nd turbine, they mix with the vortices generated by it, creating complex turbulence and reducing the power output of the subsequent 3rd turbine.

Besides the tip vortex shedding, a stable wake band is also formed near the root of the first turbine's blades. There is minimal interaction between this wake and the tip-generated wake behind the 1st turbine. Along the turbine axis, the vortices show a symmetric distribution of positive and negative values. After passing the 2nd turbine, they break down into upper and lower regions of small positive and negative vortices, respectively, and then completely mix after the 3rd turbine. The well-defined rings generated by the blade tips are replaced by a chaotic, turbulent area.

As the 3rd turbine is progressively re-positioned further in the *y*-direction, from Figure 7.20 (b) to (c), its right side encounters an area of non-turbulent flow. Additionally, well-defined vortices gradually form behind the right-side tip and root of the blades. This leads to an incremental increase in aerodynamic power, as shown in Figure 7.18 where its aerodynamic power is restored to 87% of that of the first turbine by shifting the third turbine out by one rotor diameter.

To better understand what exactly the impact of the motion of platform on the wind turbine aerodynamic features is, in this section, we study several sceneries where the platform's motion is eliminated for the 3rd turbine, i.e. Case 1b to Case 3b.

(a) Case 1

(b) Case 2

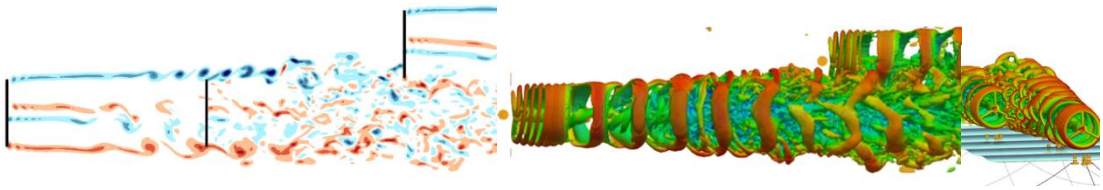

(c) Case 3

Figure 7.20 Contours of spanwise vorticity at hub height and the vortex evolution (top and side view) represented by iso-surface of q=0.002 at t=200 s of each case. The surface elevation is also presented.

The impact of platform motion on the power output can be intuitively observed in the time series of the power output in Figure 7.21. The power output of the 1st turbine is smooth and sinusoidal, possessing the same period as the incident waves. For the 2nd turbine, the power output decreases, and some high-frequency fluctuations appear on the basis of the sinusoidal power curve. Nevertheless, this curve also features a regular periodic variation, which means the power variation of the 2nd turbine is still governed by the platform's sinusoidal motion, which is well reflected from Figure 7.19 that the turbulent intensity for the 2nd turbine is not significant and has a minor effect on it. For the 3rd turbine, which is located further downstream, these high-frequency disruptions become more pronounced, indicating a substantial impact from the wake effect. The

FFT analysis in Figure 7.21 illustrate that from the 1st turbine to the 3rd turbine, there is a decline in the energy correlating with the wave frequency, while the energy associated with the blade-passing frequency exhibits an uptick. Furthermore, harmonic frequencies, which are multiples of the fundamental frequency, can also be found for downstream turbines implying the downstream turbines are more influenced by wind turbulence rather than waves. This effect is especially apparent for turbine 3, which is influenced by both turbines 1 and 2.

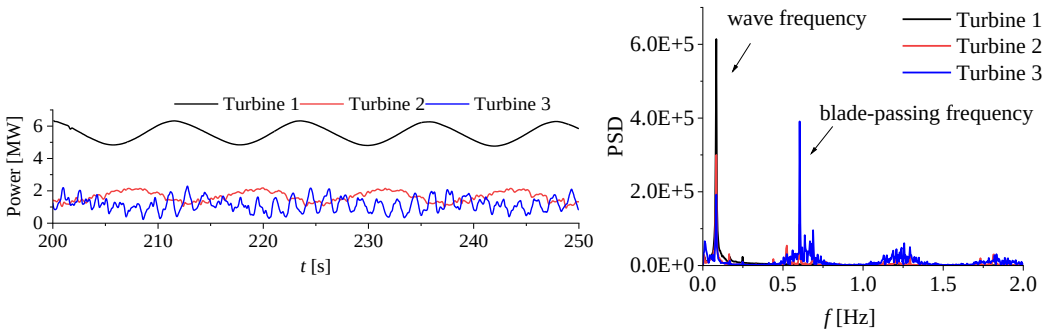

Figure 7.21 Time series and FFT analysis of the power output of three turbines in Case 1.

The time series of the 3rd FOWT is presented for different cases in Figure 7.22, including comparisons with the bottom-fixed cases. Both floating and bottom-fixed turbines appear the same motion period. The frequency components can be found in the FFT analysis shown in Figure 7.22 (a). Given case 1_b with a $\Delta y_{13} = 0$, the stationary turbine exhibits a peak at the wave frequency of 0.083 Hz. This peak results from the periodic wake oscillations induced by the upstream FOWTs. In the floating scenario, this peak is more substantial; the difference between them represents the contribution from the motion of the 3rd FOWT. With the increasing of Δy_{13} in cases 2b and 3b, the turbine moves further away from the wake zone of the upstream turbines. Consequently, the component of energy at the wave frequency becomes less pronounced.

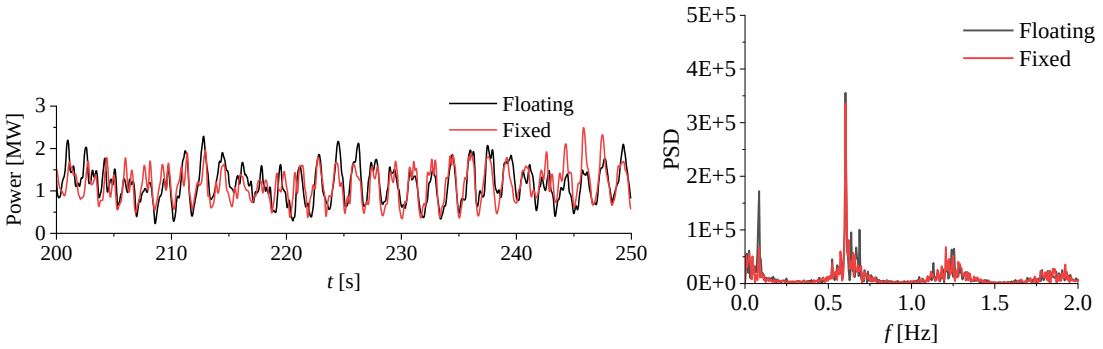

(a) Case 1 and Case 1b

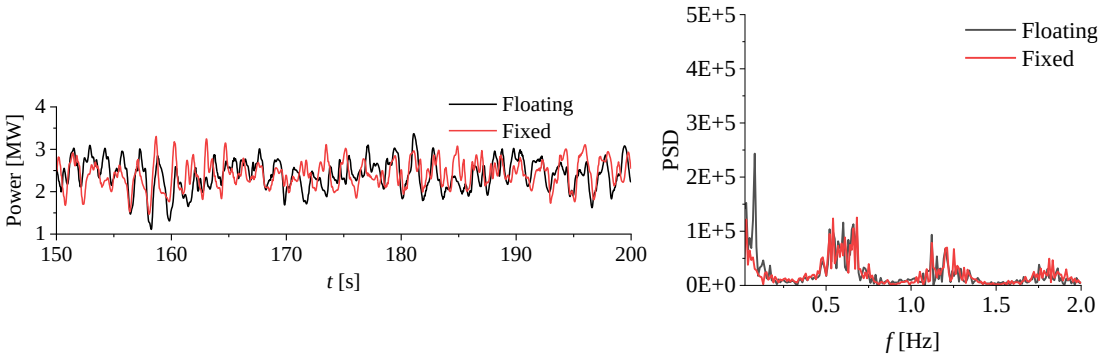

(b) Case 2 and Case 2b

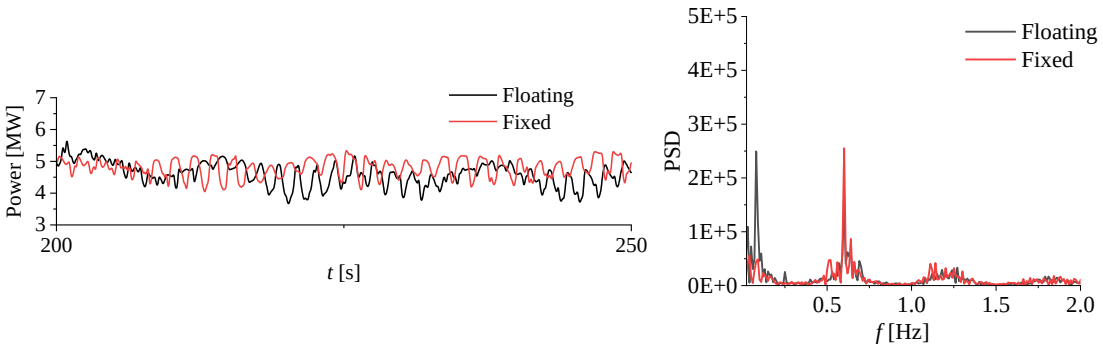

(c) Case 3 and Case 3b

Figure 7.22 Time series and FFT analysis of the power output of the third turbines

The influence of the FOWT's motion response on the aerodynamic performance is shown in Figure 7.23. The results are presented as the percentage difference between the floating and bottom-fixed cases relative to the bottom-fixed cases. It can be observed that whether the third FOWT is bottom-fixed or not only has minimal effect on the time-averaged power output, with a difference between them less than 6%. If the third turbine is bottom-fixed, the influence of the platform's motion is eliminated, and its power amplitude is generally smaller than the floating ones. The FOWT also shows a smaller thrust than the bottom-fixed one, which may be caused by the decreased

relative wind velocity for turbines when the turbine moves, thus lowering the load components on the turbines.

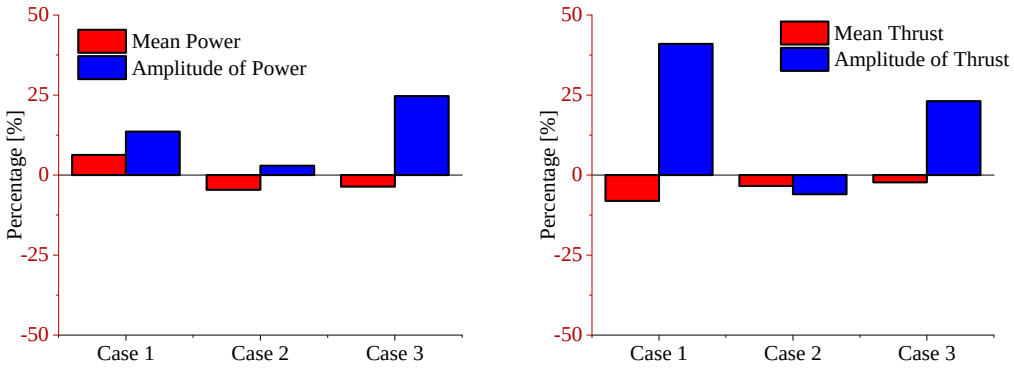

Figure 7.23 Variation in aerodynamic parameters between bottom-fixed cases and FOWT cases, expressed as the percentage difference between the floating and bottom-fixed cases relative to the bottom-fixed cases

7.6.2 Staggerd Layouts

Staggered layouts from cases 4 to 6 are studied in this section. By setting the offset Δy_{12}=1.5D between the 1st and 2nd FOWT, it is expected that the 2nd FOWT will not be affected by the wake of the 1st turbine, therefore, their power efficiency equals in these cases. By changing Δy_{13}, the power output and dynamic response of the 3rd turbine are affected. In Case 4 (Δy = 0), the 3rd turbine is only affected by the wake of the 1st turbine, whereas in Case 6 (Δy =1.5D), by the 2nd turbine. Thus, to reduce the time cost, only two turbines are simulated for these two cases.

Figure 7.24 illustrates the dynamic response of each turbine. It shows that the surge amplitude increases with a larger Δy from case 4 to case 6, whereas the pitch amplitude decreases. The previous analysis indicates that pitch motion helps to reduce the power oscillations caused by surge motion. Therefore, the increase in surge amplitude coupled with the decrease in pitch amplitude resulted in higher motion amplitude at hub height. The time-averaged surge displayed in Figure 7.24 (c) is closely related to the power output and thrust, which reach their maximum in case 4, and the pitch angles decrease when Δy gets larger.

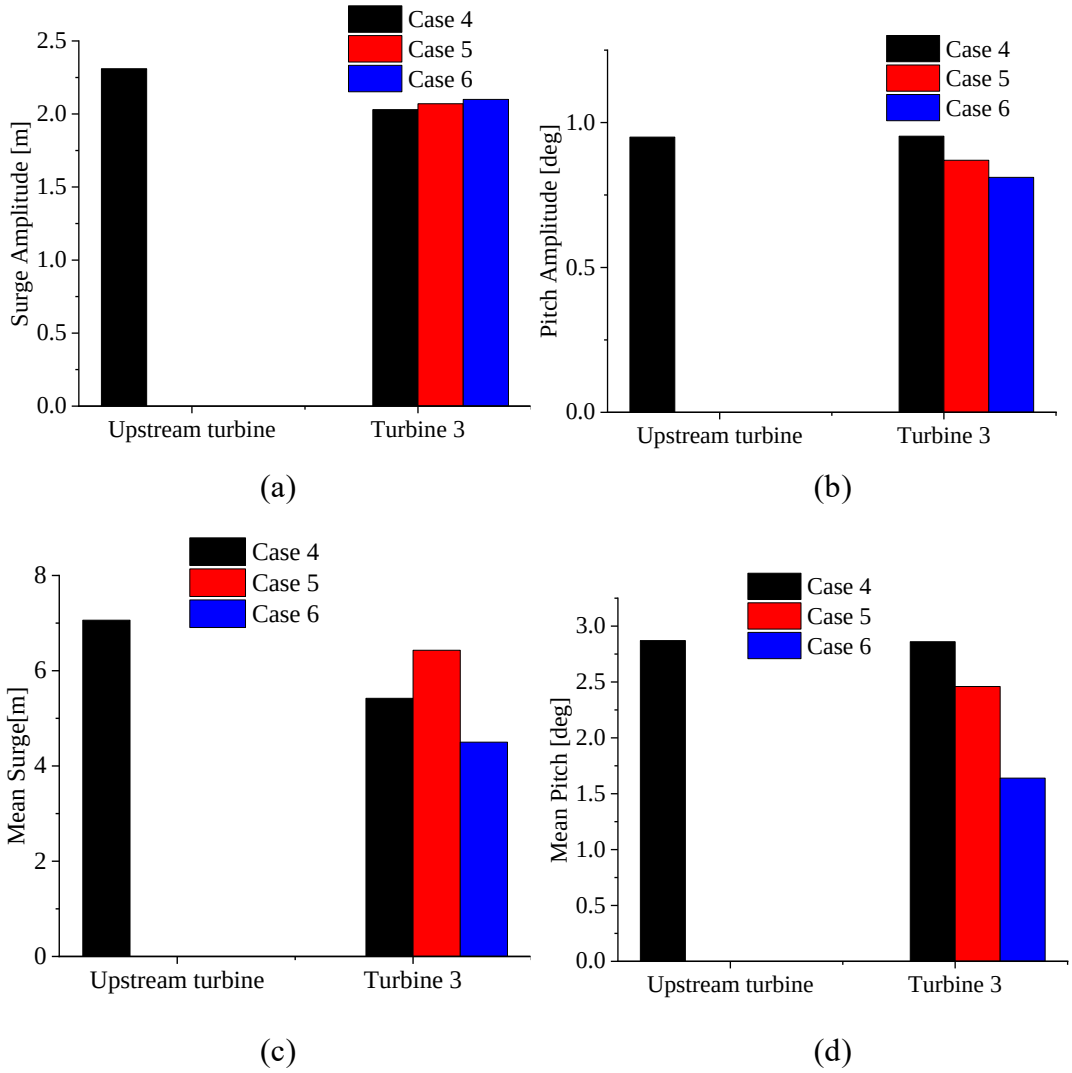

Figure 7.24 (a) Surge and (b) pitch motion amplitude, time-averaged (c) surge and (d) pitch of different FOWTs

Across three scenarios, the third turbine consistently produces less power than the upstream turbines. The maximum power output of 4.2MW occurs when the 3rd turbine is positioned between the two upstream FOWTs in Case 5. In **C**ase 4, the power output is 2.3 MW, which is higher than the 1.7 MW observed in **c**ase 6. This is because in Case 4, the 3rd turbine has a larger distance between the 1st turbine along the *x*-direction, thus benefiting from improved wake velocity recovery, resulting in an increased average power output. Compared to bottom-fixed turbines, the power output of FOWTs is marginally higher. In Figure 7.25 the amplitude of power fluctuation is the largest for case 5, which is also the case for the thrust. Both amplitude and averaged thrust reach their maximum for case 5, where the third turbine is located in the middle of upstream

turbines along the *y* direction.

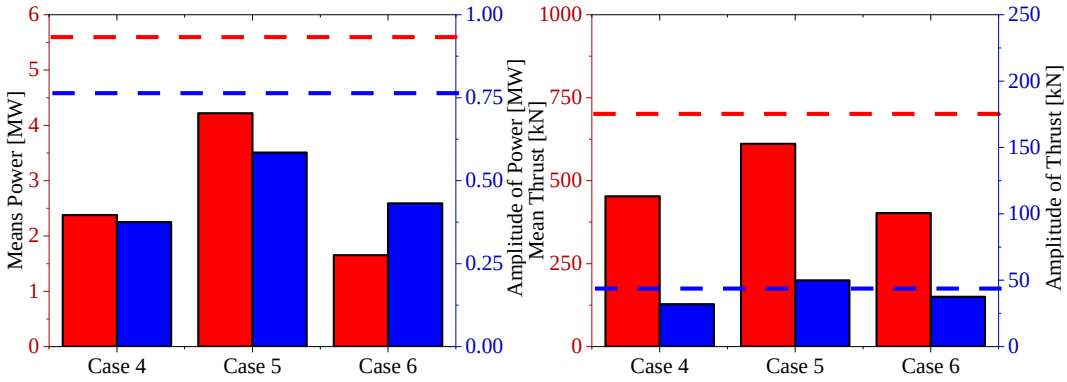

(a) (b)

In Figure 7.25 (a) Time-averaged power output and amplitude of the power output (b) Time-averaged thrust and amplitude of the thrust of the third turbine. The dashed lines denote the physical quantities of the first FOWT, while the dotted lines denote the physical quantities of the second FOWT.

From the velocity field in In Figure 7.26 (b_1), it can also be observed for case 5 that, part of the inflow to the 3rd turbine is between the wake area of the first two turbines and has a higher velocity region, which results in the highest power output among the three cases. Minimal interference between the wake loss regions of the first two turbines is evident, confirming that two turbine simulations for Cases 4 and 6 are sufficient. By comparing In Figure 7.26 (a_2) and (c_2), the wake from the upstream turbine gradually recovers its speed over a long propagation distance. Therefore, compared to Case 6 with a shorter distance between the consecutive turbines, the power output in Case 4 is greater. Additionally, in Case 4, it is observed that the intensity of turbulence increases when propagating, while in Case 6, it is lower due to short spacings. Thus, the aerodynamic performance is more influenced by platform motion than wind turbulence for Case 6. This will be further discussed in following discussion.

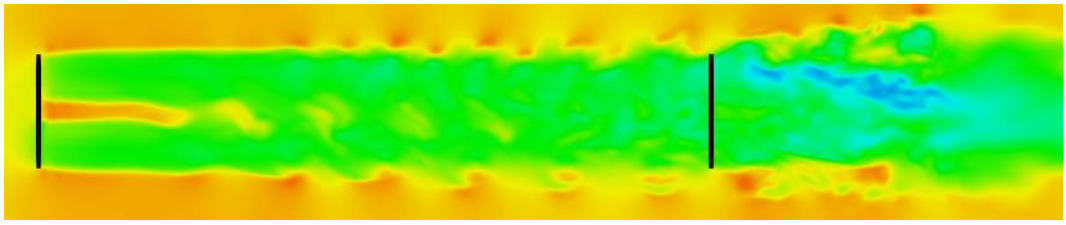

(a_1)

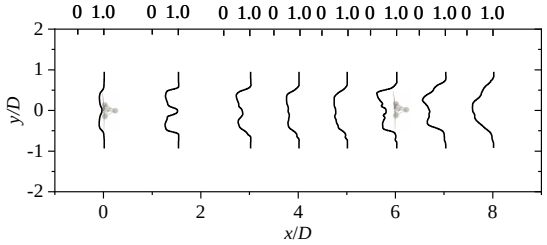

(a_2)

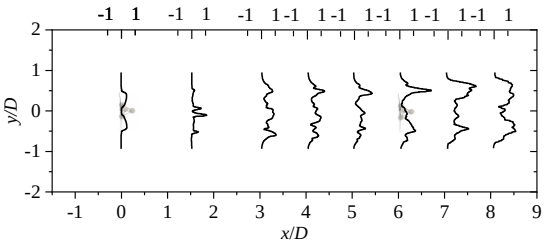

(a_3)

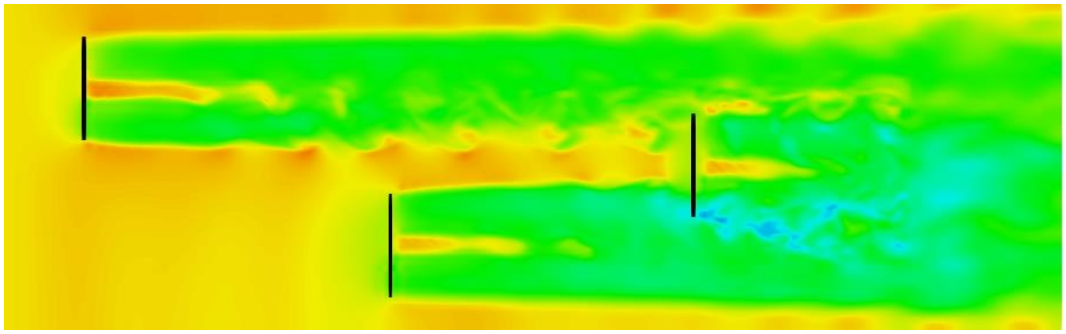

(b_1)

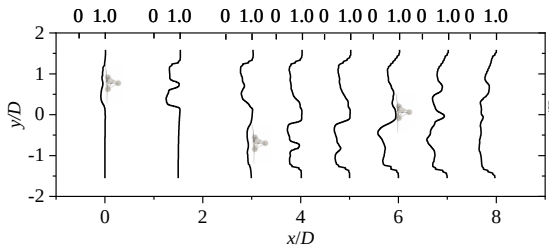

(b_2)

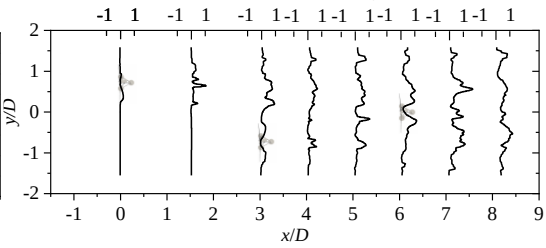

(b_3)

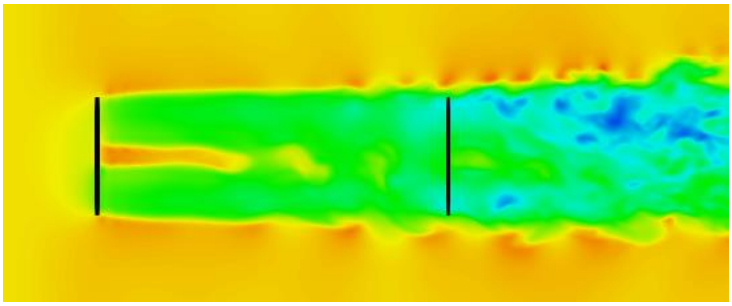

(c_1)

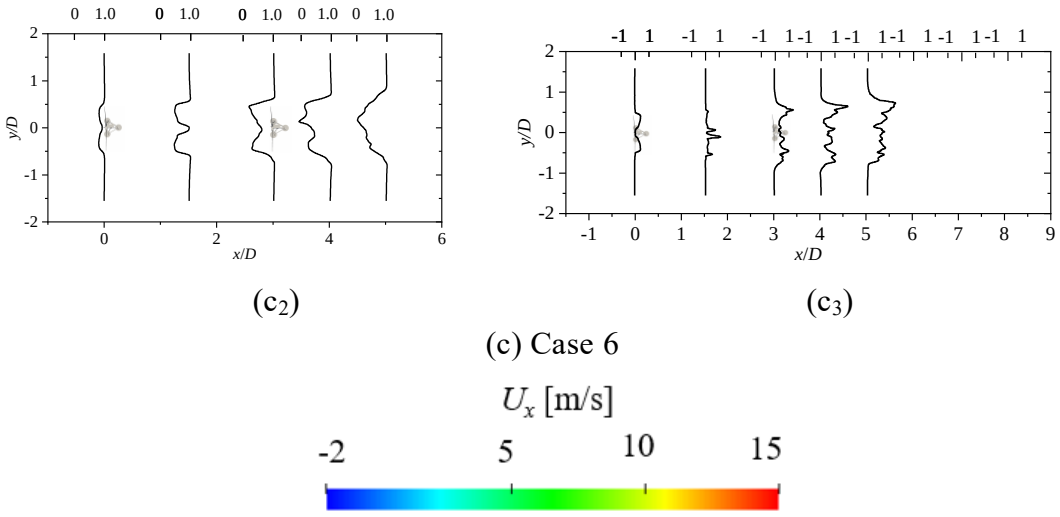

(c_2) (c_3)

(c) Case 6

Figure 7.26 (a_1) - (c_1) Contours of spanwise velocity at hub height for at t=200 s (a_2)-(c_2) denotes the time-averaged velocity profile u/U_∞ at different cross sections in the horizontal plane at hub height. (a_3)-(c_3) denotes the corresponding time-averaged turbulence intensity profile. The subscripts denote the case number

Figure 7.27 shows the visualisation of the vortex structures. For cases 4 and 6, due to the different spacings from the upstream turbine, the inflow conditions vary for the third turbine. In case 4, the vortices generated at the blade roots progressively mix, leading to stronger turbulence around the rotor centre compared to case 6. The components of wake turbulence also grow further than in case 4. Both lead to greater power fluctuation. In Case 5, the 3rd turbine is located between the two upstream turbines, a complete vortex structure is observable. The blade tips are influenced by the upstream vortices, which oppose the direction of those generated by the turbine itself, thus creating intense turbulent mixing and asymmetry downstream of the trailing edge. This phenomenon results in maximum energy at the blade passing frequency.

Figure 7.28 shows the time series of the third FOWT and the corresponding FFT analysis for different cases. In case 4, the frequencies corresponding to the blade passing frequency exhibit high energy density, particularly in the 1st and 2nd-order components. These components have an energy density comparable to that of the wave frequency, which results from the platform's motion. In addition, in case 4, it is observed that the energy at the wave frequency for the floating scenario is only slightly higher

than that in the bottom-fixed scenario. When increasing Δy from case 4 to case 6, the energy density at the wave frequency increases and becomes the dominant factor influencing power fluctuation in case 6.

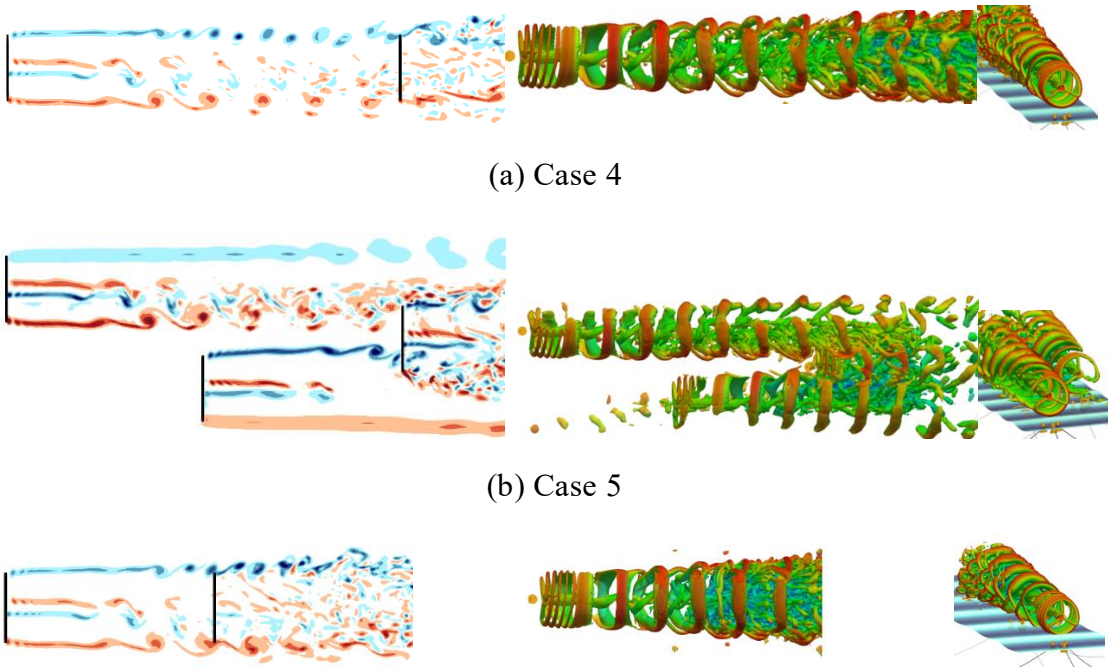

Figure 7.27 Contours of spanwise vorticity at hub height and the vortex evolution (top and side view) represented by iso-surface of q=0.002 at t=200 s of each case. The surface elevation is also presented.

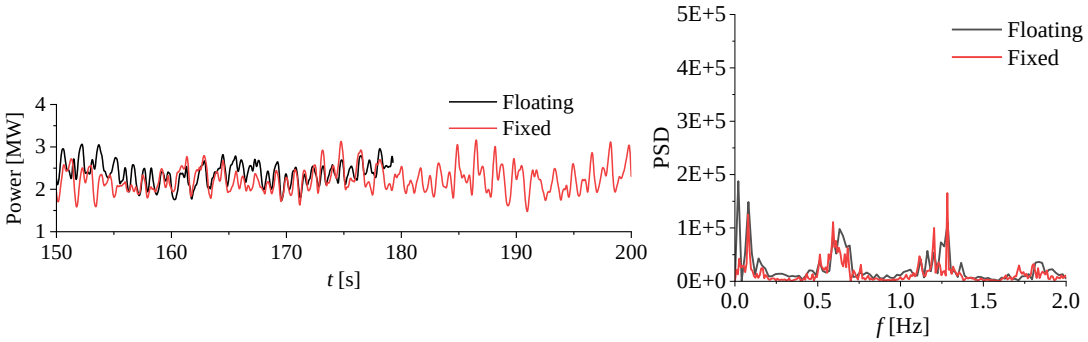

(a) Case 4 and Case 4b

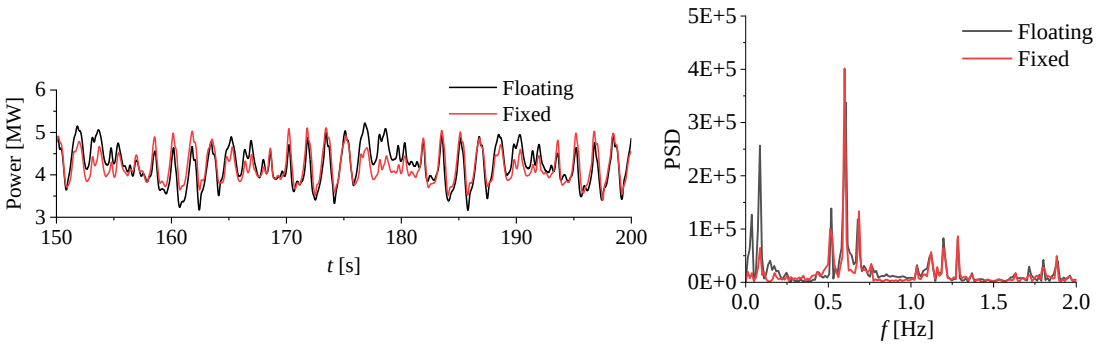

(b) Case 5 and Case 5b

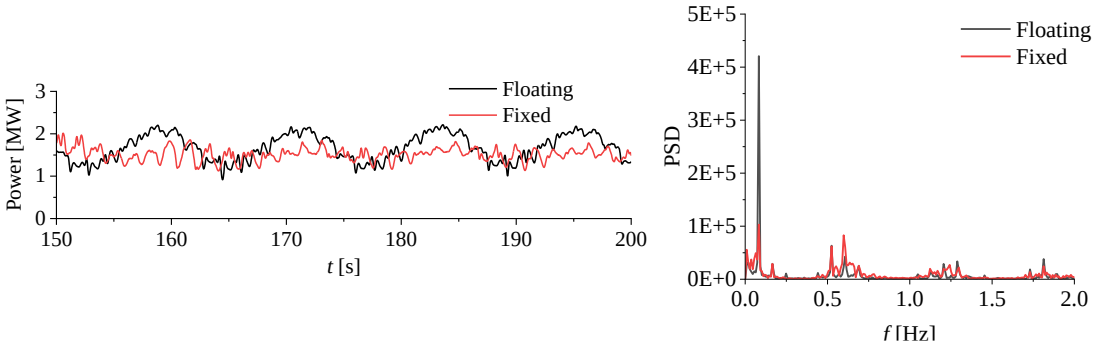

(c) Case 6 and Case 6b

Figure 7.28 Time series and FFT analysis of the power output of the third turbines

The contribution of the platform's motion varies depending on specific cases, as shown in Figure 7.29. It can be found more noticeable that the platform's motion is more influential in Case 6 than in Case 4. Combining the previous conclusion that turbulence increases with the distance between upstream and downstream turbines from the velocity profile in Figure 7.26, the main factor affecting power output becomes the turbulence rather than the platform's motion, as in Case 4. The average thrust in floating scenarios is nearly the same as in bottom-fixed ones, although the thrust amplitude in

floating scenarios is greater than in bottom-fixed ones, which is induced by the platform's motion.

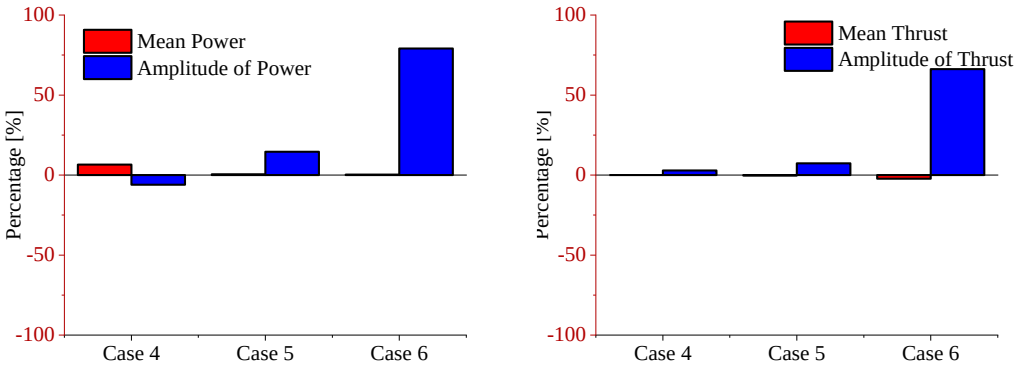

Figure 7.29 Variation in aerodynamic parameters between bottom-fixed cases and FOWT cases, expressed as a percentage of the differences observed in the FOWT cases

7.7 Concluding Remarks

This Chapter studies wave interaction with multiple FOWTs with different layouts in which a significant wake interaction exists. To save the computational time cost by avoiding the meshing of the blades, the ALM is coupled with the present tool to solve the aerodynamics. The hydrodynamics are solved simultaneously with aerodynamics in the same computational domain.

Different phenomena are observed for gridded and staggered layouts. In gridded layouts, wind speed loss is most significant at the 3rd turbine due to interference between wakes, resulting in the lowest power output. The further this turbine is moved perpendicularly from the wind direction, the greater its power output becomes. For staggered layouts, when the 3rd turbine is positioned between two upstream turbines, its power can reach 70% of the upstream turbine's output. Compared to gridded layouts, staggered arrangements allow for more turbines to be accommodated in a limited space while still achieving substantial power outputs.

The comparison reveals that whether the 3rd turbine is fixed or not has an impact on its

average power, although the difference is not particularly significant, with a gap of less than 6%. However, the motion of the turbines significantly affects the amplitude of power fluctuations. In the case of gridded layouts, the fluctuation amplitude of the mobile turbines can be up to 25% higher than that of the fixed turbines. For staggered layouts, this figure can reach 80%.

Spectral analysis also shows that in Case 1 of gridded layout, the impact of platform motion on power fluctuations diminishes from upstream to downstream while the influence of wind turbulence increases. This implies that under more turbulent wind conditions, the influence of the platform's motion on power generation is reduced.

The efficiency gap between different layouts is significant in terms of total power output. For example, for a tandem layout (case 1), the FOWT system's total power output is 50% of its total output when there is no wake interference, while it is 92% for staggered layouts (case 5). Thus, it can be concluded that staggered layouts are more efficient than gridded layouts.

Chapter 8 Conclusions and Future Work

To conduct CFD research on the FSI problems encountered for WECs and FOWTs, a further developed tool based on the original OpenFOAM is developed. Depending on different scenarios, various coupling strategies have been used. In the WEC net and flexible WEC research in Chapters 4-5, multibody dynamic and finite element solvers are coupled. In the FOWT studies in Chapter 7, ALM is integrated. The main conclusions from these studies are listed in section 8.1. The recommendations for future work, improvement, and other potential applications of the present tool have also been included.

8.1 Conclusions

8.1.1 Mechanically Interconnected WEC Net

To achieve the first objective in section 1.5, multibody solver MBDyn is coupled with the present CFD solver. With this, the WEC net, which contains multiple mechanically connected components, the Albatern squid WEC, is studied. The following conclusions are drawn from this study:

1. The mechanical linking arms play a significant role in the dynamic motion responses of individual float. It can provide significant restraints to prevent large deformation of the WEC net layout under regular wave conditions.

2. Electric damping and wave period has significant effects on the power output of WEC net. The optimal electrical damping changes with the specific wave conditions.

3. The optimal power capture increases from 4.5kW to 15kW when the wave period decreases from 10.5s to 8.5s

8.1.2 Novel Flexible WEC

To achieve the second objective in section 1.5, the finite element solver CalculiX is coupled with the present CFD solver. With this, the performance of a novel flexible WEC is studied with either linear-elastic or hyper-elastic materials. The following

conclusions are drawn from this study:

1. For the studied flexible WEC, results show that it can achieve considerable without resonance, which means there's no significant reduction in power output when the wave condition changes. This is its advantages compared to traditional WECs.

2. Material selection has a big influence on its performance. For linear elastic material, an increased water depth above the membrane worsens its deformability. This is adverse for the power output. However, hyper-elastic material is seen to do the opposite of this phenomenon.

3. By selecting the hyper-elastic material, the dynamic motion of an fWEC can be three times larger than a linear one. Adjusting the hyper-elastic mechanical parameters can increase this ratio up to six times for the hyper-elastic material.

8.1.3 FOWT Platforms in Wave-current Conditions

To achieve the third objective in section 1.5, the dynamic response of the floating platform in complex sea conditions is numerically studied using a high-fidelity CFD tool. The following conclusions are drawn from this study:

1. For current-only scenarios, compared to semi-submersible platform, obvious VIM is not seen within selected V_r for barge platform, indicating there is little chance for a floating barge platform undergoing a lock-in phenomenon.

2. For current-wave condition, the angle between the directions of wave and current significantly affect the platform's CF motion. Increasing this angle from 0◦ to 90◦ leads to a more significant VIM and larger CF motion.

3. In current-wave conditions, the most extreme sway motion does not necessarily occur with the largest wave height. With specific cases with a smaller wave height, the sway motion exceeds the sum sway motion in wave and current conditions separately.

8.1.4 Fully Coupled FOWT Array in Regular Wave Conditions

ALM is incorporated into the current tool to achieve the fourth objective in section 1.5. The dynamic response, aerodynamic performance, and wake interaction of three FOWTs in regular wave conditions are studied. The following conclusions are drawn from this study:

1. In gridded layouts, the third turbine experiences the most significant wind velocity reduction due to wake interference, leading to the lowest power output. However, as this turbine is moved along the *y*-axis, its power output increases. In staggered layouts, positioning the third turbine between two upstream ones can result in it achieving up to 70% of the power output of the upstream turbines.

2. In gridded layouts, the efficiency of the three-turbine system is lower than in staggered layouts. In the most common scenarios, the total efficiency of a tandem layout (case 1) is 50%, while it is 92% for staggered layouts (case 5).

3. The comparison shows that whether the third downstream turbine is fixed or not impacts its average power, but the difference is minor, with less than a 6% gap. However, turbine movement significantly influences power fluctuation amplitude. In gridded layouts, mobile turbines can have up to 25% higher fluctuation amplitude than fixed turbines, while in staggered layouts, this figure can reach 80%.

8.2 Future Work

This research mainly focuses on various aspects of WEC and FOWT. To achieve this goal, many open-source and in-house codes are coupled with the present OpenFOAM-based tool. However, due to the limited time and computational resources available, the present tool still has some shortcomings. In addition, it also has many other potentials in the ocean renewable energy fields, which are shown below:

1. Because of the limitations for handling moving mesh associated with large CFD mesh rotation, it is deemed unsuitable for utilising the present numerical tool to study the

Albatern WEC net with a very large rotational motion that deteriorates the mesh quality. This hinders the investigation of cases with smaller wave periods. Further developments will be needed to cope with this problem, such as using an arbitrary mesh interface (AMI) sliding mesh or an overset mesh strategy.

2. In the WEC net study in Chapter 4, the wave parameters significantly influence the optimal electric damping. Future studies should investigate the WEC performance in irregular wave conditions. Besides, to adjust the optimal electric damping according to the varying conditions, a control strategy can be applied to increase total power output.

3. For the flexible WEC study, the WEC is simplified as two-dimensional. The boundary condition is inconsistent with the real, three-dimensional application. Thus, three-dimensional research needs to be conducted in the future.

4. In wave-current interactions with FOWT, this study only considered the hydrodynamic part. The influence of the turbines is not considered. Thus, future work includes studying the fully coupled FOWT under wave-current conditions. The tool with ALM integrated in Chapter 7 can be utilised for this problem. In present studies, the rotational degrees are not enabled. In future work, the yaw motion due to VIM should be studied in detail, as well as its influence on the power output of the upper turbines.

5. The NREL 5WM turbines have been widely studied in much research. In the future. the latest FOWTs with higher power capacity should be studied using the coupled ALM CFD tool. Aeroelastic analysis can be performed on these turbines to evaluate their aerodynamic performance and motion response.

6. The present tool, which is used in separate research, involves multibody, finite element, and ALM models. Due to time limits, they are not all included in one framework into a more universal tool, which is recommended in future work. With that, more potential research can be conducted, such as hybrid WEC-FOWT systems or floating structures involving rigid and flexible sub-components.

References

Agamloh, E. B., Wallace, A. K., and Von Jouanne, A. (2008). Application of fluid–structure interaction simulation of an ocean wave energy extraction device. Renewable Energy, 33(4), 748-757.

Albert, A., Berselli, G., Bruzzone, L., and Fanghella, P. (2017). Mechanical design and simulation of an onshore four-bar wave energy converter. Renewable Energy, 114, 766-774.

Arabgolarcheh, A., Jannesarahmadi, S., and Benini, E. (2022). Modeling of near wake characteristics in floating offshore wind turbines using an actuator line method. Renewable Energy, 185, 871-887.

Arabgolarcheh, A., Micallef, D., and Benini, E. (2023). The impact of platform motion phase differences on the power and load performance of tandem floating offshore wind turbines. Energy, 129271.

Arabgolarcheh, A., Micallef, D., Rezaeiha, A., and Benini, E. (2023a). Modelling of two tandem floating offshore wind turbines using an actuator line model. Renewable Energy, 216. https://doi.org/10.1016/j.renene.2023.119067

Arabgolarcheh, A., Rouhollahi, A., and Benini, E. (2023). Analysis of middle-to-far wake behind floating offshore wind turbines in the presence of multiple platform motions. Renewable Energy, 208, 546-560.

Archer, C. L., and Jacobson, M. Z. (2005). Evaluation of global wind power. Journal of Geophysical Research: Atmospheres, 110(D12).

Avilés, A. V. (2009). Wave energy converters.

Babarit, A., Singh, J., Mélis, C., Wattez, A., and Jean, P. (2017). A linear numerical model for analysing the hydroelastic response of a flexible electroactive wave energy converter. Journal of Fluids and Structures, 74, 356-384.

https://doi.org/10.1016/j.jfluidstructs.2017.06.003

Bao, Y., Huang, C., Zhou, D., Tu, J., and Han, Z. (2012). Two-degree-of-freedom flow-induced vibrations on isolated and tandem cylinders with varying natural frequency ratios. Journal of Fluids and Structures, 35, 50-75. https://doi.org/10.1016/j.jfluidstructs.2012.08.002

Bayati, I., Belloli, M., Bernini, L., Fiore, E., Giberti, H., and Zasso, A. (2016). On the functional design of the DTU10 MW wind turbine scale model of LIFES50+ project. Journal of Physics: Conference Series,

Bayati, I., Gueydon, S., and Belloli, M. (2015). Study of the effect of water depth on potential flow solution of the OC4 semisubmersible floating offshore wind turbine. Energy Procedia, 80, 168-176.

Bayati, I., Jonkman, J., Robertson, A., and Platt, A. (2014). The effects of second-order hydrodynamics on a semisubmersible floating offshore wind turbine. Journal of Physics: Conference Series,

Beardsell, A., Alexandre, A., Child, B., Harries, R., and McCowen, D. (2018). Beyond OC5–Further advances in floating wind turbine modelling using Bladed. Journal of Physics: Conference Series,

Bergua, R., Robertson, A., Jonkman, J., Branlard, E., Fontanella, A., Belloli, M., Schito, P., Zasso, A., Persico, G., and Sanvito, A. (2022). OC6 project Phase III: validation of the aerodynamic loading on a wind turbine rotor undergoing large motion caused by a floating support structure. Wind Energy Science Discussions, 2022, 1-33.

Bose, B. K. (2010). Global warming: Energy, environmental pollution, and the impact of power electronics. IEEE Industrial Electronics Magazine, 4(1), 6-17.

Bungartz, H.-J., Lindner, F., Gatzhammer, B., Mehl, M., Scheufele, K., Shukaev, A., and Uekermann, B. (2016). preCICE–a fully parallel library for multi-physics surface

coupling. Computers and Fluids, 141, 250-258.

Burmester, S., Gueydon, S., Vaz, G., and el Moctar, B. (2017). Surge decay simulations of a semi-submersible floating offshore wind turbine. Proceedings of the 20th numerical towing tank symposium,

Burmester, S., Vaz, G., Gueydon, S., and el Moctar, O. (2020). Investigation of a semi-submersible floating wind turbine in surge decay using CFD. Ship Technology Research, 67(1), 2-14.

Cao, F., Yu, M., Han, M., Liu, B., Wei, Z., Jiang, J., Tian, H., Shi, H., and Li, Y. (2023). WECs microarray effect on the coupled dynamic response and power performance of a floating combined wind and wave energy system. Renewable Energy, 219, 119476.

Carballo, R., Iglesias, G. (2013). Wave farm impact based on realistic wave-WEC interaction. Energy, 51, 216-229.

Causin, P., Gerbeau, J.-F., and Nobile, F. (2005). Added-mass effect in the design of partitioned algorithms for fluid–structure problems. Computer Methods in Applied Mechanics and Engineering, 194(42-44), 4506-4527.

Causin, P., Gerbeau, J. F., and Nobile, F. (2005). Added-mass effect in the design of partitioned algorithms for fluid–structure problems. Computer Methods in Applied Mechanics and Engineering, 194(42-44), 4506-4527. https://doi.org/10.1016/j.cma.2004.12.005

Cermelli, C., Roddier, D., and Aubault, A. (2009). WindFloat: a floating foundation for offshore wind turbines—part II: hydrodynamics analysis. International conference on offshore mechanics and arctic engineering,

Chandrasekaran, S., and Sricharan, V. (2021). Numerical study of bean-float wave energy converter with float number parametrization using WEC-Sim in regular waves with the Levelized Cost of Electricity assessment for Indian sea states. Ocean

Engineering, 237, 109591.

Chandrasekaran, S., and Sricharan, V. V. S. (2020). Numerical analysis of a new multi-body floating wave energy converter with a linear power take-off system. Renewable Energy, 159, 250-271. https://doi.org/10.1016/j.renene.2020.06.007

Chao, Z., Yage, Y., and Aiju, C. (2018). Hydrodynamics research of a two-body articulated wave energy device. Ocean Engineering, 148, 202-210.

Chaplin, J., Heller, V., Farley, F., Hearn, G., and Rainey, R. (2012). Laboratory testing the Anaconda. Philosophical Transactions of the Royal Society A: Mathematical, Physical and Engineering Sciences, 370(1959), 403-424.

Checkmate Seaenergy Limited. (2013). Sea Energy Anaconda. https://www.checkmateukseaenergy.com/

Chen, W., Dolguntseva, I., Savin, A., Zhang, Y., Li, W., Svensson, O., and Leijon, M. (2017). Numerical modelling of a point-absorbing wave energy converter in irregular and extreme waves. Applied Ocean Research, 63, 90-105. https://doi.org/10.1016/j.apor.2017.01.004

Chourdakis, G., Davis, K., Rodenberg, B., Schulte, M., Simonis, F., Uekermann, B., Abrams, G., Bungartz, H.-J., Yau, L. C., and Desai, I. (2021). preCICE v2: A sustainable and user-friendly coupling library. arXiv preprint arXiv:2109.14470.

Clément, A., McCullen, P., Falcão, A., Fiorentino, A., Gardner, F., Hammarlund, K., Lemonis, G., Lewis, T., Nielsen, K., and Petroncini, S. (2002). Wave energy in Europe: current status and perspectives. Renewable and Sustainable Energy Reviews, 6(5), 405-431.

Collins, I., Hossain, M., Dettmer, W., and Masters, I. (2021). Flexible membrane structures for wave energy harvesting: A review of the developments, materials and computational modelling approaches. Renewable and Sustainable Energy Reviews, 151.

https://doi.org/10.1016/j.rser.2021.111478

Council, W. E. (1994). New renewable energy resources: a guide to the future. Kogan Page.

Cueva, M., Fujarra, A. L., Nishimoto, K., Quadrante, L. s., and Costa, A. P. (2006). Vortex-induced motion: model testing of a monocolumn floater. International Conference on Offshore Mechanics and Arctic Engineering,

Dang, T. D., Phan, C. B., and Ahn, K. K. (2019). Modeling and experimental investigation on performance of a wave energy converter with mechanical power take-off. International Journal of Precision Engineering and Manufacturing-Green Technology, 6(4), 751-768.

Davidson, J., and Costello, R. (2020). Efficient nonlinear hydrodynamic models for wave energy converter design—A scoping study. Journal of Marine Science and Engineering, 8(1), 35.

Degroote, J., Bathe, K.-J., and Vierendeels, J. (2009). Performance of a new partitioned procedure versus a monolithic procedure in fluid–structure interaction. Computers and Structures, 87(11-12), 793-801.

Devolder, B., Stratigaki, V., Troch, P., and Rauwoens, P. (2018). CFD simulations of floating point absorber wave energy converter arrays subjected to regular waves. Energies, 11(3), 641.

Dhondt, G. (2004). The finite element method for three-dimensional thermomechanical applications. John Wiley and Sons.

Drew, B., Plummer, A. R., and Sahinkaya, M. N. (2016). A review of wave energy converter technology. Proceedings of the Institution of Mechanical Engineers, Part A: Journal of Power and Energy, 223(8), 887-902. https://doi.org/10.1243/09576509jpe782

Du, Z., Li, X., Xu, W., Zhu, H., Feng, J., Shen, W., and Jin, R. (2022). An experimental investigation on vortex-induced motion (VIM) of a tension leg platform in irregular waves combined with a uniform flow. Applied Ocean Research, 123, 103185.

Edwards, K., Mekhiche, M. (2014). Ocean power technologies powerbuoy®: system-level design, development and validation methodology.

Eich-Soellner, E., and Führer, C. (1998). Numerical methods in multibody dynamics (Vol. 45). Springer.

Energy Institute. (2023). Statistical Review of World Energy 2023.

ESO, N. G. (2021). Future Energy Scenarios

Esteban, M. D., Diez, J. J., López, J. S., and Negro, V. (2011). Why offshore wind energy? Renewable Energy, 36(2), 444-450. https://doi.org/10.1016/j.renene.2010.07.009

[Record #448 is using a reference type undefined in this output style.]

Falnes, J. (2007). A review of wave-energy extraction. Marine Structures, 20(4), 185-201.

Fan, Z., Li, S., Gao, Z., Zhang, L., Zheng, X., Zhu, W., Shen, W., Sjöholm, M., Mikkelsen, T. K., and Wang, T. (2023). On the importance of wind turbine wake boundary to wind energy and environmental impact. Energy Conversion and Management, 277, 116664.

Farley, F., Rainey, R., and Chaplin, J. (2012). Rubber tubes in the sea. Philosophical Transactions of the Royal Society A: Mathematical, Physical and Engineering Sciences, 370(1959), 381-402.

Farrugia, R., Sant, T., and Micallef, D. (2014). Investigating the aerodynamic performance of a model offshore floating wind turbine. Renewable Energy, 70, 24-30.

Finnegan, W., and Goggins, J. (2012). Numerical simulation of linear water waves and wave–structure interaction. Ocean Engineering, 43, 23-31.

Finnigan, T., Irani, M., and Van Dijk, R. (2005). Truss Spar VIM in waves and currents. International Conference on Offshore Mechanics and Arctic Engineering,

Fleming, P., Gebraad, P. M. O., Lee, S., van Wingerden, J.-W., Johnson, K., Churchfield, M., Michalakes, J., Spalart, P., and Moriarty, P. (2015). Simulation comparison of wake mitigation control strategies for a two-turbine case. Wind Energy, 18(12), 2135-2143. https://doi.org/10.1002/we.1810

Folley, M., Babarit, A., Child, B., Forehand, D., O'Boyle, L., Silverthorne, K., Spinneken, J., Stratigaki, V., and Troch, P. (2012). A review of numerical modelling of wave energy converter arrays. International Conference on Offshore Mechanics and Arctic Engineering,

Froese, G., Ku, S. Y., Kheirabadi, A. C., and Nagamune, R. (2022). Optimal layout design of floating offshore wind farms. Renewable Energy, 190, 94-102. https://doi.org/10.1016/j.renene.2022.03.104

Fu, S., Li, Z., Zhu, W., Han, X., Liang, X., Yang, H., and Shen, W. (2023). Study on aerodynamic performance and wake characteristics of a floating offshore wind turbine under pitch motion. Renewable Energy, 205, 317-325.

Fujarra, A. L., Cenci, F., Silva, L. S., Hirabayashi, S., Suzuki, H., and Goncalves, R. T. (2022). Effect of initial roll or pitch angles on the vortex-induced motions (VIM) of floating circular cylinders with a low aspect ratio. Ocean Engineering, 257, 111574.

Ghiringhelli, G. L., Masarati, P., and Mantegazza, P. (2000). Multibody implementation of finite volume C beams. AIAA journal, 38(1), 131-138.

Glasdam, J. B., Kocewiak, L., Hjerrild, J., Bak, C. L., and Zeni, L. (2014). Comparison of field measurements and EMT simulation results on a multi-level STATCOM for grid

integration of London array wind farm. 45th 2014 CIGRE Session,

Glauert, H. (1935). Airplane propellers. Aerodynamic theory.

Gonçalves, R. T., Chame, M. E. F., Silva, L. S. P., Koop, A., Hirabayashi, S., and Suzuki, H. (2021). Experimental Flow-Induced Motions of a FOWT Semi-Submersible Type (OC4 Phase II Floater). Journal of Offshore Mechanics and Arctic Engineering, 143(1). https://doi.org/10.1115/1.4048149

Gonçalves, R. T., Fujarra, A. L., Rosetti, G. F., and Nishimoto, K. (2010). Mitigation of vortex-induced motion (VIM) on a monocolumn platform: forces and movements. Journal of Offshore Mechanics and Arctic Engineering, 132(4).

Gonçalves, R. T., Pinto, L. A., and Fujarra, A. L. C. (2020). Experimental study on vortex-induced motions of a semi-submersible platform with four square columns, part III: Effects of the collinear irregular and regular wave incidence and current. Ocean Engineering, 217. https://doi.org/10.1016/j.oceaneng.2020.107585

Gonçalves, R. T., Rosetti, G. F., Franzini, G. R., Meneghini, J. R., and Fujarra, A. L. C. (2013). Two-degree-of-freedom vortex-induced vibration of circular cylinders with very low aspect ratio and small mass ratio. Journal of Fluids and Structures, 39, 237-257. https://doi.org/10.1016/j.jfluidstructs.2013.02.004

Gonçalves, R. T., Rosetti, G. F., Fujarra, A. L., and Nishimoto, K. (2012). An overview of relevant aspects on VIM of spar and monocolumn platforms. Journal of Offshore Mechanics and Arctic Engineering, 134(1).

Gonçalves, R.T., Rosetti, G. F., Fujarra, A. L. C., and Oliveira, A. C. (2012). Experimental study on vortex-induced motions of a semi-submersible platform with four square columns, Part I: Effects of current incidence angle and hull appendages. Ocean Engineering, 54, 150-169. https://doi.org/10.1016/j.oceaneng.2012.06.032

Gonçalves, R. T., Rosetti, G. F., Fujarra, A. L. C., and Oliveira, A. C. (2013).

Experimental study on vortex-induced motions of a semi-submersible platform with four square columns, Part II: Effects of surface waves, external damping and draft condition. Ocean Engineering, 62, 10-24. https://doi.org/10.1016/j.oceaneng.2013.01.019

González-Longatt, F., Wall, P., and Terzija, V. (2012). Wake effect in wind farm performance: Steady-state and dynamic behavior. Renewable Energy, 39(1), 329-338.

Grubb, M. J., and Meyer, N. I. (1993). Wind energy: resources, systems, and regional strategies.

Habchi, C., Russeil, S., Bougeard, D., Harion, J.-L., Lemenand, T., Ghanem, A., Della Valle, D., and Peerhossaini, H. (2013). Partitioned solver for strongly coupled fluid–structure interaction. Computers and Fluids, 71, 306-319.

Haelterman, R., Bogaers, A. E., Scheufele, K., Uekermann, B., and Mehl, M. (2016). Improving the performance of the partitioned QN-ILS procedure for fluid–structure interaction problems: Filtering. Computers and Structures, 171, 9-17.

Han, C., and Nagamune, R. (2016). Position control of an offshore wind turbine with a semi-submersible floating platform using the aerodynamic force. 2016 IEEE Canadian Conference on Electrical and Computer Engineering (CCECE),

Henderson, R. (2006). Design, simulation, and testing of a novel hydraulic power take-off system for the Pelamis wave energy converter. Renewable Energy, 31(2), 271-283.

Heo, S., and Koo, W. (2021). Dynamic response analysis of a wavestar-type wave energy converter using augmented formulation in Korean nearshore areas. Processes, 9(10), 1721.

Higuera, P. (2020). Enhancing active wave absorption in RANS models. Applied Ocean Research, 94. https://doi.org/10.1016/j.apor.2019.102000

Hirt, C. W., and Nichols, B. D. (1981). Volume of fluid (VOF) method for the dynamics

of free boundaries. Journal of computational physics, 39(1), 201-225.

Holierhoek, J., De Vaal, J., Van Zuijlen, A., and Bijl, H. (2013). Comparing different dynamic stall models. Wind Energy, 16(1), 139-158.

Hoogwijk, M., and Graus, W. (2008). Global potential of renewable energy sources: a literature assessment. Background report prepared by order of REN21. Ecofys, PECSNL072975.

Huang, H., and Chen, H.-C. (2020). Investigation of mooring damping effects on vortex-induced motion of a deep draft semi-submersible by coupled CFD-FEM analysis. Ocean Engineering, 210. https://doi.org/10.1016/j.oceaneng.2020.107418

Huang, H., Gu, H., and Chen, H.-C. (2022). A new method to couple FEM mooring program with CFD to simulate Six-DoF responses of a moored body. Ocean Engineering, 250, 110944.

Huang, Y., Xiao, Q., Idarraga, G., Yang, L., Dai, S., Abad, F., Brennan, F., and Lotfian, S. (2023a). Novel computational fluid dynamics-finite element analysis solution for the study of flexible material wave energy converters. Physics of Fluids, 35(8).

Huang, Y., Xiao, Q., Idarraga, G., Yang, L., Dai, S., Abad, F., Brennan, F., and Lotfian, S. (2023b). Numerical Analysis of Flexible Tube Wave Energy Convertor Using CFD-FEA Method. International Conference on Offshore Mechanics and Arctic Engineering,

Huang, Y., Zhao, W., and Wan, D. (2023). Wake interaction between two spar-type floating offshore wind turbines under different layouts. Physics of Fluids, 35(9). https://doi.org/10.1063/5.0161759

Huang, Y., Zhuang, Y., and Wan, D. (2021). Hydrodynamic study and performance analysis of the OC4-DeepCWind platform by CFD method. International Journal of Computational Methods, 18(04), 2050020.

IRENA. (2018). Renewable energy prospects for the European Union. International

Renewable Energy Agency (IRENA), European Commission (EC), Abu Dhabi.

IRENA. (2019). global energy transformation: A roadmap to 2050 (2019 edition), international renewable energy agency.

Iwagaki, Y., and Asano, T. (1984). Hydrodynamic forces on a circular cylinder due to combined wave and current loading. Coastal Engineering.

Jeon, M., Lee, S., and Lee, S. (2014). Unsteady aerodynamics of offshore floating wind turbines in platform pitching motion using vortex lattice method. Renewable Energy, 65, 207-212.

Jiménez, Á., Crespo, A., and Migoya, E. (2010). Application of a LES technique to characterize the wake deflection of a wind turbine in yaw. Wind Energy, 13(6), 559-572.

Johansen, J., Sørensen, N. N., Michelsen, J., and Schreck, S. (2002). Detached-eddy simulation of flow around the NREL Phase VI blade. Wind Energy: An International Journal for Progress and Applications in Wind Power Conversion Technology, 5(2-3), 185-197.

Jonkman, J. M. (2007). Dynamics modeling and loads analysis of an offshore floating wind turbine. University of Colorado at Boulder.

Jonkman, J. M., and Jonkman, B. J. (2016). FAST modularization framework for wind turbine simulation: full-system linearization. Journal of Physics: Conference Series,

Karimirad, M. (2013). Modeling aspects of a floating wind turbine for coupled wave–wind-induced dynamic analyses. Renewable Energy, 53, 299-305.

Kheirabadi, and Nagamune. (2019). Modeling and power optimization of floating offshore wind farms with yaw and induction-based turbine repositioning. 2019 American Control Conference (ACC),

Kheirabadi, A. C., and Nagamune, R. (2019). A quantitative review of wind farm control with the objective of wind farm power maximization. Journal of Wind Engineering and Industrial Aerodynamics, 192, 45-73. https://doi.org/10.1016/j.jweia.2019.06.015

Kheirabadi, A. C., and Nagamune, R. (2020). Real-time relocation of floating offshore wind turbine platforms for wind farm efficiency maximization: An assessment of feasibility and steady-state potential. Ocean Engineering, 208, 107445.

Kheirabadi, A. C., and Nagamune, R. (2021). A low-fidelity dynamic wind farm model for simulating time-varying wind conditions and floating platform motion. Ocean Engineering, 234. https://doi.org/10.1016/j.oceaneng.2021.109313

King, A., Algie, C., Ryan, S., and Ong, R. (2016). Modelling of fluid structure interactions in submerged flexible membranes for the bombora wave energy converter. 20th Australasian Fluid Mechanics Conference, Perth, Australia,

Kocurek, D. (1987). Lifting surface performance analysis for horizontal axis wind turbines. NASA STI/Recon Technical Report N, 87, 29946.

Kosasih, K. M. A., Niizato, H., Okubo, S., Mitani, S., and Suzuki, H. (2019). Wave tank experiment and coupled simulation analysis of barge-type offshore wind turbine. The 29th International Ocean and Polar Engineering Conference,

Krewitt, W., Nienhaus, K., Kleßmann, C., Capone, C., Stricker, E., Graus, W., Hoogwijk, M., Supersberger, N., Winterfeld, U. v., and Samadi, S. (2009). Role and potential of renewable energy and energy efficiency for global energy supply.

Krogstad, P.-Å., Eriksen, P., and Melheim, J. (2011). Blind test workshop; calculations for a model wind turbine. Summary report, 10.

Krogstad, P.-Å., and Eriksen, P. E. (2013). “Blind test” calculations of the performance and wake development for a model wind turbine. Renewable Energy, 50, 325-333.

https://doi.org/10.1016/j.renene.2012.06.044

Kurniawan, A., Chaplin, J., Greaves, D., and Hann, M. (2017). Wave energy absorption by a floating air bag. Journal of Fluid Mechanics, 812, 294-320.

Kyle, R., and Früh, W.-G. (2022). The transitional states of a floating wind turbine during high levels of surge. Renewable Energy, 200, 1469-1489.

Kyle, R., Lee, Y. C., and Früh, W.-G. (2020). Propeller and vortex ring state for floating offshore wind turbines during surge. Renewable Energy, 155, 645-657.

Landgrebe, A. J. (1969). An analytical method for predicting rotor wake geometry. Journal of the American Helicopter Society, 14(4), 20-32.

Landgrebe, A. J. (1972). The wake geometry of a hovering helicopter rotor and its influence on rotor performance. Journal of the American Helicopter Society, 17(4), 3-15.

Lawson, M., Yu, Y.-H., Ruehl, K., and Michelen, C. (2014). Development and demonstration of the WEC-Sim wave energy converter simulation tool.

Leble, V., and Barakos, G. (2017). 10-MW wind turbine performance under pitching and yawing motion. Journal of solar energy engineering, 139(4), 041003.

Leclerc, C., Masson, C., Ammara, I., and Paraschivoiu, I. (1999). Turbulence modeling of the flow around horizontal axis wind turbines. Wind Engineering, 279-294.

Lee, H., Poguluri, S. K., and Bae, Y. H. (2018). Performance analysis of multiple wave energy converters placed on a floating platform in the frequency domain. Energies, 11(2), 406.

Li, X., Xiao, Q., Gonçalves, R. T., and Peyrard, C. (2022). A coupled wave-current-structure study for a floating offshore wind turbine platform. International Conference on Offshore Mechanics and Arctic Engineering,

Li, X., Xiao, Q., Luo, Y., Moretti, G., Fontana, M., and Righi, M. (2021). Dynamic response of a novel flexible wave energy converter under regular waves. The 14th European Wave and Tidal Energy Conference,

Li, X., Xiao, Q., Zhou, Y., Ning, D., Incecik, A., Nicoll, R., McDonald, A., and Campbell, D. (2022). Coupled CFD-MBD numerical modeling of a mechanically coupled WEC array. Ocean Engineering, 256, 111541.

Lin, L., Wang, K., and Vassalos, D. (2018). Detecting wake performance of floating offshore wind turbine. Ocean Engineering, 156, 263-276.

Lindner, F., Mehl, M., and Uekermann, B. (2017). Radial basis function interpolation for black-box multi-physics simulations.

Liu, X., Chen, Z., Si, Y., Qian, P., Wu, H., Cui, L., and Zhang, D. (2021). A review of tidal current energy resource assessment in China. Renewable and Sustainable Energy Reviews, 145. https://doi.org/10.1016/j.rser.2021.111012

Liu, Y., Ge, D., Bai, X., and Li, L. (2023). A CFD Study of Vortex-Induced Motions of a Semi-Submersible Floating Offshore Wind Turbine. Energies, 16(2). https://doi.org/10.3390/en16020698

Liu, Y., Liu, F., Xiao, Q., and Zhou, L. (2020). The effect of inclination on vortex-induced vibration of a circular cylinder with a base column. Ocean Engineering, 206. https://doi.org/10.1016/j.oceaneng.2020.107332

Liu, Y., Xiao, Q., Incecik, A., and Peyrard, C. (2019). Aeroelastic analysis of a floating offshore wind turbine in platform-induced surge motion using a fully coupled CFD-MBD method. Wind Energy, 22(1), 1-20.

Liu, Y., Xiao, Q., Incecik, A., Peyrard, C., and Wan, D. (2017). Establishing a fully coupled CFD analysis tool for floating offshore wind turbines. Renewable Energy, 112, 280-301.

Luo, Y., Xiao, Q., Shi, G., Pan, G., and Chen, D. (2020). The effect of variable stiffness of tuna-like fish body and fin on swimming performance. Bioinspiration and Biomimetics, 16(1), 016003.

Luo, Y., Xiao, Q., Zhu, Q., and Pan, G. (2020). Pulsed-jet propulsion of a squid-inspired swimmer at high Reynolds number. Physics of Fluids, 32(11). https://doi.org/10.1063/5.0027992

Luo, Y., Xiao, Q., Zhu, Q., and Pan, G. (2021). Jet propulsion of a squid-inspired swimmer in the presence of background flow. Physics of Fluids, 33(3). https://doi.org/10.1063/5.0042575

Ma, Y. (2022). Novel Modeling and Fatigue Analysis for Early-phase Design of a 15-MW FOWT NTNU].

Mahfouz, M. Y., and Cheng, P. W. (2022). A passively self-adjusting floating wind farm layout to increase the annual energy production. Wind Energy, 26(3), 251-265. https://doi.org/10.1002/we.2797

Martinot, E., Dienst, C., Weiliang, L., and Qimin, C. (2007). Renewable energy futures: Targets, scenarios, and pathways. Annu. Rev. Environ. Resour., 32, 205-239.

Martins, P., Natal Jorge, R., and Ferreira, A. (2006). A comparative study of several material models for prediction of hyperelastic properties: Application to silicone-rubber and soft tissues. Strain, 42(3), 135-147.

Masarati, P. (2017). MBDyn Input File Format Version 1.7. 3. Politecnico di Milano.

Masarati, P., and Sitaraman, J. (2011). Coupled cfd/multibody analysis of nrel unsteady aerodynamic experiment phase vi rotor. 49th AIAA Aerospace Sciences Meeting including the New Horizons Forum and Aerospace Exposition,

Matthies, H. G., and Steindorf, J. (2003). Partitioned strong coupling algorithms for fluid–structure interaction. Computers and Structures, 81(8-11), 805-812.

Maximiano, A., Koop, A., de Wilde, J., and Gonçalves, R. T. (2017). Experimental study on the vortex-induced motions (VIM) of a semi-submersible floater in waves. International Conference on Offshore Mechanics and Arctic Engineering,

Mcdonald, A., Xiao, Q., Forehand, D., Mavel, V., and Findlay, D. (2017). Experimental investigation of array effects for a mechanically coupled WEC array. 12th European Wave and Tidal Energy Conference,

Michailides, C., and Angelides, D. C. (2015). Optimization of a flexible floating structure for wave energy production and protection effectiveness. Engineering Structures, 85, 249-263. https://doi.org/10.1016/j.engstruct.2014.12.031

Moretti, G., Fontana, M., and Vertechy, R. (2015). Model-based design and optimization of a dielectric elastomer power take-off for oscillating wave surge energy converters. Meccanica, 50(11), 2797-2813. https://doi.org/10.1007/s11012-015-0235-8

Moretti, G., Papini, G. P. R., Righi, M., Forehand, D., Ingram, D., Vertechy, R., and Fontana, M. (2018). Resonant wave energy harvester based on dielectric elastomer generator. Smart Materials and Structures, 27(3). https://doi.org/10.1088/1361-665X/aaab1e

Moretti, G., Rosati Papini, G. P., Daniele, L., Forehand, D., Ingram, D., Vertechy, R., and Fontana, M. (2019). Modelling and testing of a wave energy converter based on dielectric elastomer generators. Proceedings of the Royal Society A, 475(2222), 20180566.

Moretti, G., Santos Herran, M., Forehand, D., Alves, M., Jeffrey, H., Vertechy, R., and Fontana, M. (2020). Advances in the development of dielectric elastomer generators for wave energy conversion. Renewable and Sustainable Energy Reviews, 117. https://doi.org/10.1016/j.rser.2019.109430

Moriarty, P., and Honnery, D. (2023). The energy implications of averting climate change catastrophe. Energies, 16(17), 6178.

Nicoll, R. S., Wood, C. F., and Roy, A. e. R. (2012). Comparison of Physical Model Tests with a Time Domain Simulation Model of A Wave Energy Converter OMAE2012,

Nicoud, F., and Ducros, F. (1999). Subgrid-scale stress modelling based on the square of the velocity gradient tensor. Flow, turbulence and Combustion, 62(3), 183-200.

Ning, D.-Z., Shi, J., Zou, Q.-P., and Teng, B. (2015). Investigation of hydrodynamic performance of an OWC (oscillating water column) wave energy device using a fully nonlinear HOBEM (higher-order boundary element method). Energy, 83, 177-188.

Ning, D.-Z., Wang, R.-Q., Zou, Q.-P., and Teng, B. (2016). An experimental investigation of hydrodynamics of a fixed OWC Wave Energy Converter. Applied Energy, 168, 636-648. https://doi.org/10.1016/j.apenergy.2016.01.107

Ning, D. Z., Zhao, X. L., Chen, L. F., and Zhao, M. (2018). Hydrodynamic performance of an array of wave energy converters integrated with a pontoon-type breakwater. Energies, 11(3), 685.

Nygaard, T. A., De Vaal, J., Pierella, F., Oggiano, L., and Stenbro, R. (2016). Development, verification and validation of 3DFloat; aero-servo-hydro-elastic computations of offshore structures. Energy Procedia, 94, 425-433.

Papi, F., Troise, G., Behrens de Luna, R., Saverin, J., Perez-Becker, S., Marten, D., Ducasse, M.-L., and Bianchini, A. (2023). A Code-to-Code Comparison for Floating Offshore Wind Turbine Simulation in Realistic Environmental Conditions: Quantifying the Impact of Modeling Fidelity on Different Substructure Concepts. Wind Energy Science Discussions, 2023, 1-34.

Pelc, R., Fujita, R. M. (2002). Renewable energy from the ocean. Marine Policy, 26(6), 471-479.

Penalba, M., Kelly, T., and Ringwood, J. (2017). Using NEMOH for modelling wave energy converters: A comparative study with WAMIT.

Petrilli, J. L., Paul, R. C., Gopalarathnam, A., and Frink, N. T. (2013). A CFD database for airfoils and wings at post-stall angles of attack. 31st AIAA applied aerodynamics conference,

Pierella, F., Krogstad, P.-Å., and Sætran, L. (2014). Blind Test 2 calculations for two in-line model wind turbines where the downstream turbine operates at various rotational speeds. Renewable Energy, 70, 62-77. https://doi.org/10.1016/j.renene.2014.03.034

Qian, G.-W., and Ishihara, T. (2021). Wind farm power maximization through wake steering with a new multiple wake model for prediction of turbulence intensity. Energy, 220. https://doi.org/10.1016/j.energy.2020.119680

Qiao, D., Haider, R., Yan, J., Ning, D., and Li, B. (2020). Review of wave energy converter and design of mooring system. *Sustainability*, *12*(19), 8251.

Qiu, Y.-X., Wang, X.-D., Kang, S., Zhao, M., and Liang, J.-Y. (2014). Predictions of unsteady HAWT aerodynamics in yawing and pitching using the free vortex method. Renewable Energy, 70, 93-106.

Rainey, R. (1989). A new equation for calculating wave loads on offshore structures. Journal of Fluid Mechanics, 204, 295-324.

Renzi, E. (2016). Hydroelectromechanical modelling of a piezoelectric wave energy converter. Proceedings of the Royal Society A: Mathematical, Physical and Engineering Sciences, 472(2195), 20160715.

Rezaeiha, A., and Micallef, D. (2021). Wake interactions of two tandem floating offshore wind turbines: CFD analysis using actuator disc model. Renewable Energy, 179, 859-876.

Robertson, A., Jonkman, J., Masciola, M., Song, H., Goupee, A., Coulling, A., and Luan, C. (2014). Definition of the semisubmersible floating system for phase II of OC4.

Rodrigues, S. F., Teixeira Pinto, R., Soleimanzadeh, M., Bosman, P. A. N., and Bauer,

P. (2015). Wake losses optimization of offshore wind farms with moveable floating wind turbines. Energy Conversion and Management, 89, 933-941. https://doi.org/10.1016/j.enconman.2014.11.005

Rogner, H., Barthel, F., Cabrera, M., Faaij, A., Giroux, M., Hall, D., Kagramanian, V., Kononov, S., Lefevre, T., and Moreira, R. (2000). Energy Resources in Word Energy Assessment–Energy and the Challenges of Sustainability. USA: United Nations Development Programme.

Rosati Papini, G. P., Moretti, G., Vertechy, R., and Fontana, M. (2018). Control of an oscillating water column wave energy converter based on dielectric elastomer generator. Nonlinear Dynamics, 92(2), 181-202.

Rusche, H. (2003). Computational fluid dynamics of dispersed two-phase flows at high phase fractions Imperial College London (University of London)].

Sagrilo, L. s. V. S., Queija de Siqueira, M., Gonc¸alves de Lacerda, T. A. n., Ellwanger, G. B., Castro Prates de Lima, E., and Siqueira, E. F. N. (2009). VIM and wave-frequency fatigue damage analysis for SCRs connected to monocolumn platforms. International Conference on Offshore Mechanics and Arctic Engineering,

Saito, M., Masanobu, S., Taniguchi, T., Otsubo, K., Asanuma, T., and Maeda, K. (2012). Experimental evaluation of VIM on MPSO in combined environmental conditions for waves and current. International Conference on Offshore Mechanics and Arctic Engineering,

Sarpkaya, T. (1986). Force on a circular cylinder in viscous oscillatory flow at low Keulegan—Carpenter numbers. Journal of Fluid Mechanics, 165, 61-71.

Sarpkaya, T. (2004). A critical review of the intrinsic nature of vortex-induced vibrations. Journal of Fluids and Structures, 19(4), 389-447.

SBM Offshore. (2021). SBM Offshore S3® Wave Energy Converter.

https://iro.nl/app/uploads/2021/03/SBM-Offshore-S3%C2%AE-Wave-Energy-Converter.pdf

Sen, S., Ganguly, S. (2017). Opportunities, barriers and issues with renewable energy development–A discussion. Renewable and Sustainable Energy Reviews, 69, 1170-1181.

Shabana, A. A. (1997). Flexible multibody dynamics: review of past and recent developments. Multibody system dynamics, 1(2), 189-222.

Shakoor, R., Hassan, M. Y., Raheem, A., and Wu, Y.-K. (2016). Wake effect modeling: A review of wind farm layout optimization using Jensen′ s model. Renewable and Sustainable Energy Reviews, 58, 1048-1059.

Shen, W. Z., Mikkelsen, R., Sørensen, J. N., and Bak, C. (2005). Tip loss corrections for wind turbine computations. Wind Energy: An International Journal for Progress and Applications in Wind Power Conversion Technology, 8(4), 457-475.

SMart Wind. (2014). Hornsea Offshore Wind Farm Project One.

So, R., Simmons, A., Brekken, T., Ruehl, K., and Michelen, C. (2015). Development of pto-sim: A power performance module for the open-source wave energy converter code wec-sim. International Conference on Offshore Mechanics and Arctic Engineering,

Sorensen, J. N., and Shen, W. Z. (2002). Numerical modeling of wind turbine wakes. J. Fluids Eng., 124(2), 393-399.

Sorensen, N., and Hansen, M. (1998). Rotor performance predictions using a Navier-Stokes method. 1998 ASME wind energy symposium,

Sricharan, V., and Chandrasekaran, S. (2021). Time-domain analysis of a bean-shaped multi-body floating wave energy converter with a hydraulic power take-off using WEC-Sim. Energy, 223, 119985.

Sumer, B. M. (2006). Hydrodynamics around cylindrical strucures (Vol. 26). World scientific.

Thiagarajan, K., and Dagher, H. (2014). A review of floating platform concepts for offshore wind energy generation. Journal of Offshore Mechanics and Arctic Engineering, 136(2), 020903.

Ticona Rollano, F., Tran, T. T., Yu, Y.-H., García-Medina, G., and Yang, Z. (2020). Influence of Time and Frequency Domain Wave Forcing on the Power Estimation of a Wave Energy Converter Array. Journal of Marine Science and Engineering, 8(3), 171.

Tran, T., Kim, D., and Song, J. (2014). Computational fluid dynamic analysis of a floating offshore wind turbine experiencing platform pitching motion. Energies, 7(8), 5011-5026.

Tran, T. T., and Kim, D.-H. (2016a). Fully coupled aero-hydrodynamic analysis of a semi-submersible FOWT using a dynamic fluid body interaction approach. Renewable Energy, 92, 244-261.

Tran, T. T., and Kim, D.-H. (2016b). A CFD study into the influence of unsteady aerodynamic interference on wind turbine surge motion. *Renewable Energy*, *90*, 204-228.

Troldborg, N., Sorensen, J. N., and Mikkelsen, R. (2010). Numerical simulations of wake characteristics of a wind turbine in uniform inflow. Wind Energy: An International Journal for Progress and Applications in Wind Power Conversion Technology, 13(1), 86-99.

Troldborg, N., Sørensen, J. N., and Mikkelsen, R. (2007). Actuator line simulation of wake of wind turbine operating in turbulent inflow. Journal of physics: conference series,

Van Rees, W. M., Leonard, A., Pullin, D. I., and Koumoutsakos, P. (2011). A

comparison of vortex and pseudo-spectral methods for the simulation of periodic vortical flows at high Reynolds numbers. Journal of Computational Physics, 230(8), 2794-2805.

van Rij, J., Yu, Y.-H., McCall, A., and Coe, R. G. (2019). Extreme load computational fluid dynamics analysis and verification for a multibody wave energy converter. International Conference on Offshore Mechanics and Arctic Engineering,

Vinayan, V., Antony, A., Halkyard, J., Kim, S.-J., Holmes, S., and Spernjak, D. (2015). Vortex-induced motion of deep-draft semisubmersibles: A CFD-based parametric study. International Conference on Offshore Mechanics and Arctic Engineering,

Vries, O. d. (1979). Fluid dynamic aspects of wind energy conversion. AGARD Report AG-243.

Wagenaar, J. W., Machielse, L., and Schepers, J. (2012). Controlling wind in ECN's scaled wind farm. Proc. Europe Premier Wind Energy Event, 1(01).

Walhorn, E., Hübner, B., and Dinkler, D. (2002). Space-Time Finite Elements for Fluid-Structure Interaction. PAMM: Proceedings in Applied Mathematics and Mechanics,

Wang, L., Robertson, A., Jonkman, J., Yu, Y.-H., Koop, A., Borràs Nadal, A., Li, H., Shi, W., Pinguet, R., and Zhou, Y. (2021). Investigation of nonlinear difference-frequency wave excitation on a semisubmersible offshore-wind platform with bichromatic-wave CFD simulations. International Conference on Offshore Mechanics and Arctic Engineering,

Wang, R.-q., and Ning, D.-z. (2020). Dynamic analysis of wave action on an OWC wave energy converter under the influence of viscosity. Renewable Energy, 150, 578-588.

Wang, W., Caro, S., Bennis, F., and Salinas Mejia, O. R. (2014). A simplified morphing blade for horizontal axis wind turbines. Journal of solar energy engineering, 136(1),

011018.

Wei, G., and Kirby, J. T. (1995). Time-dependent numerical code for extended Boussinesq equations. Journal of waterway, port, coastal, and ocean engineering, 121(5), 251-261.

Wilson, R. E., and Lissaman, P. B. (2018). Applied aerodynamics of wind power machines. Renewable Energy, Vol3_71-Vol73_120.

Wood, C., Gil, A., Hassan, O., and Bonet, J. (2010). Partitioned block-Gauss–Seidel coupling for dynamic fluid–structure interaction. Computers and Structures, 88(23-24), 1367-1382.

Wu, H., Zhu, F., and Yuan, Z. (2024). Effects of the WEC shape on the performance of a novel hybrid WEC-FOWT system. Energy, 288, 129907.

Wu, Y.-T., and Porté-Agel, F. (2011). Large-eddy simulation of wind-turbine wakes: evaluation of turbine parametrisations. Boundary-layer meteorology, 138, 345-366.

Wu, Y.-T., and Porté-Agel, F. (2015). Modeling turbine wakes and power losses within a wind farm using LES: An application to the Horns Rev offshore wind farm. Renewable Energy, 75, 945-955.

Xu, B., Wang, T., Yuan, Y., Zhao, Z., and Liu, H. (2018). A simplified free vortex wake model of wind turbines for axial steady conditions. Applied Sciences, 8(6), 866.

Xu, S., Zhuang, T., Zhao, W., and Wan, D. (2023). Numerical investigation of aerodynamic responses and wake characteristics of a floating offshore wind turbine under atmospheric boundary layer inflows. *Ocean Engineering*, *279*, 114527.

Xue, L., Wang, J., Zhao, L., Wei, Z., Yu, M., and Xue, Y. (2022). Wake Interactions of Two Tandem Semisubmersible Floating Offshore Wind Turbines Based on FAST.Farm. Journal of Marine Science and Engineering, 10(12). https://doi.org/10.3390/jmse10121962

Yao, T., Lu, Q., Wang, Y., Zhang, Y., Kuang, L., Zhang, Z., Zhao, Y., Han, Z., and Shao, Y. (2023). Numerical investigation of wake-induced lifetime fatigue load of two floating wind turbines in tandem with different spacings. Ocean Engineering, 285, 115464.

Yazdi, H., Ghafari, H. R., Ghassemi, H., He, G., and Karimirad, M. (2023). Wave power extraction by Multi-Salter's duck WECs arrayed on the floating offshore wind turbine platform. Energy, 278, 127930.

Yu, X., and Chwang, A. T. (1994). Wave-induced oscillation in harbor with porous breakwaters. Journal of waterway, port, coastal, and ocean engineering, 120(2), 125-144.

Yu, Z., Zheng, X., and Ma, Q. (2018). Study on actuator line modeling of two NREL 5-MW wind turbine wakes. Applied Sciences, 8(3), 434.

Zhang, L., Li, Y., Xu, W., Gao, Z., Fang, L., Li, R., Ding, B., Zhao, B., Leng, J., and He, F. (2022). Systematic analysis of performance and cost of two floating offshore wind turbines with significant interactions. Applied Energy, 321, 119341.

Zhao, M., and Cheng, L. (2014). Vortex-induced vibration of a circular cylinder of finite length. Physics of Fluids, 26(1). https://doi.org/10.1063/1.4862548

Zhao, M., Kaja, K., Xiang, Y., and Yan, G. (2013). Vortex-induced vibration (VIV) of a circular cylinder in combined steady and oscillatory flow. Ocean Engineering, 73, 83-95. https://doi.org/10.1016/j.oceaneng.2013.08.006

Zhao, W., Wolgamot, H., Taylor, P., and Taylor, R. E. (2017). Gap resonance and higher harmonics driven by focused transient wave groups. Journal of Fluid Mechanics, 812, 905-939.

Zhao, X., Ning, D., and Liang, D. (2019a). Experimental investigation on hydrodynamic performance of a breakwater-integrated WEC system. Ocean

Engineering, 171, 25-32.

Zhao, X., Ning, D., Zou, Q., Qiao, D., and Cai, S. (2019b). Hybrid floating breakwater-WEC system: A review. Ocean Engineering, 186, 106126.

Zheng, S., Greaves, D., Meylan, M. H., and Iglesias, G. (2020). Wave power extraction by a submerged piezoelectric plate. Developments in Renewable Energies Offshore: Proceedings of the 4th International Conference on Renewable Energies Offshore (RENEW 2020, 12-15 October 2020, Lisbon, Portugal)

Zhong, W., Zhang, X., and Wan, D. (2023). Hydrodynamic characteristics of a 15 MW semi-submersible floating offshore wind turbine in freak waves. *Ocean Engineering*, *283*, 115094.

Zhou, Xiao, Liu, Incecik, Peyrard, Li, and Pan. (2019). Numerical Modelling of Dynamic Responses of a Floating Offshore Wind Turbine Subject to Focused Waves. Energies, 12(18). https://doi.org/10.3390/en12183482

Zhou, Y., Ning, D., Liang, D., and Cai, S. (2021). Nonlinear hydrodynamic analysis of an offshore oscillating water column wave energy converter. Renewable and Sustainable Energy Reviews, 145, 111086.

Zhou, Y., Xiao, Q., Peyrard, C., and Pan, G. (2021). Assessing focused wave applicability on a coupled aero-hydro-mooring FOWT system using CFD approach. Ocean Engineering, 240. https://doi.org/10.1016/j.oceaneng.2021.109987

ZOIA, C. (2022). Modeling of an offshore wind power plant: the Hornsea II test case.

Zurkinden, A. S., Ferri, F., Beatty, S., Kofoed, J. P., and Kramer, M. (2014). Non-linear numerical modeling and experimental testing of a point absorber wave energy converter. Ocean Engineering, 78, 11-21.